QSO Absorption Lines

John Kelvin Webb

Trinity Hall, Cambridge

and

The Institute of Astronomy, Cambridge

February 1987

A dissertation submitted to the University of Cambridge in accordance with the regulations for admission to the degree of Doctor of Philosophy

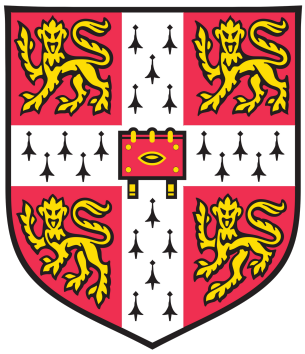

Typeset in LaTeX 2_ε.

Preface

This dissertation is the result of my own work and other than where specifically stated includes nothing which is the outcome of work done in collaboration. It is not substantially the same as any work that I have submitted or will submit for a degree, diploma or other qualification at another university.

February 1987 J.K. Webb

Abstract

The absorption lines found in the spectra of distant quasars provide a unique method of probing the physical conditions in the universe at early epochs.

This thesis describes a study of the Lyman alpha forest absorption systems seen in the spectra of high redshift QSOs. The Anglo-Australian Telescope has been used to obtain high resolution spectra of several bright QSOs.

Considerable effort has gone into developing statistical techniques for profile fitting to the data to objectively and reliably extract the parameters associated with each absorbing cloud. The distribution functions for these are given and discussed.

Particular attention has been paid to the clustering properties of the Lyman alpha clouds and it is found that they are weakly (but significantly) clustered on small velocity scales. Possible interpretations of this result are discussed.

One especially interesting aspect of QSO absorption systems concerns the potential for measuring, or obtaining limits on, the deuterium to hydrogen abundance at high redshifts. A knowledge of this quantity is important for constraining cosmological models and can also help us to understand the chemical evolution of light elements in galaxies. A series of numerical simulations has been carried out to explore the potential for such measurements and an absorption system has been analysed to obtain an upper limit to D/H at z = 3.

Acknowledgments

It has been a pleasure to work with Bob Carswell, my supervisor, and I thank him for his patient guidance throughout this work. I am grateful also to Mike Irwin for his expert help and advice on the statistical methods developed in Chapters 3 and 4. Early on in this project, Donald Lynden-Bell offered invaluable advice and I am indebted to him for that. I have enjoyed numerous stimulating and educational discussions with many people at the IOA and in particular I am grateful to Nick Kaiser and Paul Hewett for valuable suggestions. My various office colleagues, past and present, deserve a mention and I thank them for their ideas, arguments, enlightenment and humour. I thank the staff of the Anglo-Australian Telescope for their assistance during the many observing runs required to obtain the data presented in this thesis and I am grateful to PATT and to the SERC for making these trips possible. I acknowledge the financial support of the SERC and the Cambridge Philosophical Society during my time in Cambridge and I thank the Institute of Astronomy and Trinity Hall for hospitality and travel grants. Last but not least I especially thank Linda Saunt for proof reading this manuscript and for her encouragement.

Contents

1 Introduction

Shortly after the identification of the first quasar (Schmidt, 1963) came the realisation that in addition to being fascinating objects in their own right, quasars could also be used as background probes to study the physical properties and distribution of matter over vast path lengths through the universe (Scheuer, 1965; Gunn and Peterson, 1965; Bahcall and Salpeter, 1965). The absorption lines detected in quasar spectra, arising in gas clouds intersecting the line of sight, subsequently created enormous interest and controversy as to their origin.

There are three basic categories of absorption systems: very broad absorption troughs, generally believed to be associated with matter ejected from a host QSO, narrow absorption line systems identified transitions of several different ions at the same redshift (e.g. HI, CIV and SIV), and narrow absorption line systems comprising only transitions of the hydrogen Lyman series (the Lyman alpha forest lines). The latter forms the basis of the study described here. For a comprehensive and general review of quasar absorption lines, see Weymann et al. (1981). A recent review concerning just the Lyman forest lines is given by Sargent and Boksenberg (1983).

In order for the Lyα transition to be shifted into the visible part of the spec-

trum, the redshift of an absorption system must be greater than about 1.7. At present, the majority of published Lyα absorption spectra are at a spectral resolution (around 1Å FWHM or lower) sufficiently high to clearly detect the stronger absorption features (Sargent et al., 1980; Carswell et al., 1982) but not high enough to resolve individual absorption profiles. The information that can be extracted from such data, for any absorption feature, is the redshift and the equivalent width. Several important discoveries on the properties of the Lyα systems have been made, the most notable perhaps being that the number of Lyα lines per unit redshift interval increases rapidly with redshift (Peterson, 1978; Murdoch et al., 1986). The evolution in the number density is considerably faster than can be accounted for by cosmological effects alone, indicating evolution in the absorption cross section of the Lyα clouds. The statistical properties of the Lyman clouds are discussed in detail in the reviews by Weymann et al. (1981) and Sargent and Boksenberg (1983)

In spite of the fairly large existing Lyα line sample, the nature of these objects is still poorly understood. Sargent et al. (1980) carried out a statistical survey of the Lyα clouds in the spectra of six high redshift QSOs. one of the results of that work was that the Lyα clouds are a population of objects which are physically distinct from the less abundant metal containing absorption systems (and therefore, presumably, also distinct from the galaxies). The main argument leading to this belief was derived from clustering analyses of the Lyα clouds and a sample of CIV absorption lines; whilst a strong peak was found in the correlation function of the CIV lines on a scale of around 150 km/s, no such peak was detected for the Lyα lines. An apparent reinforcement of the separate population hypothesis came from subsequent work (Chaffee et al., 1985; Sargent and Boksenberg, 1983) which suggested that the Lyα clouds are poor in heavy elements. However, this last fact does not necessarily indicate that the Lyα only systems are physically distinct from the metal-line systems; we

do not yet know whether there exists a continuous distribution of abundances for QSO absorption systems.

Concerning the observed differences in the clustering properties in the two types of absorption systems, it is possible that real differences are enhanced by selection effects; CIV absorption is usually identified through its doublet (1548 and 1550 Å). Having a close doublet free from confusion with numerous other lines makes deblending much easier. The analogy for the Lyman clouds would be to use Lyα and Lyβ to define a sample for a clustering analysis. However, for Lyβ to be detectable, the neutral hydrogen column density must be higher than the average Lyα forest system; this of course means that the absorption lines are broader and that close pairs are difficult to deblend. The Lyβ line itself is quite likely to be blended with a lower redshift Lyα line, confusing the issue further still. The magnitude of these effects is not yet clear.

In summary then, it appears that we do not know whether the Lyα forest systems and metal-containing systems are physically distinct or whether they belong to one contiguous population of objects. A claim supporting the latter has been made recently by Tytler (1987). He finds that the distribution of equivalent widths of the Lyα forest and Lyα metal-containing systems form a continuous distribution. If the result is confirmed, this would be strong evidence for a continuous population of objects, or a remarkable coincidence.

The aim at the begining of the work for this thesis was to collect data, at high resolution, on some of the brightest QSOs. When the spectral resolution is high enough, the profile of a single absorbing cloud can be resolved and model fitted to extract the more physically interesting column density of absorbing atoms and velocity dispersion parameter, in addition to the redshift. Such data, although far more difficult to obtain and analyse, provide us with more

reliable information on both metal-abundances and the redshift distribution of QSO absorption systems. The spectral resolution of the Lyα samples of Sargent et al. (1980), restricted previous clustering analyses to scales above about 300 km/s. Consequently, an important motivation for collecting the high resolution data is to extend the correlation function down to around 50 km/s.

The structure of the remainder of the thesis is as follows. In Chapter 2, I give some of the observational details and show plots of the data. The profile fitting procedure adopted is described in Chapter 3. The techniques outlined in that chapter differ significantly from those used previously; to make the best use of the high quality data obtained at the AAT, more sophisticated methods were desirable. Chapter 4 is devoted to a discussion on the deuterium abundance in absorption systems and a series of numerical simulations are described which attempt to demonstrate how D/H may be estimated from several Lyman lines. Chapter 5 contains the results of the profile fitting to the data shown in Chapter 2 and examples of blended profiles are shown along with their final best fit models. Chapter 6 concentrates mainly on a clustering analysis of the Lyα clouds and Chapter 7 outlines the main achievements of this thesis and offers some possible interpretations of the clustering properties.

2 Observations and data reduction

2.1 Introduction

The QSO's observed were selected as part of a general programme to investigate the statistical properties of the Lyα clouds. They were chosen because they were the brightest accessible at a suitable redshift at the time of observation. Table 2.1 is a list of the objects observed and gives their redshifts, optical magnitudes and references for their discovery and redshift estimates. A journal of the observations carried out at the AAT is given in Table 2.2.

Table 2.1: QSOs observed

Object	z_e	M_V	**References (Finding chart; redshift)**
0207-398	2.805	17.15	Smith, 1976; Osmer and Smith, 1976
1158-187	2.448	17.01	Kunth et al., 1981
1358+113	2.571	16.5	Hazard et al., 1986
1448-232	2.208	16.96	Savage et al., 1977, 1976
2204-573	2.725	17.36	Bolton and Savage, 1977; Savage et al., 1976

(Where only one reference is given, it contains both the finding chart and redshift details.)

Table 2.2: Journal of QSO observations

Object	**Date**	**Seeing**	**Int**	λ**(Å)**
Q207-398	4-12-82	1-1.8	100	4527
”	”	”	160	4418
”	5-12-82	1-1.5	160	3733
”	27-10-83	1-1.5	290	4531
”	28-10-83	1.2-2	50	4503
”	1-8-84	2	197	4123
”	2-8-84	1.5	200	”
1158-187	13-2-85	1.5	183	4065
”	14-2-85	3-4	128	”
”	15-2-85	2	179	”
”	17-2-85	5-6	100	”
1358+113	21-6-85	3-5	133	4255
”	22-6-85	4-5	109	”
”	23-6-85	3	133	”
”	24-6-85	1.5-2.5	200	”
1448-232	31-7-84	2.3-3.5	200	3745
”	1-8-84	1.4-2	200	”
”	2-8-84	1.5	200	”
2204-573	30-7-84	3-4	50	4410
”	31-7-84	2.5	99	4300
”	1-8-84	2	150	”
”	2-8-84	1.5	125	”
”	3-8-84	1.5-2	200	4180
”	21-6-85	4-5	67	4410
”	23-6-85	2.5	200	”

The seeing values are approximate and are in arcseconds. The fourth column is the integration time in minutes. The wavelength given in column five is the starting value for the interval observed; the coverage per integration is about 140Å.

2.2 Instrumental details and data reduction

The QSO spectra were obtained using the IPCS mounted on the RGO spectrograph at the f/8 Cassegrain focus of the 3.9m Anglo-Australian Telescope. A 1200 lines/ram grating was used in second order together with the 82cm focal length camera. The resulting dispersion was about 5Å/mm giving a wavelength coverage of around 140Å for each exposure.

The number of detector elements spanned by the object in the spatial direction is evidently seeing-dependent but typically was between 2 and 5 pixels. In order to reduce the effect of any possible change in system response during the observing run, and also to take into account any intensity variations along the spectrograph slit, the object was "aperture-switched" between two positions on the IPCS. The integration time for any sequence of exposures was kept constant where possible, with integration times between 1200 and 2000 seconds. Between each object exposure, the spectrum from a Cu-Ar lamp was recorded. The techniques used for extracting the calibrated one-dimensional spectra are the same as described by Carswell et al. (1982) and Carswell et al. (1984). Consequently, only brief details are given here together with details of a few minor modifications to the previous methods.

To minimise the noise introduced into the reduced spectrum by sky subtraction, the sky contribution was estimated from an extended sky area of about 30 increments. The advantage of doing this is that a considerable reduction in the noise over the absorption line profiles is achieved. Strictly, a full two-dimensional wavelength calibration should be done before extracting in this way; if there is significant structure in the sky spectrum and the wavelength varies along the increments, then sky subtraction without a 2-d wavelength calibration could cause unwanted structure to appear in the final object spec-

trum. However, for speed and simplicity, only the summed object and sky increments were used in the wavelength calibration. In each case a visual check for structure was made in the summed sky spectrum. The Cu-Ar arc spectra were extracted in exactly the same way as the object and the FWHM of unblended lines used to estimate the spectral resolution as a function of wavelength. Individual object runs were added together using weights appropriate to their signal-to-noise ratio. The wavelength scale for each run was established in the usual way, using a polynomial fit to the unblended arc lines. The r.m.s. residuals were approximately 0.01Å or less, which is about an order of magnitude below the absorption line redshift error obtained from the profile fitting analysis. Although exposures of a continuum source were recorded at the telescope, the QSO spectra were not flat-fielded since the pixel to pixel sensitivity variation was much smaller than the noise in the data. Also, it was decided not to remove the instrumental response using a standard star spectrum since response variations occur on a larger scale than absorption feature. (Nevertheless, standard stars were observed in case future analyses of the same data should require response corrected spectra.)

Figures 2.1 to 2.11 show the reduced spectra. Also plotted is the estimated 1σ error term (Carswell et al., 1984) and the adopted continuum level (see next section).

2.3 Continuum fitting

Before estimating wavelengths and equivalent widths, or fitting absorption profiles to the data, a continuum level must be determined. Continuum fitting to absorption line spectra has been discussed by several authors (Carswell et al., 1982; Trew and Brand, 1984; Young et al., 1979). After experimenting with a variety of procedures, a new method was devised which, although differing

from those discussed in the literature, is effectively a refined version of previous attempts.

The technique adopted may be summarised as a weighted least-squares cubic spline fitting algorithm with optimal sigma clipping incorporating a method to correct for non-random noise properties.

A weighted least-squares spline fit to the spectrum is obtained using the NAG library Fortran IV subroutines EO2BAF and EO2BBF. The input parameters for the fit are the number and positions of the knots, or nodes. Experiments with several spectra and varying numbers of nodes indicated that roughly 7 nodes per 1000 data points gave satisfactory results. Where there were no rapid changes in the shape of the continuum, (i.e. no emission lines), evenly spaced knots were used. Over emission lines, a higher knot density was necessary. This could, in principle, be quantified by relating the knot density to the derivative of the continuum; a region of spectrum where the derivative is high would indicate the need for a higher knot density and vice would have to be incorporated. In general, less than 7 knots per 1000 channels gave a significantly poorer normalised chi-squared, whilst more than this number did not make much difference. Since there are no physical grounds on which to base an estimate for the number of free parameters that should be associated with the continuum fit, this node density was taken as standard. Exceptionally, in spectra containing a region with a particularly high relative absorption line density, where interpolation across the region becomes extremely unreliable, less than 7 knots per 1000 channels were used.

Once the first fit is obtained, the data is subjected to a σ-clipping process. A data-block size is chosen to match the expected width of an absorption feature and, starting at one end of the spectrum and stepping along to the other one

channel at a time, we calculate

$$S_{\rm b} = \Sigma(c_i - d_i), \text{and} \tag{2.3.1}$$

$$\sigma_b^2 = \Sigma\sigma_i^2 \tag{2.3.2}$$

where c_i is the value of the current continuum fit at the $i^{\rm th}$ channel in the block, d_i is the data value, σ_i^2 is the variance estimated from Poisson counting statistics of both object and sky, and the summation is taken over the m channels in the block. Then, if $S_b < k\sigma_b$, each channel in the block is flagged to be included in the next iteration of the fit, and if $S_b \geq k\sigma_b$, each channel is flagged to be discarded before the next iteration. The choice of the value of k is obviously important; if it is very large no clipping occurs and vice versa. Consequently, the following objective procedure was used to determine an "optimal" value of k.

Let the value of k be such that, on average, the maximum number of block-data points that will be clipped which are random noise and not real features be 1.0. If the total number of clipping trials is N_C, then

$$1/(2N_C) = p = 1/\sqrt{2\pi}\int_{-\infty}^{-x_p} e^{-u^2/2}du \tag{2.3.3}$$

for $-\infty < x_p < \infty$, where x_p is the deviate associated with the lower tail probability of the standardised normal distribution. The value of k is then simply $k = x_p$.

Note that the above is only true for Poisson noise. It is found that the noise in the continuum is significantly non-Poisson; there are several possible explanations for this: (i) rebinning to a linear wavelength scale smooths the data slightly, (ii) the adopted parameterisation is an inadequate representation of

the true underlying continuum level, (iii) there are weak undetected features in the data (i.e. absorption or emission lines), and (iv) adjacent pixels in the detector are correlated. This departure from Poisson errors may be taken into account (see section 5.4) simply by rescaling the variance array for the data by the normalised χ^2 for the continuum fit at each iteration. This is only an approximation since the implicit assumption is that the noise properties do not change with wavelength. Note that the iteratlve rescaling reduces the effect of the clipping procedure for data having smaller than $\sqrt{n}$ scatter, but that it is required in order for the amount of clipping to be consistent with the chosen criterion.

2.3.1 The effects of errors in the continuum

In spectral regions where the number density of absorption lines is high, it seems likely that the continuum may be placed lower than the true level. Also, there could be a population of weak absorption lines which individually are not detectable but which collectively result in a systematically lowered continuum. We can estimate the effect of this on the inferred absorption line properties in the following way. Assume that weak absorption lines are approximately triangular. Let the true continuum level be i, and the estimated level be $1-\epsilon$. If the depth of the line centre is f, and the FWHM of the line is w_h, the true equivalent width is

$$W = w_h f \tag{2.3.4}$$

The estimated FWHM is

$$w'_h = w_h - w_h \epsilon / h \tag{2.3.5}$$

and so the estimated equivalent width is

$$W' = w_h (1 - \epsilon/f)(f - \epsilon) \tag{2.3.6}$$

therefore the fractional change in the equivalent width is

$$(W - W')/W = 2\epsilon/f - \epsilon^2/f^2 \tag{2.3.7}$$

The FWHM of a weak absorption line is approximately $2.35\lambda b/c\sqrt{2}$, so for a line with $b = 30$ km/s at 3500Å, the FWHM is 0.6Å(which corresponds to 10 channels in the AAT data). If we take $N(\mathrm{HI}) = 2 \times 10^{13}$ atoms/cm^2 as an example of a weak line, the observed equivalent width (at 3500Å) is about 0.25Åso $f \simeq 0.4$. Suppose that the continuum has been placed too low by about 5 percent (this is probably an overestimate for low redshifts but an underestimate for high redshifts), then the fractional error in the equivalent width is roughly 20 percent. At low column densities, $W \propto N(\mathrm{HI})$, so the column density estimates may be in error by as much as 20 percent. Note that this source of error is comparable in magnitude to that associated with the profile fitting error estimate (for weak lines). For stronger lines (where the line centres go to zero intensity) the error in the $N(\mathrm{HI})$ estimate due to continuum placement will be far less for two reasons: firstly, the profile becomes more rectangular than triangular, so lowering the continuum has a smaller effect on the equivalent width; secondly, on the flat part of the curve of growth $N(\mathrm{HI})$ is far less sensitive to W.

Figure 2.1: Q0207-398 from 3730 to 3870 Å

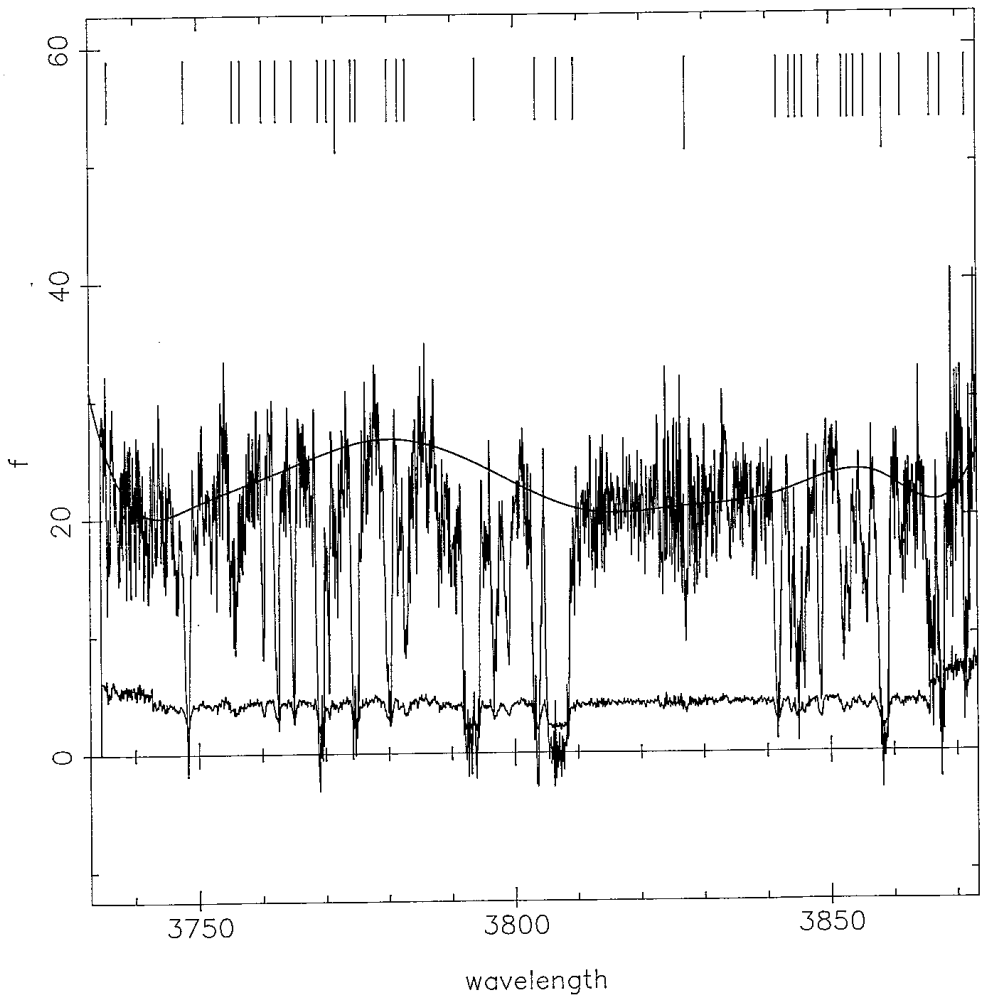

Figure 2.2: Q0207-398 from 4120 to 4250 Å

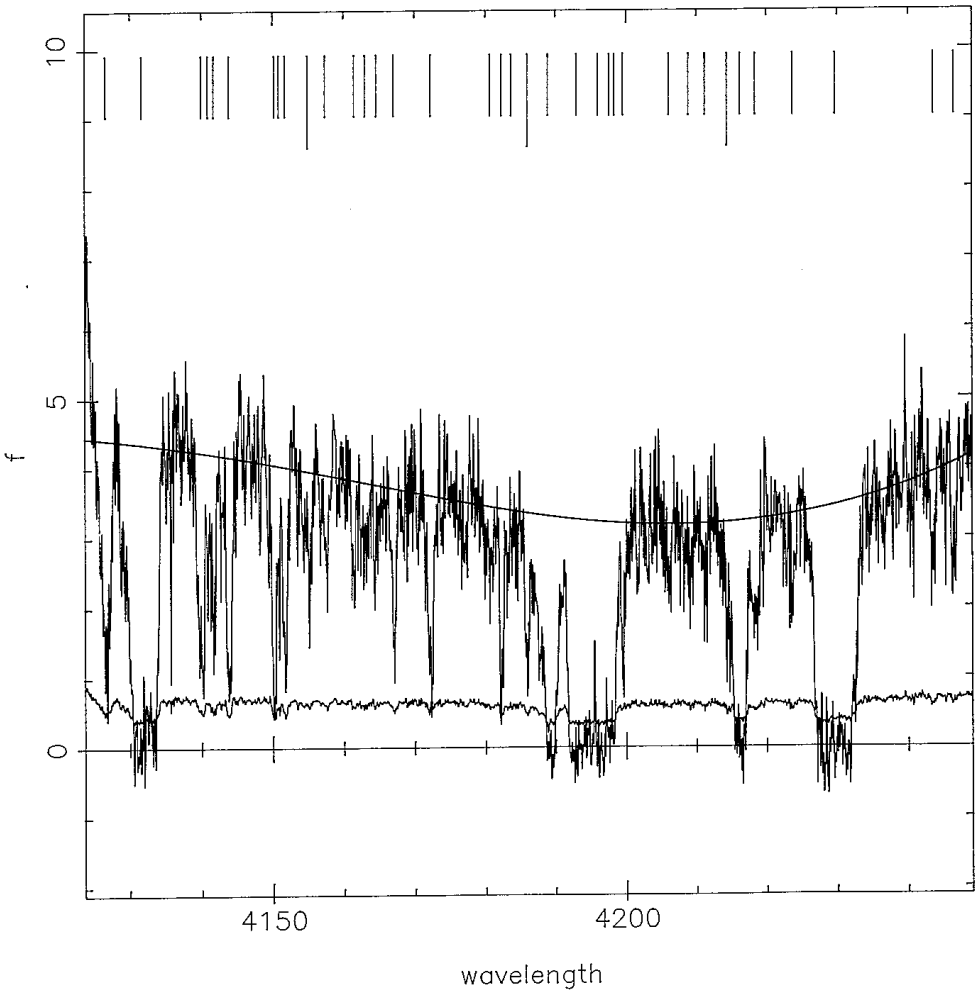

Figure 2.3: Q0207-398 from 4420 to 4550 Å

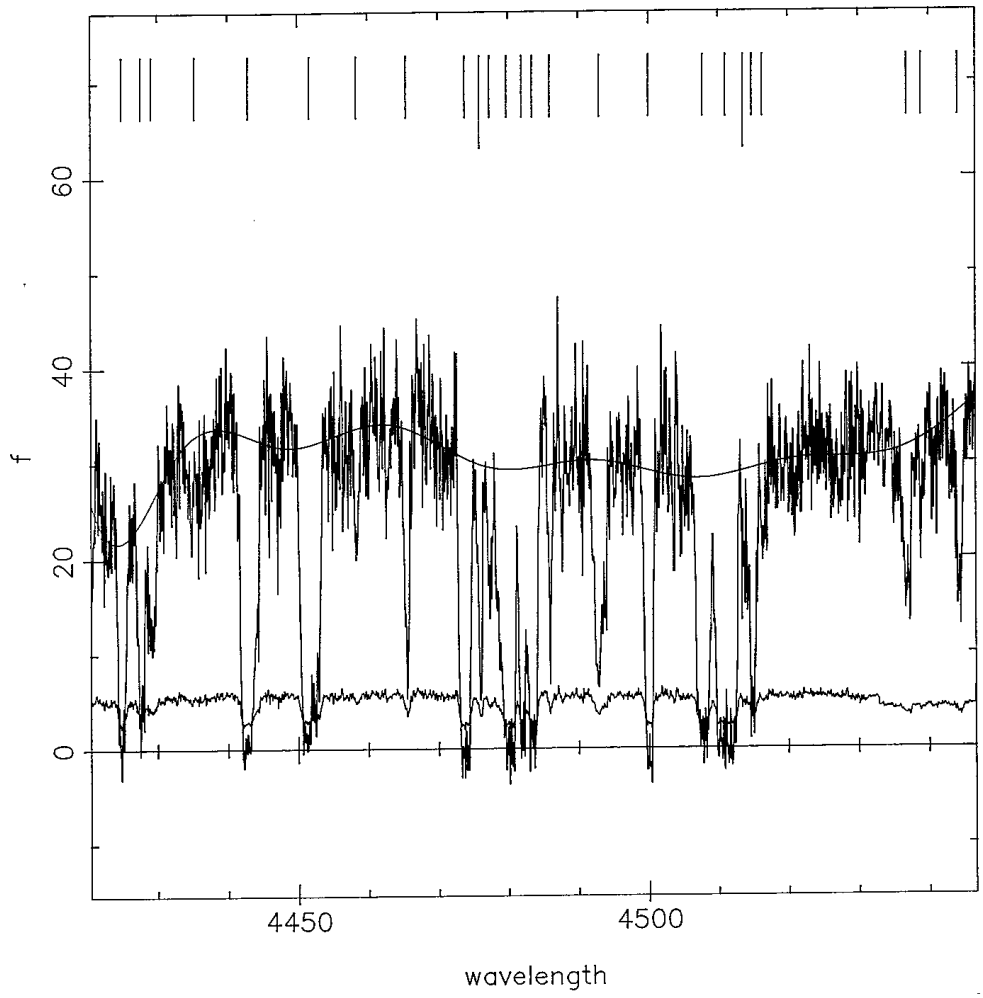

Figure 2.4: Q0207-398 from 4470 to 4600 Å

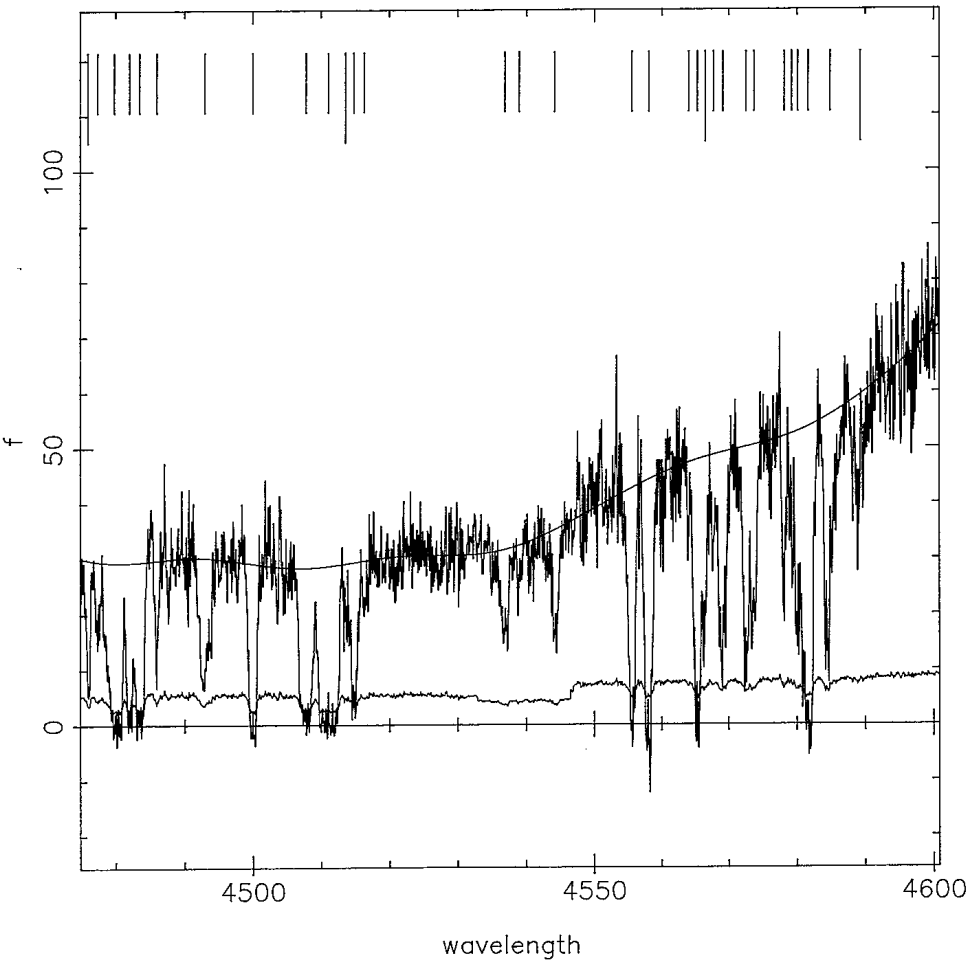

Figure 2.5: Q0207-398 from 4530 to 4650 Å

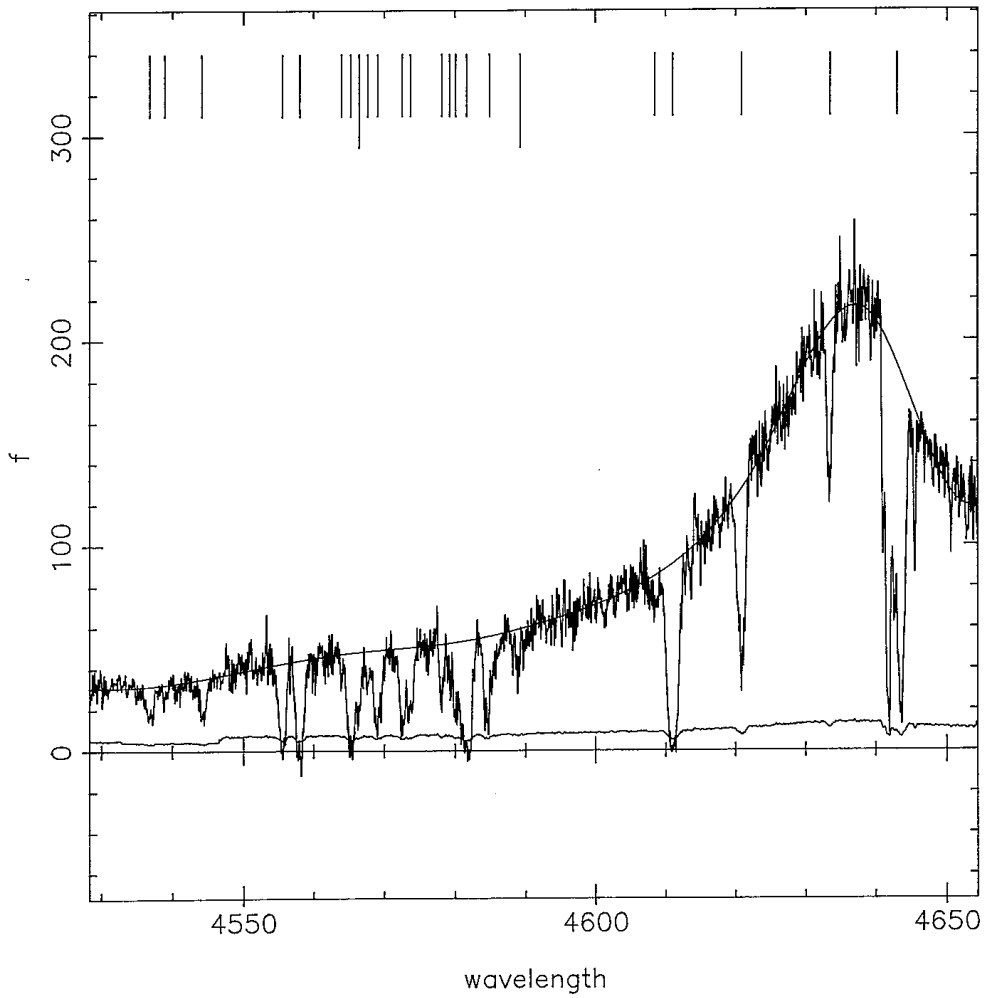

Figure 2.6: Q1158-187 from 4050 to 4200 Å

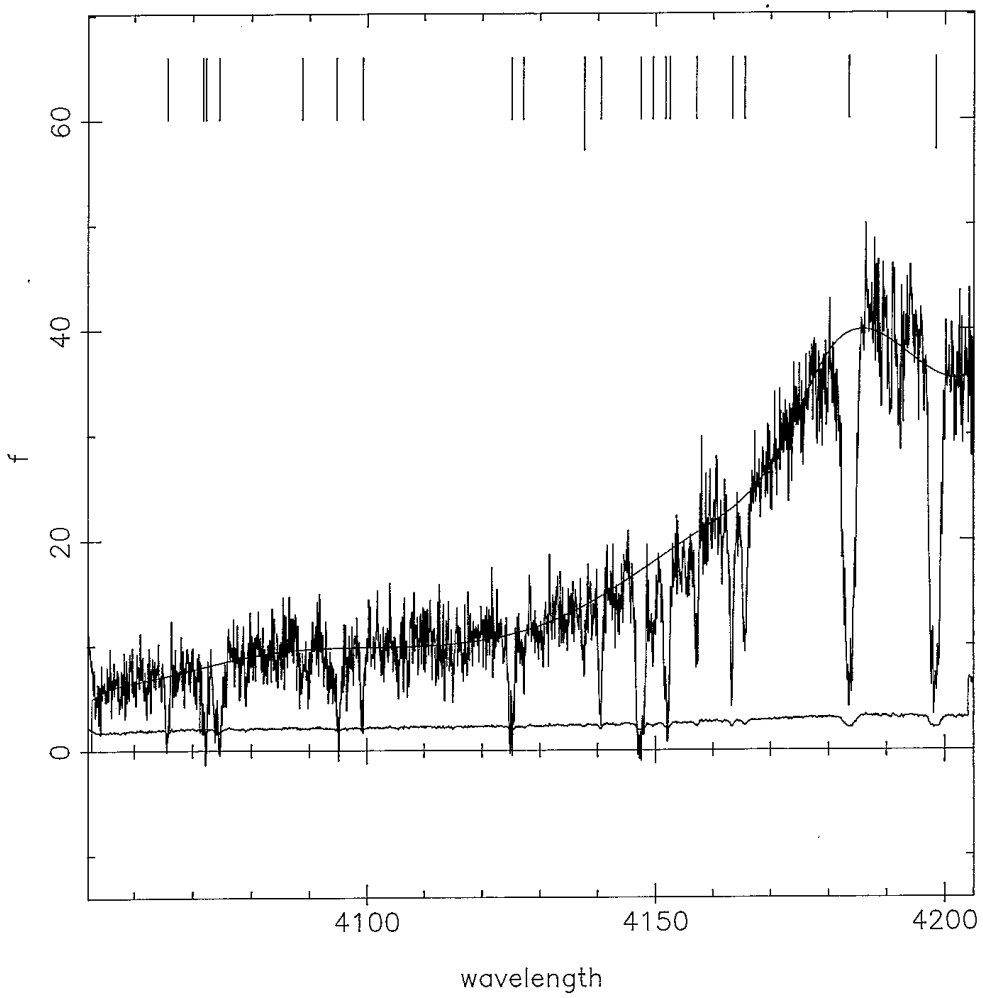

Figure 2.7: Q1358+113 from 4250 to 4390 Å

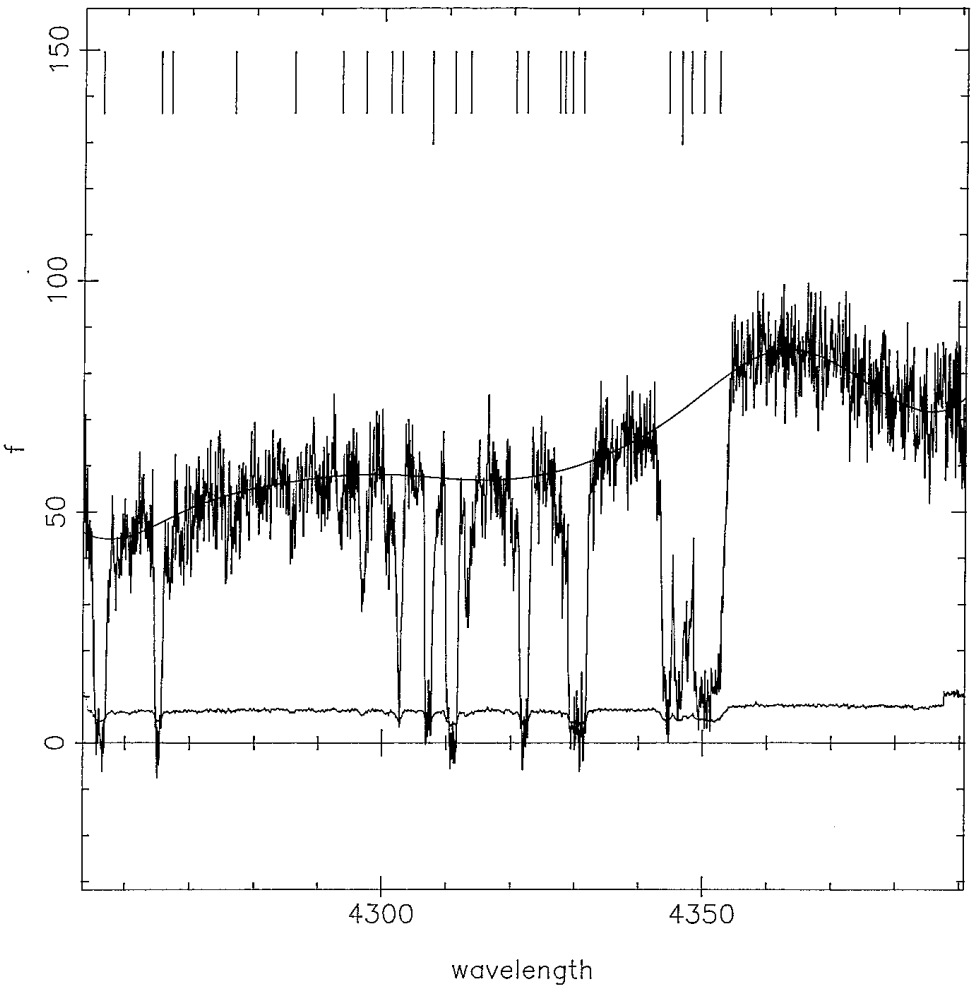

Figure 2.8: Q1448-232 from 3740 to 3870 Å

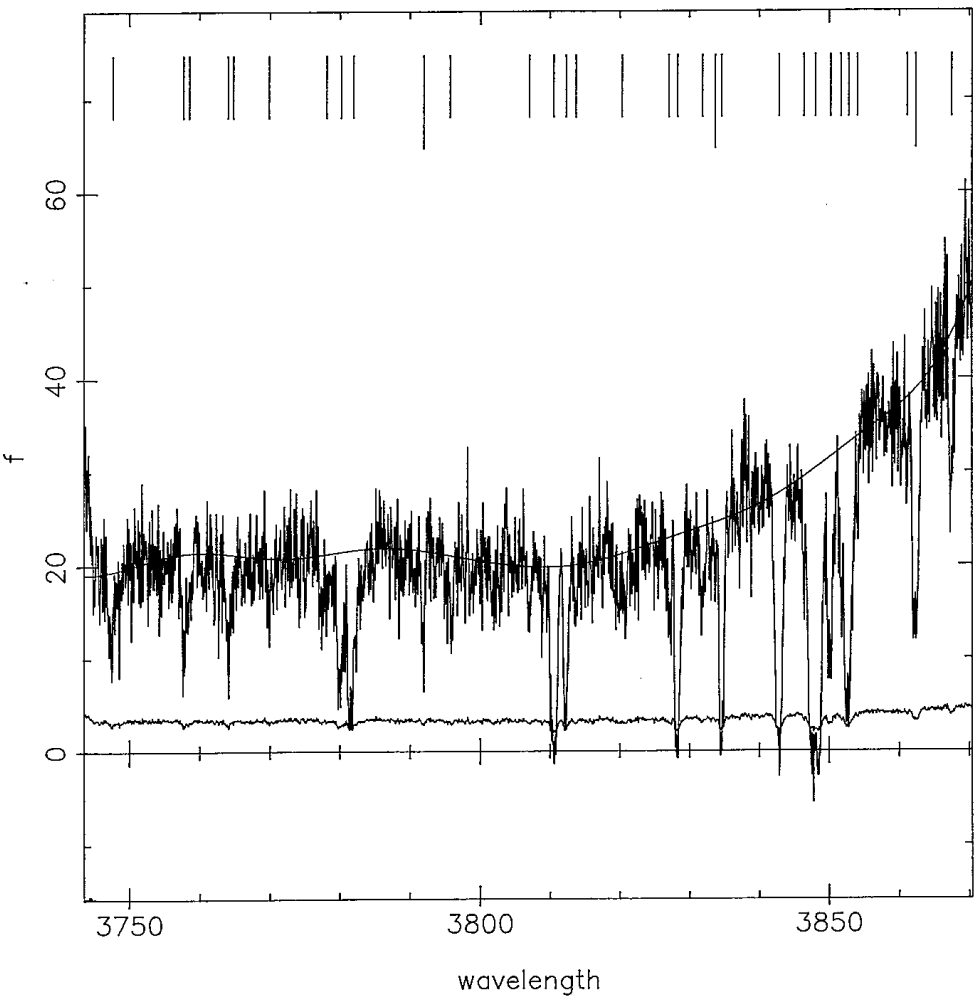

Figure 2.9: Q2204-573 from 4180 to 4310 Å

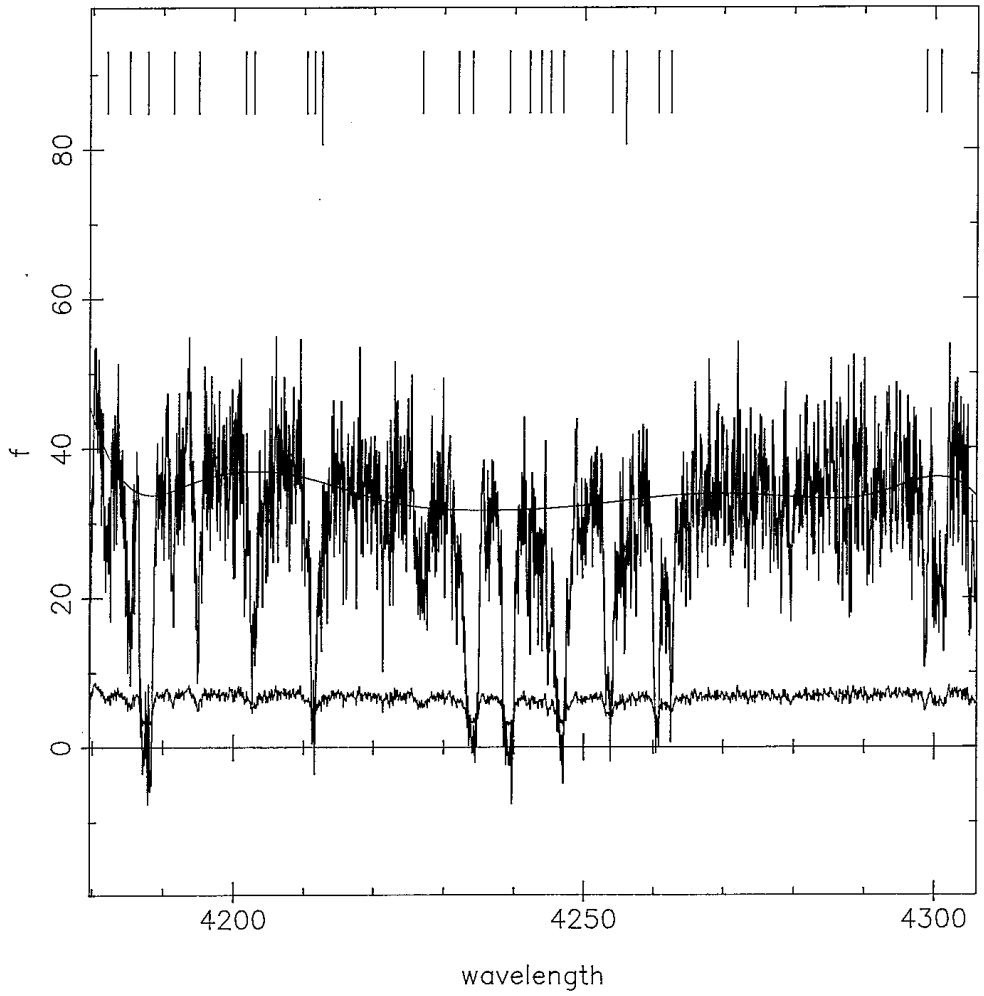

Figure 2.10: Q2204-573 from 4300 to 4420 Å

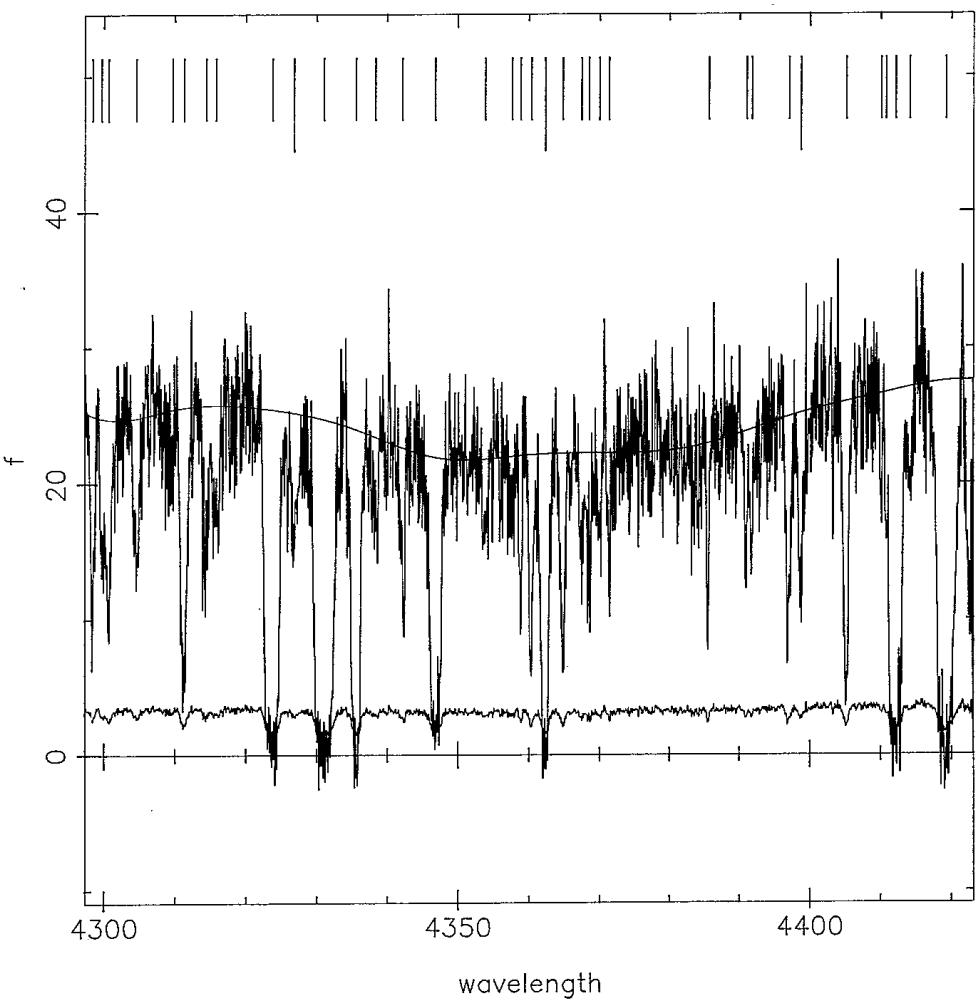

Figure 2.11: Q2204-573 from 4400 to 4550 Å

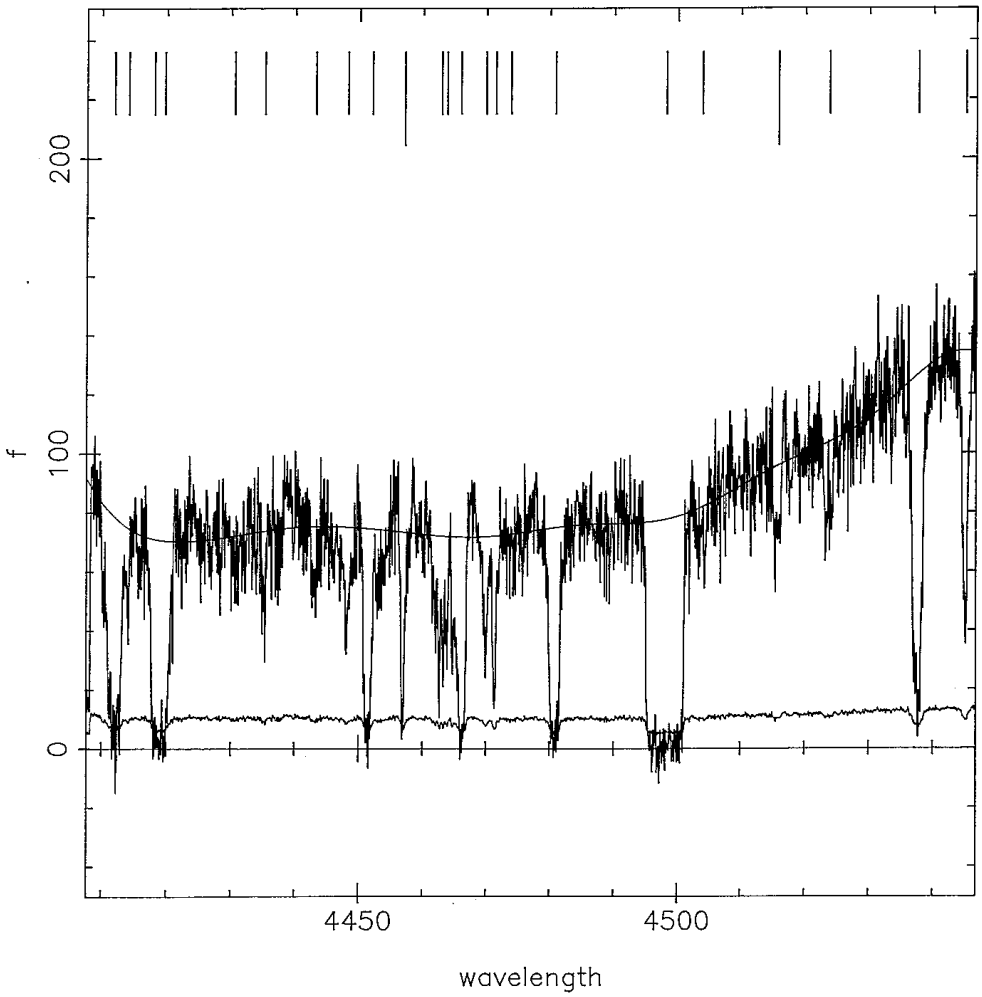

3 Maximum likelihood optimisation

Introduction

Faced with the task of profile matching to a complex of several blended absorption lines, existing techniques required that one component at a time be extracted (Carswell et al., 1984). Whilst this may be an adequate approach for well separated lines, it fails for badly blended features and the results can depend heavily on the judgement of the analyst. Consequently, an optimisation technique was developed which enables a search in parameter space of several variables and can therefore fit a complex blend of several absorption lines simultaneously. This Chapter is concerned with the details of that technique, but first an outline is given on the calculation of a model absorption line.

3.1 Basic absorption line theory

To calculate a theoretical absorption profile, we define the model function as follows.

Assume that, in the rest frame of the cloud, the probability distribution function for atomic velocities is Maxwellian, i.e.

$$\psi(v)dv = \frac{1}{b\sqrt{\pi}} \exp\left[-\frac{v^2}{b^2}\right] dv \tag{3.1.1}$$

b is the velocity dispersion parameter and, if the line broadening is thermal, it is related to the cloud temperature T by

$$b = \left[\frac{2kT}{M_a}\right]^{1/2} \tag{3.1.2}$$

where M_a is the atomic mass.

If turbulent motions contribute to the observed velocity dispersion, the thermal and non-thermal components add in quadrature (Struve and Elvey, 1934) and the value of T obtained from the relation above may be considered as an upper limit to the cloud temperature.

The absorption coefficient in a line at central frequency ν_o is calculated from the theory of damped quantum mechanical oscillators, (see for example Mihalas, 1970), to be

$$\alpha(\nu) = \frac{\pi e^2}{m_e c} f \frac{\Gamma/4\pi^2}{(\nu - \nu_0)^2 + (\Gamma/4\pi)^2} \tag{3.1.3}$$

where f is the oscillator strength associated with the transition, m_e and e refer to the electron mass and charge and c is the velocity of light. If the transition is from the ground state then the sum of the spontaneous emission rates is

$$\Gamma = \sum_j A_{kj} \text{ for } j, k \tag{3.1.4}$$

where k refers to the upper level. If the lower level is also an excited state,

$$\Gamma = \Gamma_l + \Gamma_u = \sum_i A_{ui} + \sum_i A_{li} \tag{3.1.5}$$

Note that the principle of detailed balancing, and hence thermodynamic equilibrium, has been assumed to apply in deriving equation 3.1.3.

If we observe at frequency ν, then an atom with a line of sight velocity v is absorbing at a frequency $\nu(1-v/c)$ due to the Doppler effect. The absorption coefficient, taken over the whole distribution, becomes

$$\bar{\alpha}(\nu) = \int_{-\infty}^{\infty} \alpha(\nu(1-v/c))\psi(v)\mathrm{d}v \tag{3.1.6}$$

In the temperature ranges of interest $b/c \ll 1$ and also $\nu - \nu_0$ is small compared with ν_0, so we may put $\nu \simeq \nu_0$. Then,

$$\bar{\alpha}(\nu) = \frac{\sqrt{\pi}e^2 f}{m_e c\pi} \int_{-\infty}^{\infty} \frac{(\Gamma/4\pi)\exp\left(-v^2/b^2\right)\mathrm{d}v/b}{\left(\nu - \nu_0 - \nu_0 v/c\right)^2 + \left(\Gamma/4\pi\right)^2} \tag{3.1.7}$$

To simplify the above expression, we define the following quantities:

$$\begin{aligned} \Delta\nu_d &= b\nu_0/c \\ \Delta\nu &= v\nu_0/c \\ u &= (\nu - \nu_0)/\Delta\nu_d \\ y &= v/b \\ a &= \Gamma/4\pi\Delta\nu_d \end{aligned} \tag{3.1.8}$$

where $\Delta\nu_d$ is called the Doppler width, and $\Delta\nu$ is the Doppler shift. Then,

$$\bar{\alpha}(\nu) = \frac{\sqrt{\pi}e^2 f H(a,u)}{m_e c\Delta\nu_d} \tag{3.1.9}$$

where the Voigt function $H(a,u)$ is given by

$$H(a,u) = \frac{a}{\pi} \int_{-\infty}^{\infty} \frac{e^{-y^2}\mathrm{d}y}{(u-y)^2 + a^2} \tag{3.1.10}$$

and has been tabulated by Harris (1948), Finn and Mugglestone (1965) and Hummer (1965). To calculate an absorption profile in practice, tables of

$H(a,u)$ are stored in a computer file, and interpolation is used to obtain intermediate values.

For illustrative purposes, the Voigt profile can be represented by the expression

$$H(a,u) = e^{-u^2} + a/u^2\sqrt{\pi}$$

where the first term dominates in the line core and the second in the wings. The intensity profile is now given by

$$I_\nu = I_0 e^{-\tau^\nu} \tag{3.1.11}$$

where I_0 is the continuum intensity, and

$$\tau^\nu = \int_0^l \bar{\alpha}(\nu) n \mathrm{d}s$$

is the optical depth, n is the particle density and l is the length through the cloud.

Assuming $\bar{\alpha}(\nu)$ is independent of s

$$\begin{aligned} \tau^\nu &= \bar{\alpha} \int_0^l n \mathrm{d}s, \text{ so} \\ \tau^\nu &= \bar{\alpha}(\nu) N \end{aligned} \tag{3.1.12}$$

where N is the column density of absorbing particles.

Equations 3.1.11 and 3.1.12 allow us to compute a single absorption profile. To calculate a complex of m blended profiles, we simply sum over the optical depths

$$I_\nu^c = I_0 \exp\left(-\sum_i \tau_i^\nu\right) \tag{3.1.13}$$

3.2 Optimisation methods; the need and choice

Having defined the model absorption line, we can use least-squares to match the model to the data. In practice, using a direct search least-squares procedure is not practical for many more than 3 or 4 parameters because of the prohibitive amounts of computer time required. However, in spectral regions where individual absorption features are clearly isolated, direct search techniques are feasible and even preferable since a complete mapping of the χ^2-parameter space provides accurate information on the parameter errors. Unfortunately, many of the absorption features seen in QSO spectra are not single but blended. Under these conditions, it is not only preferable (for economy of computer time) to find more efficient modelling procedures but also essential to model the entire complex simultaneously. If this is not done, it is impossible to decide objectively on the number of free parameters to use in the model. In addition, unknown biases will be introduced into the parameter estimates if we select restricted regions of the spectrum to model, section by section. Consequently, an optimised least-squares method has been applied to absorption line modelling.

There are essentially two aspects of any model fitting problem which should be considered in order to choose between the large number of optimisation techniques available; the properties of the objective function, i.e. the function to be minimised, and the properties of the parameter constraints.

In our problem of fitting absorption lines to an observed spectrum the objective function $F(x)$ is χ^2 and there are no constraints on the fitting parameters x; this narrows the choice slightly to an unconstrained method. These may be classified into 2 basic approaches; Newton-type methods which rely on 1st and 2nd order derivative information to descend to the solution, and Gradient

methods which use only 1st order derivatives. In general, the most powerful of the unconstrained methods available are the Newton-type methods which usually converge faster and are more robust than other techniques. The speed at which a Newton-type method converges depends on the form of the objective function. The nearer $F(x)$ is to being well approximated by a quadratic model, the faster the convergence. The minimum of $F(x)$ is found in 1 iteration if it is exactly quadratic. It is worth noting that for problems where the noise residuals for the best fit are multi-variate Gaussian, non-linear least-squares techniques are essentially equivalent to Maximum Likelihood methods, and provide best estimates of the fitting parameters. An additional important advantage of Newton-type methods is that parameter error estimates are also available at virtually no extra computing cost.

The principles of optimisation are discussed fully in Practical Optimisation (Gill, Murray, and Wright, 1981). In the following sections, this reference is abbreviated to GMW.

3.3 Optimisation applied to least-squares model fitting

3.3.1 Outline of the problem; searching parameter space

To fit an absorption line to a set of n observed data points we wish to minimise the function

$$\chi^2 = \sum \left(I(N, b, z)_i - d_i\right)^2 / \sigma_i^2 \tag{3.3.1}$$

where $I(N, b, z)_i$ is the value of the model absorption profile at the i^{th} data point d_i, and is a function of the column density of absorbing atoms N, the velocity dispersion parameter b, and the redshift z. σ_i^2 is the estimated vari-

ance at the i^{th} pixel. The summation is taken over the $i = 1, 2, \ldots, m$ data points.

Using a more general notation, we minimise a function of the set of variables x (dropping vector notation from here on)

$$\begin{aligned} F(x) &= \frac{1}{2}\sum \left(I(x)_i - d_i\right)^2 / \sigma_i^2 \\ &= \frac{1}{2}\sum f(x)_i^2 \\ &= \frac{1}{2}\|f(x)\|_2^2 \end{aligned} \tag{3.3.2}$$

where $\|f(x)\|$ is the 2-norm of the m-vector $f(x)$. A factor of 1/2 has been included to avoid a factor of 2 appearing in subsequent expressions involving derivatives of this equation.

We now choose a quadratic model for the objective function by taking the first three terms of a Taylor series expansion about the current point k in parameter space

$$F(x_k + p) \simeq F(x_k) + g^T(x_k)p + \frac{1}{2}p^T G(x_k)p \tag{3.3.3}$$

where p is the predicted parameter unit vector update to minimise $F(x_k + p)$, $g(x)$ is the matrix of partial derivatives of F with respect to the parameters x (the gradient vector), $G(x)$ is the matrix of partial second derivatives, (the Hessian matrix), and T denotes transpose.

In order to minimise the right hand side of 3.3.3 by the choice of some suitable value of p it is convenient to formulate a quadratic function in terms of p, the step to the minimum, rather than the predicted minimum itself. The minimum of 3.3.3 is obtained when p_k is the minimum of the function

$$\Phi_k = g^T(x_k)p + \frac{1}{2}p^T G(x_k)p \tag{3.3.4}$$

A stationary point p_k of 3.3.4 satisfies the linear system of equations

$$G(x_k)p_k = -g(x_k) \tag{3.3.5}$$

An algorithm in which the search direction is defined by 3.3.5 is a "Newton type method", with the solution of 3.3.5, p_k, being the "Newton direction".

3.3.2 Calculating the gradient vector and Hessian matrix

In the context of least-squares problems, it is fortunate that both the gradient vector and Hessian matrix take on a rather simplified form making computation not only easier, but also more numerically stable. This can be shown as follows.

The q^{th} component of the gradient vector is obtained by differentiating 3.3.2

$$g(x_q) = \frac{\partial F(x)}{\partial x_q} = \sum \frac{\partial I(x)_i}{\partial x_q} \left(I(x)_i - d_i\right) / \sigma_i^2 \tag{3.3.6}$$

where the summation is taken over the $i = 1, 2, \ldots, n$ data points and the subscript q refers to the q^{th} parameter in the model function. In the simplest case of a single absorption profile there will be three components of the gradient vector: $x_1 = N$, $x_2 = b$, and $x_3 = z$. In general, where we may be attempting to fit a complex of absorption lines, there will be a total of m variable parameters, and hence m components of the gradient vector, corresponding to the $m/3$ absorption lines in the model.

The derivatives may in principle be calculated either using analytic expressions or numerically. For this application however, it was decided to use finite difference derivatives for both simplicity and speed of computation. This is

discussed in more detail in section 3.3.4.

The qr^{th} component of the Hessian matrix is obtained by differentiating equation 3.3.2 a second time to give

$$G(x)_{qr} = \frac{\partial^2 F(x)}{\partial x_q \partial x_r} = \left[\sum_{i=1}^{n} \frac{\partial^2 I(x)_i}{\partial x_q \partial x_r} \frac{(I(x)_i - d_i)}{\sigma_i^2}\right] + \left[\sum_{i=1}^{n} \frac{\partial I(x)_i}{\partial x_q} \frac{\partial I(x)_i}{\partial x_r} \frac{1}{\sigma_i^2}\right] \tag{3.3.7}$$

$$= Q(x) + J(x)J^T(x) \tag{3.3.8}$$

where $J(x)$ is the $m \times n$ Jacobian matrix of $f(x)$.

Consider the first term $Q(x)$. If the adopted model function is an adequate representation of the data, then at the solution x^*, it should be true that $\sum f(x)_i \to 0$ as $n \to \infty$. Since each $f(x)_i$ may be considered as an independent random variable with $\langle f(x)_i \rangle = 0$, we may expect that the first order term in equation 3.3.8 above dominates the second order term. This rather useful property mean that the Hessian matrix can be approximated using only first order derivatives, i.e.

$$G(x)_{qr} \approx \sum_{i=1}^{n} \frac{\partial I(x)_i}{\partial x_q} \frac{\partial I(x)_i}{\partial x_r} \frac{1}{\sigma_i^2} \tag{3.3.9}$$

Not only does this make calculating $G(\underline{x})$ somewhat easier but it also has the advantage that $G(\underline{x})$ is forced to be positive-definite, which guarantees a descent direction (if the equations are not ill-conditioned).

At each iteration of the algorithm we evaluate $G(\underline{x})$ and $g(\underline{x})$ and approximate the Newton direction by solving

$$\alpha G(\underline{x})\underline{p} = -g(\underline{x}) \tag{3.3.10}$$

where the scalar α has been introduced in order to allow for the fact that the adopted quadratic model is unlikely to be perfect, particularly away from the solution. For an exact quadratic function $\alpha = 1$. The most suitable value of α, at each iteration, is estimated by univariate minimisation of $F(\underline{x}+\alpha\underline{p})$ with respect to α. To do this we evaluate $F(\underline{x}+\alpha\underline{p})$ with $\alpha = 1/8, 1/4, \ldots, 2^n/8$, where $n = 0, 1, 2, \ldots$. The value of α which gives a minimum of $F(\underline{x}+\alpha\underline{p})$ found by fitting a second order polynomial to the points $\{F(\underline{x}+\alpha\underline{p}), \alpha\}$ and finding the minimum. In practice, α was found to vary between 0 and about 1.5.

At each iteration of the multivariate minimisation, we test for convergence; if $F(\underline{x}+\alpha\underline{p}) - F(\underline{x}) \leq \Delta$, the algorithm is terminated. Δ is a preselected convergence criterion which relates to the accuracy with which one may hope to estimate the parameters $\underline{x}$. The value adopted for fitting absorption profiles was 0.001 since it was found that the change in the parameter values became much smaller than the estimated parameter errors. If the convergence criterion is not satisfied, at a particular iteration, the current parameter estimates are updated by the vector $\alpha\underline{p}$ and the whole procedure repeated.

3.3.3 Finding the Newton direction; solving $Ax = b$

Faced with the task of solving a system of linear equations one may opt either for a direct method or an iterative method. The former is any method which, after a finite number of operations gives the exact solution, (disregarding rounding errors), and is usually the most efficient when A is full meaning that most of the elements of A axe non-zero. When A is sparse i.e. has a high proportion of zero-valued elements, iterative methods may offer some advantages or may even be indispensible. For the problem in hand, A is always full and so a direct method has been employed. From a multitude of methods available, two have been explored - Gaussian elimination and Cholesky factori-

sation. Since this subject has been discussed in detail by several authors (see for example Dahlquist and Bjorck, 1974; Gill, Murray, and Wright, 1981), only a sketch of the basic principles is given here, together with a brief comparison of the two.

3.3.3.1 Gaussian elimination

The principle on which Gaussian elimination is based is to eliminate the unknowns in a systematic way so that we end up with a triangular system which we know how to solve. Since the solution of the transformed problem $MAx = Mb$ is the same as the solution of $Ax = b$, we generate a non-singular matrix M such that MA is triangular.

Consider the system of n equations

$$\begin{aligned} a_{11}x_1 + a_{12}x_2 + \cdots + a_{1n}x_n &= b_1 \\ a_{21}x_1 + a_{22}x_2 + \cdots + a_{2n}x_n &= b_2 \\ a_{n1}x_1 + a_{n2}x_2 + \cdots + a_{nn}x_n &= b_n \end{aligned}$$

The matrix A is reduced to upper-triangular form in $n-1$ operations. At the k^{th} step, the $(j,k)^{\text{th}}$ element will be eliminated by subtracting a multiple m_{jk} of row k from row j where

$$m_{jk} = a_{jk}^{(m)} / a_{kk}^{(k)}$$

This is equivalent to the procedure used to solve a small linear system by hand.

The $(k,k)^{\text{th}}$ element of $a_{kk}^{(m)}$ of the partially reduced matrix is termed the pivot element. In principle, when the pivot elements are always non-zero, Gaussian elimination is well defined. In practice, poor scaling and/or a large dynamic range in A can present instabilities and introduce large errors. The use of a pivoting strategy to select the most suitable pivot element improves

numerical stability (see for example GMW, p.36).

Once A has been fully reduced to upper-triangular form, then the solutions (x_j) are found by straightforward back-substitution.

3.3.3.2 Cholesky factorisation

One way of reducing the risk of numerical instabilities due to error growth is to find a method for solving $Ax = b$ where no pivoting is necessary. Cholesky factorisation meets this requirement. A positive-definite symmetric matrix A can be written

$$A = L_u D L_u^T$$

where L_u is a unit lower triangular matrix, (i .e. all its diagonal elements are 1), and D is a diagonal matrix whose elements are all positive. This can be written as

$$\begin{aligned} A &= L_u D^{1/2} D^{1/2} L_u^T \\ &= L L^T \end{aligned} \tag{3.3.11}$$

where L is a general lower triangular matrix called the Cholesky factor or square root of A. The Cholesky factor may be computed as follows.

Since A is positive-definite symmetric, equation 3.3.11 is

$$\begin{bmatrix} a_{11} & a_{12} & \dots & a_{1n} \\ a_{12} & a_{22} & \dots & a_{2n} \\ \vdots & \vdots & \ddots & \vdots \\ a_{1n} & a_{2n} & \dots & a_{nn} \end{bmatrix} = \begin{bmatrix} l_{11} & & & \\ l_{12} & l_{22} & & \\ \vdots & \vdots & \ddots & \\ l_{1n} & l_{2n} & \dots & l_{nn} \end{bmatrix} \begin{bmatrix} l_{11} & l_{12} & \dots & l_{1n} \\ & l_{22} & \dots & l_{2n} \\ & & \ddots & \vdots \\ & & & l_{nn} \end{bmatrix}$$

Equating the $(1,1)^{\text{th}}$ element gives

$$a_{11} = l_{11}^2$$

Equating the first rows of both sides gives

$$a_{12} = l_{11}l_{12}$$

$$a_{13} = l_{11}l_{13}$$

$$a_{1n} = l_{11}l_{1n}$$

and so $l_{12}, l_{13}, \ldots, l_{1n}$ can all be found once l_{11} is known. Then, for the $(2,2)^{\text{th}}$ element,

$$a_{22} = l_{12}^2 + l_{22}^2$$

and since l_{12} is known, l_{22} can be found, and so on.

Generalising the procedure just outlined, the elements of the matrix L are defined by the expressions

$$\begin{aligned} l_{kj} &= \left(a_{kj} - \sum l_{kp}l_{jp}\right)/l_{jj} \\ l_{kk} &= \sqrt{\left(a_{kk} - \sum l_{kp}^2\right)} \end{aligned} \tag{3.3.12}$$

for $j = 1, 2, \ldots, k-1$

When L is known, we may find the unknowns x by back-substitution. Since,

$$L(L^T) = b$$

to find x we first solve

$$Ly = b \text{ for } y$$

and then,

$$L^T x = y \text{ for } x$$

3.3.3.3 Comparative comments

We have used both Gaussian elimination and Cholesky Factorisation to solve the matrix equations and determine the Newton direction and both produce

almost identical results in the majority of cases. However, when A has a particularly large dynamic range, the pivoting procedure inherent in Gaussian elimination can cause error growth in the elements of L due to rounding errors, even when the algorithm is implemented in double precislon. Since no pivoting is needed in Cholesky factorisation, these rounding errors are kept to a minimum. An additional advantage of Cholesky factorisation over Gaussian elimination is that the relative number of computations involved in both techniques is approximately 1:2 when $n^2 \gg n$. For these reasons, Cholesky factorisation has been adopted in preference to Gaussian elimination.

3.3.4 Calculating the derivatives $\partial \mathbf{I}/\partial \mathbf{x}$

3.3.4.1 Finite difference approximations

The function derivatives at each data point $\frac{\partial I(x)_i}{\partial x_q}$ may in principle be calculated either numerically or using analytic approximations. At present only numerical derivatives have been used. This has been purely for simplicity and is justified by the fact that the stability and convergence rate of the profile fitting algorithm are not highly sensitive to the accuracy of the gradient vector and Hessian matrix. Exact function derivatives with respect to the parameters N and b cannot be obtained analytically and one would have to resort to the use of series approximations to the voigt function $H(a, u)$.

We can approximate the derivates of a smooth unvariate function $f(x)$ by the forward-difference approximation

$$f'(x) = \frac{f(x+h)-f(x)}{h} - 1/2hf''(x+\theta h)$$

where $0 \leq \theta \leq 1$. This can be written

$$f'(x) = \frac{f(x+h)-f(x)}{h} - \mathcal{O}(h)$$

where $\mathcal{O}(h)$ refers to the truncated terms in the Taylor series expansion of $f(x)$, and h is the finite-difference interval.

The values chosen for the flnite-difference increments are

$$h(N) = 0.01N.\text{cm}^{-2}$$

$$h(z) = 0.00001$$

$$h(b) = 0.5 \text{ km/s}$$

and were chosen simply on the basis that, approximately,

$$0.1\sigma(x_q^*) \leq h(x_q^*) \leq \sigma(x_q^*)$$

i.e. the increments are between 1 and 0.1 times the value of the estimated best-fit parameter errors.

3.3.4.2 Finite differences; improvement in accuracy

Although the convergence rate and stabillty of the fitting algorithm is unlikely to improve significantly with the use of more accurate derivative estimates, there is at least one motivation for improving the accuracy of the derivative estimates. At the solution, the parameter errors are estimated from the covariance matrix of the best-fit parameters, which itself is obtained from the inverse of the Hessian matrix (section 3.3.6). A more accurate Hessian matrix thus provides more reliable parameter error estimates.

Two ways in which the accuracy of the finite-difference approximations in current use could be improved will now be described.

There are three sources of error in finite-difference approximations to derivatives; (1) the truncation error, (2) the condition error, and (3) the rounding

error.

The truncation error is caused by neglecting the terms $\mathcal{O}(h)$ in the Taylor series expansion of $f(x)$ and the condition error is the error associated with the calculation of $f(x)$ itself. The rounding error associated with calculations carried out in finite length arithmetic is negligible compared with the first two sources of error and will be ignored.

It can be shown that (GMW, p.128) the bound on the error in the value of $f'(x)$ due to the truncation and condition errors is given by $\frac{h}{2}f''(\xi) + \frac{2}{h}\epsilon_A$ and $x \leq \xi \leq x + h$ and ϵ_A is a bound on the error in f at (x) and $(x + h)$.

We can minimise this expression with respect to h to obtain optimal values of the finite difference increments,

$$h_f = 2\left[\frac{\epsilon_a}{f''(\xi)}\right]^{1/2}$$

We will assume that ϵ_A is the error in calculating $H(a, u)$ and this is easily obtained by comparing computed values of $H(a, u)$ with tabulated values of known accuracy (e.g. Posener, 1959). This has been done with the result that $\epsilon_A \leq 5 \times 10^{-4}$. Estimates for $f''(\xi)$ can be obtained by differentiating equations 3.3.13, 3.3.15 and 3.3.16, using numerical approximations for the partial derivatives of $H(a, u)$. When this is done however, a large dynamic range is found which maps through to the predicted optimal finite-difference increments. A solution to this problem would be to choose an optimal finite-difference increment for each point in the data for each variable.

The second way in which the accuracy of the function derivatives could be

improved is by using finite-difference approximations

$$f'(x) = \frac{f(x+h) - f(x-h)}{2h} - \mathcal{O}(h^2)$$

for the derivatives. The disadvantage is that twice the number of function evaluations are required, compared to forward-difference values. More importantly, twice the number of convolutions (to take into account the instrumental resolution) are required. However, the switch to central-difference approximations need only be made for the final iteration.

3.3.4.3 Analytic expressions

Ignoring instrumental resolution, it is easy to see that

$$\frac{\partial I_\nu}{\partial N} = -\alpha_\nu I_\nu \tag{3.3.13}$$

Unfortunately, $\partial I_\nu / \partial b$ and $\partial I_\nu / \partial z$ are not quite so straightforward.

$$I_\nu = I_0 e^{-N\alpha_\nu} \tag{3.3.14}$$

where

$$\alpha_\nu = \frac{\sqrt{\pi}e^2}{m_e} f \frac{H(a,u)b}{\nu_0}$$

v_0 is the rest frequency of the line center, and the Voigt function $H(a,u)$ depends on both v_0 and b. Differentiating 3.3.14 with respect to b and rearranging gives

$$\frac{\partial I_\nu}{\partial b} = \frac{N\alpha_\nu I_\nu}{b}\left[1 - \frac{b}{H(a,u)}\frac{\partial H(a,u)}{\partial b}\right] \tag{3.3.15}$$

and with respect to z we get

$$\frac{\partial I_\nu}{\partial z} = \frac{N\alpha_\nu I_\nu}{(1+z)}\left[1 - \frac{\nu_0}{H(a,u)}\frac{\partial H(a,u)}{\partial \nu_0}\right] \tag{3.3.16}$$

and we cannot obtain $\partial H(a,u)/\partial b$ or $\partial H(a,u)/\partial \nu_0$ without resorting to a series approximation for $H(a,u)$. Accurate approximations to $H(a,u)$ which can be differentiated are given by Whiting (1968) and it should be possible to use his expressions to estimate $\partial I/\partial b$ and $\partial I/\partial z$; this remains to be explored.

Probably the most computationally efficient way to obtain $\partial I/\partial b$ and $\partial I/\partial z$ is to tabulate the derivatives of $H(a,u)$ with respect to b and z, and interpolate to the required (a,u) in an analagous way as is done in calculating the absorption line profile.

When estimating the derivatives using analytic approximations, the instrumental profile g_I must be taken into account. Since, for a function $f(x)$,

$$\frac{\mathrm{d}\{f(x) * g_I\}}{\mathrm{d}x} = \left[\frac{\mathrm{d}f(x)}{\mathrm{d}x}\right] * g_I$$

equations 3.3.13, 3.3.15 and 3.3.16 must be convolved with g_I to obtain the true derivatives.

3.3.5 Scaling

Scaling problems are common in optimisation algorithms and the one described in this chapter is unfortunately no exception. Two basic types of problems can be distinguished: dynamic range problems and ill-conditloning. The first is usually easily dealt with by suitable variable transformations at appropriate points in the algorithm. The second normally requires more subtle handling and is often associated with the particular model fitting problem or perhaps with the way in which the problem has been formulated.

The relevance of both types of scaling problems to profile fitting and how the problems are overcome is described in detail in the following two sections.

3.3.5.1 Stage 1; rounding error problems

Since all computations are done in finite precision arithmetic, problems frequently arise in an unconstrained optimisation algorithm due to poor scaling. The way in which this is dealt will depends greatly on the particular application.

That scaling is a problem in fitting absorption lines can easily be demonstrated and line 29 in Q1101-264, Table 5.4 has been chosen to illustrate this.

The best fit parameters are

$$N = 1.64e14,\ b = 35,\ z = 2.10389$$

and the first-guess parameter estimates were

$$N = 1.00e14,\ b = 30,\ z = 2.10391$$

which are significantly far from the correct values since the a $\chi^2_n \simeq 10$ compared with the final value of around 1.

The convergence criterion of $\chi^2_n \leq 0.001$ was satisfied in 5 iterations which was fairly typical and the finite-difference derivative increments (Section 3.3.4) were

$$\Delta N = 0.01N,\ \Delta b = 0.5,\ \Delta z = 0.00001$$

The fit was computed over 43 data points. The values of the function derivatives $\frac{\partial I(x)_i}{\partial x_q}$ with respect to q^{th} parameter, at the i^{th} channel in the data lay within the following ranges at the first iteration of the algorithm.

$$\begin{aligned} 10^{-18} < & \left[\tfrac{\partial I}{\partial N}\right]_i & < 10^{-14} \\ 1 < & \left[\tfrac{\partial I}{\partial z}\right]_i & < 10^{5} \\ 10^{-6} < & \left[\tfrac{\partial I}{\partial b}\right]_i & < 1 \end{aligned}$$

Although the derivative values changed as the algorithm converged, these order-of-magnitude ranges still held. The individual values changed by roughly a factor of $2 \sim 4$ between the first and the final iteration.

The first and obvious lesson to be learnt from the ranges above is that when computing the elements of the Hessian matrix we will be rather close to exceeding the allowed VAX variable ranges of $10^{\pm 38}$ so before proceeding any further into the algorithm we must rescale the function derivatives. In practice this is achieved simply by multiplying each $\left[\frac{\partial I}{\partial N}\right]_i$ a default value of $10^1 4$. This value is suitable for profile by fitting to any of the "Lyman-forest" systems, since generally $10^{12} < N < 10^{16}$ atoms cm^{-2}. In optically-thick absorption systems, column densities as high as 10^{22} atoms cm^{-2} may occur and this scaling factor can be adjusted accordingly.

An alternative to rescaling the $(\partial I/\partial N)_i$'s is to transform the variable N into log space. An ideal variable transformation would be such that contours of constant probability levels in parameter space would be exactly ellipsoid. The reason for this is due to the choice of a quadratic model to approximate the objective function χ^2 in the vicinity of the current point in parameter space. The shape of the parameter-χ^2 m-dimensional surface will change with the choice of variable transformation as well as with the actual parameter values. Although, in principle, the estimates for the best-fit parameters should not be affected by a variable transformation, the parameter error-ranges derived will.

After scaling the derivatives in the manner just described, it is still possible to end up with an undesirably large dynamic range in the Hessian matrix $G(x)$. This may occur when fitting a complex of several absorption features where the column densities could range between 10^{13} and 10^{20} atom/cm^2 for example.

This is dealt with by pre- and post-multiplying $G(x)$ by a diagonal matrix D_S^{-1} so that

$$G(x) \rightarrow D_S^{-1} G(x) D_S^{-1}$$

where the i^{th} component of D_S is related to the i, i^{th} component of $G(x)$ by

$$d_i = 1/\sqrt{g_{ii}}$$

So the linear system of equations $G(x)p = -g(x)$ now becomes

$$D_S^{-1} G(x) D_S^{-1} (D_S P) = -D_S^{-1} g(x)$$

and the solutions p are simply rescaled after Cholesky decomposition and back-substitution.

This procedure has two attractive qualities: 1) it significantly reduces the dynamic range in $G(x)$, and 2) $G(x)$ becomes normalised so that $g_{ii} = 1.0$ which is a useful feature when faced with an ill-conditioned system as discussed in the next section.

For the example given at the start of this section, the unscaled Hessian is

$$\begin{array}{rrr} 1.1e4 & 5.6e5 & 1.1e2 \\ 5.6e5 & 2.5e11 & -4.1e3 \\ 1.1e2 & -4.1e3 & 13 \end{array}$$

which, after normalisation, becomes

$$\begin{array}{rrr} 1 & 1.1e-2 & 0.29 \\ 1.1e-2 & 1 & -2.3e-3 \\ 0.29 & -2.3e-3 & 1 \end{array}$$

3.3.5.2 Stage 2; ill-conditioning

Occasionally, the situation can arise where a very small change in the objective function at the solution can lead to a huge change in the estimates. This phenomenon is known as is not related to floating point computation. Consider, as a simple example of this, the equations

$$x + y = 2$$
$$x + 1.01y = 2.01$$

which have the obvious solutions $x = 1$, $y = 1$. If we now make relatively small changes in the coefficients,

$$x + y = 2$$
$$x + 0.99y = 2.02$$

the solutions become $x = 4$, $y = -2$. This problem does not occur in profile fitting to single or fairly well separated absorption features, but may arise when modelling badly blended complexes of absorption lines. Closely overlapped profiles can result in the coefficients in the Hessian matrix $G(x)$ not being linearly-independent causing rank-deficiency and hence ill-conditioning.

A way of visualising the effect of this problem is to consider the shape of the χ^2-parameter surface in the vicinity of the solution. For a well-conditioned problem, the minimum χ^2 is well-defined and, hopefully, well represented by a quadratic function. For an ill-conditioned problem, the shape of the surface becomes less well-defined with small or negligible slope near the correct solution. Another way of stating this is to say that $G(x)$ is not sufficiently positive-definite to provide a reasonable estimate for the Newton descent dlrection.

It is unfortunate, but probably inevitable, that the model-fitting problems for which the matrices are ill-conditioned often turn out to be those of greatest

interest. For example, attempts to deblend deuterium from the blue wing of a Lyman absorption system may, in some cases, lead to an ill-conditioned Hessian matrix. Ill-conditionlng may also occur in profile fitting to metal-containing absorption systems where damping effects or velocity broadening conceal velocity structure in HI, for example, which may be claimed to be present from an analysis of the SilI or CII lines. These considerations are obviously important when attempting to estimate the metal abundances.

Fortunately there are fairly simple ways of detecting ill-conditioned matrices. More numerically stable matrix factorisation procedures can be implemented in those cases. These are always less efficient and are therefore only used when necessary.

3.3.5.3 Detecting ill-conditioning; modified Cholesky factorisation

Recall from section 3.3.3 that the Cholesky decompostion of a positive-definite symmetric matrix A can be written

$$A = LL^T$$

where the Cholesky factor L is a general lower triangular matrix for which the diagonal elements are all strictly positive. If A is not sufficiently positive-deflinite then, from equation 3.3.12,

$$a_{kk} - \sum l_{kp}^2 \simeq 0$$

and we may use this as a test for ill-conditioning. In some cases Cholesky factorisation may fail if l_{kk} becomes the square root of a negative small number. The remedy is to add an offset to the diagonal terms of A so that factorisation works. The Hessian matrix $G(x)$ then becomes $G(x) + E$ where E is

a non-negative diagonal matrix. This procedure is called Modified Cholesky Factorisation. Since $G(x)$ has been normalised so that $g_{ii} = l$, the choice of a suitable offset is relatively straightforward (GMW, p109) and we have taken E to be a unit diagonal matrix.

There is a trade-off between the increased numerical stability and the convergence rate of the algorithm. As already mentioned, the fastest convergence rate that can be achieved with a Gauss-Newton optimisation technique is quadratic, so that if the objective function is exactly quadratic, minimisation occurs in one iteration. The effect of modifying $G(x)$ to $G(x) + E$ is that the descent direction obtained tends towards the steepest descent direction which has only a linear convergence rate. Modified Cholesky factorisation is therefore only used when neccessary and not as default.

For the system $Ax = b$, a measure of the stability can be obtained from the condition number, κ, of the system. Derived from perturbation theory (e.g. GMW, p28; Dahlquist and Bjorck, p176), κ is defined by

$$\text{Cond}(A) = \kappa = (\lambda_{\max}/\lambda_{\min}),$$

the ratio of the maximum and minimum eigenvalues of the system. It can be shown that a reasonable and also convenient approximation to κ is given by

$$\kappa \simeq (\max(l_{ii})/\min(l_{ii}))^2$$

the squared ratio of the maximum and minimum diagonal terms in the Cholesky factor. The condition number indicates the maximum effect of the perturbations in A or b on the exact solution of $Ax = b$. If κ is "large", the solution may be changed substantially by very small changes in the data and the problem is ill-conditioned. The value of κ as an indicator of the accuracy of the solution has not been explored here for two reasons. Firstly, in cases of extreme

ill-conditioning the problem becomes immediately evident because no convergence at all occurs. Secondly, when the problem is only mildly ill-conditioned, this becomes apparent after convergence through unreasonably large parameter error estimates, which are obtained from $G(x)$. To check whether the error estimates are reasonable, and also whether the best-fit parameters have been found, the problem can be run using both modified and un-modified Cholesky factorisation and the results compared.

3.3.6 Parameter error estimates

If some or all of the parameters in a non-linear least-squares problem are correlated, the off-diagonal terms in the covariance matrix at the solution are non-zero. This in itself is not a major difficulty, since it is only a question of convention to decide how best to quote the errors associated with any variable. The most popular convention is to use only the diagonal terms. However, variables which are not normally distributed (as they can be with absorption line modelling; see Carswell et al., 1984) do present problems for non-linear least-squares procedures. The main motivation for using Gauss-Newton methods is that there are too many parameters for a direct search routine, which would require a vast amount of computer time to fully map the χ^2-parameter space. The assumption built into most optimised techniques is that the χ^2-parameter space can be adequately represented by a general quadratic function in the vicinity of the solution. Adopting this functional form offers enormous benefits in terms of the speed, stablity and simplicity of Gauss-Newton minimisation algorithms as has already been discussed. It is clear that the quadratic approximation is perfectly adequate and does not significantly affect the accuracy of the parameter estimates. However, the methods used to obtain parameter error estimates are based on the same assumption i.e. they are multivariate Gaussian (and may therefore be correlated). When there are gross asymme-

tries in the χ^2-parameter space, these error estimates are only approximate, and in some sense must be an average over the true ranges. Discussions on parameter error estimation can be found in Bevington (1969), Dahlquist and Bjorck (1974), Gill, Murray, and Wright (1981) and Irwin (1985).
Recall from section 3.3 (equations 3.3.7 to 3.3.9) that the Hessian matrix is related to the Jacobian matrix of $f(x)$ (equation 3.3.2) by

$$G(x) = J(x)J^T(x)$$

This expression is correct if the noise in the data is random and uncorrelated. For the general noise case (Irwin, 1985)

$$G(x) = J(x)C^{-1}J^T(x)$$

where C is the noise or residual covariance matrix. The Hessian matrix is also the inverse of the Fisher information matrix $I_f(x)$. Fisher (1958) showed that the parameter covariance matrix is given by

$$V(x)_{ij} \geq I_f^{-1}(x)_{ij}$$

for the ij^{th} parameter. Therefore, simply by inverting the Hessian matrix at the parameter solution, we obtain an approximation to the parameter covariance matrix. In practice, the error estimates are rescaled since the error array associated with each absorption line is modified in the way described in section 5.4 (see also section 2.3). This rescallng of the spectral error array propagates through to the Hessian matrix.

All of the error estimates quoted in the absorption line tables have been obtained in this way. Because of the assumptions built into this procedure, a set of numerical simulations were carried out to check on how reliable the er-

ror estimates are. The simulations described in Chapter 4 provided a good check for cases where several Lyman lines are fitted simultaneously (and also where features are badly blended together). The results of that analysis suggest that, in general, the error estimates obtained from the Hessian matrix are very reliable. Further simulations have been done for the more usual cases (in the data used here) of only fitting to Lyα. In all cases, the agreement between the estimated errors and the true errors was good. 100 Lyα lines were generated (with the same signal-to-noise ratio and spectral resolution as the previous simulations) and profile fitted and this was done for a range of parameters. For one of these numerical experiments the input parameter values were $N(\mathrm{HI}) = 9.10^{13}$ and $b = 25$. Figure 3.3.1 shows the histogram of results for $N(\mathrm{HI})$ and b. For $N(\mathrm{HI})$, the observed scatter is 1.08×10^{13} atoms/cm^2. The mean parameter error estimate is $1.01 \times 10^{13} \pm 0.34 \times 10^{13}$. For b, the observed scatter is 2.15 km/s. The mean parameter error estimate is 2.67 ± 0.25. The histograms for the distribution of best-fit values appear fairly symmetric. The column density parameter search was performed in $N(\mathrm{HI})$ space, (as opposed to log NHI). Perhaps, for certain ranges in $N(\mathrm{HI})$, the χ^2-parameter space is more symmetric in linear space than it is in log space. This problem needs to be explored more thoroughly. From all of the simulations done so far, the inference seems to be that the error estimates derived from the Hessian matrix are very reliable.

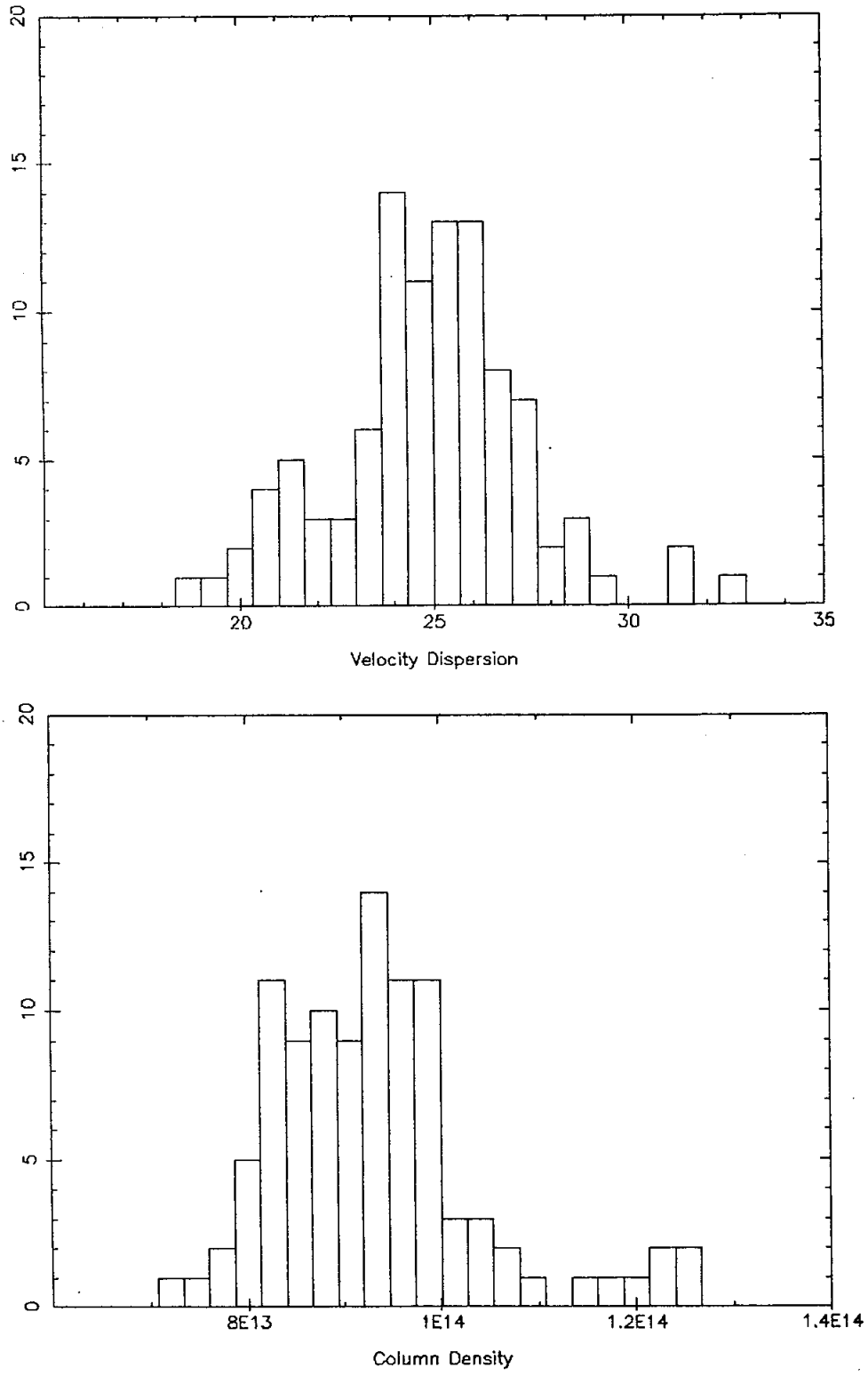

Figure 3.1: Numerical simulation of profile fitting to 100 Lyα lines

4 The D/H abundance

4.1 Introduction

Big bang nucleosynthesis calculations provide firm predictions of the abundances of the light elements. The first calculations were made two decades ago, and since then many modifications have been made in order to refine the early results of Peebles (1966), Peebles (1966), and Wagoner et al., 1967.

Since there are few plausible post-big bang processes for producing and injecting significant quantities of deuterium into the interstellar medium (Epstein, Lattimer, and Schramm, 1976), it is generally accepted that any observed deuterium is of primordial origin and therefore provides a lower limit to the primordial D/H value.

The primordial D/H ratio is assumed to be higher than any observed value by some unknown factor, f, due to astration (the destruction of D in the interstellar gas recycled through stars). Different models for the chemical evolution of the light elements give estimates of f varying from about 2 or 3 (Audouze and Tinsley, 1974; Clayton, 1985) up to around 15 (Delbourgo-Salvador, Gry, Malinie, and Audouze, 1985).

In the standard isotropic, homogeneous big bang model, (3 light neutrino species), the predicted light element abundances depend on just one parameter η, the baryon to photon ratio, which was established within the first few seconds after the big bang. Deuterium in particular is highly sensitive to η. D/H measurements therefore potentially provide very tight constraints on the standard model. Big bang neucleosynthesis and observational constraints have been discussed by numerous authors. Recent comprehensive reviews may be found in Boesgaard and Steigman (1985) and Yang et al. (1984). See also Pagel (1986), Shaver et al. (1983), and Pagel (1982).

4.2 UV absorption lines in the ISM

Motivated by the potential importance of deuterium for providing tight constraints on big bang cosmology, many different attempts have been made to estimate the D/H ratio, (see reviews referenced in last section). A direct way of measuring D/H is in UV absorption studies of the ISM. Deuterium is detected in absorption as a weak feature blueshifted by 81 km/s in the wing of a Lyman transition of hydrogen. Recent studies suggest that the most probable present day value of D/H lies in the range $8^{-6} < \mathrm{D/H} < 2 \times 10^{-5}$ (Boesgaard and Steigman, 1985). It has however been noted that the upper limit should be treated with caution. It is possible for a low column density hydrogen cloud with a line of sight velocity component of -81 km/s with respect to a stronger companion to mimic deuterium. The cause for suspicion was prompted initially by the fairly large scatter in the various D/H measurements. Variability in the apparent deuterium column density subsequently confirmed that some of the previous D/H estimates were spurious (Vidal-Madjar and Gry, 1984).

4.2.1 A suggested modification to current ISM analysis techniques

It is perhaps worth noting here that tests could be devised to check the cause for the observed scatter in D/H measurements in existing measurements which are not obviously spurious. If anomalies do exist in estimates for D/H, then these should show up in the probability distribution of all of the observed values. If the scatter is due entirely to measurement error, then the probability distribution should be well defined (although not necessarily normal). If the scatter is real, for whatever reason, then significant departures from the expected distribution should be seen. However, since there may have been systematic problems with the various techniques used to estimate D/H in individual cases, this could add to any measurement scatter and confuse the issue. It would be worthwhile to compile a library of the existing data which has been used to estimate D/H and subject it to the sort of procedure described in Chapter 3. Additionally, it might be informative to simultaneously model all of the data using a single variable for D/H. This greatly reduces the number of free parameters used in all previous measurements. For a single H-D Lyman system the fitting parameters are N(HI), the neutral hydrogen column density, b(HI), the neutral hydrogen velocity dispersion, the redshift z, and the D/H ratio, b(DI) is usually constrained by the assumption that the gas has a thermal velocity distribution so that $b(\mathrm{DI}) = b(\mathrm{HI})/\sqrt{2}$.

Therefore, for n clouds, with the assumption of entirely thermal line broadening and constant D/H abundance, the number of free parameters in a simultaneous fit would be $3n + 1$. A novel extension of this approach may be to include as an extra free parameter for each cloud the turbulent component of the velocity dispersion, b_{t}, retaining the constant D/H assumption. If, under these circumstances, a globally satisfactory fit was obtained, the average

value of the solution for b_t would represent an approximate upper limit to the turbulence in the absorbing clouds. If no satisfactory fit is found, this would clearly demonstrate that D/H is not constant. One of the attractive qualities of the modelling technique detailed in chapter 3 is the ability to combine, in a consistent and optimal way, data of varied resolution and signal to noise. Also, assuming a statistically satisfactory fit is found, at least for the bulk of the data, the parameter error estimates should be considerably tightened compared to all previous efforts. This is for two reasons: (i) a general $\sqrt{n}$ reduction in the errors would be expected simply due to the combination of n data sets, and (ii) the number of free parameters used in estimating D/H has been reduced by $n-1$.

Further indications that D/H estimates from measurements of the ISM may in some cases be in error are provided by the data of Landsman et al. (1984). They have collected high resolution spectra of the late-type star αCenA. Their data set consists of Copernicus observations and also a sequence of IUE images. The D(Lyα) interstellar absorption feature apparently appeared slightly stronger in one of the Copernicus spectra than in the rest of the data. Also, the deuterium feature appeared blue-shifted by 8$\pm$2 km/s from its expected position, suggesting possible HI contamination in the profile.

What seems clear is that either the modelling procedures used so far are inadequate or/and anomalous results can be obtained using the ISM to estimate D/H.

Even once the difficulties in interpreting local D/H measurements have been overcome, there still remains the problem of estimating (from theoretical arguments) the astration factor to derive the primordial D/H ratio.

4.3 QSO absorption systems

Another possible line of investigation is to search for deuterium in absorption systems in QSO spectra. At high enough redshifts, the UV Lyman lines are shifted into the visible waveband, permitting groundbased spectroscopy. So far searches for candidate absorption systems in the supposedly metal-free Lyman clouds have been disappointing, (Atwood, Baldwin, and Carswell, 1982). This is mainly because the high HI column density systems necessary to measure D/H $\leq 10^{-4}$ are exceedingly rare (e.g. Atwood, Baldwin, and Carswell, 1985; Carswell, Webb, Baldwin, and Atwood, 1987). Such searches however should and will continue. A complementary approach may be to use the metal-containing systems. Here the neutral hydrogen column densities are generally higher, although so too will be the astration factor.

The remainder of this chapter is concerned with the potential for measuring D/H in QSO absorption systems.

4.3.1 D/H simulations

In order to investigate the accuracy with which the D/H ratio may potentially be measured in QSO absorption systems, a series of simulations have been carried out. First we generate a synthetic spectrum of Lyman absorption lines for D and H using Voigt profiles. The spectrum is convolved with a Gaussian corresponding to an instrumental resolution of $\sigma \simeq 0.13$Å. The data are binned in channels of 0.07 Å. Gaussian noise is then added to give a signal to noise ratio of 10 per channel. These values were chosen to compare closely with real data as may be obtained, for example, using the IPCS with the 82cm camera on the RGO spectrograph at the AAT.

In generating the synthetic spectra it was assumed that thermal broadening

applied to the atomic velocity dispersions so that $b(\mathrm{D}) = b(\mathrm{H})/\sqrt{2}$. This choice of thermal rather than turbulent line broadening was made because it results in a lower deuterium equivalent width and hence more conservative constraints on the D/H error ranges.

As pointed out by Adams (1976), D will only appear as a distinguishable feature in the blue wing of the hydrogen Lyα line for a rather narrow range in N(HI)-b(H) parameter space. If we assume that D/H $\simeq 10^{-6}$, then we are unlikely to be able to detect DI in a cloud with N(HI) much below 10^{17} atoms/cm^2 unless the data quality is significantly better than any so far obtained, simply because its equivalent width would be sufficiently low as to be below the detection threshold. Furthermore, once N(HI) increases much above 10^{17}, the deuterium feature becomes engulfed in the hydrogen profile wings. However, if we include several lines in the Lyman series these difficulties are largely removed. This limits potentially interesting absorption systems to $z > 2.5$ for ground based observations.

Having generated a simulated spectrum, the technique described in Chapter 3 was applied to the data to estimate the hydrogen and deuterium column densities and the velocity dispersion parameter. There are two important differences between modelling hydrogen-only systems and the procedure adopted here, concerning the number of free parameters in the least-squares fitting procedure. Firstly, b(D) is removed as a free parameter and fixed as $b(\mathrm{H})/\sqrt{2}$. In estimating the Gauss-Newton search direction at each iteration, the components in the hessian matrix associated with the hydrogen and deuterium velocity dispersions contain contributions from not only the χ^2 derivatives with respect to b(H), but also with respect to b(D). In this way, the resulting search direction has been correctly influenced by the presence of the deuterium. The consequences of not allowing the possibility of turbulent broadening where

$b(\mathrm{H}) \geq b(\mathrm{D})$ are discussed briefly later.

Secondly, the redshift was treated as a fixed parameter. The only reason for this was to economise on computing time. Initial tests on a spectrum, first fitting with z free and then fixed, produced no detectable changes in the column density and velocity dispersion error estimates. The reason for this is easy to see. For absorption systems with $N(\mathrm{HI})$ just above the detection threshold (i.e. $N(\mathrm{HI})$ just above 10^{17} atoms/cm^2) the deuterium is too weak to be detected in the higher order lines, so they serve the purpose of effectively fixing the redshift. As $N(\mathrm{HI})$ increases, the damping wings of Lyα (and perhaps Lyα for high enough $N(\mathrm{HI})$) completely obliterate the deuterium, which becomes easier to detect in the higher order lines. In this case, it is the Lyα line which constrains the redshift.

There is one final difference between the simulations described here and profile fits to real data. In this case we already know the answer. The first guess parameters entered were the correct solutions. The most obvious advantage of doing this is that the number of iterations required to reach the best-fit solution is kept to a minimum, economising further on computing time. It is assumed that the final fit parameters obtained do not depend sensitively on the first guesses. This has been checked, in some cases, by profile fitting to the same spectrum a number of times, each time starting with a different set of first guesses. In all cases the algorithm iterated to almost exactly the same solutions. A slightly more refined version of the experiment described here would be to estimate the first guess parameters from the line widths and central depths. Potential complications would be how to obtain the initial guesses for badly blended lines.

The simulations have been done for two values of D/H; 10^{-4} and 10^{-5}, two

values of b(H); 25 and 35 km/s, and four values of N(HI); log$N$(HI)= 17, 18, 19 and 20. The lower D/H value was chosen on the assumption that we are unlikely to see less deuterium at higher redshifts than we do locally. How much more deuterium there may be evidently depends on how fast it is destroyed and the primordial D/H value. The upper D/H value used in the simulations is simply a guess for what we may find in a gas cloud less processed than the Galactic interstellar medium, based on theoretical expectations for the rate of destruction of deuterium. The original intention was to generate and profile fit 100 spectra for each combination of b(H), N(HI) and D/H, i.e. 1600 runs. In fact computing restrictions curtailed this ambition and resulted in rather more modest simulations, with various run lengths for each set of input parameters.

However, one or two long runs probably suffice to test for systematic biasses in the procedure. Also, the scatter in the N(HI) and b(H) parameter error estimates is small. Consequently, for the purposes of estimating the error ranges on D/H, only a few runs are required.

4.3.1.1 Results

The results of the simulations are summarised in Table 4.1. There are six columns associated with each of the parameters N(HI), b(H) and N(DI). In the first column, the input parameters θ_t are given. The next column is the mean result θ_0 of the set of simulations. Column 3 is the observed scatter $\sigma(\theta_0)$ about θ_t and column 4 is the mean parameter error estimate $\sigma(\theta_e)$, obtained from the covariance matrix at the solution. Column 5 is the significance of the discrepancy between the true and mean parameter values, obtained from

$$s = \text{mod}\left[\frac{\theta_t - \theta_0}{\sigma(\theta_e)/\sqrt{n}}\right] \tag{4.3.1}$$

where n is the number of runs for the simulation (column 6).

Under each set of parameters is the error on the D/H ratio shown first in linear space and then as a range in log space. (The least-squares search was performed in linear space). The distribution of the ratio of two random variables is given by a Cauchy distribution which has an undefined variance. Consequently, we use the approximation

$$\sigma^2\left(\frac{x}{y}\right) = \left(\frac{\langle x\rangle}{\langle y\rangle}\right)^2 \left[\frac{\sigma(x)^2}{\langle x\rangle^2} + \frac{\sigma(y)^2}{\langle y\rangle^2} - 2\rho_{xy}\frac{\sigma(x)\sigma(y)}{\langle x\rangle\langle y\rangle}\right] \tag{4.3.2}$$

(see for example Eadie et al., 1971). where ρ is the correlation coefficient for N(HI) and N(DI) which is taken to be zero. Note that in interpreting s and σ(D/H) as one sigma probability limits, we assume that all parameters are uncorrelated and normally distributed. Note however that any correlation between parameters reduces σ(D/H). However Carswell et al., (1984), have demonstrated that, when profile fitting to a single Lyα line profile, N(HI) and b(H) may be strongly correlated and that contours of constant confidence limits in the log N(HI) - log b(H) plane can be highly asymmetric about the best fit. Their example was for a cloud with log N(HI) = 14.10 and b(H) = 19 km/s. Here we are dealing with larger hydrogen column densities and also simultaneously modelling six blended profiles in the hydrogen-deuterium Lyman series and so the situation is not necessarily directly comparable. We can use the results of the simulations to check on this, firstly by plotting scatter diagrams for the three combinations of the parameters N(HI), b(H) and N(DI) and also the histograms of results for each parameter. The four longest runs in the simulations were n=100, 50, 36 and 29, corresponding to

```
a) log N(HI) = 17, b(H) = 25, log D/H = -4

b) log N(HI) = 17, b(H) = 35, log D/H = -5

c) log N(HI) =_18, b(H) - 25, log D/H = -4
```

d) log N(HI) = 20, b(H) = 25, log D/H = -5

and so these have been chosen as illustrative examples. Figures 4.1a-4.1d shows the first six lines in the Lyman series for each parameter combination. The Lyman series with and without deuterium are plotted. Figures 4.2a-4.2d are the scatter plots and histograms illustrating the distribution of results. A brief discussion of each follows.

a) log N(HI) = 17 ; b(H) = 25 ; log D/H = -4 ; 100 runs

N(HI) and b(H) are strongly correlated. There is no evidence for any correlation between N(DI) and b(D) or between N(HI) and N(DI). In the histogram plots we see no sign of asymmetry in the distribution of velocity dispersions, but slightly extended wings in the two column density distributions towards values higher than the mean. This asymmetry is fairly weak and we may expect that the assumption of normality does not have any disastrous consequences. The mean b(H) and N(DI) agree with the true values to within two decimal places but there is a 1.68σ difference for N(HI). The observed and mean estimated scatter are in excellent agreement for all three parameters.

b) log N(HI) = 17 ; b(H) = 35 ; log D/H = –5 ; 50 runs

N(HI) and b(H) are strongly correlated but no significant correlation seems to exist between the other variables. This parameter combination is such that detecting deuterium at all is not really possible; only an upper limit to the D/H abundance can be obtained. Out of the 50 runs, the deuterium column density iterated to zero 10 times. (In practice, the algorithm was terminated as soon as N(DI)¡10^{10} since this is well below any possible detection). This is the only parameter combination for which this occurred.

The b(H) and N(HI) distributions appear reasonably symmetric although the mean of each differs from the input values by 3.48σ and 4.65σ respectively.

The mean N(HI) is shifted up by 10 percent and the mean b(H) down to 34.64. The N(DI) distribution bears no resemblance to a normal distribution, but instead appears more like a power law. The estimated significance of the discrepency of the mean value from the true value is 2.36σ but this number now becomes meaningless. The mean of the N(DI) distribution is a factor of 3 too high. Since the observed and estimated scatter agree well in all cases, it seems that there is genuine bias away from the correct solutions. The asymmetry in the N(DI)-χ^2 parameter space is, by itself, easy to understand and is to be expected whenever the magnitudes of the parameters and associated error estimates become comparable. If N(DI) is systematically overestimated, this must be compensated for by a reduction in the strength of the hydrogen absorption. This reduction can be achieved by systematically underestimating either N(HI) or b(H). That this effect occurs so significantly, and particularly in such a way as to retain symmetry in the N(HI) and b(H) distributions is rather surprising. From the point of view of detecting deuterium, it is probably not worth exploring this further; the potential constraints on D/H are cosmologically uninteresting. There may however be more serious consequences concerning analyses of the Lyman forest absorbing clouds. Estimates of the column. density and velocity dispersion distribution functions (Carswell et al.,1984, Atwood, Baldwin and Carswel1,1985, Carswell et al.,1987) may need ultimately to take into account effects such as the one discovered here. If such strong systematic biases occur frequently in blended absorption features where one or more components in the blend have σ(N) (and/or σ(b)) = N (and/or b), then it seems possible that the observed and true distribution functions may be significantly different. The magnitude of this effect must depend on the number density of absorption lines.

c) log N(HI) = 18 ; b(H) = 25 ; log D/H = -4 ; 36 runs

The correlation between N(HI) and b(H) is still apparent, but there are no

strong correlations in the other two scatter diagrams. Since the run length is short, it is difficult to comment on the asymmetry of the parameter histograms. There are no significant differences between the true and mean parameters and the observed and estimated scatters are in good agreement.

d) log N(HI) = 20 ; b(H) = 25 ; log D/H = -5 ; 29 runs
The situation has changed slightly. The hydrogen column density is now on the logarithmic part of the curve of growth for Lyα. The correlation between N(HI) and b(H) has disappeared and a weak trend has become apparent between N(DI) and b(D). The mean and true hydrogen column densities agree to within the quoted accuracy whereas the b(H) and N(DI) discrepancies are 1.96σ and 1.64σ. Longer run lengths are necessary to check these further. The observed and estimated scatters are in good agreement.

A convenient and simple way of representing the results for the detectability of D/H is to plot the estimated 1σ error contours on log D/H as a function of log D/H and N(HI). Figure 4.3 shows two sets of curves; the lower set corresponds to an input log D/H of -4 and the upper set to -5, each with b(H) = 25 and 35 km/s. These curves can be used to give a guide to the potential accuracy with which D/H may be estimated in any particular absorption system. The error ranges have been plotted relative to the true parameter values and not the observed ones, the assumption being that either no biasing of the best-fit parameters occurs, or that where it does, numerical simulations can provide a correction. (The point at log N(HI) = 17, b(H) = 35, log D/H = -5 may not be accurate since it is for this parameter combination that the N(DI) distribution becomes highly non-normal. However, the observed and estimated errors are in good agreement and so the approximation is probably adequate).

It is apparent from figure 4.3 that D/H may potentially be estimated with

reasonable error ranges for a large range of absorbing cloud parameters, given the assumptions and conditions described. Within the ranges investigated, higher hydrogen column densities yield more accurate D/H estimates. This trend is due to using not only Lyα, but also the higher order lines.

At high enough hydrogen column densities the deuterium feature is completely swamped by the Lyα damping wings and may appear strongest in Lyβ or a higher order line still. As N(HI) increases further, (beyond log N(HI) = 20), eventually all the Lyman series must become damped so that the log D/H - log N(HI) error contours should begin to diverge. At low hydrogen column densities the deuterium is strongest in the Lyα line. The higher order lines serve the purpose of establishing the hydrogen column density.

4.3.2 Candidate absorption systems

Many QSO metal line absorption systems could have measurable deuterium. The outlook for the hydrogen-only systems seems a little bleaker since hydrogen column densities as high as log N(HI) = 17 are extremely rare. An exception is the $z_a = 2.9998$ system towards PKS2126-158 (Sargent and Boksenberg, 1983). This has a column density of log N(HI) = 17.3 and a velocity dispersion of 23 km/s. No metals have been detected associated with this system, no high resolution data has been published for this QSO and no reliable D/H estimates have been made. It is clear from Figure 4 that an investigation of the D/H ratio for this system would be worthwhile.

If the D/H ratio in the low or zero metallicity Lyman clouds is significantly higher than that observed locally, $\log D/H > -4$ for example, as has been suggested by Pagel (1985), then detections with reasonable error ranges may eventually be possible in systems with log N(HI) as low as 16 for low enough

b(H). Unfortunately though, even this column density is uncommon.

A high N(HI) candidate, with no detectable metals in the window observed, was discovered in Q2204-573 (line 22 in table 5.11). Both Lyα and Lyβ have been observed and simultaneously fitted. The resulting error ranges obtained were $-\infty < \log(D/H) < -5.24$. The fit was done under the assumption of thermal broadening. However, another minimum in χ^2-parameter space was found corresponding to a low column density solution, although the minimum χ^2 was larger (but still acceptable). With the existing data, no further progress is possible; observations of more lines in the Lyman series are required to distinguish between these two solutions.

Another approach is to concentrate on the metal line systems where N(HI) is high and b(H) low, and, if possible, where there are indications of lower than solar metal abundances so that less deuterium destruction may have occurred. A candidate fitting this description may exist in Q2206-199 which has log N(HI) = 20.6 and b(H) = 4 km/s at z = 2.0763. The silicon abundance in this object may be as low as 1/100 solar (Carswell et al., 1987, in preparation). However, this system must await observation from space since all the Lyman lines from Lyβ down are below the atmospheric cut-off.

High resolution observations by Atwood, Baldwin and Carswell (1985) of the spectrum of Q0420-388 provided information on a metal containing system at z = 3.0857. The column density and velocity dispersions were found to be log N(HI) = 19.4 and b = 9 km/s, suggesting that deuterium might be detectable. More data has since been collected and a detailed analysis of this system has revealed extensive velocity structure. However D/H has been estimated and the range is $2\times10^{-5} < (D/H) < 10^{-4}$, with a best-fit value of $D/H = 4\times10^{-5}$ (Webb et al., 1987, submitted to Ap.J. Letters). This error range is larger than expected mainly because of bad blending of a lower redshift hydrogen Lyα line

at the position of the deuterium Lyβ feature. It is at Lyβ where the deuterium appears strongest and so this blend is at the worst possible position. However this at least represents a step forward in that it is the first estimate of (or upper limit to) D/H made in an object outside the Galaxy. A preliminary version of this paper is included as an appendix at the end of this Chapter.

4.3.3 Discussion, future work and conclusions

A series of numerical simulations have been done with the aim of

(i) estimating the accuracy with which D/H may potentially be measured in QSO absorption systems,

(ii) providing a check on the parameter error estimates obtained in an optimised Gauss-Newton least-squares algorithm applied to absorption profile fitting, and

(iii) investigating systematic biases in the derived parameter estimates introduced by blending.

There are three effects which have not been taken into account in this work and which could lead to different D/H error ranges. The first, and probably most important, is due to complex velocity structure i.e. blending between adjacent lines. This is demonstrated in the results for Q0420-388. Optical observations down to Ly-6 require $z > 2.5$ where the number of hydrogen systems per unit redshift is high. More free parameters inevitably have to be included in the modelling procedure where blending occurs, causing larger error ranges. Lower redshift observations from above the atmosphere will reduce these difficulties.

The second effect not considered is the possibility of turbulent, rather than thermal, line broadening. When the absorption system under investigation

contains metals, the turbulent component b_t may be estimated. Given observations of several metal lines, the hydrogen velocity dispersion can be well constrained. This leads to smaller column density errors and a more reliable D/H estimate. This was done for Q0420-388. For the hydrogen-only systems, the possibility of turbulent broadening should be allowed for by including b_t as a variable, but constrained, parameter in the fitting procedure, the constraint being $b_t = 2b(D)^2_{obs} - b(H)^2_{obs}$, or $0 < b_t < b(H)$. The Importance of this effect is not clear; further simulations are required.

The third effect which may introduce errors is the uncertainty in the continuum level in the spectrum. In the simulations here, the correct continuum was used. In real data, the most likely bias will be towards a low continuum which would result in a lowered D/E estimate. Again, at lower redshifts the effect becomes less important.

The general conclusions from the simulations are:

1) D/H may potentially be estimated, with cosmologically interesting error ranges, from observations of QSO absorption systems, for a large range in N(HI) - b(H) parameter space. This is subject to high resolution data covering several lines in the Lyman series, and other favourable conditions.

2) The parameter error estimates obtained in an optimised least-squares fitting routine are reliable. Minimisation in linear space only (rather than log) has been investigated. Error contour asymmetry seems small, (given several lines in the Lyman series), except where the parameter value and error estimate are comparable.

3) When the parameter value and error estimate are comparable, for one cloud

in a blend, the resulting best-fit parameters for that cloud and others in the fit can in some cases be subject to serious bias where there are gross asymmetries in χ^2-parameter space. The full extent of this effect is not yet known; further simulations are required.

TABLE 4.1 – Results of simulations.

	θ_t	θ_o	$\sigma(\theta_o)$	$\sigma(\theta_e)$	s		n
N(HI)	1.0×10^{17}	9.36×10^{16}	1.85×10^{16}	2.46×10^{16}	0.86	}	11
b(H)	25	25.17	0.45	0.69	0.82	}	
N(DI)	1.0×10^{12}	1.54×10^{12}	1.54×10^{12}	1.68×10^{12}	1.07	}	
	$\sigma(D/H) = 1.70\times10^{-5}$; $-\infty < \log(D/H) < -4.57$						
N(HI)	1.0×10^{17}	1.10×10^{17}	2.05×10^{16}	2.03×10^{16}	3.48	}	50
b(H)	35	34.64	0.68	0.70	4.65	}	
N(DI)	1.0×10^{12}	3.07×10^{12}	5.08×10^{12}	6.19×10^{12}	2.36	}	
	$\sigma(D/H) = 6.19\times10^{-5}$; $-\infty < \log(D/H) < -4.14$						
N(HI)	1.0×10^{17}	1.05×10^{17}	3.12×10^{16}	2.98×10^{16}	1.68	}	100
b(H)	25	25.00	0.75	0.72	0.00	}	
N(DI)	1.0×10^{13}	1.00×10^{13}	2.13×10^{12}	2.11×10^{12}	0.00	}	
	$\sigma(D/H) = 3.65\times10^{-5}$; $-4.19 < \log(D/H) < -3.86$						
N(HI)	1.0×10^{17}	1.32×10^{17}	–	2.67×10^{16}	1.20	}	1
b(H)	35	33.99	–	0.75	1.35	}	
N(DI)	1.0×10^{13}	9.44×10^{12}	–	8.07×10^{12}	0.07	}	
	$\sigma(D/H) = 8.50\times10^{-5}$; $-4.82 < \log(D/H) < -3.73$						
N(HI)	1.0×10^{18}	1.02×10^{18}	2.80×10^{17}	2.71×10^{17}	0.74	}	10
b(H)	25	25.04	0.66	0.64	0.63	}	
N(DI)	1.0×10^{13}	9.90×10^{12}	4.89×10^{12}	5.18×10^{12}	0.21	}	
	$\sigma(D/H) = 5.85\times10^{-6}$; $-5.38 < \log(D/H) < -4.80$						
N(HI)	1.0×10^{18}	1.02×10^{18}	1.01×10^{17}	2.44×10^{17}	0.18	}	5
b(H)	35	34.95	0.37	0.69	0.16	}	
N(DI)	1.0×10^{13}	1.55×10^{13}	1.17×10^{13}	2.99×10^{13}	0.41	}	
	$\sigma(D/H) = 3.00\times10^{-5}$; $-\infty < \log(D/H) < -4.40$						
N(HI)	1.0×10^{18}	1.02×10^{18}	1.59×10^{17}	1.50×10^{17}	0.80	}	36
b(H)	25	25.01	0.39	0.36	0.17	}	
N(DI)	1.0×10^{14}	9.69×10^{13}	1.20×10^{13}	1.31×10^{13}	1.42	}	
	$\sigma(D/H) = 1.99\times10^{-5}$; $-4.10 < \log(D/H) < -3.92$						
N(HI)	1.0×10^{18}	9.57×10^{17}	2.22×10^{17}	2.46×10^{17}	0.30	}	3
b(H)	35	35.12	0.69	0.77	0.27	}	
N(DI)	1.0×10^{14}	8.67×10^{13}	3.84×10^{13}	4.08×10^{13}	0.56	}	
	$\sigma(D/H) = 4.76\times10^{-5}$; $-4.28 < \log(D/H) < -3.83$						

N(HI)	1.0×10^{19}	9.92×10^{18}	1.83×10^{17}	1.09×10^{18}	0.16	} 5
b(H)	25	24.95	0.23	0.10	1.12	}
N(DI)	1.0×10^{14}	1.03×10^{14}	7.16×10^{12}	2.51×10^{13}	0.29	}

$\sigma(D/H) = 2.74\times10^{-6}$; $-5.14 < \log(D/H) < -4.89$

N(HI)	1.0×10^{19}	9.98×10^{18}	3.58×10^{16}	7.35×10^{17}	0.06	} 5
b(H)	35	35.02	0.13	0.15	0.30	}
N(DI)	1.0×10^{14}	8.00×10^{13}	4.47×10^{13}	2.15×10^{14}	0.21	}

$\sigma(D/H) = 2.15\times10^{-5}$; $-\infty < \log(D/H) < -4.50$

N(HI)	1.0×10^{19}	1.00×10^{19}	8.94×10^{16}	1.25×10^{18}	0.00	} 5
b(H)	25	25.07	0.08	0.06	2.61	}
N(DI)	1.0×10^{15}	8.83×10^{14}	3.57×10^{13}	9.63×10^{13}	2.72	}

$\sigma(D/H) = 1.58\times10^{-5}$; $-4.07 < \log(D/H) < -3.94$

N(HI)	1.0×10^{19}	1.00×10^{19}	9.50×10^{16}	8.47×10^{17}	0.00	} 3
b(H)	35	34.87	0.12	0.13	1.73	}
N(DI)	1.0×10^{15}	9.57×10^{14}	1.11×10^{14}	3.01×10^{14}	0.25	}

$\sigma(D/H) = 3.26\times10^{-5}$; $-4.17 < \log(D/H) < -3.88$

N(HI)	1.0×10^{20}	1.00×10^{20}	1.68×10^{18}	1.74×10^{18}	0.00	} 29
b(H)	25	25.08	0.25	0.22	1.96	}
N(DI)	1.0×10^{15}	9.45×10^{14}	1.45×10^{14}	1.81×10^{14}	1.64	}

$\sigma(D/H) = 1.82\times10^{-6}$; $-5.09 < \log(D/H) < -4.93$

N(HI)	1.0×10^{20}	1.01×10^{20}	9.31×10^{18}	8.21×10^{18}	0.47	} 15
b(H)	35	35.06	0.38	0.36	0.65	}
N(DI)	1.0×10^{15}	1.23×10^{15}	1.92×10^{15}	1.70×10^{15}	0.52	}

$\sigma(D/H) = 1.70\times10^{-5}$; $-\infty < \log(D/H) < -4.56$

N(HI)	1.0×10^{20}	1.00×10^{20}	6.82×10^{18}	1.01×10^{19}	0.00	} 12
b(H)	25	24.92	0.41	0.42	0.66	}
N(DI)	1.0×10^{16}	9.98×10^{15}	2.03×10^{14}	1.97×10^{14}	0.35	}

$\sigma(D/H) = 1.03\times10^{-5}$; $-4.05 < \log(D/H) < -3.96$

N(HI)	1.0×10^{20}	9.75×10^{19}	6.74×10^{18}	6.93×10^{18}	1.08	} 9
b(H)	35	34.98	0.83	0.87	0.07	}
N(DI)	1.0×10^{16}	1.02×10^{16}	2.16×10^{15}	2.30×10^{15}	0.26	}

$\sigma(D/H) = 2.40\times10^{-5}$; $-4.12 < \log(D/H) < -3.91$

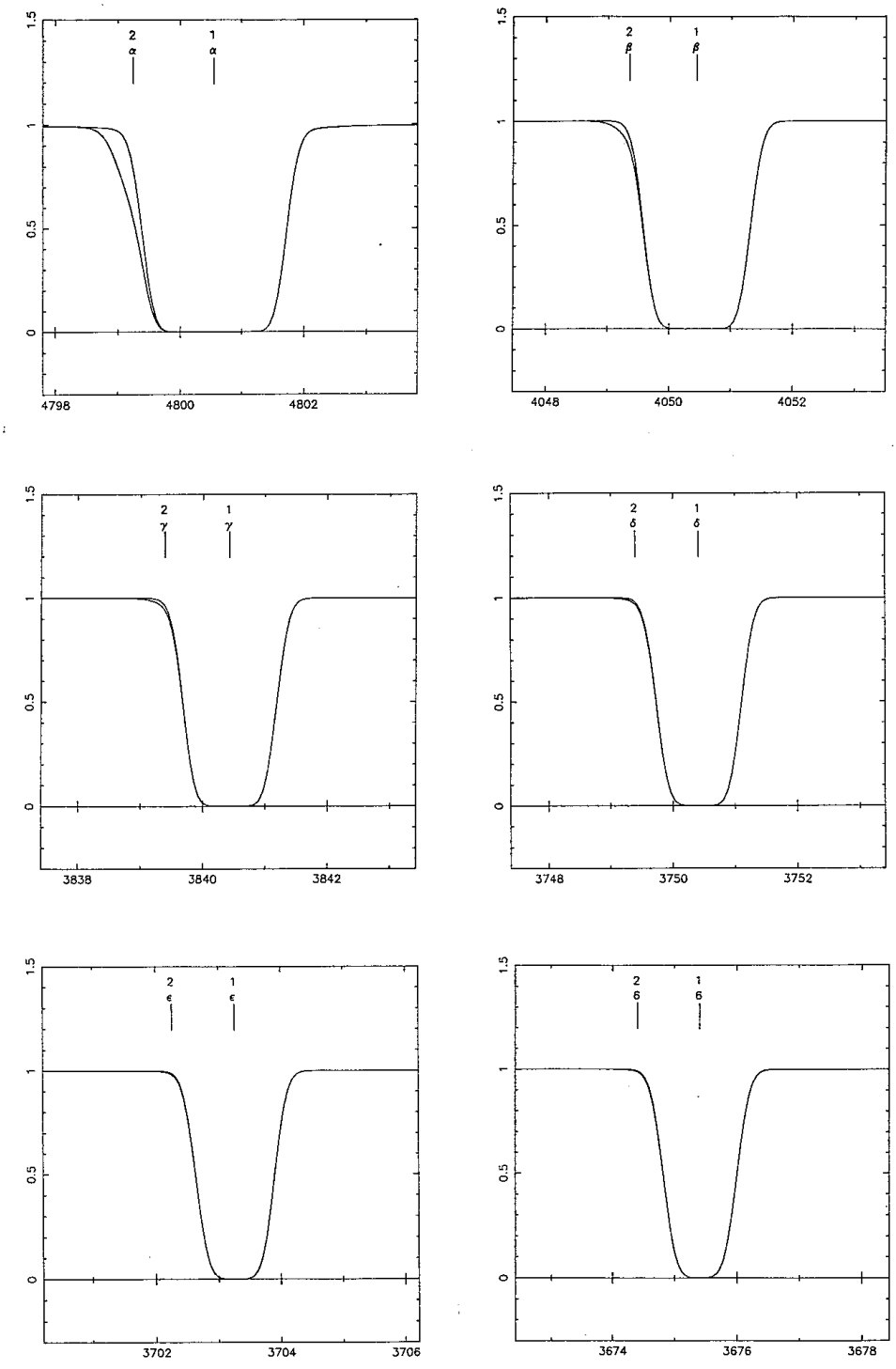

Figure 4.1a: The first 6 lines in the Lyman series of HI and DI for Simulation a: $\log N(HI) = 17$, $b(HI) = 25$ km/s, $\log D/H = -4$

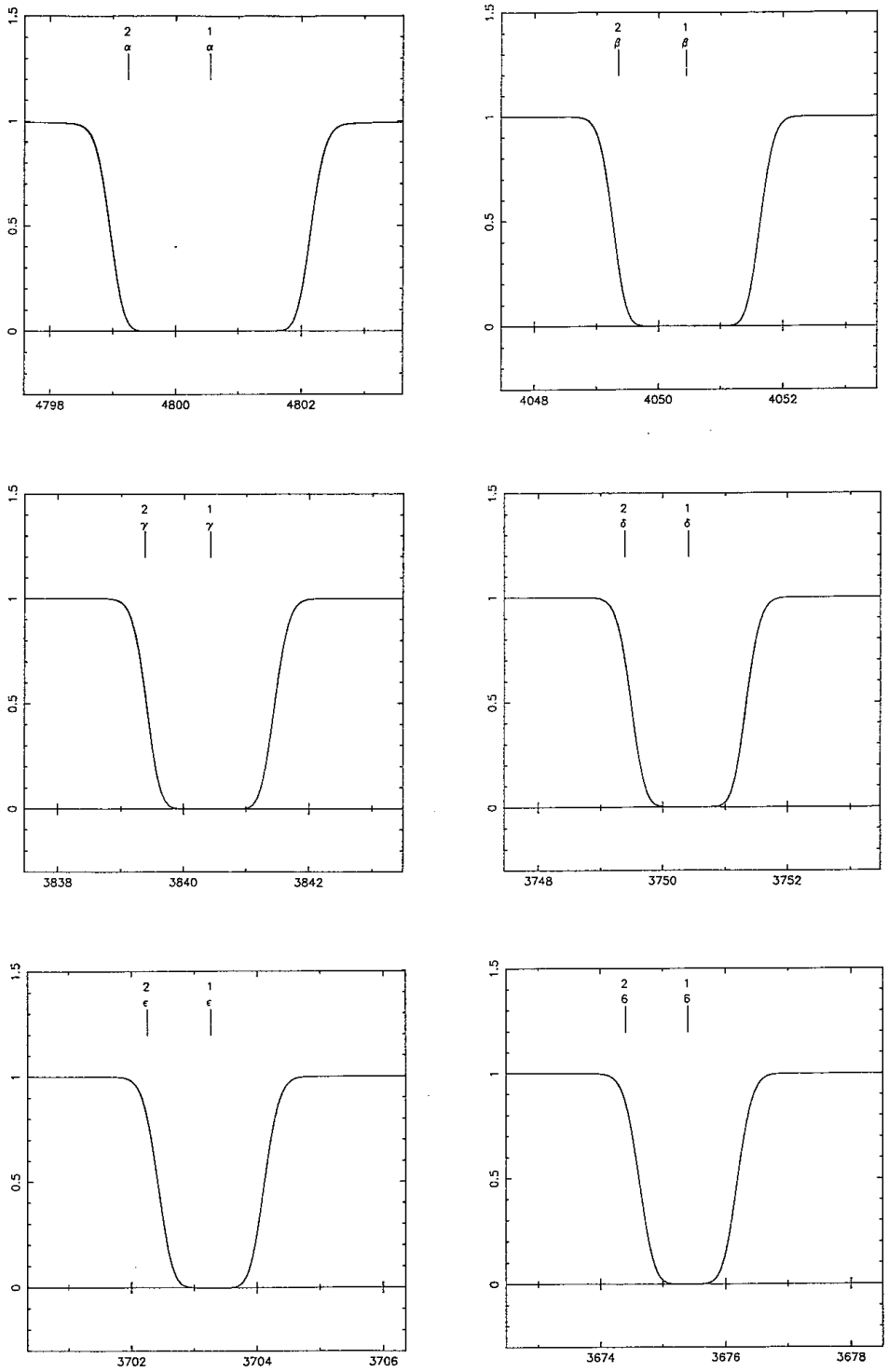

Figure 4.1b: The first 6 lines in the Lyman series of HI and DI for Simulation b: $\log N(HI) = 17$, $b(HI) = 35$ km/s, $\log D/H = -5$

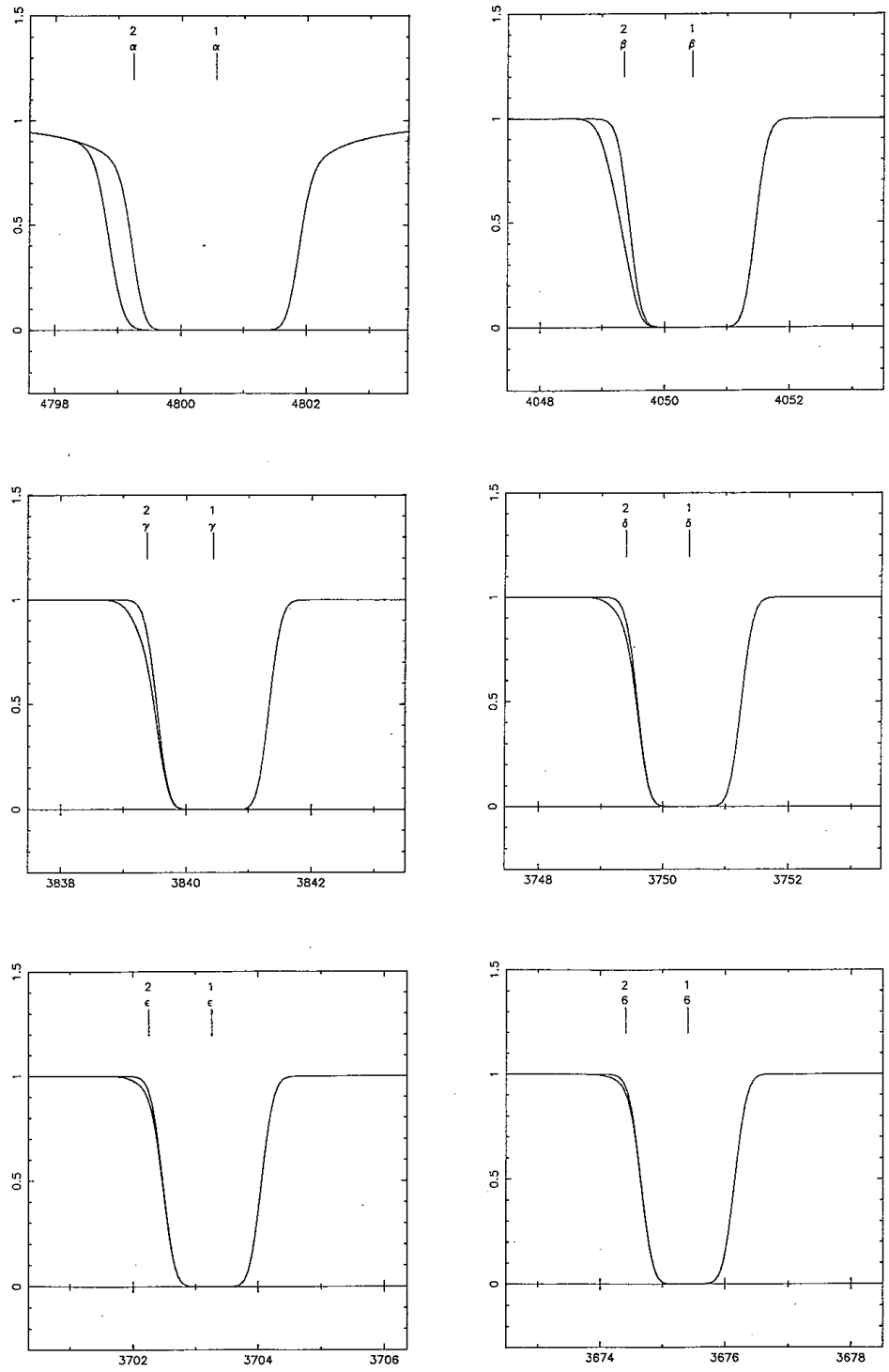

Figure 4.1c: The first 6 lines in the Lyman series of HI and DI for Simulation c: $\log N(HI) = 18$, $b(HI) = 25$ km/s, $\log D/H = -4$

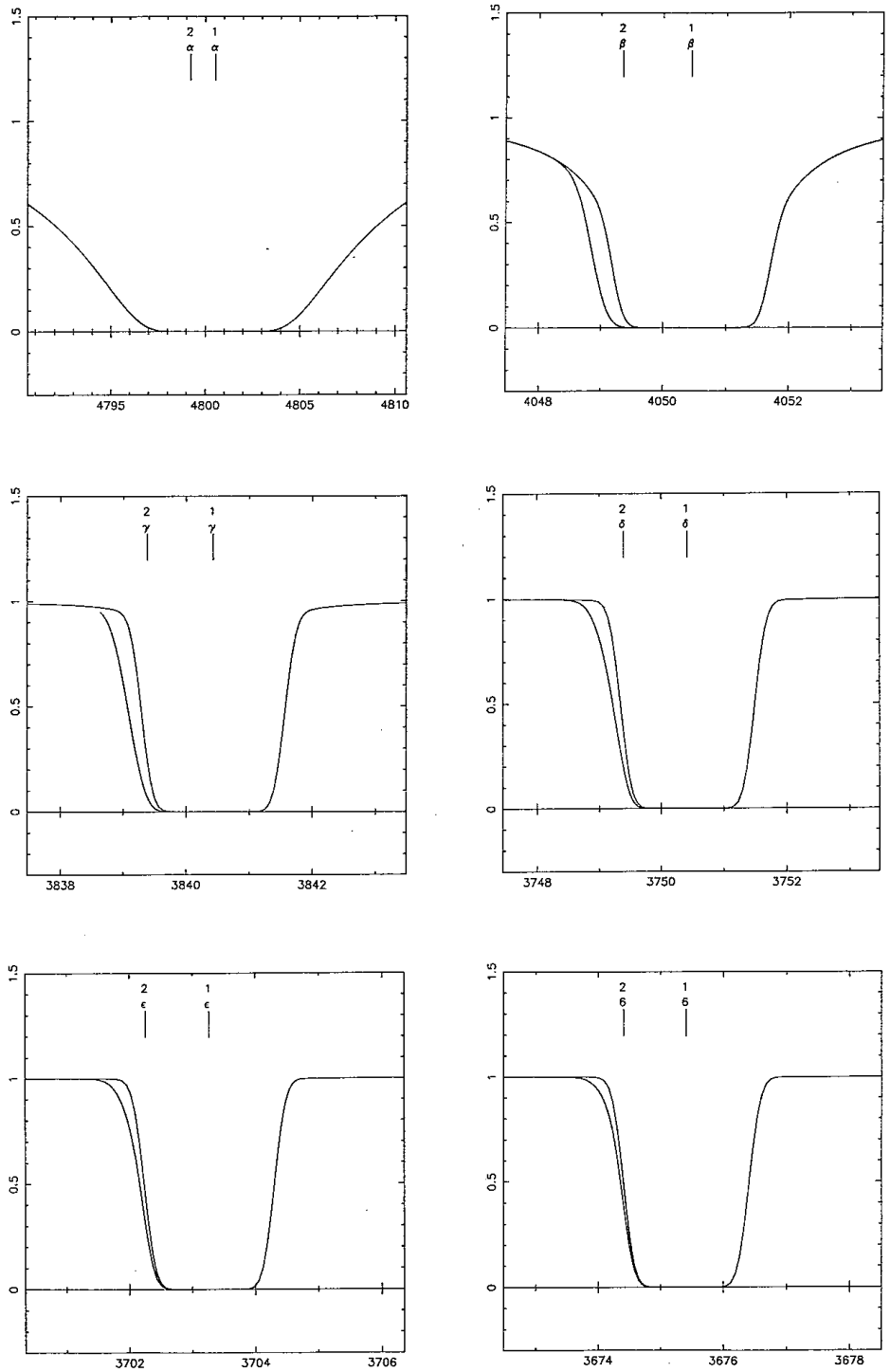

Figure 4.1d: The first 6 lines in the Lyman series of HI and DI for Simulation d: $\log N(HI) = 20$, $b(HI) = 25$ km/s, $\log D/H = -5$

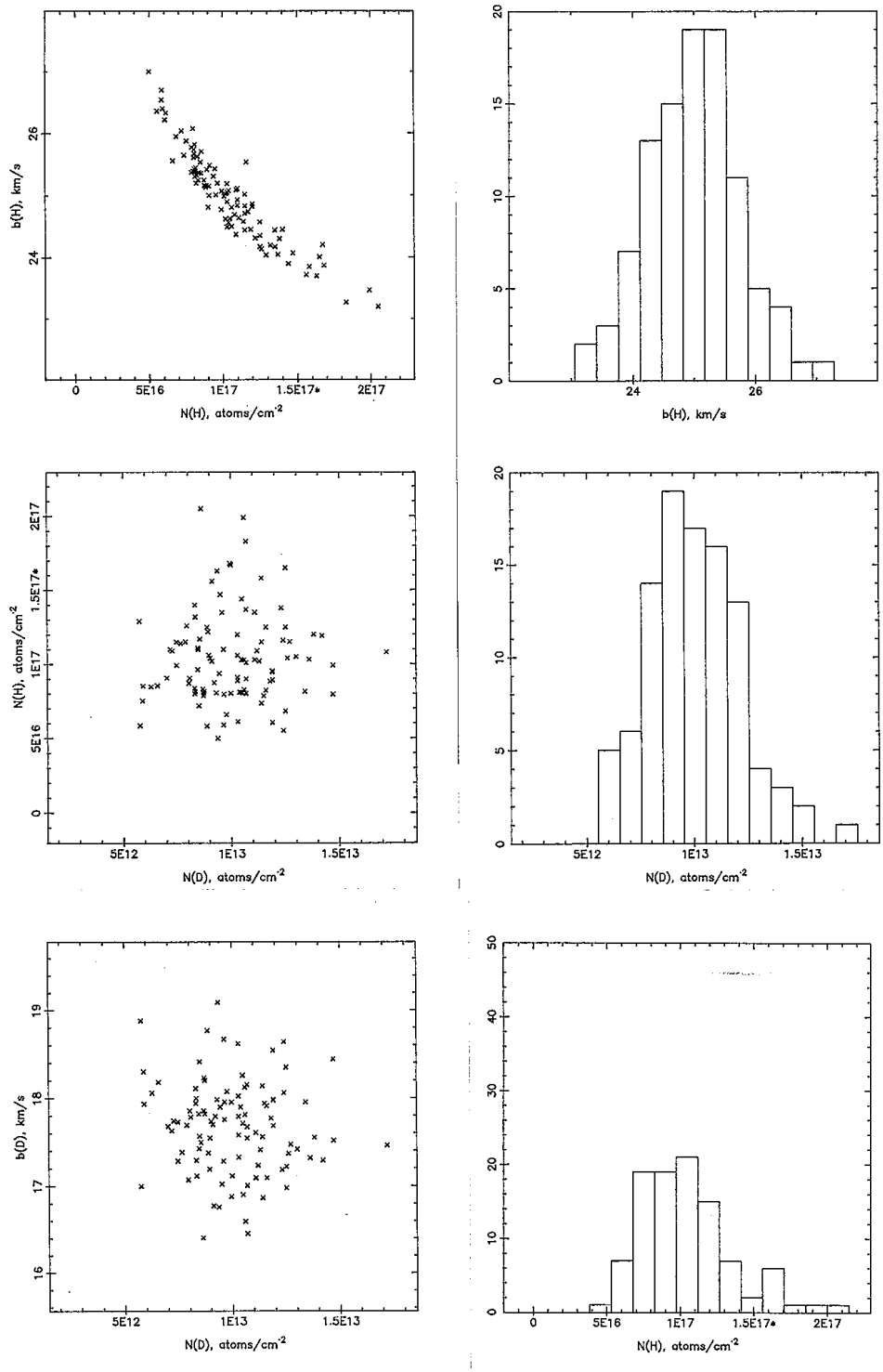

Figure 4.2a: Distribution of results for Simulation a: $\log N(HI) = 17$, $b(HI) = 25$ km/s, $\log D/H = -5$

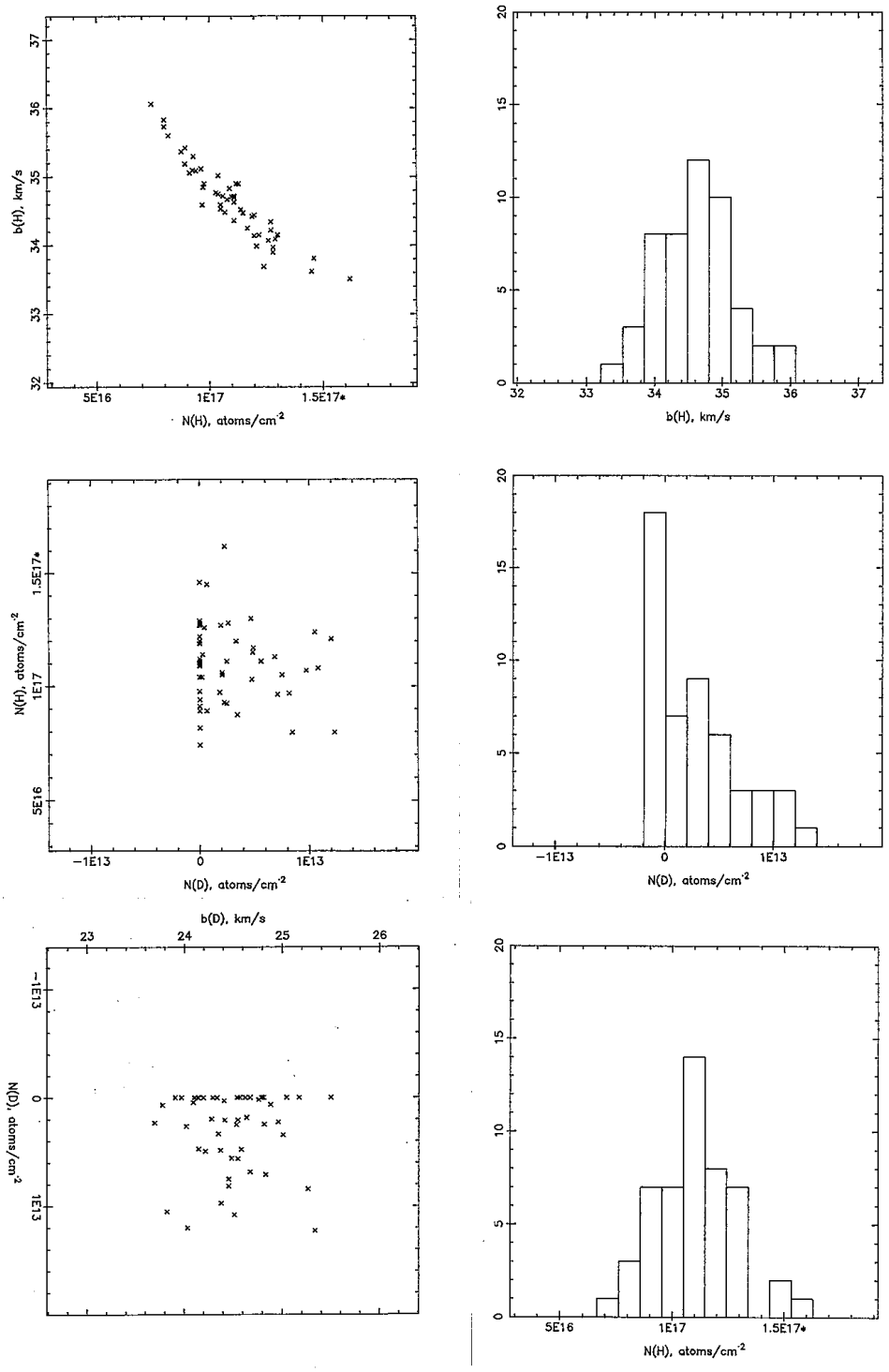

Figure 4.2b: Distribution of results for Simulation b: $\log N_{HI} = 17$, $b(HI) = 35$ km/s, $\log D/H = -5$

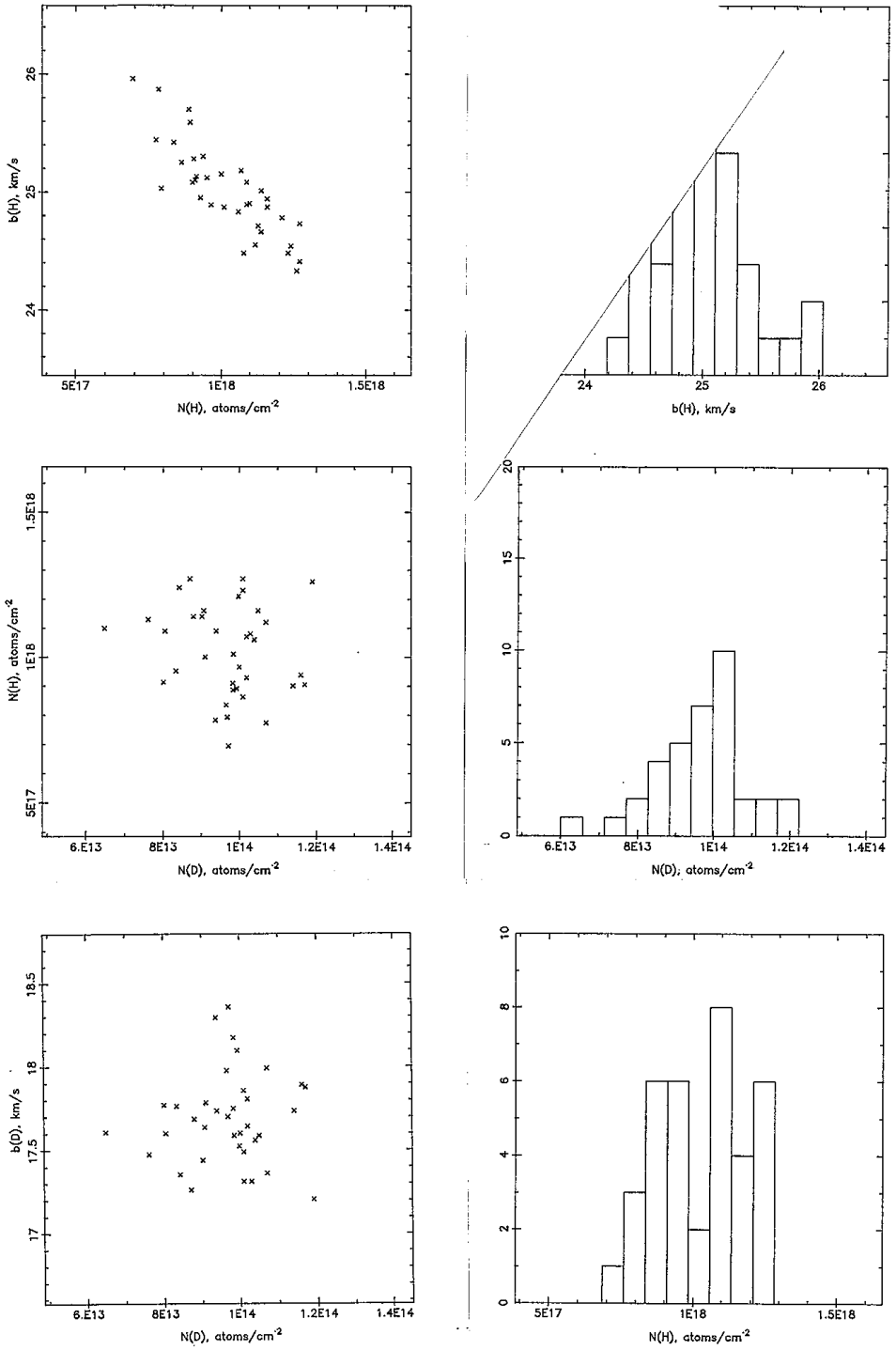

Figure 4.2c: Distribution of results for Simulation c: $\log N(HI) = 18$, $b(HI) = 25$ km/s, $\log D/H = -4$

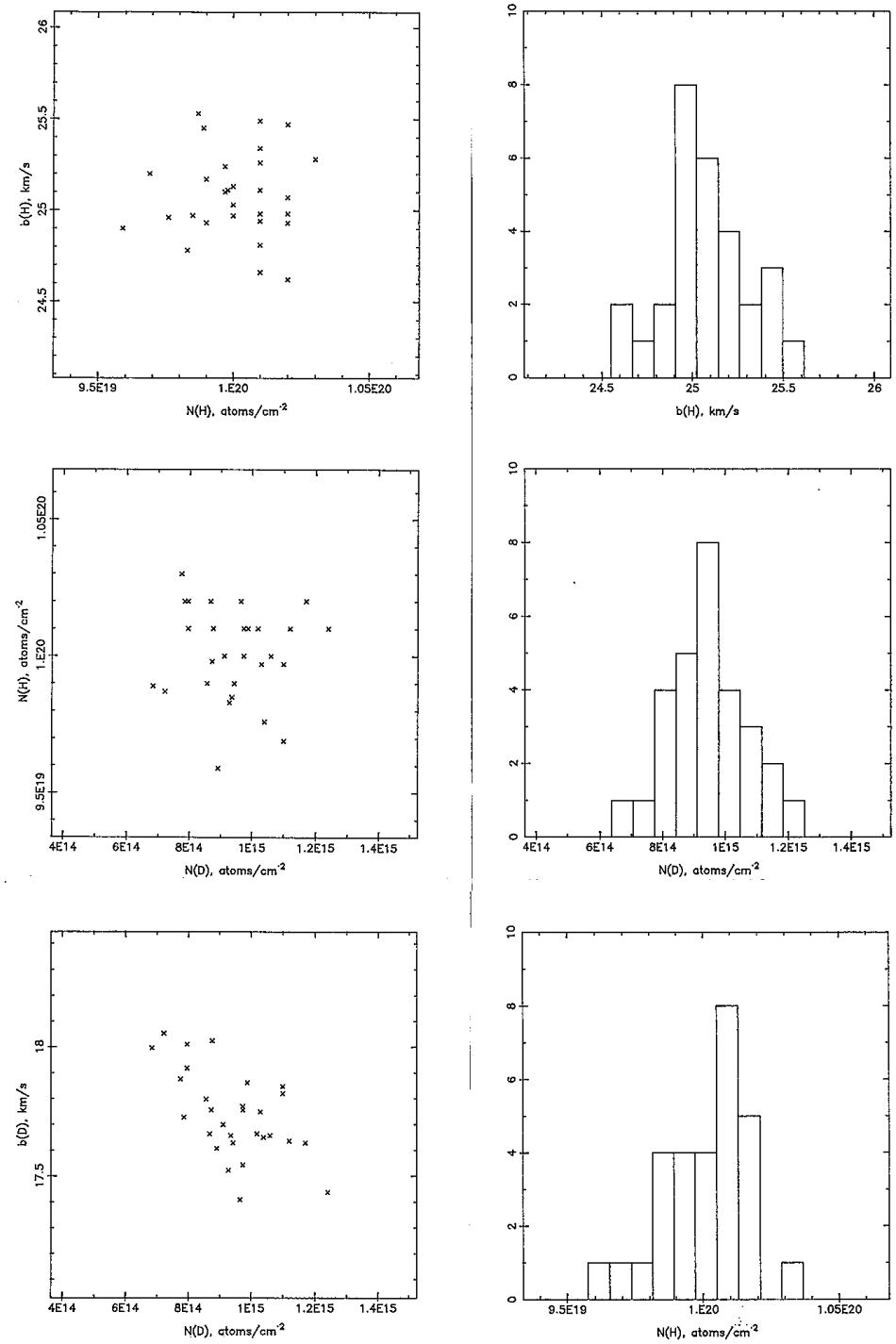

Figure 4.2d: Distribution of results for Simulation *d*: $\log N(HI) = 20$, $b(HI) = 25$ km/s, $\log D/H = -5$

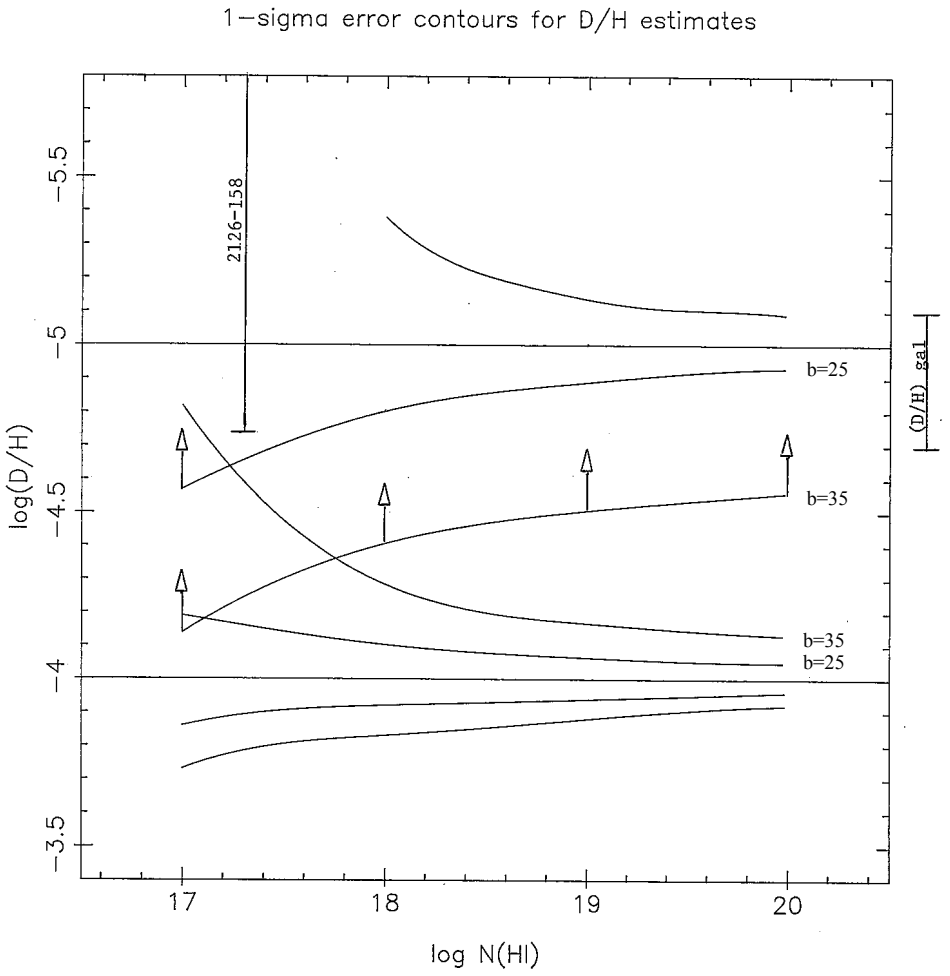

Figure 4.3: The detectability of D/H, estimated from numerical simulations. The arrows indicate where DI was too weak to obtain a lower limit on D/H. The inner curves are for a velocity dispersion parameter of $b = 25$ km/s. No lower limit on D/H could be obtained for $b = 35$ km/s for any value of $N(HI)$.

Appendix to Chapter 4

LIMITS FOR THE D/H RATIO IN A QUASAR ABSORPTION SYSTEM AT REDSHIFT Z=3.08.

J.K. Webb

Sterrewacht Leiden

R.F. Carswell[1], **M.J. Irwin**

Institute of Astronomy, Cambridge

J.A. Baldwin, B. Atwood

Cerro Tololo Interamerican Observatory,

National Optical Astronomy

Observatories[2]

J.G. Robertson,

Anglo-Australian Observatory

and

P.A. Shaver,

European Southern Observatory

[1] Visiting Astronomer, Cerro Tololo Interamerican Observatory.

[2] Gene Tololo Interamerican Observatory, National Optical Astronomy Ob-

servatories, are operated by the Association of Universities for Research in Astronomy, Inc., under contract with the National Science Foundation.

Abstract

The Lyγ and Lyδ lines in a previously reported metal line absorption system at $z = 3.08571$ in the quasar Q0420—388 appear to have short wavelength structure which is consistent with a detection of deuterium at the same redshift. If this interpretation is correct, the best estimate for the D/H ratio in this system, which has a silicon abundance $\sim 1/5$ solar, is $\sim 4 \times 10^{-5}$. It is possible that instead the structure in these lines arises from confusing HI systems. Whether or not we have detected deuterium the upper limit for the D/H ratio at $z = 3.08571$ towards Q0420-388 is $\sim 10^{-4}$.

1. Introduction

Searches for deuterium in high redshift quasar absorption systems have been considered, and undertaken, since the possibility of its detection was investigated by Adams(1976). Much of the emphasis has been on measurement of the primordial D/H ratio for constraining cosmological models, but determination of this quantity in heavy element systems at high redshifts is useful as a sensitive discriminator between different chemical evolution models for galactic gas. The D lines are separated from the corresponding H lines by only 81 km s^1 (or 0.33Å at Lyα in the rest frame), and so, if the HI lines are strong then the presence of DI is masked. Adams showed that, if the D/H ratio is of order 10^{-5}, then for only a small range of HI column densities around N(HI) $\sim 10^{18}$ cm^{-2} and low velocity dispersions (typically ≤ 20 km s^{-1}) could one expect to separate the two Lyα lines. At higher HI column densities than those considered by Adams, the D/H ratio may be investigated be examining higher order Lyman lines, where, since the oscillator strengths are smaller, the saturation effects are less severe.

The absorption line spectrum of the quasar Q0420-388 has been the subject of a recent study by Atwood, Baldwin and Carswell (1985 - hereafter ABC).

They conclude that, for the Lyman forest clouds, there are no systems of high enough HI column density for astrophysically interesting quantities of DI to be detectable. However, they report that there is a complex metal-lined system at $z = 3.086$ where the HI column density is sufficiently high that DI could be detectable under favourable circumstances. In the lowest redshift component they found that the velocity dispersion (for SiII) is of order 8 km s^{-1}. This component has a silicon abundance of about 1/5 solar, and so is similar in content to clouds in the interstellar medium in the Galaxy. It is therefore of interest to ask if the D/H ratio is also typical of that found locally.

2. The Data

Spectra of Q0420-388 covering the wavelength range $3816 - 5235$Å with a resolution 33 km s^{-1} (FWHM) have been published by ABC. Further spectra with a resolution of 26 km s^{-1} were obtained at the Anglo-Australian Telescope during 1985. These cover the wavelength range $3862 - 4003$Å with a total integration time of 3h 20m on the nights of 15 and 18 February, 1985, and $3857 - 4001$Å with an integration time of 3h 10m over the nights 7 and 8 September, 1985. Spectra covering the Lyman α, β, γ and δ lines at $z = 3.086$ are shown in fig 1. Evidently there is structure in the short wavelength wings of the Ly$y\gamma$ and Lyδ lines which may be consistent with deuterium at the lowest redshift of the HI (or SiII) components. There is no sign of similar structure in Lyα or Lβ, but there it would be lost in the saturated HI lines.

We have re-analysed the lines in the $z = 3.086$ absorption complex using all the available spectroscopic data, and employing a maximum likelihood optimisation technique (Webb, Irwin and Carswell, in preparation) programmed for use on the Starlink VAX computer in Cambridge. We have fitted the SiII lines along with the hydrogen lines to constrain the redshifts and velocity dispersions in each component. For any ion in a given cloud the measured velocity dispersion consists of a turbulent component, b_{turb}, independent of the ion

involved, and a thermal component which depends on the mass of the ion, $b_t = \sqrt{\frac{2kT}{m}}$. The measured quantity is then $b = \sqrt{b_{turb}^2 + b_T^2}$. In particular, the velocity dispersions of hydrogen, deuterium and silicon are linked as a combination of these two parameters, so $b_T(H) = \sqrt{2}b_T(D) = \sqrt{28}b_T(Si)$. This provides a useful constraint only where all three species are seen, so was used only for the $z = 3.08571$ component where the HI, DI and SiII line profiles were fitted simultaneously. The results are given in Table 1. For the $z = 3.08571$ component the parameters z, b_{turb}, b_T and the column densities N(HI), N(DI) and N(SiII) and their errors were estimated by searching a grid of values. The error estimates were determined by examining the behaviour of χ^2 relative to the best fit value, as in Atwood et al. (1985). The turbulent component of the velocity dispersion is only a little greater than the total Doppler parameter for SiII, at $b_{turb} = 9^{+3}_{-2}$ km s^{-1}. The best estimate for the thermal component is $b_T(H) = 0$ km s^{-1}, with a maximum value of 11 km s^{-1} (8 km s^{-1} for D, 2 km s^{-1} for Si) allowed with 70% confidence at $b_{turb} = 9$ km s^{-1}. For the system at $z = 3.08646$ DI was not detected, as might be expected from the relatively low HI column density, and at redshift $z = 3.08823$ DI is not measurable since the deuterium lines fall in regions of the spectrum which have been totally absorbed by the corresponding HI lines at lower redshifts. For these two systems the parameters were determined first for SiII, and the HI redshifts then fixed at the best estimates derived from the SiII lines. This procedure saved a large amount of computing time and does not significantly affect the results for the $z = 3.08571$ system. However, the errors in the HI velocity dispersion and HI column density for the two higher redshift components, particularly at $z = 3.08823$, are underestimated as a consequence. The Lyman α, β, γ and δ features were fitted simultaneously for all three systems in the complex, and for the lowest redshift system a simultaneous fit with SiII was also required. Lyα components in the wings of the heavy element system Lyman lines were fitted without reference to their corresponding higher order Lyman lines. The

results are summarised in Table 1. There are some small differences from the values published by ABC, but these are not significant. The fitted Lyman line profiles are shown in fig. 1.

On the basis of these data, for $z = 3.08571$ the SiII to HI ratio, logN(SiII)/N(HI) = —5.2±0.5. We do not have the wavelength coverage necessary to investigate the silicon abundance in detail, but if most of the silicon in the HI region exists as SiII then its abundance is approximately 1/5 solar, with a 70% confidence interval of a factor of about 3. This should be compared with the results for the interstellar medium in the Galaxy, where towards ζ Puppis, for example, [Si/H] = —0.74 (Morton, 1978).

The measured deuterium to hydrogen ratio for the $z = 3.08571$ system is given by $\log N(DI)/N(HI) = -4.43^{+0.45}_{-0.26}$, so $D/H = 4 \times 10^{-5}$ to within a factor of less than 3. This compares with a value for the Galaxy somewhere in the range $0.8 - 2 \times 10^{-5}$ (Boesgaard and Steigman, 1985).

We should examine the possibility that the presence of deuterium is not required toexplain these observations. There are a number of alternatives which we should consider here:

(i) We cannot differentiate between a genuine deuterium detection and an HI system offset by about -81 km s^{-1} from the $z = 3.08571$ system, since isotope shifts and velocity shifts are indistinguishable. If we interpret the lines we have identified with DI as HI instead, and so do not constrain the redshift, then the best fit velocity relative to $z = 3.08571$ is -82 ± 3 km s^{-1}. We do not know what the density of Lyman line systems is near a strong system, so, while noting that the velocity agreement for an identification with deuterium is remarkably good, we cannot rule out the possibility of a confusing HI system.

(ii) We cannot rule out the presence of two lower redshift Lyα lines with the right relative strengths and redshifts to mimic D_γ and D_δ, though this is not very likely.

(iii) If we choose to omit the feature entirely, then the overall fit is acceptable

but somewhat worse, with each of Lyγ and Lyδ having deviations from the best fit at the 5% level. Under these circumstances the component at $z = 3.08646$ has a velocity dispersion $b = 68$ km s^{-1}, and log N(HI) = 16.9. This is shown in fig. 2. It is the broad lines from this component which are necessary to make up the extended short wavelength wings we had identified as Dγ and Dδ. The parameters for HI in the other two components differ very little from those given in table 1. If the HI velocity dispersion is predominantly thermal in origin, the temperature T $> 1.5 \times 10^5$ K, which is hardly likely to be appropriate for a low ionization region. Instead, it is possible that we are seeing a warmer component of the interstellar medium superimposed on a cool component. This would apply also at $z = 3.08571$, where if we add an additional warm component, it has logN(HI) = 16.82 and $b = 39$ km s^{-1}, corresponding to T $\sim 9 \times 10^9$ K, though in this case the fit is not as good.

3. Discussion

For a high redshift absorbing cloud at $z = 3.08571$ towards the quasar Q0420-388 we have found that the Si/H ratio is similar to that found in interstellar clouds in the Galaxy. If our identification of deuterium is correct, the best estimate of the D/H ratio is a factor of two or more higher, though the data are consistent with a similar value to that found in the Galaxy. This inferred D/H value of 4×10^{-5}, with an estimated 70% error of about a factor of two-three, should be treated as tentative, since we cannot differentiate between the presence of deuterium and a separate lower redshift HI cloud at -81 km s^{-1} lower redshift in individual cases such as this. Even if we have not detected deuterium, but a confusing HI system or systems, then we may still infer an upper limit to the D /H ratio equal to the maximum allowed within the error range. Thus, with 70% confidence, D/H $< 10^{-4}$ at $z = 3.08571$.

It is also possible that the features we have seen could be explained by a high velocity dispersion component associated with one or more of the HI clouds.

It would be of value to see if such possible warm components are a general feature, and a determination of the D/H ratio requires analysis of a number of such clouds so that we may be sure that velocity shifted systems are not responsible.

On the basis of the data presented here it appears that the abundances, and degree of nuclear processing of the primordial material, as measured by the silicon and deuterium abundances relative to hydrogen, could be quite similar in the redshift $z = 3.08571$ system described here and in the Galaxy. Given the silicon abundance, it is hardly surprising that the deuterium abundance is similar, since both reflect the degree of nuclear processing of the primordial material. Perhaps the most important result is that a combination of redshift information from heavy element lines and high resolution spectra of the Lyman lines does allow a limit for the D/H ratio to be obtained. It would be of interest to examine other such systems in detail, since only then can allowance be made for the possibility of confusing velocity structure.

Acknowledgements:

We are grateful to many people for their unbiased comments on the data, notably Ray Weymann, Craig Foltz, Fred Chaffee and Bob Williams. We also thank the telescope operators and support staff at the Anglo-Australian and CTIO 4m. telescopes, without whose expert assistance the observations would not have been possible. RFC is grateful to the Radcliffe Trust for support during the early part of this investigation, and the UK Science and Engineering Research Council for travel grants.

REFERENCES:

Adams, T.F., 1976. Astron. Ap., 50, 461.

Atwood, B., Baldwin, J.A., and Carswell, R.F., 1985. Ap.J., 292, 58.

Boesgaard, A.M., and Steigman, G., 1985. Ann. Rev. Astron. Astrophys, 23,

319.

Morton, D.C., 1978. Ap.J., 222, 863.

Figure Captions:

Fig 1. The Lyman α, β, γ and δ lines in the $z = 3.086$ systems in the spectrum of Q0420-388, showing the fitted line profiles. The individual systems are numbered to correspond to those given in Table 1, so, in particular, the number 6 indicates the position of deuterium at the same redshift as the system 5 hydrogen lines. Unlabelled tick marks correspond to additional Lyα components which have been added for illustrative purposes only. They do not constrain the parameters for the lines of interest, and are not in the parts of the spectrum used to fit the line profiles.

Fig 2. The Lyman γ and δ lines at $z = 3.086$ showing the best fit obtained under the assumption that deuterium is not detectable. For this example, a broad component attributed to system 7 at $z = 3.08646$ is required to obtain an adequate fit to the data, as described in the text.

Authors' Addresses:

B. Atwood, Cerro Tololo Interamerican Observatory, Casilla 603, La Serena, Chile

J.A. Baldwin, Department of Astronomy, Ohio State University, Columbus OH 43210

R.F.Carswell and M.J.Irwin, Institute of Astronomy, Madingley Road, Cambridge CB3 OHA, England

J.G.Robertson, Anglo-Australian Observatory, P.O.Box 296, Epping, N.S.W. 2121, Australia

P.A.Shaver, European Southern Observatory, Karl—Schwarzschild—Strasse 2, D-8046 Garching—bei—Munchen, Federal Republic of Germany

J.K.Webb, Sterrewacht Leiden, P.O.Box 9513, 2300 RA Leiden, The Netherlands

Table 1: Redshift Systems

n	**Ion**	**Redshift**	±	b	±	**logN**	±
	SiII	3.08571	0.00006	9	$^{+3}_{-2}$	14.17	0.50
	SiII	3.08646	0.00007	21	6	13.68	0.11
	SiII	3.08823	0.00003	4	1	15.78	0.18
1	HI	3.07434	0.00003	27	4	13.95	0.09
2	HI	3.07762	0.00007	12	13	13.22	0.16
3	HI	3.07946	0.00018	33	19	13.32	0.17
4	HI	3.08075	0.00005	27	4	14.69	0.16
5	HI	3.08571	0.00006	9	$^{+5}_{-2}$	19.37	0.06
6	DI	3.08571	0.00006	9	$^{+3}_{-2}$	14.94	$^{+0.39}_{-0.20}$
7	HI	3.08646	—	47	17	17.94	1.64
8	HI	3.08823	—	25	2	19.24	0.04
9	HI	3.09385	0.00010	20	14	13.03	0.16
10	HI	3.10023	0.00004	41	4	13.82	0.04
11	HI	2.44558	0.00008	38	12	14.10	0.15
12	HI	2.45084	0.00014	18	28	14.09	0.97
13	HI	2.26704	0.00002	6	12	14.10	3.76
14	HI	2.27161	0.00084	23	23	15.25	3.17
15	HI	2.18981	0.00008	18	12	13.16	0.19
16	HI	2.19045	0.00005	29	8	13.63	0.08

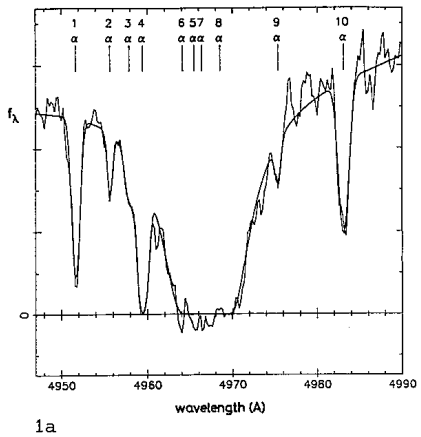

1a

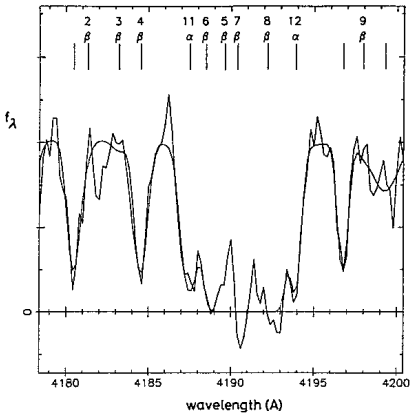

1b

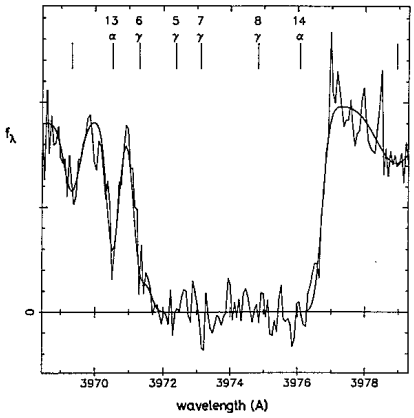

1c

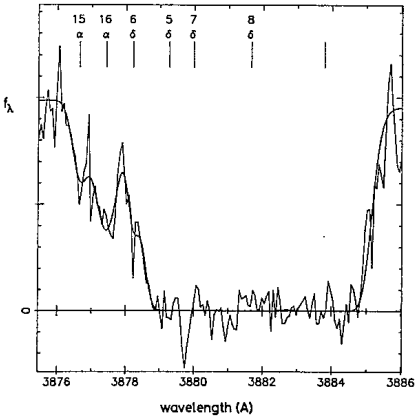

1d

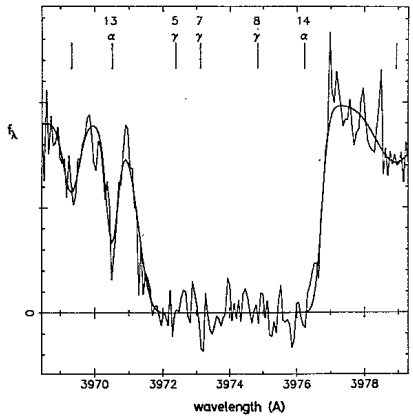

2a

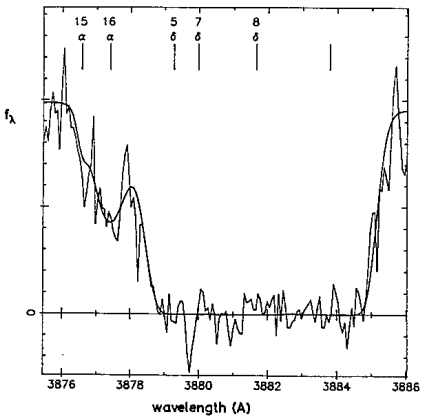

2b

5 Applications

5.1 Introduction

The Maximum Likelihood Optimisation technique developed in Chapter 3 is a significant improvement over previous direct search methods in terms of computing time requirements, accuracy and objectivity. It also makes available a new range of problems, as is demonstrated by the work described in the appendix to Chapter 4. In this chapter, the results of the profile fitting analysis to the AAT sample are given. In addition to the objects and wavelength regions listed in Tables 2.2 and 2.2, existing data on Q1101-264 (Carswell et al., 1984) was re-analysed since the profile fitting techniques used originally on this data differ from those described in Chapter 3. The instrumental setup used to collect the Q1101-264 spectra was identical to that for the other AAT observations.

5.2 Absorption line lists

The initial stage in identifying individual absorption clouds is to locate absorption features in the spectra above a limiting significance level. The method used to do this is described by Young et al., (1979). Only features which deviated from the adopted continuum level by 4σ or more were selected for further

analysis.

Tables 5.1 to 5.11 give the profile details for the complete AAT sample. Columns 2 and 3 are the air and vacuum corrected wavelengths for the observed absorption features. Columns 4,5 and 6 are the vacuum wavelength error estimate, the equivalent width and the error in the equivalent width. These quantities were obtained using the procedures developed by Young et al., (1979) which are not repeated here since only the parameters obtained through profile fitting are used for the statistical analyses described later. Column 7 shows the suggested identification for each absorption line. Columns 8 to 13 are the z, b and N(HI) parameter and error estimates. In column 14 is the instrumental resolution at the mean wavelength of each absorption feature. Columns 15 and 16 are the number of channels included in the fitting procedure, and the number of degrees of freedom. The last two columns are the χ^2 for the fit and the associated significance level, which should be considered as an approximation. This is for two reasons: the noise properties of the data are not Poisson (although a scaling factor has been included in the χ^2 value to allow for this - see section 2.3). Also, where more than one data region has been included in the fitting procedure (e.g. Lyα and Lyβ) the individual regions are no longer statistically independent and the number of degrees of freedom is no longer simply the number of data channels minus the number of free parameters.

Following the absorption line lists in Tables 5.1 to 5.11 is an appendix containing specific comments on some of the profile fits.

Table 5.1 Absorption lines in Q2237-398

	λ_{air}	λ_{vac}	±	EW(Å)	±	ID	z	±	b (km/s)	±	N(HI)	±	σ_{res}(Å)	n_{ch}	ν	χ^2	sig
1	3735.91	3736.97	0.04	0.22	0.04	Ly-b	2.64319	0.00003	26	3	1.22e14	1.87e13					
2						Ly-b	2.64445	0.00005	40	7	5.05e13	6.19e12	0.184	46	48	44.41	0.291
3	3747.98	3748.96	0.05	1.26	0.08	Ly-b	2.65538	0.00002	19	3	1.05e15	1.57e15					
4						Ly-b	2.65588	0.00006	69	3	2.12e14	2.30e13	0.166	73	64	58.59	0.889
5	3755.62	3756.68	0.06	0.59	0.06	Ly-b	2.66253	0.00004	46	4	2.79e14	2.33e13					
6	3756.83	3757.90	0.06	0.13	0.04	Ly-b	2.66374	0.00005	37	5	1.00e14	1.32e13	0.154	44	33	57.98	0.978
7	3760.21	3761.28	0.03	0.38	0.04	Ly-a	2.09401	0.00002	10	6	4.28e13	3.57e13	0.140	30	27	22.30	0.738
8	3762.46	3763.52	0.04	0.73	0.06	Ly-a	2.09581	0.00002	26	3	7.75e13	9.30e12					
9						Ly-b	2.66847	0.00005	25	7	1.64e13	3.21e12	0.145	37	24	32.64	0.112
10	3765.03	3766.10	0.04	0.57	0.05	Ly-a	2.09798	0.00002	19	3	6.59e13	1.06e13	0.142	32	23	29.48	0.868
11	3769.15	3770.22	0.03	1.40	0.06	Ly-a	2.10142	0.00002	27	7	9.68e14	1.5e15					
12	3770.52	3771.59	0.02	0.34	0.03	Ly-a	2.10247	0.00003	15	5	3.62e13	7.74e12					
13	3771.85	3772.92	0.06	0.41	0.05	Ly-a	2.10359	0.00003	50	12	3.21e13	6.00e12	0.133	100	91	129.77	0.006
14	3774.28	3775.36	0.03	0.55	0.04	Ly-b	2.68075	0.00006	18	3	5.20e14	1.62e14					
15	3775.10	3776.18	0.02	0.76	0.04	Ly-b	2.68138	0.00006	22	3	7.61e14	2.15e14					
16	3779.98	3781.05	0.03	1.10	0.05	Ly-b	2.68549	0.00043	53	28	8.73e13	7.12e13					
17						Ly-b	2.68637	0.00004	35	3	7.44e14	1.05e14					
18	3781.67	3782.75	0.04	0.24	0.04	Ly-b	2.68785	0.00003	25	3	1.44e14	1.82e13					
19	3782.83	3783.90	0.04	0.71	0.05	Ly-b	2.68904	0.00002	35	2	3.78e14	3.42e13	0.122	202	175	270.28	0.000
20	3793.87	3794.95	0.09	5.69	0.14	Ly-a	2.11705	0.00008	48	11	2.82e13	5.36e12					
21						Ly-a	2.11857	0.00012	66	20	3.28e13	1.00e13					
22						Ly-b	2.69591	0.00004	58	4	1.91e14	7.11e12					
23						Ly-a	2.12103	0.00002	35	8	2.88e17	1.06e18					
24						Ly-a	2.12359	0.00052	208	76	8.13e13	3.03e13					
25						Ly-b	2.70269	0.00002	30	2	3.24e14	4.24e13					
26						Ly-a	2.12587	0.00004	37	6	4.52e13	8.07e12	0.115	228	199	167.83	0.947
27	3803.58	3804.58	0.03	1.42	0.06	Ly-b	2.70939	0.00003	49	4	3.83e14	7.78e13					
28						Ly-a	2.12962	0.00003	37	5	2.13e14	7.07e13					
29	3806.87	3807.95	0.03	3.83	0.07	Ly-b	2.71179	0.00002	34	4	6.44e17	9.79e17					
30						Ly-a	2.13276	0.00351	53	89	3.54e15	4.70e17					
31						Ly-b	2.71395	0.00008	23	12	1.34e13	6.54e12					
32	3809.51	3810.59	0.05	0.10	0.03	Ly-b	2.71492	0.00003	33	4	9.30e13	8.07e12	0.117	169	148	165.10	0.159
33	3827.24	3828.33	0.04	0.27	0.05	Ly-a	2.14912	0.00006	20	8	2.17e13	5.76e12	0.120	26	23	39.95	0.015
34	3841.70	3842.79	0.03	0.98	0.05	Ly-a	2.16104	0.00003	34	3	9.96e13	1.14e13					
35	3843.77	3844.86	0.03	0.32	0.04	Ly-b	2.74343	0.00002	28	2	1.87e14	2.35e13					
36	3844.79	3845.88	0.02	0.70	0.04	Ly-a	2.16361	0.00003	31	4	6.84e13	7.99e12					
37	3845.87	3846.96	0.03	0.57	0.04	Ly-b	2.75047	0.00002	31	2	3.17e14	3.72e13	0.122	108	96	108.73	0.177
38	3848.39	3849.48	0.03	0.57	0.04	Ly-a	2.16656	0.00002	22	2	6.61e13	7.41e12	0.126	23	20	11.70	0.926
39	3851.99	3853.08	0.03	0.51	0.05	Ly-b	2.75643	0.00002	28	2	2.38e14	2.32e13					
40	3852.99	3854.08	0.04	0.39	0.04	Ly-b	2.75734	0.00004	24	5	3.71e13	5.25e12					
41						Ly-a	2.17022	0.00005	37	8	2.84e13	4.31e12					
42	3853.98	3855.07	0.08	0.15	0.04	Ly-b	2.75835	0.00005	20	6	1.27e13	2.70e12					
43						Ly-a	2.17121	0.00016	8	15	6.49e12	2.72e12					
44	3855.54	3856.63	0.05	0.59	0.06	Ly-b	2.75951	0.00003	41	3	7.88e13	5.33e12					
45						Ly-a	2.17262	0.00004	36	6	3.14e13	4.07e12	0.133	95	71	43.18	0.996
46	3858.36	3859.45	0.03	1.81	0.06	Ly-a	2.17448	0.00224	53	82	8.07e13	5.43e14					
47						Ly-b	2.76239	0.00004	28	4	6.18e13	7.47e12					
48						Ly-a	2.17497	0.00058	44	22	1.71e14	5.67e14					
49						Ly-b	2.76338	0.00005	34	5	5.11e13	6.53e12	0.146	51	39	42.77	0.312
50	3861.26	3862.35	0.06	0.20	0.05	Ly-a	2.17722	0.00038	33	12	1.69e13	4.22e12	0.152	25	22	19.97	0.585
51	3865.92	3867.02	0.05	0.83	0.08	Ly-b	2.76935	0.00004	41	4	3.39e14	5.52e13					
52						Ly-a	2.18134	0.00069	17	18	2.75e13	1.27e13	0.162	66	51	92.13	0.000
53	3867.59	3868.68	0.05	0.92	0.09	Ly-a	2.19231	0.00004	27	7	1.32e14	5.79e13					
54						Ly-b	2.77219	0.00004	28	7	5.17e13	2.19e13	0.164	45	36	51.03	0.054
55	3871.45	3872.55	0.04	0.52	0.07	Ly-a	2.19553	0.00005	26	8	5.60e13	1.21e13					
56						Ly-b	2.77598	0.00011	69	13	2.06e13	4.45e12	0.173	25	19	28.45	0.075

Table 5.2 Absorption lines in Q0207-398

	λ_{air}	λ_{vac}	±	EW(A)	±	ID	z	±	b(km/s)	±	N(HI)	±	$\sigma_{res}(\AA)$	n_{ch}	ν	χ^2	sig
1	4126.60	4127.76	0.04	1.12	0.06	Ly-a	2.39552	0.00003	52	4	9.57e13	6.26e12	0.179	54	51	45.45	0.693
2	4131.59	4132.76	0.03	4.48	0.07	Ly-a	2.39742	0.00008	32	10	2.48e13	7.10e12					
3						Ly-a(M)	2.39933	0.00006	79	11	6.24e14	1.16e14					
4						Ly-a	2.40101	0.00006	36	5	1.96e14	4.25e13	0.165	110	101	77.45	0.961
5	4139.91	4141.07	0.03	0.82	0.04	Ly-a	2.40619	0.00005	25	6	3.51e13	6.34e12					
6						SiII 1190	2.47891	0.00002	19	2	3.00e13	4.81e12					
7	4140.84	4142.00	0.02	0.14	0.02	SiII 1190	2.47948	0.00002	2	2	1.95e14	6.70e14					
8	4141.69	4142.86	0.03	0.40	0.04	SiII 1190	2.48017	0.00002	24	2	2.76e13	2.14e12	0.116	54	42	37.50	0.669
9	4143.83	4145.00	0.02	0.73	0.04	Ly-a	2.40963	0.00003	33	4	7.33e13	7.92e12	0.117	41	38	55.68	0.032
10	4150.16	4151.33	0.02	0.61	0.03	SiII 1193	2.47891	0.00002	19	2	3.80e13	4.81e12					
11	4150.85	4152.02	0.02	0.18	0.03	SiII 1193	2.47948	0.00002	2	2	1.95e14	6.70e14					
12	4151.73	4152.90	0.02	0.57	0.04	SiII 1193	2.48017	0.00002	2	2	2.76e13	2.14e12	0.118	65	56	65.25	0.186
13	4154.91	4156.08	0.06	0.45	0.05	Ly-a	2.41330	0.00007	53	9	3.18e13	4.54e12					
14	4157.37	4158.54	0.09	0.33	0.06	Ly-a	2.42389	0.00007	34	8	1.88e13	3.66e12	0.118	92	86	84.83	0.543
15	4161.46	4162.63	0.05	0.28	0.04	Ly-a	2.42407	0.00004	19	6	1.60e13	3.00e12					
16	4162.98	4164.15	0.08	0.32	0.05	Ly-a	2.42530	0.00010	53	15	2.19e13	4.64e12					
17	4164.58	4165.75	0.08	0.22	0.05	Ly-a	2.42663	0.00007	29	9	1.50e13	3.55e12	0.119	92	83	68.39	0.876
18	4167.03	4168.20	0.04	0.47	0.05	Ly-a	2.42876	0.00002	24	3	3.48e13	3.04e12	0.120	26	23	18.84	0.985
19	4172.24	4173.42	0.04	0.78	0.06	Ly-a	2.43300	0.00003	37	4	6.11e13	5.75e12	0.120	39	36	28.31	0.797
20	4180.59	4181.77	0.12	0.38	0.06	Ly-a	2.43981	0.00014	53	17	2.19e13	7.91e12					
21	4182.26	4183.44	0.03	0.51	0.04	Ly-a	2.44123	0.00002	14	4	5.98e13	2.10e13					
22	4183.67	4184.85	0.08	0.19	0.04	Ly-a	2.44224	0.00048	123	67	3.15e13	1.53e13					
23	4185.98	4187.16	0.03	0.58	0.04	Ly-a	2.44432	0.00003	21	4	4.21e13	6.00e12					
24	4188.88	4190.06	0.03	2.86	0.07	Ly-a	2.44556	0.00016	51	18	4.45e13	1.61e13					
25						Ly-a	2.44787	0.00005	61	6	3.92e14	5.51e13					
26	4192.94	4194.12	0.02	3.32	0.06	Ly-a	2.45057	0.00005	75	8	3.39e15	1.93e16					
27	4195.99	4197.17	0.02	2.57	0.05	SiIII 1206	2.47891		17	23	8.68e14	9.60e15					
28						SiIII 1206	2.47948		6	25	8.18e14	2.25e16					
29	4197.59	4198.77	0.01	0.53	0.02	SiIII 1206	2.48017		57	5	5.27e13	1.44e13					
30	4198.32	4199.50	0.02	0.77	0.04	Ly-a	2.45441	0.00009	7	32	1.63e14	3.96e15					
31	4199.53	4200.71	0.04	0.40	0.04	SiIII 1206	2.48172	0.00003	18	4	7.92e12	1.30e12	0.123	361	328	270.75	0.991
32	4206.02	4207.20	0.08	0.22	0.05	Ly-a	2.46087	0.00006	25	8	1.32e13	3.13e12	0.125	26	23	17.47	0.786
33	4208.84	4210.02	0.10	0.27	0.06	Ly-a	2.46342	0.00067	99	78	2.90e13	2.26e13	0.125	35	32	29.70	0.584
34	4211.19	4212.37	0.06	0.23	0.05	Ly-a	2.46510	0.00006	24	9	1.43e13	3.56e12	0.125	34	31	30.38	0.498
35	4214.30	4215.48	0.06	0.61	0.06	Ly-a	2.46797	0.00022	59	18	5.79e13	2.14e13					
36	4216.19	4217.37	0.02	2.14	0.06	Ly-a	2.46914	0.00004	39	9	1.19e15	1.25e15					
37	4218.35	4219.54	0.04	0.56	0.05	Ly-a	2.47089	0.00008	55	11	4.63e13	6.83e12	0.126	118	109	99.30	0.736
38	4223.68	4224.87	0.05	0.29	0.05	Ly-a	2.47520	0.00011	57	14	2.72e13	5.38e12	0.127	37	34	30.89	0.621
39	4229.65	4230.84	0.03	6.37	0.09	Ly-a(M)	2.48330	0.00032	63	1	4.77e18	1.15e18	0.128	167	164	174.64	0.270
40	4243.47	4244.67	0.05	0.26	0.04	Ly-a	2.49162	0.00004	24	5	1.74e13	2.48e12	0.130	31	28	15.59	0.972
41	4246.39	4247.59	0.04	0.29	0.04	Ly-a	2.49403	0.00004	25	6	1.97e13	3.22e12	0.130	23	20	17.03	0.651

Table 5.3 Absorption lines in 0B207-398

	λ_{air}	λ_{vac}	±	EW(A)	±	ID	z	±	b(km/s)	±	N(HI)	±	σ_{res}(Å)	n_{ch}	ν	χ^2	sig
1	4424.95	4426.19	0.03	1.22	0.06	Ly-a	2.64293	0.00002	17	12	5.14e15	3.76e16					
2	4427.65	4428.90	0.03	0.93	0.05	Ly-a	2.64319	0.00003	26	3	1.22e14	1.87e13					
3	4429.16	4430.40	0.04	0.70	0.05	Ly-a	2.64445	0.00005	40	7	5.05e13	6.10e12	0.170	122	113	97.06	0.967
4	4435.26	4436.50	0.12	0.49	0.07	Ly-a	2.64943										
5	4442.93	4444.18	0.02	2.46	0.05	Ly-a	2.65529	0.00003	18	4	2.41e15	3.15e15					
6						Ly-a	2.65587	0.00007	70	4	2.17e14	2.82e13	0.124	83	74	58.12	0.912
7	4451.69	4452.94	0.02	2.73	0.06	Ly-a	2.66253	0.00004	46	4	2.79e14	2.39e13					
8						Ly-a	2.66374	0.00005	37	5	1.50e14	1.32e13	0.120	86	83	35.58	1.000
9	4458.39	4459.64	0.05	0.28	0.04	Ly-a	2.66847	0.00005	25	7	1.64e13	3.21e12	0.129	51	49	31.45	0.969
10	4465.45	4466.70	0.04	0.68	0.05	Ly-a	2.67431	0.00002	25	3	5.35e13	5.17e12	0.137	93	82	57.27	0.880
11	4473.77	4475.02	0.02	1.06	0.05	Ly-a	2.68075	0.00006	18	3	5.20e14	1.62e14					
12						Ly-a	2.68138	0.00005	22	3	7.61e14	2.15e14					
13	4475.92	4477.18	0.03	0.57	0.05	Ly-a	2.68293	0.00003	20	3	5.50e13	6.53e12					
14	4477.33	4478.59	0.05	0.35	0.05	Ly-a	2.68402	0.00006	21	8	1.36e13	4.63e12					
15	4479.76	4481.02	0.02	2.50	0.06	Ly-a	2.68549	0.00043	53	28	8.73e13	7.10e13					
16						Ly-a	2.68637	0.00004	35	3	7.44e14	1.05e14					
17	4481.95	4483.21	0.01	1.09	0.03	Ly-a	2.68785	0.00003	25	3	1.44e14	1.82e13					
18	4483.45	4484.71	0.02	1.40	0.04	Ly-a	2.68904	0.00002	35	2	3.70e14	3.42e13					
19	4485.95	4487.21	0.03	0.35	0.04	Ly-a	2.69114	0.00003	15	4	2.42e13	4.02e12	0.133	257	239	183.14	0.990
20	4492.95	4494.21	0.03	1.24	0.06	Ly-a	2.69691	0.00001	58	4	1.01e14	7.11e12					
21	4499.98	4501.24	0.02	1.45	0.05	Ly-a	2.70269	0.00002	30	2	3.24e14	4.24e13	0.124	194	178	152.06	0.921
22	4507.76	4509.03	0.03	2.08	0.06	Ly-a	2.70939	0.00003	49	4	3.93e14	7.73e13					
23	4511.04	4512.31	0.02	3.25	0.06	Ly-a	2.71179	0.00002	34	4	6.77e17	9.79e17					
24	4513.56	4514.83	0.04	0.19	0.04	Ly-a	2.71395	0.00008	23	12	1.34e13	6.54e12					
25	4514.82	4516.09	0.03	1.05	0.05	Ly-a	2.71492	0.00003	33	4	9.30e13	8.87e12					
26	4516.31	4517.58	0.05	0.18	0.04	Ly-a	2.71619	0.00009	30	12	1.33e13	3.99e12	0.114	212	197	148.87	0.996
27	4536.81	4538.09	0.05	0.78	0.05	Ly-a	2.73290	0.00008	46	8	2.48e13	3.85e12					
28						SiII 1304	2.47891	0.00002	19	2	3.30e13	4.81e12					
29						SiII 1304	2.47948	0.00002	2	2	1.95e14	6.72e14					
30						SiII 1304	2.48317	0.00002	24	2	2.76e13	2.14e12	0.139	54	42	37.50	0.669
31	4538.91	4540.91	0.07	0.18	0.04	Ly-a	2.73531										
32	4544.11	4545.38	0.05	0.73	0.05	Ly-a	2.73913	0.00004	42	4	4.26e13	3.61e12	0.118	97	54	62.15	0.299
33	4555.53	4556.81	0.02	1.23	0.05	Ly-a	2.74843	0.00002	28	2	1.87e14	2.35e13					
34	4558.05	4559.33	0.02	1.53	0.05	Ly-a	2.75047	0.00002	31	2	3.17e14	3.72e13	0.122	100	94	95.26	0.416
35	4563.96	4565.24	0.04	0.12	0.03	Ly-a	2.75532	0.00003	6	6	7.28e12	2.35e12					
36	4565.26	4566.54	0.02	1.25	0.04	Ly-a	2.75643	0.00002	28	2	2.38e14	2.32e13					
37	4566.46	4567.74	0.02	0.51	0.04	Ly-a	2.75734	0.00004	24	5	3.71e13	5.25e12					
38	4567.68	4568.96	0.05	0.25	0.04	Ly-a	2.75835	0.00005	20	6	1.27e13	2.70e12					
39	4569.09	4570.37	0.03	0.98	0.05	Ly-a	2.75951	0.00003	41	3	7.80e13	5.32e12	0.120	114	99	69.50	0.989
40	4572.53	4573.81	0.02	0.74	0.04	Ly-a	2.76239	0.00004	28	4	6.10e13	7.47e12					
41	4573.70	4574.98	0.03	0.63	0.04	Ly-a	2.76330	0.00005	34	5	5.11e13	6.50e12	0.119	62	55	39.24	0.957
42	4578.13	4579.41	0.03	0.36	0.04	Ly-a	2.76697	0.00004	18	5	2.34e13	4.10e12					
43	4579.24	4580.52	0.03	0.24	0.03	Ly-a	2.76790	0.00011	21	13	1.43e13	6.87e12					
44	4580.12	4581.40	0.02	0.57	0.03	Ly-a	2.76862	0.00006	26	11	4.04e13	1.13e13					
45	4581.65	4582.93	0.02	1.83	0.05	Ly-a	2.76985	0.00004	41	4	3.39e14	5.02e13	0.118	92	84	187.10	0.023
46	4584.87	4586.16	0.06	1.12	0.06	Ly-a	2.77219	0.00004	28	7	5.17e13	2.10e13					
47						Ly-a	2.77290	0.00053	63	32	3.02e13	2.35e13	0.117	65	59	45.08	0.890
48	4589.25	4590.54	0.06	0.37	0.04	Ly-a	2.77598	0.00011	69	13	2.06e13	4.45e12	0.116	67	64	64.35	0.605
**** No Lyman beta observations for lines at higher wavelengths ****																	
49	4608.43	4609.72	0.07	0.21	0.03	Ly-a	2.79196	0.00009	49	11	1.29e13	2.35e12					
50	4611.02	4612.31	0.02	2.08	0.04	Ly-a	2.79407	0.00001	48	2	2.57e14	1.91e13	0.113	114	100	93.54	0.839
51	4620.92	4622.11	0.02	0.06	0.03	Ly-a	2.80215	0.00002	39	2	6.10e13	2.63e12	0.110	64	61	68.78	0.231
52	4633.42	4634.71	0.03	0.35	0.02	Ly-a	2.81247	0.00002	29	2	2.20e13	9.86e11	0.100	37	34	21.93	0.945
53	4642.99	4644.29	0.02	2.73	0.03	CII 1334	2.47963	0.00001	5	2	4.54e13	1.40e13					
54						CII 1334	2.47921	0.00001	23	1	3.30e14	1.30e13					
55						CII 1334	2.47982	0.00001	10	3	5.27e13	7.60e12					
56						CII 1334	2.48053	0.00001	41	2	3.92e14	1.24e13					
57						CII 1334	2.48200	0.00001	11	2	3.93e13	3.36e12	0.106	106	91	80.04	0.569

Table 5.4 Absorption lines in Q1101-264

	λ_{air}	λ_{vac}	±	EW(A)	±	ID	z	±	b(km/s)	±	N(HI)	±	σ_{res}(Å)	n_{ch}	ν	X^2	sig
1	3695.78	3696.83	0.03	0.66	0.03	OI 1302	1.83874	0.00002	26	5	1.87e14	3.38e13					
2						OI 1302	1.83905	0.00002	16	7	1.71e14	4.20e13					
3						OI 1302	1.83938	0.00002	8	5	1.03e14	2.55e13					
4	3698.94	3700.00	0.03	0.93	0.04	Ly-a	2.04361	0.00002	46	2	9.50e13	4.93e12					
5	3701.27	3702.33	0.02	1.00	0.03	Ly-a	2.04545	0.00001	32	2	1.54e14	7.12e12					
6						SiII 1304	1.83838	0.00003	9	7	5.22e12	2.43e12					
7						SiII 1304	1.83874	0.00002	17	4	4.37e13	7.20e12					
8						SiII 1304	1.83905	0.00002	7	2	3.26e13	7.15e12					
9	3702.63	3703.69	0.02	0.29	0.02	SiII 1304	1.83938	0.00002	24	5	1.30e13	2.13e12					
10						Ly-a	2.04666	0.00004	28	6	1.75e13	2.52e12	0.106	125	98	128.28	0.063
11	3706.05	3707.11	0.03	0.61	0.03	Ly-a	2.04944	0.00001	26	1	6.15e13	3.29e12	0.106	41	38	25.95	0.931
12	3716.12	3717.18	0.04	0.22	0.03	Ly-a	2.05773	0.00003	23	4	1.54e13	1.76e12	0.106	34	31	22.02	0.882
13	3727.14	3728.20	0.03	0.32	0.03	Ly-a	2.06678	0.00002	17	4	1.97e13	2.75e12					
14	3728.12	3729.18	0.02	0.44	0.03	Ly-a	2.06753	0.00003	39	5	3.97e13	3.49e12	0.106	71	65	66.73	0.417
15	3731.88	3732.86	0.03	0.19	0.02	Ly-a	2.07062	0.00004	25	5	1.36e13	2.33e12	0.106	33	30	27.01	0.623
16	3736.60	3737.66	0.02	0.36	0.02	Ly-a	2.07463	0.00003	29	4	3.30e13	3.78e12					
17	3737.25	3738.31	0.01	0.24	0.02	Ly-a	2.07513	0.00002	12	5	1.62e13	3.23e12					
18	3738.01	3739.08	0.02	0.52	0.02	Ly-a	2.07572	0.00001	21	2	5.58e13	3.39e12					
19	3740.09	3741.15	0.01	0.81	0.03	Ly-a	2.07739	0.00002	24	2	1.01e14	1.09e13					
20	3740.96	3742.02	0.01	0.25	0.02	Ly-a	2.07810	0.00006	41	20	3.68e13	1.53e13					
21	3741.75	3742.82	0.02	0.45	0.03	Ly-a	2.07885	0.00007	32	7	3.01e13	8.91e12	0.106	117	99	72.28	0.985
22	3746.37	3747.44	0.02	1.53	0.04	Ly-a	2.08195	0.00004	21	5	1.80e13	4.16e12					
23						Ly-a	2.08273	0.00002	39	2	2.04e14	1.46e13	0.106	59	53	42.29	0.854
24	3750.53	3751.59	0.05	0.17	0.02	Ly-a	2.08602	0.00003	23	5	1.18e13	1.63e12					
25	3751.46	3752.52	0.04	0.12	0.02	Ly-a	2.08679	0.00004	22	7	8.47e12	1.63e12					
26	3752.69	3753.76	0.02	0.78	0.03	Ly-a	2.08780	0.00001	37	2	7.22e13	2.84e12	0.106	78	69	51.17	0.947
27	3758.73	3759.80	0.04	0.18	0.02	Ly-a	2.09283	0.00003	22	5	1.14e13	1.59e12	0.106	28	25	23.89	0.526
28	3762.78	3763.85	0.07	0.16	0.03	Ly-a	2.09618	0.00007	50	10	1.24e13	2.03e12	0.106	39	36	30.91	0.709
29	3772.21	3773.28	0.02	1.19	0.03	Ly-a	2.10389	0.00001	35	1	1.64e14	1.01e13					
30	3773.95	3775.02	0.05	0.13	0.02	Ly-a	2.10529	0.00006	33	8	9.36e12	1.83e12	0.106	78	72	85.83	0.112
31	3787.44	3788.51	0.02	1.29	0.03	CII 1334	1.83838	0.00003	12	5	4.13e13	9.52e12					
32						CII 1334	1.83874	0.00002	11	5	3.48e14	3.02e14					
33						CII 1334	1.83905	0.00002	8	6	3.97e14	7.72e14					
34						CII 1334	1.83938	0.00002	13	3	6.26e13	8.69e12	0.106	33	25	10.15	0.996
35	3791.71	3792.78	0.03	0.31	0.02	MgII 2796	0.35637	0.00007	24	2	8.38e12	6.32e11	0.106	29	26	48.43	0.005
36	3795.56	3796.64	0.07	0.11	0.02	Ly-a	2.12311	0.00018	59	13	8.43e12	1.57e12	0.106	41	38	30.56	0.799
37	3799.27	3800.35	0.01	0.36	0.01	MgII 2796	0.35904	0.00002	8	1	2.53e13	4.60e12					
38	3799.83	3800.91	0.01	0.33	0.01	MgII 2796	0.35922	0.00003	14	1	1.21e13	5.72e11	0.106	32	26	23.59	0.599
39	3801.61	3802.69	0.02	0.26	0.02	MgII 2803	0.35637	0.00007	24	2	8.38e12	6.32e11	0.106	23	20	75.48	0.003
40	3803.39	3804.47	0.02	0.56	0.02	Ly-a	2.12950	0.00003	36	3	3.95e13	3.91e12					
41	3804.42	3805.50	0.02	0.23	0.01	Ly-a	2.13025	0.00006	38	6	2.05e13	3.81e12	0.105	51	45	35.87	0.863
42	3809.04	3810.12	0.01	0.34	0.01	MgII 2803	0.35904	0.00002	8	1	2.53e13	4.60e12					
43	3809.61	3810.69	0.01	0.23	0.01	MgII 2803	0.35922	0.00003	14	1	1.21e13	5.72e11	0.106	34	28	59.47	0.003

Table 5.5 Absorption lines in Q1101-264

	λ_{air}	λ_{vac}	±	EW(A)	±	ID	z	±	b(km/s)	±	N(HI)	±	σ_{res}(Å)	n_{ch}	ν	X^2	sig
1	3508.23	3509.23	0.04	0.17	0.03	Ly-a	1.88569	0.00005	23	9	1.31e13	3.29e12					
2	3510.01	3511.01	0.03	1.06	0.05	Ly-a	1.88814	0.00002	42	3	1.34e14	1.37e13	0.106	65	59	51.21	0.755
3	3514.60	3515.61	0.01	1.17	0.04	Ly-a	1.89190	0.00008	25	6	5.74e14	7.22e14					
4	3515.79	3516.80	0.01	1.13	0.04	Ly-a	1.89274	0.00009	39	13	2.54e14	7.90e13					
5	3517.86	3518.87	0.03	0.59	0.04	Ly-a	1.89385	0.00007	50	12	6.76e13	1.26e13					
6	3518.54	3519.55	0.02	1.19	0.04	Ly-a	1.89518	0.00003	30	7	5.21e14	4.77e14					
7	3519.88	3520.81	0.02	1.06	0.04	Ly-a	1.89616	0.00004	42	5	1.70e14	2.25e13	0.106	122	107	80.25	0.975
8	3525.08	3526.09	0.02	0.12	0.02	Ly-a	1.90056	0.00005	17	9	1.16e13	3.33e12	0.106	14	11	12.55	0.324
9	3526.34	3527.34	0.04	0.19	0.03	Ly-a	1.90157	0.00003	16	5	1.48e13	2.33e12	0.106	17	14	6.89	0.939
10	3532.71	3533.72	0.03	0.19	0.03	FeII 2600	0.35903	0.00001	5	8	3.87e13	1.50e14					
11	3533.25	3534.26	0.05	0.14	0.03	FeII 2600	0.35921	0.00001	11	7	1.00e13	1.99e12	0.105	20	14	7.28	0.923
12	3542.09	3543.10	0.04	0.11	0.03	Ly-a	1.91451	0.00004	3	25	1.35e13	1.83e14					
13	3543.03	3544.04	0.02	1.18	0.04	Ly-a	1.91530	0.00003	43	4	1.80e14	2.28e13	0.106	48	42	41.40	0.497
14	3546.92	3547.93	0.04	0.99	0.06	Ly-a	1.91852	0.00002	42	3	1.05e14	9.00e12	0.106	38	35	27.82	0.831
15	3557.14	3558.16	0.05	0.21	0.04	Ly-a	1.92692	0.00006	37	10	1.64e13	3.24e12	0.106	28	25	16.11	0.911
16	3559.72	3560.73	0.04	0.27	0.04	Ly-a	1.92905	0.00004	21	6	2.12e13	4.15e12	0.106	34	31	40.73	0.113
17	3575.83	3576.85	0.04	0.17	0.03	Ly-a	1.94230	0.00003	7	7	1.63e13	8.99e12					
18	3577.23	3578.25	0.02	1.35	0.05	SiII 1260	1.83838	0.00003	9	7	6.22e12	2.43e12					
19						SiII 1260	1.83874	0.00002	17	4	4.37e13	7.20e12					
20						SiII 1260	1.83905	0.00002	7	2	3.62e13	7.15e12					
21						SiII 1260	1.83938	0.00002	24	5	1.30e13	2.18e12					
22	3578.82	3579.84	0.05	0.21	0.04	Ly-a	1.94480	0.00005	23	7	1.54e13	3.25e12	0.106	65	47	37.27	0.844
23	3580.90	3581.92	0.02	0.44	0.04	Ly-a	1.94646	0.00001	19	1	4.86e13	3.53e12	0.105	21	18	4.89	0.999
24	3598.83	3599.86	0.03	0.28	0.03	Ly-a	1.96120	0.00002	18	4	2.51e13	3.43e12	0.106	28	25	22.59	0.601
25	3601.72	3602.74	0.02	0.66	0.04	Ly-a	1.96359	0.00001	21	2	1.06e14	2.17e13	0.106	36	33	28.49	0.691
26	3614.05	3615.09	0.02	1.66	0.04	Ly-a	1.97372	0.00001	35	4	8.80e14	5.14e14					
27	3616.47	3617.50	0.03	0.54	0.04	Ly-a	1.97577	0.00008	62	12	5.64e13	9.00e12					
28	3617.69	3618.72	0.04	0.42	0.04	Ly-a	1.97680	0.00006	36	10	2.58e13	7.77e12	0.106	102	93	103.14	0.222

Table 5.6 Absorption lines in Q1158-187

	λ_{air}	λ_{vac}	±	EW(A)	±	ID	z	±	b(km/s)	±	N(HI)	±	σ_{res}(Å)	n_{ch}	ν	χ^2	sig
1	4065.72	4066.87	0.04	0.65	0.07	Ly-a	2.34536	0.00003	19	5	8.91e13	4.49e13	0.130	29	26	22.3	0.674
2	4071.74	4072.89	0.03	0.23	0.04	Ly-a	2.35327	0.00010	6	22	3.02e13	2.94e15	0.130	25	19	27.9	0.086
3	4072.27	4073.42	0.02	0.55	0.05	Ly-a	2.35077	0.00038	23	10	8.13e13	3.25e13					
4	4074.50	4075.65	0.06	1.41	0.11	Ly-a	2.35206	0.00006	20	8	4.68e13	1.31e13	0.130	42	33	24.2	0.869
5						Ly-a	2.35273	0.00005	22	8	1.00e14	3.52e13					
6						Ly-a	2.35348	0.00012	21	18	1.15e13	6.37e12					
7	4088.78	4089.85	0.08	0.29	0.07	Ly-a	2.36421	0.00028	28	11	1.91e13	5.32e12	0.130	40	34	31.6	0.588
8						Ly-a	2.36519	0.00037	23	11	1.55e13	5.03e12					
9	4094.64	4095.79	0.07	1.21	0.10	Ly-a	2.36844	0.00020	51	29	2.75e13	1.24e13	0.130	46	43	43.6	0.443
10						Ly-a	2.36953	0.00006	34	7	7.24e13	1.34e13					
11	4099.21	4100.36	0.06	0.56	0.07	Ly-a	2.37290	0.00003	24	4	4.68e13	6.48e12	0.130	26	23	13.1	0.951
12	4125.03	4126.20	0.03	0.96	0.06	Ly-a	2.39421	0.00004	36	5	1.10e14	2.03e14	0.130	27	24	34.9	0.087
13	4127.08	4128.24	0.09	0.24	0.06	Ly-a	2.39592	0.00006	26	8	1.55e13	3.23e12	0.130	25	22	12.1	0.955
14	4137.65	4138.82	0.06	0.26	0.05	Ly-a	2.40455	0.00004	21	6	1.70e13	3.15e12	0.130	26	23	18.0	0.757
15	4140.52	4141.69	0.03	0.57	0.04	Ly-a	2.40692	0.00003	23	4	5.37e13	7.44e12	0.130	28	25	27.0	0.354
16	4147.45	4148.62	0.02	1.74	0.06	Ly-a	2.41264	0.00002	39	5	4.90e14	2.46e14	0.130	39	36	48.7	0.077
17	4149.56	4150.73	0.05	0.61	0.05	Ly-a	2.41435	0.00007	58	10	4.37e13	5.04e12	0.130	39	36	49.7	0.525
18	4151.72	4152.89	0.03	0.63	0.04	Ly-a	2.41609	0.00120	35	60	2.95e13	1.04e15	0.130	30	24	26.1	0.350
19	4152.48	4153.65	0.02	0.45	0.03	Ly-a	2.41655	0.00027	29	13	7.41e13	1.92e14					
20	4157.10	4158.28	0.04	0.48	0.04	Ly-a	2.42064	0.00003	24	4	3.24e13	3.73e12	0.130	18	15	19.3	0.202
21	4163.31	4164.49	0.03	0.62	0.04	Ly-a	2.42567	0.00002	27	3	4.90e13	4.52e12	0.130	29	26	23.5	0.602
22	4165.49	4166.66	0.04	0.63	0.04	Ly-a	2.42753	0.00002	35	2	4.17e13	1.92e12	0.130	31	28	10.7	0.999
23	4183.45	4184.63	0.03	2.16	0.04	Ly-a	2.44044	0.00021	63	30	1.10e13	4.68e12	0.130	80	74	79.1	0.559
24						Ly-a	2.44237	0.00003	78	3	1.86e14	8.58e12					
25	4198.42	4199.60	0.02	1.74	0.04	Ly-a	2.45489	0.00011	37	6	7.00e13	3.02e13	0.130	60	54	65.7	0.133
26						Ly-a	2.45484	0.00013	47	8	1.00e14	3.04e13					

Table 5.7 Absorption Lines in Q1338+113

	λ_{air}	λ_{vac}	±	EW(A)	±	ID	z	±	b(km/s)	±	N(HI)	±	σ_{res}(Å)	n_{ch}	ν	χ^2	sig
1	4256.28	4257.48	0.03	2.17	0.07	Ly-a	2.50287	0.00002	43	4	6.74e14	2.59e14	0.180	61	58	43.15	0.927
2	4265.18	4266.38	0.02	1.34	0.05	Ly-a	2.50948	0.00002	22	6	1.34e15	2.74e15					
3	4266.83	4268.03	0.06	0.24	0.04	Ly-a	2.51080	0.00008	34	11	1.60e13	3.47e12	0.150	74	68	70.24	0.403
4	4276.64	4277.85	0.06	0.15	0.03	Ly-a	2.51865	0.00020	74	24	1.70e13	4.59e12	0.133	59	56	74.80	0.047
5	4285.87	4287.07	0.08	0.19	0.04	Ly-a	2.52649	0.00007	32	9	1.07e13	2.26e12	0.123	52	49	38.08	0.870
6	4293.33	4294.53	0.06	0.16	0.03	Ly-a	2.53266	0.00008	29	10	9.47e12	2.39e12	0.123	40	37	35.30	0.549
7	4297.03	4298.24	0.04	0.47	0.04	Ly-a	2.53566	0.00003	35	4	3.06e13	2.84e12	0.123	48	45	39.77	0.732
8	4305.94	4307.15	0.07	0.30	0.04	Ly-a	2.53906	0.00021	89	46	3.08e13	1.23e13					
9	4307.64	4308.85	0.02	0.84	0.04	Ly-a	2.54037	0.00002	27	3	6.72e13	8.50e12	0.123	65	59	72.25	0.115
10	4307.36	4308.57	0.03	1.37	0.05	Ly-a	2.54135	0.00002	17	7	3.94e15	1.44e16					
11						Ly-a	2.54166	0.00058	58	35	2.42e13	2.45e13					
12	4310.92	4312.14	0.01	1.98	0.04	Ly-a	2.54713	0.00001	30	4	5.50e15	6.12e15					
13	4313.33	4314.54	0.05	0.60	0.04	Ly-a	2.54910	0.00004	44	5	3.83e13	3.35e12	0.124	156	144	138.86	0.635
14	4320.37	4321.58	0.05	0.24	0.03	Ly-a	2.55493	0.00006	29	7	1.52e13	2.77e12					
15	4322.11	4323.32	0.02	1.59	0.04	Ly-a	2.55634	0.00001	32	3	5.47e14	2.43e14	0.124	84	78	86.32	0.243
16	4327.21	4328.42	0.06	0.15	0.03	Ly-a	2.56043	0.00027	45	30	1.20e13	7.33e12					
17	4328.04	4329.26	0.04	0.17	0.02	Ly-a	2.56146	0.00010	35	21	2.10e13	1.05e13					
18	4329.20	4330.42	0.02	0.89	0.03	Ly-a	2.56258	0.00005	24	11	1.59e15	4.19e15					
19	4330.96	4332.17	0.02	2.27	0.04	Ly-a	2.56398	0.00005	30	6	8.39e14	6.71e14	0.124	122	110	156.04	0.003
20	4344.30	4345.52	0.02	1.68	0.04	Ly-a	2.57473	0.00003	56	3	1.30e14	9.88e12					
21	4346.33	4347.55	0.01	1.43	0.03	Ly-a	2.57630	0.00003	47	5	1.53e14	1.11e13					
22	4347.81	4349.04	0.01	0.81	0.02	Ly-a	2.57737	0.00004	26	6	3.04e13	1.03e13					
23	4349.74	4350.96	0.01	2.11	0.03	Ly-a	2.57932	0.00014	116	17	3.68e14	5.01e13					
24	4352.22	4353.44	0.02	2.11	0.04	Ly-a	2.58122	0.00012	72	8	1.38e14	4.26e13	0.125	219	201	187.61	0.788

Table 5.8 Absorption lines in Q1448-232

	λ_{air}	λ_{vac}	±	EW(Å)	±	ID	z	±	b(km/s)	±	N(HI)	±	σ_{res}(Å)	n_{ch}	ν	χ^2	sig
1	3747.67	3748.74	0.07	0.50	0.06	Ly-a	2.08347	0.00005	36	7	3.07e13	4.92e12	0.130	54	51	58.68	0.215
2	3757.67	3758.74	0.03	0.34	0.03	CIV 1548	1.42787	0.00002	4	4	1.10e14	3.84e14					
3	3758.52	3759.59	0.05	0.24	0.04	CIV 1548	1.42804	0.00006	63	10	6.93e13	9.89e12	0.130	43	37	36.54	0.491
4	3764.00	3765.07	0.04	0.42	0.04	CIV 1550	1.42787	0.00002	4	4	1.10e14	3.84e14					
5	3764.76	3765.83	0.06	0.07	0.03	CIV 1550	1.42804	0.00006	63	10	6.93e13	9.89e12	0.130	37	31	41.52	0.098
6	3769.84	3770.91	0.04	0.15	0.03	Ly-a	2.10283	0.00038	36	11	1.51e13	3.66e12	0.130	30	27	26.26	0.504
7	3778.07	3779.14	0.10	0.51	0.06	Ly-a	2.10304	0.00008	20	19	1.93e13	1.21e13					
8						Ly-a	2.10371	0.00041	58	60	1.57e13	2.02e13					
9	3780.16	3781.23	0.03	0.79	0.04	Ly-a	2.11026	0.00004	31	10	4.32e13	1.62e13					
10	3781.93	3783.00	0.04	1.25	0.06	Ly-a	2.11142	0.00036	154	33	1.08e14	3.22e13					
11						Ly-a	2.11156	0.00004	27	6	6.43e13	1.33e13	0.130	139	124	102.95	0.916
12	3791.90	3792.97	0.04	0.30	0.04	Ly-a	2.12008	0.00003	16	5	2.52e13	4.43e12	0.130	40	37	41.28	0.289
13	3795.63	3796.71	0.06	0.33	0.05	SiIV 1393	1.72415	0.00007	63	11	2.40e13	3.37e12	0.130	41	38	46.45	0.163
14	3807.04	3808.12	0.04	0.15	0.03	Ly-a	2.13252	0.00004	14	8	1.14e13	2.66e12					
15	3810.51	3811.59	0.03	1.20	0.05	Ly-a	2.13542	0.00002	30	3	2.63e14	9.09e13					
16	3812.30	3813.38	0.03	0.61	0.04	Ly-a	2.13683	0.00002	23	3	7.07e13	9.12e12					
17	3813.72	3814.80	0.04	0.12	0.03	Ly-a	2.13801	0.00005	17	9	9.26e12	2.57e12	0.130	137	125	105.95	0.891
18	3820.32	3821.40	0.07	0.38	0.05	SiIV 1402	1.72415	0.00007	63	11	2.40e13	3.37e12	0.130	40	37	49.36	0.084
19	3827.05	3828.13	0.04	0.34	0.04	CIV 1548	1.47269	0.00003	33	7	4.29e13	5.93e12					
20	3828.29	3829.38	0.02	0.89	0.03	CIV 1548	1.47343	0.00001	14	6	4.82e15	1.51e16					
21						CIV 1548	1.47389	0.00010	22	17	2.18e13	1.27e13	0.130	59	50	67.75	0.043
22	3831.86	3832.94	0.05	0.30	0.04	Ly-a	2.15293	0.00006	37	8	2.17e13	3.63e12					
23	3833.69	3834.78	0.05	0.11	0.03	CIV 1550	1.47269	0.00003	33	7	4.29e13	5.93e12					
24	3834.60	3835.69	0.02	0.80	0.03	CIV 1550	1.47343	0.00001	14	6	4.82e15	1.51e16					
25						CIV 1550	1.47389	0.00010	22	17	2.18e13	1.27e13	0.130	75	63	62.78	0.484
26	3842.84	3843.93	0.02	1.30	0.04	Ly-a	2.16197	0.00001	37	2	2.11e14	2.26e13	0.130	60	57	33.49	0.995
27	3846.38	3847.48	0.03	0.15	0.02	Ly-a	2.16490	0.00003	3	33	2.19e13	6.02e14					
28	3848.05	3849.14	0.02	2.31	0.04	Ly-a	2.16623	0.00001	47	4	1.20e15	5.53e14					
29	3850.21	3851.31	0.02	0.71	0.03	Ly-a	2.16799	0.00002	38	3	6.10e13	4.22e12					
30	3851.68	3852.77	0.03	0.29	0.03	Ly-a	2.16924	0.00005	17	7	1.70e13	4.51e12					
31	3852.77	3853.87	0.02	1.13	0.03	Ly-a	2.17003	0.00005	37	6	1.20e14	2.41e13					
32	3854.04	3855.14	0.04	0.10	0.02	Ly-a	2.17077	0.00048	52	30	2.37e13	2.17e13	0.130	147	129	127.87	0.532
33	3861.12	3862.22	0.03	0.11	0.02	Ly-a	2.17603	0.00016	52	24	1.05e13	3.62e12					
34	3862.38	3863.47	0.03	0.73	0.03	Ly-a	2.17685	0.00002	37	3	6.54e13	4.44e12	0.130	77	71	72.61	0.425
35	3867.48	3868.58	0.03	0.29	0.02	Ly-a	2.18225	0.00004	29	5	2.98e13	2.72e12	0.130	33	30	44.50	0.043

Table 5.9 Absorption lines in Q2204-573

	λ_{air}	λ_{vac}	±	EW(Å)	±	ID	z	±	b(km/s)	±	N(HI)	±	σ_{res}(Å)	n_{ch}	ν	χ^2	sig
1	4182.04	4183.22	0.06	0.36	0.05	Ly-a	2.44113	0.00007	41	8	2.55e13	3.89e12	0.158	43	40	30.41	0.864
2	4185.19	4186.37	0.04	0.59	0.06	Ly-a	2.44376	0.00005	41	6	5.24e13	5.98e12					
3	4187.77	4188.95	0.02	2.04	0.05	Ly-a	2.44577	0.00002	20	8	1.67e16	5.50e16	0.154	103	97	96.74	0.488
4	4191.43	4192.61	0.04	0.21	0.04	Ly-a	2.44883	0.00003	10	7	1.77e13	5.23e12	0.144	33	30	26.76	0.636
5	4195.00	4196.18	0.04	0.47	0.05	Ly-a	2.45173	0.00033	26	4	3.70e13	4.66e12	0.125	38	35	32.43	0.593
6	4201.66	4202.85	0.05	0.15	0.04	Ly-a	2.45724	0.00003	4	12	1.69e13	5.79e13					
7	4202.88	4204.07	0.03	0.78	0.05	Ly-a	2.45823	0.00005	39	6	6.31e13	8.29e12					
8						Ly-a	2.45949	0.00025	59	32	1.73e13	7.67e12	0.124	90	81	74.51	0.681
9	4210.33	4211.52	0.04	0.15	0.03	Ly-a	2.46442	0.00017	30	22	1.30e13	1.71e13					
10	4211.47	4212.66	0.02	1.07	0.05	Ly-a	2.46527	0.00003	21	6	1.33e14	5.55e13					
11	4212.54	4213.72	0.03	0.19	0.03	Ly-a	2.46586	0.00058	87	42	5.90e13	4.15e13	0.116	97	88	83.28	0.623
12	4225.91	4228.10	0.08	0.56	0.07	Ly-a	2.47303	0.00038	62	10	3.61e13	5.14e12	0.115	66	63	51.27	0.855
13	4232.00	4233.19	0.07	0.22	0.05	Ly-a	2.48285	0.00086	99	67	5.34e13	5.21e13					
14	4234.00	4235.19	0.03	2.00	0.06	Ly-a	2.48396	0.00003	43	7	4.35e14	1.30e14	0.116	83	77	49.66	0.993
15	4239.23	4240.42	0.03	1.99	0.06	Ly-a	2.48816	0.00002	37	4	1.06e15	6.33e14	0.117	78	75	68.75	0.681
16	4242.11	4243.30	0.04	0.22	0.04	Ly-a	2.49053	0.00036	24	9	1.57e13	4.13e12					
17	4243.75	4244.94	0.09	0.28	0.05	Ly-a	2.49175	0.00012	48	18	2.19e13	5.72e12					
18	4245.00	4246.27	0.04	0.41	0.05	Ly-a	2.49287	0.00003	17	5	3.08e13	5.52e12					
19	4246.87	4248.06	0.03	1.98	0.07	Ly-a	2.49435	0.00003	61	4	2.47e14	2.26e13	0.118	135	123	122.71	0.490
20	4253.90	4255.09	0.04	1.39	0.07	Ly-a	2.50008	0.00004	46	4	1.26e14	1.21e13					
21	4255.93	4257.13	0.06	0.33	0.05	Ly-a	2.50166	0.00015	70	22	3.66e13	8.95e12	0.124	84	78	76.77	0.518
22	4260.59	4261.79	0.03	1.22	0.06	Ly-a	2.50568	0.00002	33	3	1.37e14	1.68e13					
23	4262.45	4263.65	0.04	0.81	0.05	Ly-a	2.50725	0.00004	53	5	7.73e13	6.72e12	0.136	96	90	80.25	0.760
24	4298.79	4300.00	0.04	0.43	0.05	Ly-a	2.53716	0.00003	11	6	5.20e13	3.90e13					
25	4300.89	4302.10	0.06	0.84	0.07	Ly-a	2.53885	0.00007	66	8	6.17e13	6.35e12	0.187	99	93	94.61	0.434

Table 5.10 Absorption lines in Q2204-573

	λ_{air}	λ_{vac}	±	EW(A)	±	ID	z	±	b(km/s)	±	N(HI)	±	σ_{res}(Å)	n_{ch}	ν	χ^2	sig
1	4298.48	4299.61	0.02	0.38	0.03	Ly-a	2.53682	0.00002	16	3	3.33e13	3.72e12	0.170	21	18	11.98	0.848
2	4299.67	4300.88	0.02	0.21	0.03	Ly-a	2.53793	0.00004	17	6	1.79e13	3.23e12					
3	4300.65	4301.86	0.04	0.60	0.04	Ly-a	2.53868	0.00004	30	5	3.90e13	3.83e12	0.160	52	46	29.96	0.968
4	4304.56	4305.77	0.04	0.36	0.04	Ly-a	2.54192	0.00003	30	4	2.49e13	2.30e12	0.160	43	40	24.81	0.979
5	4309.66	4310.88	0.04	0.10	0.02	Ly-a	2.54575	0.00013	55	17	1.30e13	3.15e12					
6	4311.33	4312.54	0.03	0.87	0.04	Ly-a	2.54744	0.00002	33	2	7.82e13	5.00e12	0.152	94	88	77.52	0.720
7	4314.42	4315.63	0.04	0.43	0.04	Ly-a	2.54996	0.00003	29	4	2.80e13	3.14e12					
8	4315.83	4317.04	0.04	0.38	0.03	Ly-a	2.55117	0.00006	47	8	2.79e13	3.44e12	0.144	70	64	52.49	0.848
9	4323.73	4324.95	0.02	2.20	0.04	Ly-a	2.55763	0.00001	44	3	7.72e14	2.15e14					
10	4326.78	4328.00	0.07	0.42	0.05	Ly-a	2.56022	0.00010	86	13	3.47e13	4.27e12					
11	4331.03	4332.25	0.02	2.94	0.05	Ly-a	2.56362	0.00015	58	11	7.95e14	1.23e15					
12						Ly-a	2.56437	0.00594	63	204	5.07e13	9.03e14					
13	4335.57	4336.79	0.02	1.55	0.04	Ly-a	2.56742	0.00001	33	2	3.16e14	6.96e13					
14	4338.33	4339.55	0.05	0.23	0.03	Ly-a	2.56966	0.00006	34	8	1.40e13	2.60e12	0.120	307	289	249.36	0.956
15	4342.16	4343.38	0.05	0.38	0.04	Ly-a	2.57294	0.00003	24	4	2.53e13	2.95e12	0.120	45	42	42.97	0.429
16	4346.83	4348.05	0.03	1.65	0.05	Ly-a	2.57670	0.00002	51	2	1.91e14	1.26e13	0.120	81	78	78.80	0.453
17	4353.85	4355.07	0.06	0.21	0.04	Ly-a	2.58243	0.00006	36	8	1.43e13	2.44e12	0.121	37	34	23.28	0.917
18	4357.65	4358.88	0.05	0.14	0.03	Ly-a	2.58552	0.00008	32	11	1.09e13	2.68e12					
19	4358.88	4360.10	0.03	0.25	0.03	Ly-a	2.58659	0.00002	11	3	1.92e13	2.88e12					
20	4360.37	4361.60	0.03	0.48	0.03	Ly-a	2.58780	0.00002	21	2	3.96e13	3.50e12					
21	4362.29	4363.52	0.02	1.29	0.04	Ly-a	2.58939	0.00001	30	2	2.18e14	3.87e13	0.122	119	107	99.76	0.677
22	4364.81	4366.04	0.03	0.55	0.03	Ly-a	2.59150	0.00002	26	2	4.33e13	2.98e12	0.123	40	37	23.41	0.960
23	4367.44	4368.67	0.06	0.27	0.04	Ly-a	2.59365	0.00005	20	6	1.52e13	2.95e12					
24	4368.49	4369.72	0.03	0.27	0.03	Ly-a	2.59455	0.00005	31	7	2.32e13	3.51e12					
25	4369.97	4371.20	0.05	0.17	0.03	Ly-a	2.59576	0.00005	19	7	1.04e13	2.42e12					
26	4371.33	4372.56	0.03	0.19	0.03	Ly-a	2.59692	0.00003	17	5	1.52e13	2.54e12	0.124	103	91	101.66	0.289
27	4385.60	4386.83	0.04	0.24	0.03	Ly-a	2.60858	0.00001	6	4	3.58e13	5.78e13	0.127	29	26	18.78	0.846
28	4391.00	4392.23	0.04	0.20	0.03	Ly-a	2.61302	0.00002	8	4	1.52e13	3.04e12					
29	4391.79	4393.02	0.04	0.20	0.03	Ly-a	2.61366	0.00003	17	4	1.34e13	1.88e12	0.128	50	44	28.64	0.965
30	4397.05	4398.29	0.03	0.49	0.03	Ly-a	2.61797	0.00002	25	3	3.56e13	3.10e12					
31	4398.76	4399.99	0.04	0.44	0.04	Ly-a	2.61942	0.00003	29	4	2.90e13	2.89e12	0.136	85	79	75.97	0.576
32	4405.14	4406.37	0.03	0.70	0.04	Ly-a	2.62465	0.00002	23	2	6.79e13	5.88e12	0.158	42	39	34.87	0.659
33	4410.00	4411.32	0.05	0.13	0.03	Ly-a	2.62874	0.00005	3	32	1.20e13	1.30e14					
34	4410.77	4412.01	0.03	0.12	0.02	Ly-a	2.62932	0.00008	6	23	1.09e13	1.48e13					
35	4412.14	4413.38	0.02	1.94	0.04	Ly-a	2.63040	0.00003	36	8	1.06e15	1.09e15					
36	4414.12	4415.36	0.05	0.23	0.03	Ly-a	2.63200	0.00012	43	16	1.63e14	4.44e12	0.179	182	90	88.07	0.538
37	4419.23	4420.48	0.02	2.75	0.05	Ly-a	2.63624	0.00002	65	3	4.69e14	5.39e13	0.207	91	88	95.48	0.275

Table 5.11 Absorption lines in Q2204-573

	λ_{air}	λ_{vac}	±	EW(A)	±	ID	z	±	b(km/s)	±	N(HI)	±	σ_{res}(Å)	n_{ch}	ν	χ^2	sig
1	4411.91	4413.14	0.03	2.41	0.06	Ly-a	2.62888	0.00006	9	17	1.27e13	6.76e12					
2						Ly-a	2.63034	0.00003	61	5	3.06e14	2.28e13					
3	4414.06	4415.30	0.03	0.22	0.03	Ly-a	2.63205	0.00005	7	16	1.83e13	3.13e13	0.213	94	85	97.79	0.162
4	4418.01	4419.25	0.02	0.93	0.04	Ly-a	2.63525	0.00010	11	23	9.58e13	4.78e14					
5	4419.65	4420.89	0.02	2.03	0.05	Ly-a	2.63621	0.00006	70	4	4.04e14	7.25e13	0.185	100	94	110.89	0.113
6	4430.50	4431.75	0.06	0.16	0.04	Ly-a	2.64552										
7	4435.21	4436.46	0.05	0.27	0.04	Ly-a	2.64943	0.00005	24	7	1.75e13	3.40e12	0.122	43	37	56.66	0.020
8	4443.17	4444.42	0.05	0.28	0.04	Ly-a	2.65600	0.00007	41	8	2.07e13	3.23e12	0.119	42	39	39.63	0.442
9	4448.16	4449.41	0.07	0.63	0.06	Ly-a	2.66007	0.00007	71	8	4.39e13	4.49e12					
10	4451.95	4453.20	0.05	1.81	0.07	Ly-a	2.66276	0.00002	34	3	1.88e14	2.61e13					
11						Ly-a	2.66430	0.00012	63	15	2.75e13	5.13e12	0.118	147	138	141.53	0.481
12	4457.03	4458.28	0.03	0.73	0.04	Ly-a	2.66727	0.00002	18	2	7.05e13	1.03e13	0.117	52	49	52.34	0.346
13	4462.98	4464.16	0.05	1.29	0.06	Ly-a/SiIII	2.67146	0.00008	35	9	2.69e13	5.33e12					
14						Ly-a/at z=	2.67207	0.00002	5	11	1.07e14	1.07e15					
15						Ly-a/2.780	2.67253	0.00002	6	7	5.09e13	1.60e14					
16						Ly-a/SiIII	2.67301	0.00003	13	4	2.42e13	3.75e12					
17	4463.77	4465.03	0.02	0.42	0.03	Ly-a/at z=	2.67382	0.00003	18	4	3.04e13	4.04e12					
18	4465.91	4467.16	0.02	1.82	0.05	Ly-a/2.782	2.67491	0.00002	36	3	2.81e14	2.84e13	0.117	116	98	138.28	0.224
19	4469.88	4471.14	0.05	0.59	0.05	Ly-a	2.67804	0.00002	28	3	3.08e13	2.51e12					
20	4471.45	4472.70	0.03	0.69	0.04	Ly-a	2.67918	0.00001	21	2	4.92e13	3.50e12	0.117	75	69	48.75	0.997
21	4473.83	4475.09	0.10	0.21	0.04	Ly-a	2.68117										
22	4480.82	4482.08	0.02	1.89	0.05	Ly-a	2.68693	0.00001	16	1	6.72e17	1.11e17	0.116	103	100	98.18	0.533
23	4498.16	4499.43	0.02	6.19	0.06	Ly-a	2.69963	0.00009	26	4	1.46e17	2.30e17					
24						Ly-a	2.70200	0.00010	40	4	1.44e18	5.20e17	0.118	144	138	139.85	0.440
25	4503.87	4505.14	0.08	0.34	0.05	Ly-a	2.70631	0.00013	60	16	1.58e13	3.44e12	0.132	56	53	54.55	0.415
26	4515.80	4517.07	0.06	0.32	0.04	Ly-a	2.71565	0.00007	36	8	1.88e13	3.10e12	0.160	48	45	64.08	0.032
27	4523.75	4525.02	0.06	0.36	0.04	Ly-a	2.72223	0.00007	53	8	2.26e13	2.75e12	0.179	55	52	46.26	0.698
28	4537.65	4538.92	0.03	1.72	0.05	Ly-a	2.73371	0.00002	50	2	1.64e14	8.00e12	0.210	105	102	111.58	0.243
29	4545.06	4546.33	0.04	0.67	0.04	Ly-a	2.73981	0.00002	29	2	5.64e13	2.97e12	0.220	51	48	36.21	0.894

5.2.1 Appendix to absorption line tables

Q0207-398 - Table 5.1

Lines 11-13:

The fit significance for this blend of Lya lines is rather low. The best fit did not seem to match the red wing of the feature very well; more components may be present.

Lines 14-19:

This is a blend of Lyβ lines. The χ^2 is high in this region but acceptable for the corresponding Lyα region. The two regions were fitted simultaneously. The problem might be due to a poor continuum fit in the Lyβ region.

Line 24:

The b parameter is unreasonably high (208 km/s). This is probably a blend but further deblending is impossible with existing data.

Lines 51-52:

This is fitted as a Lya line blended in a Lyp complex. The xz is unacceptably high. The corresponding Lya region also has a poor fit significance.

Q0207-398 - Table 5.2

Lines 2-4:

Lyα with associated metal lines.

Lines 5-8:

SiII 1190 complex with Lyα blended in blue wing. Fitted simultaneously with

Sill 1193 and 1304 regions.

Line 9:

Fitted as single - possibly an additional component in blue wing.

Lines 20-31:

This is a blend of 8 Lyα lines plus a SiIII 1206 complex. The whole feature was fitted simultaneously. The redshifts of the three SiIII lines were taken to be those of the SiII lines (since the blending is so bad in this region). Line 31 has been assumed to be SiIII because of similar structure in CII 1334. However it could be Lyα.

Line 39:

Lyα feature with associated metal lines. It appears single and symmetric although structure in the Sin, SiIII and CII lines is clearly present. Higher order Lyman lines may permit deblending.

Q0207-398 - Table 5.4

Lines 1-3:

01 1302 could be blended in here at z=2.40, but the z agreement with SiII is poor.

Lines 20-21:

These two lines were fitted simultaneously, although they are well separated, because of bad blending in the Lyβ region.

Lines 27-30:

line 27 has been fitted as Lyα but could well be CII 1334 at 2=2.40. Obser-

vations of more metal lines are required to establish the velocity structure in this system.

Lines 42-45:

Poor χ^2 - probably more components present but with the existing data it is difficult to see where they could be. The corresponding Lyβ region also has a poor statistic.

Lines 53-57:

CII 1334 complex at z=2.48. The redshift agreement between these lines and the Sill lines is poor. This may be due to inadequate wavelength calibration in the CII region; there were too few Cu-Ar lines in this spectral region. CII 1036 observations would be useful to check the redshifts and also the velocity structure.

Q1101-264 - Table 5.5

Lines 1-10:

Blend of several Lyα lines, DI 1302, and SiII 1304 complex. SiII 1304 is badly blended; the velocity structure was constrained by fitting SiII 1260 and 1526 simultaneously. The redshifts of CII 1334, DI and SiII were all tied together; if real redshift differences exist between these ions, perhaps this explains the poor fit statistic.

Q1358+113 - Table 5.7

Lines 16-19:

Poor statistic; possible explanations are that more components may be present, errors in sky subtraction, or that the absorbing clouds do not completely oc-

cult the continuum source.

Q2204-573 - Table 5.9

Lines 13-14:

FeII 1144 at z=2.70 could be present in this feature; no other FeII lines available to check velocity structure, so assumed to be Lyαs.

Q2204-573 - Table 5.11

Lines 1-3:

SiII 1193 at z=2.70 is very probably in here but no other SiII lines are available to check redshifts, and the SiIII lines are very badly blended; Sill 1260 observations would be very useful and are longwards of the Lyα emission line.

Lines 13-18:

Deblending was very difficult for this complex, and the suggested parameters may not be correct; Lyβ observations would help.

General Comments:

Where more than one line in a series (e.g. Lyα and Lyβ) has been included in a fit, the number of degrees of freedom associated with any of the data regions is not really correct since they are not statistically independent. The entry for the fit significance level should, in these cases, therefore be considered as only a guide.

The spectral resolution varies with wavelength but has been taken as constant over any isolated absorption complex. Some of these can extend over many channels so this may be a problem where the resolution is changing fairly rapidly with wavelength (i.e. near the detector edges). The number of such

cases should however be small and no significant biases are likely.

In a few cases, the parameter error estimates are larger than the parameters themselves. This does not mean that the existence of the features is doubtful. The error estimates are based on the assumption of symmetric error contours. Whilst this is a reasonable approximation in many cases, for bad blends it is sometimes not, and the quoted errors are effectively an average of the true limits.

5.3 Example profile fits

To illustrate some of the difficulties associated with extracting profile parameters from complex absorption blends, a series of examples are plotted in Figures 5.1 to 5.11 and a brief discussion on each is given below.

Example profile fits in Q0207-398

Figure 5.1: complex at 4129-4134Å; line numbers 2-4 in Table 5.2.
This system is probably a metal line system at z=2.4. No associated metals are found in this high resolution data (SiIII 1206 and NV 1238/1242 fall within the data window). However a weak SiIV 1393 line is seen to the red of the emission line in lower resolution data (Carswell, private communication).

Figure 5.2: complex at 4139-4142Å and 4150-4152Å; line numbers 5-8 and 10-12 in Table 5.2.
These two regions were fitted simultaneously. The final best fit comprised a 3 component SiII 1190/1193 doublet in the z=2.48 system with a Lyα line blended into the blue wing of the lowest redshift SiII 1190 line. The line at 4144Å was sufficiently well separated from the SiII lines to be fitted alone and

is assumed to be Lyα.

Figure 5.3: complex at 4180-4200Å; line numbers 20-31 in Table 5.2.
This blend comprises 8 hydrogen clouds along with 4 components of a SiIII 1206 complex at z=2.48. The redshifts of the 3 bluest SiIII components were determined from the rather cleaner SiII lines and were fixed in the profile fitting. The fourth right hand SiIII component may be Lyα or something else but has been interpreted as SiIII because of a narrow CII 1334 feature at approximately the corresponding position. The broad weak Lyα line (b=123 km/s) at z=2.44224 could be 2 or more weak lines but further deblending is impossible in data with this signal to noise ratio.

Figure 5.4: complexes at 4473-4486Å (Lyα) and 3774-3785Å (Lyβ); line numbers 11-19 in Table 5.3 and 14-19 in Table 5.1.
The final fit to this clump of absorption lines comprised 9 clouds. 8 of these are immediately obvious from inspection of the Lyα region alone. The Lyα line at 4474Å appears single but at Lyβ seems to be split into 2 components. To decide whether this apparent splitting was real or due to noise, a single cloud fit was tried first, fitting only to this spectral region. Although an acceptable fit was found at Lyα ($\chi^2 = 44.4$ over 54 channels), the Lyβ fit was poor ($\chi^2 = 74.1$ over 39 channels). A two cloud fit gave $\chi^2(Ly\alpha) = 43.4$ and $\chi^2(Ly\beta) = 26.9$ and the extra component appears to be confirmed.

The overall fit at Lyβ seems good visually but in fact has an unacceptably high χ^2 of 270.3 over 202 channels. All but two of the clouds (z=2.68402 and 2.69114) have high enough neutral hydrogen column density to produce detectable Lyβ absorption. Both of these Lyβ lines appear to sit in a region of the spectrum where the observed continuum level may be slightly higher than the adopted level. If this is true then the poor χ^2 at Lyβ may be due

entirely to a poor continuum fit in this region. Also, just to the blue of the Lyβ 2=2.69114 position there is a very narrow dip in the continuum which may or may not be due to an additional absorption component; it was not found to be significant in the initial selection procedure.

Figure 5.5 : complex at 4507-45178 (Lyα) and 3803-3811Å (Lyβ); line numbers 22-26 in Table 5.3 and 27-32 in Table 5.1.
This blend comprised 5 clouds in the redshift range 2.71-2.72 plus a further 2 lower redshift Lyα lines blended into the Lyβ region associated with the higher redshift Lyα complex. The strong line at 3803.5Å appears single and is at the position expected for Lyβ at z=2.70909. However, no satisfactory fit could be found using a single cloud model for the α and β regions and the introduction of a Lyα line at z=2.11709, blended into the z=2.70909 Lyβ feature was necessary. An alternative model which may prove acceptable might be a double system at z=2.709; this has not been tried. The blue wing of the strong feature at 3805-3809Å is well fitted by Lyβ at z=2.71179 but there is clear additional absorption to the red.

Example profile fits in Q1358+113

Figure 5.6: complex at 4307-4313Å; lines 10-13 in Table 5.7.
There are 4 components in this blend, two of which have fairly high column densities. The strong left hand line may be a double system (the line bottom appears to be above zero) but better signal to noise would be needed to check this. The huge errors quoted for the column densities of the two strong systems are due to the shape of the curve of growth in this region and reflect the large asymmetry in χ^2-parameter space.

Figure 5.7: complex at 4320-4323Å and 4326-4332Å lines 14-19 in Table 5.7.

The left hand blend is a simple 2 cloud fit. Four components have been fitted to the right hand blend. The overall χ^2 is 156 over 122 channels and the fit and data differ at approximately the 3σ level. The cause of the poor fit is the strong feature at 4330Å; the line bottom appears to be significantly above zero. Assuming sky subtraction is not the problem, more lower column density components are probably present but the blending is so bad that they cannot be resolved. Another possibility is that the cloud does not quite cover the continuum source from the QSO and there is residual emission in the line centre. Lyβ observations may help to determine which of these possibilities is correct; if structure is found in the Lyβ profile, multiple clouds could explain the poor fit at Lyα.

Figure 5.8: complex at 4344-4354Å; lines 20-24 in Table 5.7.
There are 5 components to this blend; none of the line centres go to zero intensity. The mean velocity dispersion parameter for the group is 63 ± 15 km/s which is somewhat higher than the mean of around 35 km/s found for a large sample of lines (see for example Carswell et al., 1986). If this is a real effect and not just random then we may be seeing the effect on these clouds of the increased radiation field in the vicinity of the QSO. (These 5 absorption features are in the blue wing of the Lyα emission line). Alternatively, it may be that this absorption complex does not completely occult the emission region. An interesting experiment would be to artificially raise the zero intensity level in the data to coincide with the observed line bottoms and then to refit and see if an acceptable profile match can be found. If it cannot the first explanation would be preferred. Additional β observations would be useful to help distinguish between these possibilities.

Example profile fits in Q1448-232

Figure 5.9: complex at 3777-3784Å; lines 7-11 in Table 5.8.

This is a relatively straightforward 5 cloud fit. The main point of interest is in the way the profile fitting procedure iterated. The initial guesses corresponded to 5 fairly well separated components. The highest redshift component in the initial guess (z=2.1126) slowly iterated across the position of the 4th component (which remained static at z=2.1116) down to 2.1114, with a final b parameter of 154 km/s. Whilst the parameter solutions given in Table 5.8 may be correct, it is more likely that an extra component may exist at about 3783Åwhich could result in a more reasonable b value for the wandering component. Better signal to noise is required to check this.

Figure 5.10 : complexes at 3826-3829Å (CIV 1548) and 3833-3835Å (CIV 1550); lines 19-25 in Table 5.8.

This system comprises a 3 component CIV doublet at z=1.473. There is a strong central system with a weak but well separated component to the blue and another weak component blended into the red wing of the central line. Between the 1548 and 1550 features is an additional weak line interpreted as Lyα. This absorption system was not found by Chen et al.,(1984) in their lower resolution data, and the identification rests entirely on these CIV lines. Sill 1526 also falls in the data window but is not present. There are no lines in the absorption line list which can easily be associated with this system. However the profile similarities and the good wavelength agreement leaves little doubt that this is CIV absorption.

Figure 5.11: complex at 3846-3854Å; lines 27-32 in Table 5.8.

Two fits are shown in the figure. The strong line at 3848Å has two possible solutions; a high N(HI)-low b and a low N(HI)- higher b. The χ^2 for the high column density solution, taken over that part of the blend only, indicated that the fit was good. The same was not true for the low column density

solution and an extra weak component had to be introduced in the blue wing of the stronger feature in order to obtain a satisfactory χ^2. If the high N(HI) solution were correct (logN(HI)=18.3, b=22) then associated metals might be expected. The rest frame spectral coverage for this system is 1183-1222Å and so SiII 1190/1193 and SiIII 1206 fall in the observed window; these are not detected. However, in lower resolution data covering the wavelength range 3300-5200Å there is an unidentified absorption feature longwards of the Lyα emission line at 4910Å (Chen et al., 1984) which could correspond to CIV. Given the information available it is not possible to be sure which of the two solutions for the 3848Å feature is correct; the low N(HI) solution is the one tabulated.

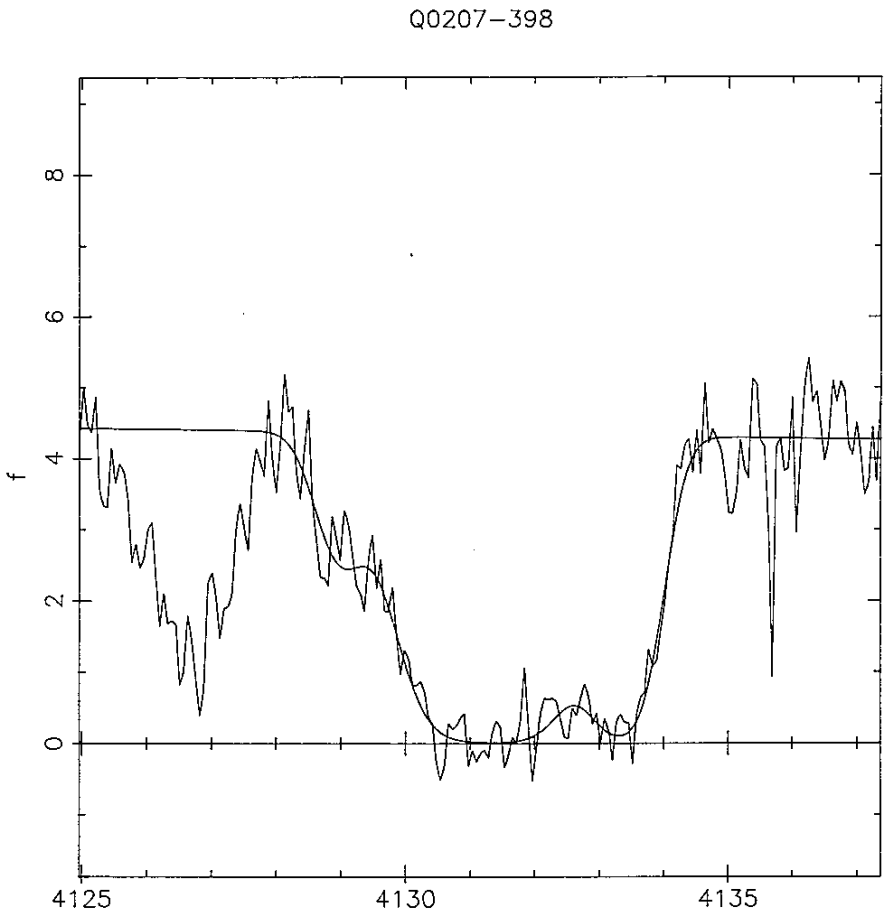

Figure 5.1

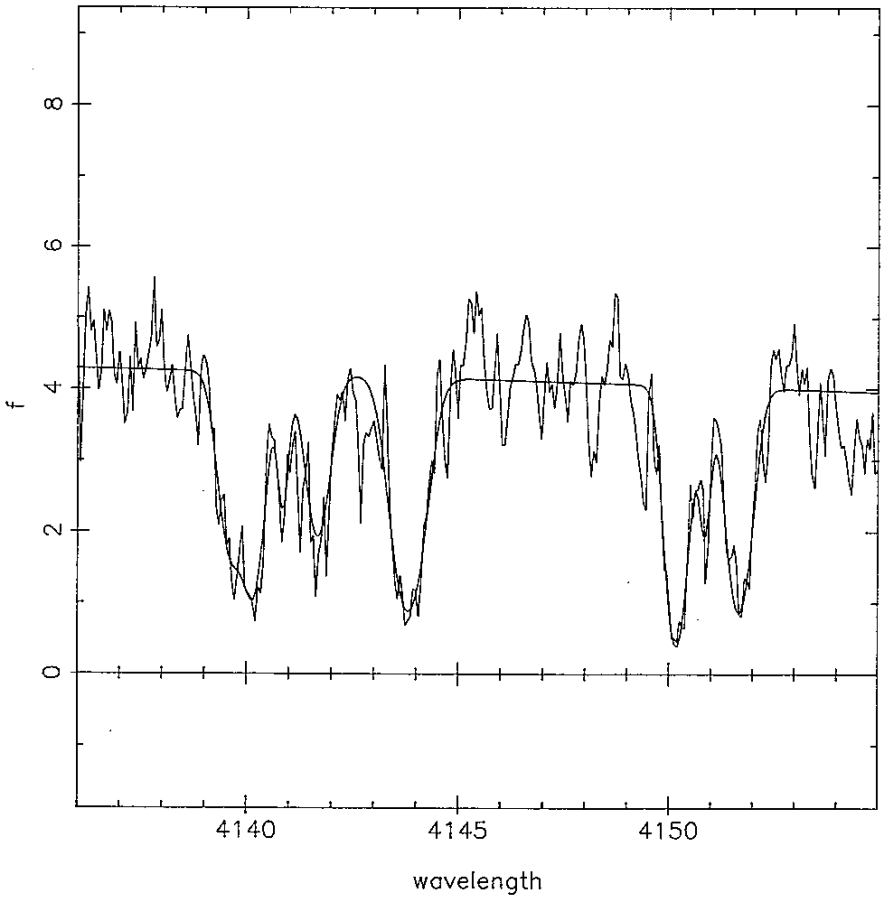

Figure 5.2

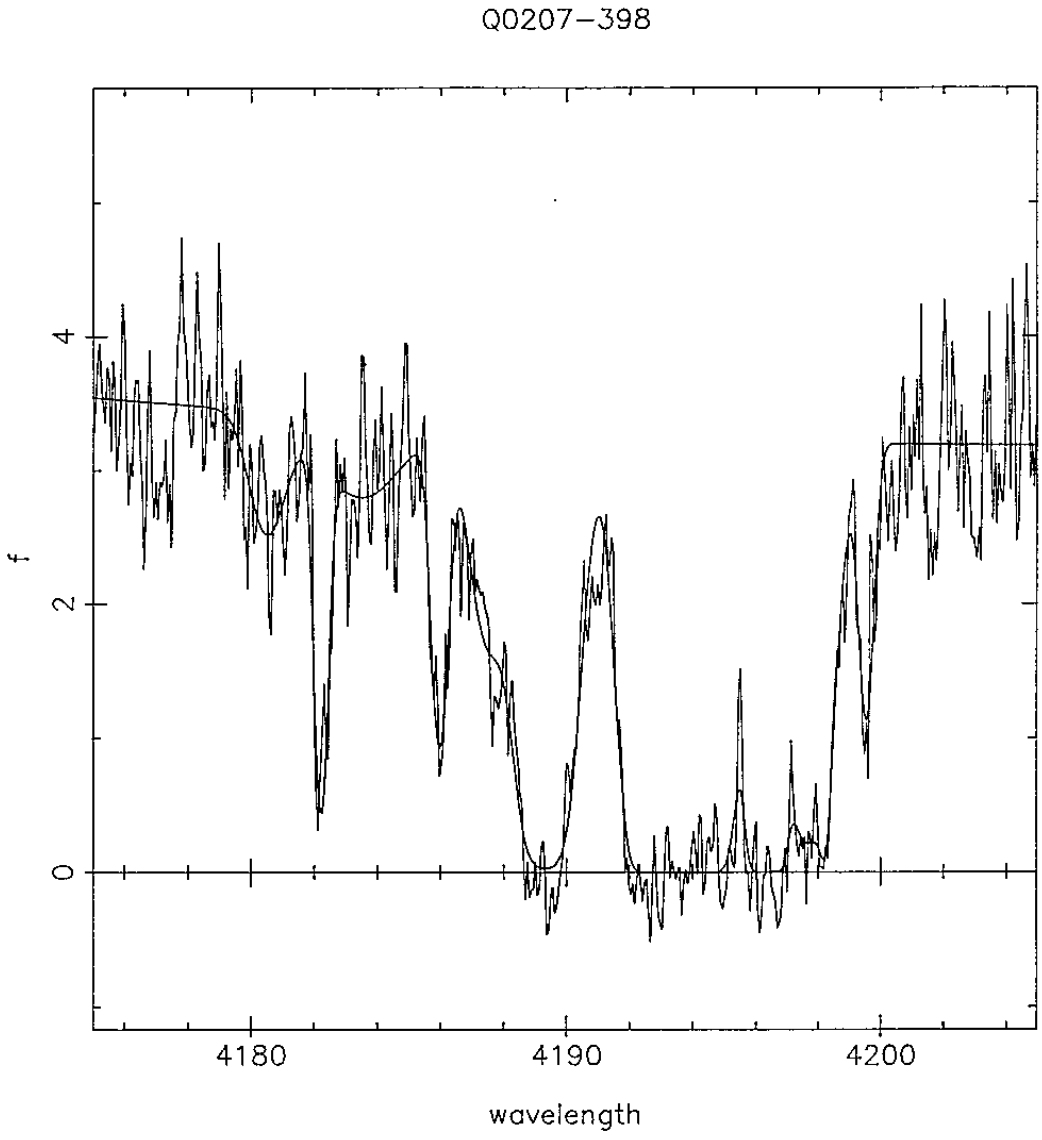

Figure 5.3

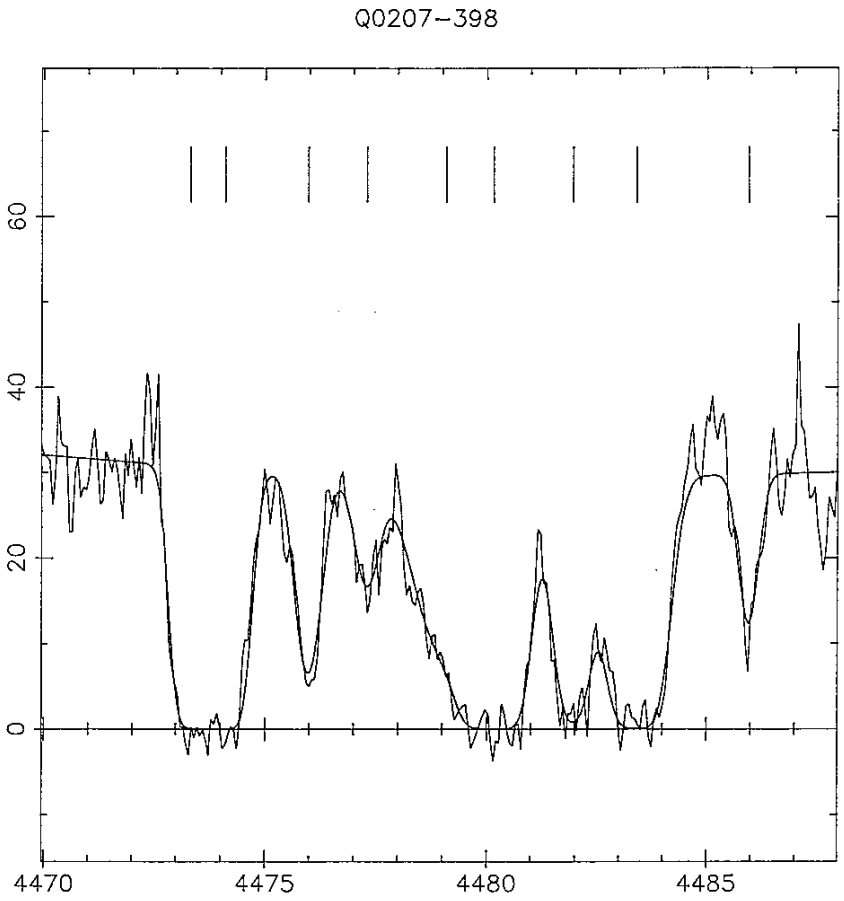

Figure 5.4

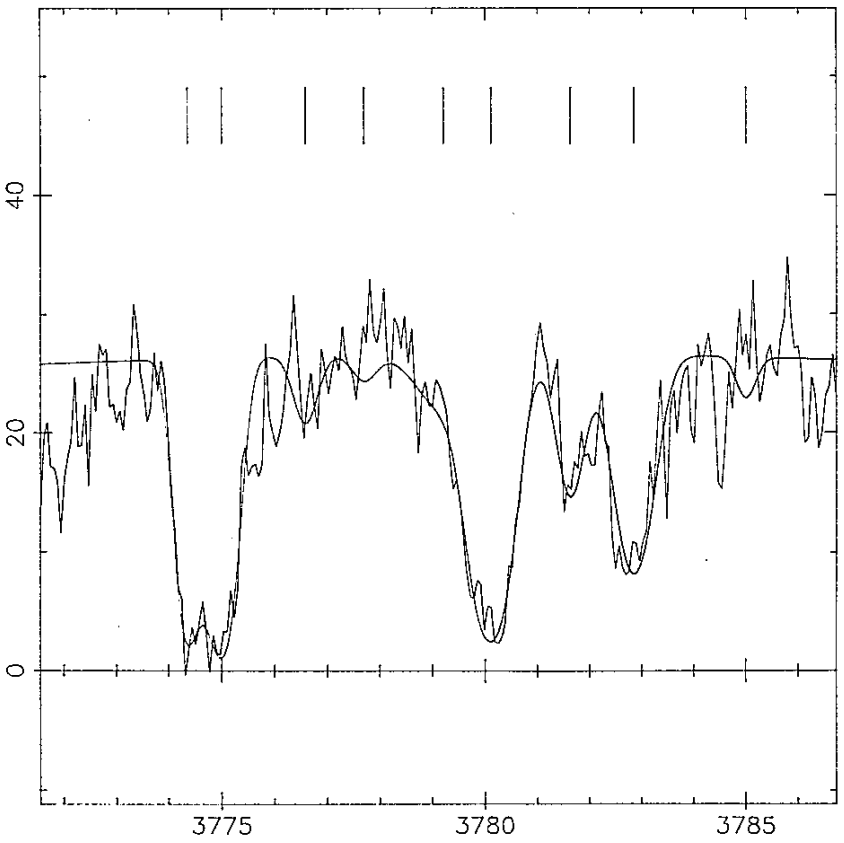

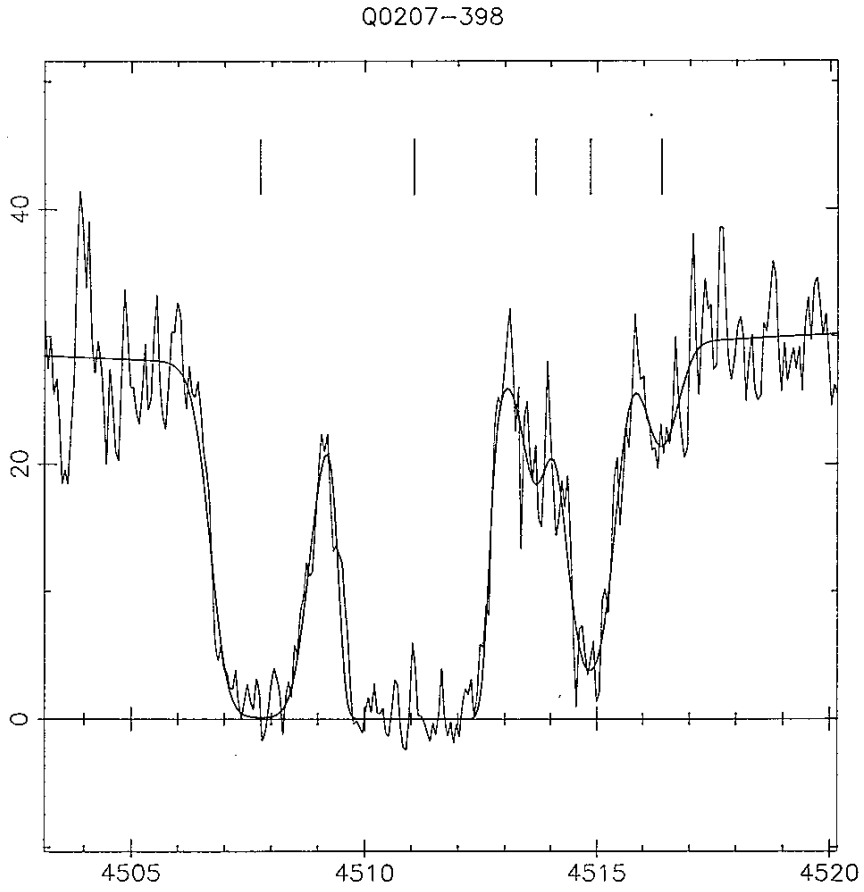
Q0207-398
40
20
0
4505
4510
4515
4520

Figure 5.5

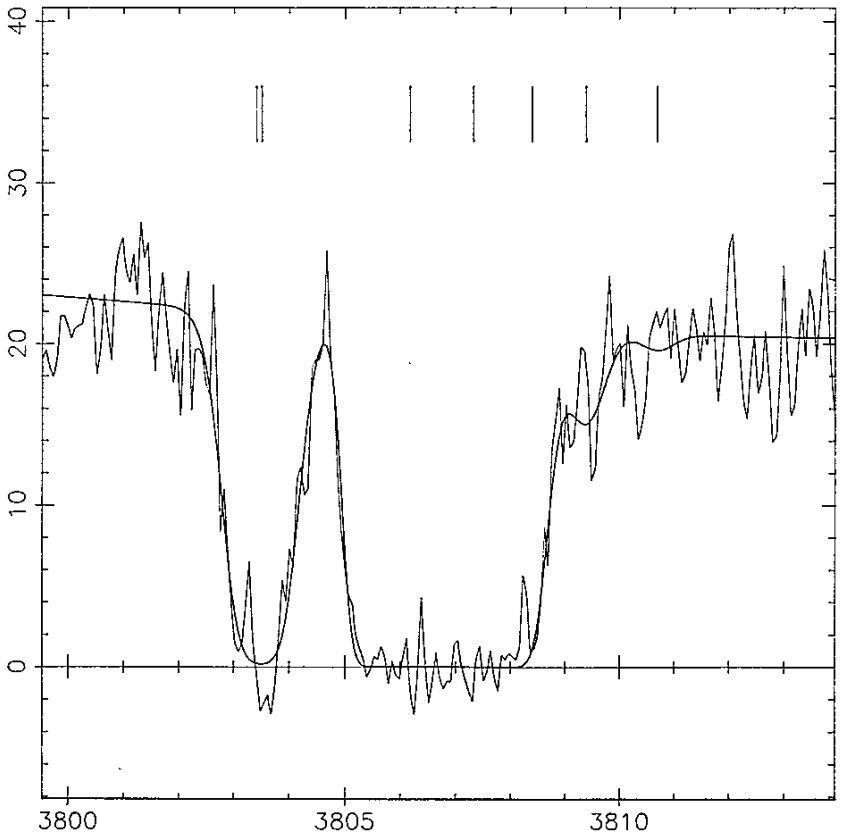
40
30
20
10
0
3800
3805
3810

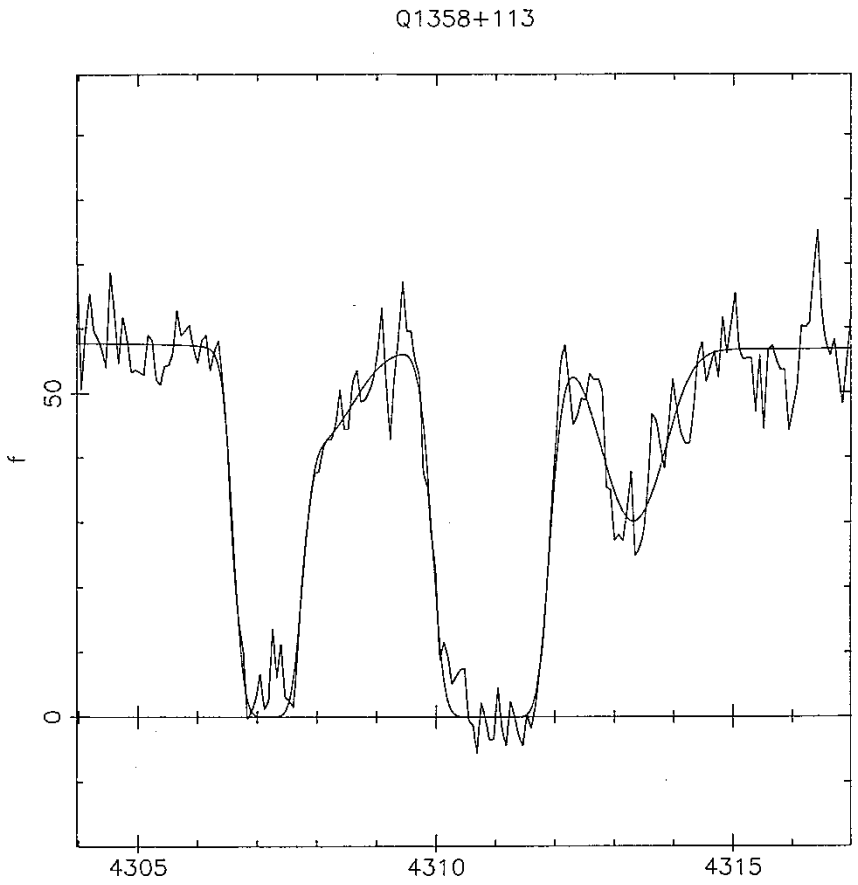

Figure 5.6

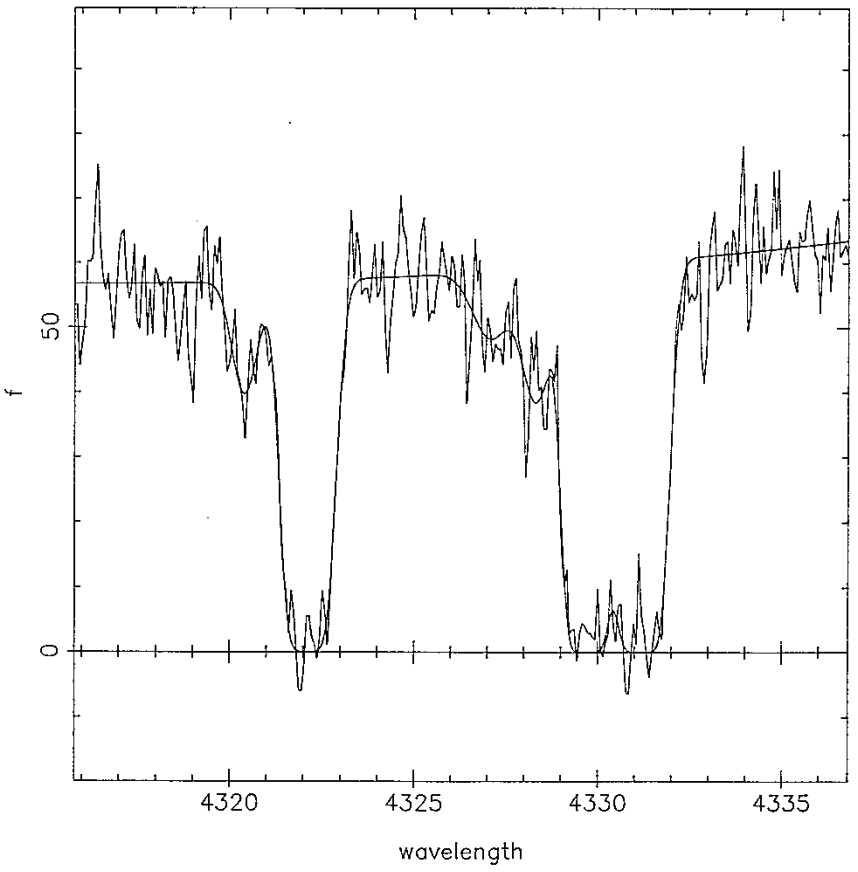

Figure 5.7

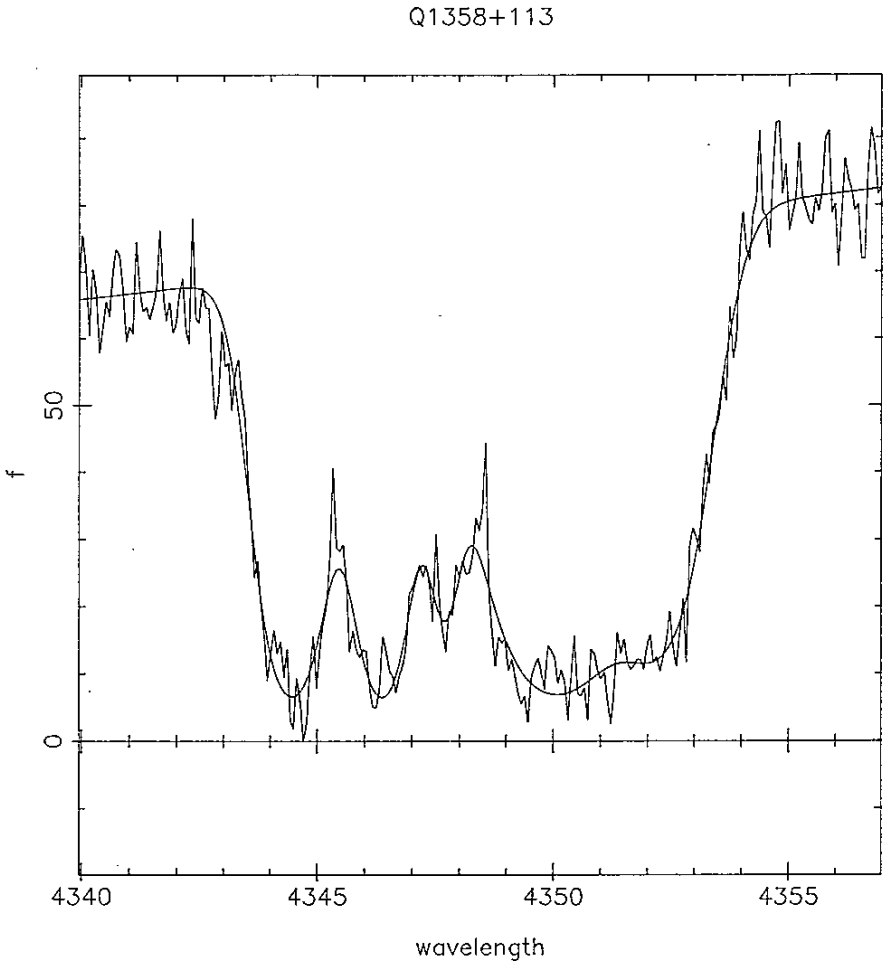

Figure 5.8

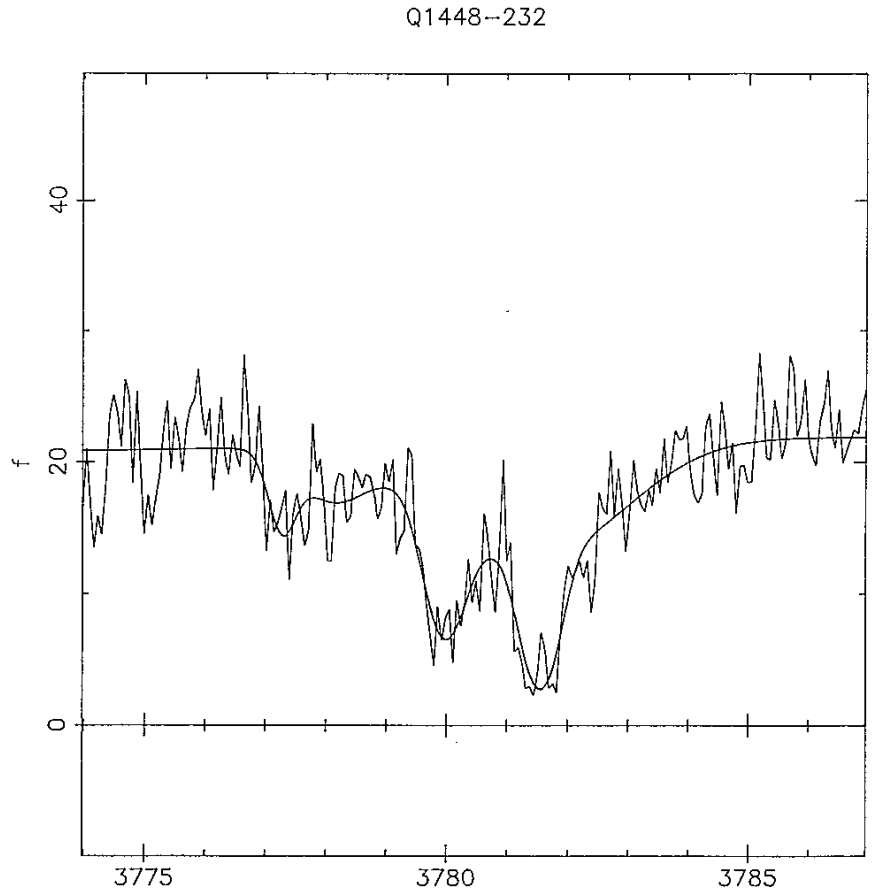

Figure 5.9

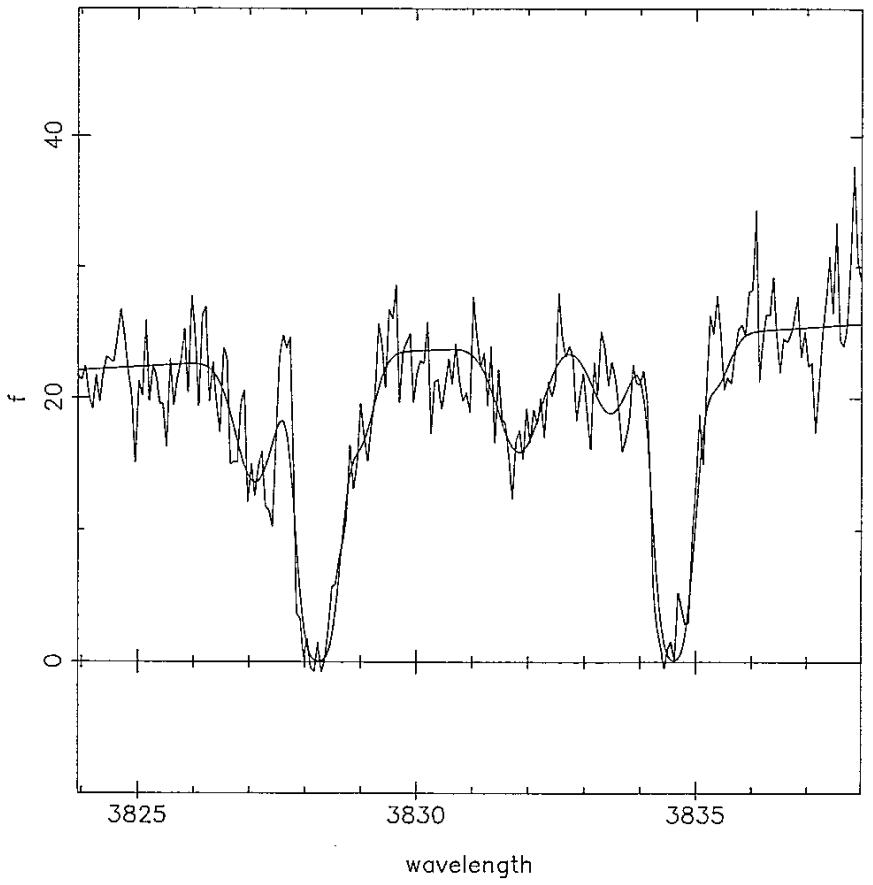

Figure 5.10

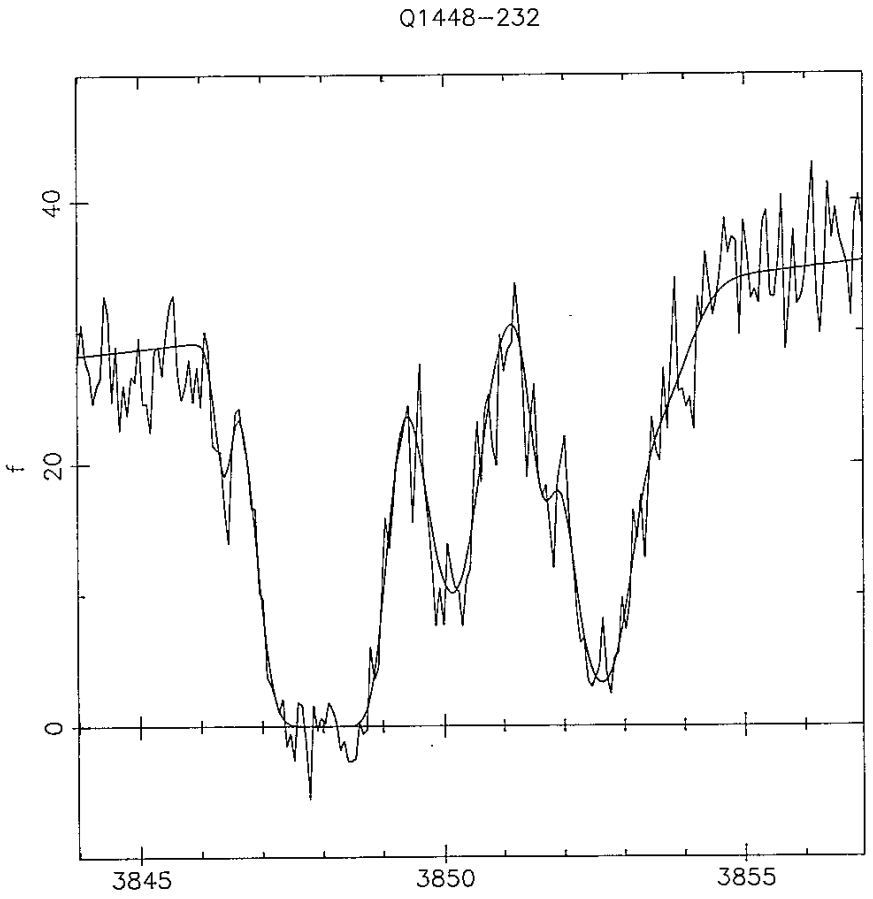
Q1448−232
f
40
20
0
3845
3850
3855

Figure 5.11

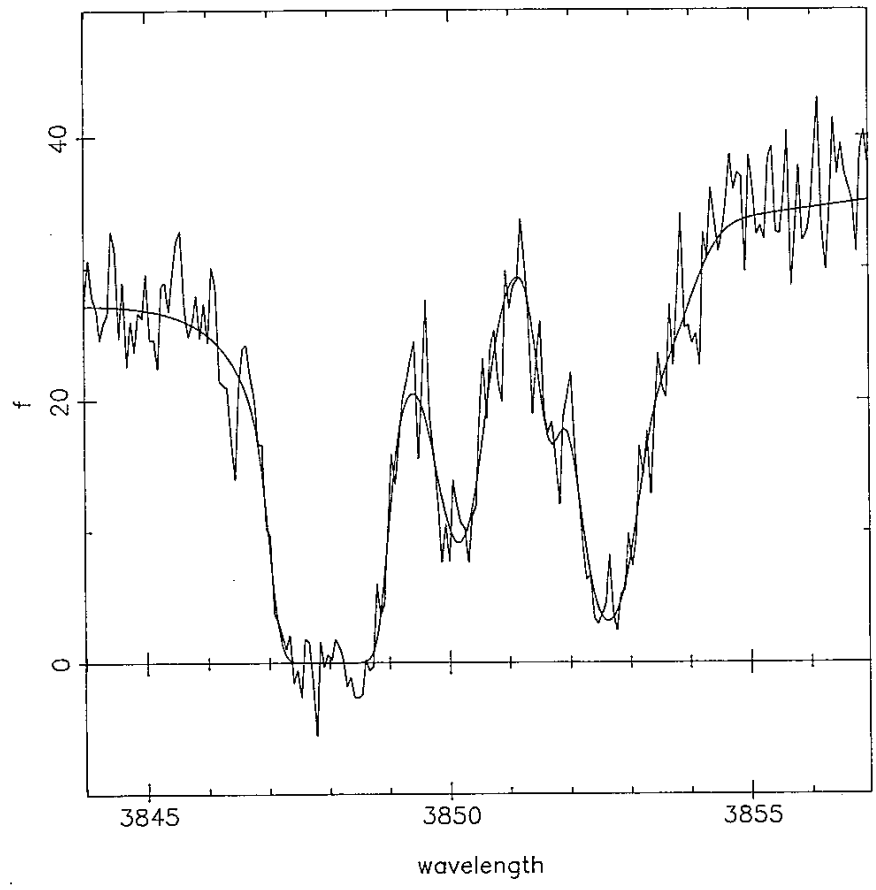
f
40
20
0
3845
3850
3855
wavelength

5.4 Profile fitting statistical summary

The values of χ^2 derived in each individual fit can be combined to provide a test on the average goodness of fit for blended and apparently single absorption features. It is particularly important for a clustering analysis to check whether badly blended features have been over-fitted with too many components, resulting in apparent excess of small scale separations. This problem can be investigated very simply by comparing the summed normalised χ^2's for all the blended and all the single features. A significant difference between the two would be evidence for either over or under-fitting depending on which normalised χ^2 was smaller. No significant difference between the two would suggest (but not confirm) that both single and blended features had, on average, been equally successfully fitted. The reason that this test is not definitive is that we have no knowledge of how sensitive χ^2 is to over-fitting. However, since we have chosen to use a normalised χ^2, which takes into account the number of degrees of freedom, it is likely that any serious over-fitting would be detected; for the summed single and blended features, a difference of only 3 percent or less between the two normalised χ^2's would be detectable at the lσ level.

Table 5.1 is a summary of the statistics associated with both continuum and profile fitting to each object or wavelength region. Columns 1 and 2 identify the spectrum. Columns 3 to 8 refer only to the continuum fit for each object (see section 2.3). Columns 3 and 4 show the number of data points and number of knots in the least-squares cubic spline fit. Column 5 indicates the number of degrees of freedom in each case. Columns 6 and 7 give the χ^2 and normalised χ^2. Column 8 is an estimate of the lσ error on the expected normalised χ^2 and is derived as follows. For $\nu \geq 30$, $\sqrt{2\chi^2} - \sqrt{2\nu - 1}$ is normally distributed with zero mean and unit variance (see for example Eadie et al., 1971). Therefore,

the $\pm 1\sigma$ error range on the un-normalised χ^2 is

$$\chi^2_{1\sigma} = \frac{1}{2}\left[\sqrt{2\nu - 1} \pm 1\right]^2 \tag{5.4.1}$$

and the magnitude of the lσ error on χ^2 is $1/(2\nu - 1)$. Therefore, for the normalised χ^2, the lσ error is

$$\sigma_A\left(\chi^2_n(c)\right) = \sqrt{2\nu - 1}/\nu \tag{5.4.2}$$

where the subscript A is meant to infer that this is an absolute error on the expected normalised χ^2 of 1.

For a Poisson distribution of data points, the expected value of χ^2_n is 1. Column 8 shows clearly that in every spectrum the observed χ^2_n is significantly lower than 1 from which we can infer that the data has been smoothed by the process of re-binning to a linear wavelength scale. Thus the observed scatter in the data, relative to the true noise level, appears smaller. It is important to correct for this effect; the parameter error estimates and goodness of fit significance levels for each profile fit depend directly on χ^2. To compensate for the smoothing, the error array for the data is multiplied by a correction factor of $\sqrt{\chi^2_n(c)}$, obtained in the way described in section 2.3. Alternatively, it can be quantitatively estimated from the noise covariance matrix.

The remaining columns in Table 5.12 relate to the profile fitting statistics. Columns 9, 10 and 11 are the number of degrees of freedom, χ^2 and normalised χ^2 summed over all the Lyα absorption lines in the spectrum. Column 12 is the error on the expected normalised χ^2 of 1. In estimating $\chi^2_n(a)$, the correction factor of $\chi^2_n(c)$ has been included and so the error on $\chi^2_n(c)$ must be taken into

account in $\sigma_A(\chi^2_n(a))$. In effect,

$$\chi^2_n(a) = \chi^2_n(o)/\chi^2_n(c) \tag{5.4.3}$$

where $\chi^2_n(o)$ is the observed value without modifying the error array. The distribution of the ratio of two random variables is given by the Cauchy distribution which has an undefined variance. A. reasonable approximation however may be obtained from

$$\sigma^2\left(\frac{x}{y}\right) \approx \left(\frac{\langle x\rangle}{\langle y\rangle}\right)^2 \left[\frac{\sigma(x)^2}{\langle x\rangle^2} + \frac{\sigma(y)^2}{\langle y\rangle^2}\right] \tag{5.4.4}$$

for 2 normally distributed variables x and y (see for example Eadie et al., 1971). In some cases, the details of the continuum fits were not retained and so there is no entry in column 12.

In the six spectra where $\sigma(\chi^2_n(a))$ has been estimated, we can use it to check whether there is a significant difference between the goodness of fit for the continuum level and for the absorption profiles. In four out of the six cases, $\chi^2_n(a)$ is less than 1 but only in one instance is the difference significant. This is for Q0207-398, Table 5.1, where $\chi^2_n(a)$ is about 3σ below its expected value of 1.

There are two possible interpretations of this general trend. Either the number of free parameters associated with the continuum fit was too low to provide an adequate fit to the true continuum level, or there may be many weak undetected absorption features which fall below the equivalent width cut-off criterion chosen to select absorption features for profile analysis.

In the remaining 2 cases, $\chi^2_n(a)$ is higher, but not significantly, than 1. This is for Q1358+113 and Q0207-398 Table 5.1. The latter is a spectral region cov-

ering Lyβ absorption lines and so deblending becomes slightly more difficult due to the presence of low redshift Lya lines. Consequently, the interpretation of the χ^2 from these data is unclear since the Lyα and Lyβ regions are not statistically independent.

The next two sections of the table give a breakdown of the statistics for single and blended lines. Columns 13, 14 and 15 are the number of degrees of freedom, χ^2 and normalised χ^2 for single lines. Column 16 is the estimated lσ error on the normalised χ^2 and is obtained from

$$\sigma_R(\chi^2_n(s)) = \sqrt{2\nu - 1}/\nu \tag{5.4.5}$$

The error associated with the correction factor $\chi^2(c)$ has not been included and so the subscript R is intended to signify that this is, in some sense, a relative error rather than an absolute error; $\sigma_R(\chi^2_n(s))$ cannot be used to test for significant differences between 1 and $\chi^2(s)$ but it can be used, along with the analogous quantity for blended lines, to compare normalised χ^2s for single and blended features.

Columns 17, 18 and 19 are the number of degrees of freedom, χ^2 and normalised χ^2 for blended lines. Column 20 is the relative error on $\chi^2_n(b)$.

Having estimated all the quantities described, we are now in a position to test for over-fitting. In column 21 the ratio of the normalised χ^2s for single and blended lines is given which, for no over or under-fitting, should be 1. The error on the ratio can be obtained from equation (5.4.1) and is given in column 22. The last column in the table, column 23, shows the significance level, in units of σ, of the difference between 1 and $\chi^2_n(s)/\chi^2_n(b)$. A minus sign indicates that $\chi^2_n(s)$ is greater than $\chi^2_n(b)$. As can be seen, in no case is there any significant

effect, nor any obvious trend. The largest deviation is found in the Lyβ region of Q0207-398, for which the interpretation is unclear, for the reasons already discussed.

CONTINUUM STATISTICS								PROFILE STATISTICS														
								ALL LINES				SINGLES				BLENDS						
Object	Table	n_p	n_k	ν_c	$\chi^2(c)$	$\chi^2_n(c)$	$\sigma_A(\chi^2_n(c))$	ν_a	$\chi^2(a)$	$\chi^2_n(a)$	$\sigma_A(\chi^2_n(a))$	ν_s	$\chi^2(s)$	$\chi^2_n(s)$	$\sigma_R(\chi^2_n(s))$	ν_b	$\chi^2(b)$	$\chi^2_n(b)$	$\sigma_R(\chi^2_n(b))$	$\chi^2_n(b)/\chi^2_n(s)$	σ_{sb}	sig
1	2	3	4	5	6	7	8	9	10	11	12	13	14	15	16	17	18	19	20	21	22	23
0207-398	5.1	826	8	800	438.63	0.55	0.050	1212	1390.91	1.15	0.112	121	114.02	0.94	0.128	1091	1276.89	1.17	0.043	0.80	0.11	1.8
0207-398	5.2	608	4	590	374.67	0.64	0.058	594	533.56	0.90	0.058	316	281.84	0.89	0.079	278	251.72	0.91	0.085	0.98	0.13	0.2
0207-398	5.3	1719	15	1679	1173.04	0.70	0.035	1711	1428.48	0.83	0.054	343	311.93	0.91	0.076	1368	1116.55	0.82	0.038	1.11	0.11	-1.0
1101-264	5.4	1174	8	1148	944.79	0.82	0.042	493	436.07	0.89	0.078	192	160.07	0.83	0.102	301	276.00	0.92	0.081	0.90	0.14	0.7
1101-264	5.5	1086	8	1060	739.78	0.70	0.043	601	516.51	0.86	0.078	198	160.34	0.81	0.100	403	356.17	0.88	0.070	0.92	0.14	0.6
1158-187	5.6									1.02		284	278.30	0.98	0.084	278	295.20	1.06	0.085	0.92	0.11	0.7
1358+113	5.7	1016	8	990	774.91	0.78	0.045	908	941.42	1.04	0.076	245	230.10	0.94	0.090	663	711.32	1.07	0.055	0.88	0.10	1.2
1448-232	5.8	777	8	751	676.87	0.90	0.052	651	610.79	0.94		202	202.21	1.00	0.099	449	408.58	0.91	0.067	1.10	0.14	-0.7
2204-573	5.9									1.04		525	559.49	1.07	0.062	524	530.81	1.01	0.062	1.06	0.09	-0.7
2204-573	5.10									0.89		402	353.58	0.88	0.070	898	803.43	0.89	0.047	0.99	0.10	0.1
2204-573	5.11									0.92		243	209.62	0.86	0.091	727	678.53	0.93	0.052	0.92	0.11	0.7

Table 5.12 Summary of profile fitting statistics

5.5 Summary and conclusions

1) After re-binning each spectrum to a linear wavelength scale, the scatter in the apparently featureless regions is significantly lower than expected for random uncorrelated counts. Since some necessary degree of smoothing has been done, a correction factor is estimated for each spectrum which is used to rescale the error array. It is important to do this so that the parameter error estimates and significance levels obtained from the profile fitting analysis are approximately correct.

2) Once the correction factor has been applied and all the profile fitting done, the average residual scatter in the data over the spectral regions containing absorption lines is still less than expected for the corrected noise levels obtained from continuum-only data regions.

The most likely explanations are either that the adopted continuum level did not adequately follow the overall trend in the spectral continuum and/or that there are numerous weak undetected absorption lines in the continuum regions which give rise to a scatter which is larger than expected for purely Poisson statistics modified by the re-binning procedure.

3) The most important result of this analysis is that there is no evidence for either over or under-fitting of blended absorption features compared to single lines.

5.6 Further comments and future work

The basic approach in this profile fitting analysis has been to deblend complex absorption features using the minimum number of free parameters required to give a "satisfactory" fit, where "satisfactory" is rather loosely defined but in practice meant that where possible, an acceptance level for the observed χ^2 of better than 95 percent (i.e. about 2σ) was aimed for. The result of this approach is probably that some complex blends have been under-fitted and a few (about 5 percent) have been over-fitted.

Of course, in any particular case, it is impossible to know exactly the right number of components in any blend and so some *a priori* guidelines for deblending have to be defined which hopefully give, on average, a good approximation to reality. It seems likely that we can ultimately use the results of numerical simulations to create a set of tuned, *a priori* guidelines which give optimum results. Apart from the obvious advantage of greater reliability, more precisely defined procedures must eventually allow the whole process to be completely automated and hence be non-subjective. Considerable effort has gone into speeding up and optimising profile fitting to absorption spectra but nevertheless it is still fairly time-consuming and there remains a small degree of subjectivity.

As more high resolution data becomes available, and the statistics for the absorption line parameter distribution functions improve, it will become more and more important to fully understand selection effects and biases introduced by line blending. The only way to investigate these reliably is through experiments with synthetic data whose parameter distributions are known exactly. This highlights the necessity to develop more sophisticated automated techniques for handling large amounts of high quality, high resolution data.

6 Statistical analyses

6.1 Clustering properties of the Lyman clouds

6.1.1 Introduction

In general, the two—point correlation function (TPCF) has been used in attempts to test for non—randomness in the distribution of the Lyman clouds. The conclusions of all analyses published so far is that the Lyman clouds are randomly distributed, (i.e. the TPCF is flat), on all scales from 300 to 30,000 km/s, (Sargent et a1., 1980; Zou et a1., 1982; Sargent et a1., 1982). The data used for these analyses have a spectral resolution of about 1-2Å FWHM. At this resolution, almost all of the Lyman lines are unresolved. The lower limit of 300 km/s is related to the spectral properties (i.e. signal to noise ratio and resolution), and the method used to identify absorption features, as well as, to some extent, the intrinsic line profile properties. Carswell et a1., (1984) extended the previous null results down to around 50 km/s with higher resolution data on Q1101-264 although their sample was rather small, (roughly 50 absorption lines).

In high resolution data, the smallest scale down to which clustering can be reliably investigated depends on the intrinsic line profiles and the spectral signal to noise ratio, provided that the resolution is much better than the line widths

and that a reliable and objective procedure for line identification, such as the one described earlier, is used.

For considerations of the clustering properties it is clearly desirable to have as large a dataset as possible. A strong motivation for obtaining much of the data presented here was to explore more thoroughly the small scale (< 500 km/s) clustering properties of the Lyman clouds.

For our high resolution spectra, the wavelength coverage in each observation is small (≈ 130Å) and so the number of absorption lines per region is also fairly small (about 25 per region). There are several disadvantages in using the TPCF as implemented previously. The most obvious of these is loss of information caused by binning the data. Also, for small samples, (and therefore individual objects or wavelength regions), the number of counts per bin in the correlation function is small. This violates the assumption implicit in a simple chi-squared test of normally distributed counts. Finally, there is evidence both in the results presented here and those of Sargent et al., (1980) that the observed scatter in the correlation function is somewhat smaller than would be expected from Poisson counting statistics. There are two possible non-physical explanations for this:

i) correlations between adjacent bins may be a natural consequence of the way in which the correlation function is computed, and

ii) the blending of lines on small scales might result in the lines which are detected being slightly more regularly spaced than expected for randomly placed lines. This point is discussed in more detail later.

Consequently, in addition to, and complementing the TPCF, another statistic

has been applied to the data, which is sensitive only to small scale clustering. Descriptions of the new statistic and the correlation function follow in the next two sections. For both statistics the choice of working in velocity space rather than inferred comoving distances was made, since the latter depends on the choice of cosmological model. Also, there is no reason to suppose that a velocity clustering scale follows the evolution of the comoving scale length of the Universe, although it would be surprising if the velocity scale did not evolve dynamically.

6.1.2 Cumulative distribution of velocity splittings

For any two lines at redshifts z_1, z_2, the separation in velocity space is, for small separations,

$$v = \frac{c\Delta z}{1+\bar{z}} \tag{6.1.1}$$

where

$$\Delta z = z_2 - z_1 \tag{6.1.2}$$

and

$$\bar{z} = (z_1 + z_2)/2 \tag{6.1.3}$$

The cumulative distribution function (CDF) for the velocity splittings is obtained by calculating v for each neighbouring pair of lines and then plotting the number of separations less than or equal to v against v. This observed distribution may then be compared with any hypothetical distribution. The significance of the largest difference between the two distributions may be estimated using the Kolmogorov-Smirnov (KS) test. There are several advantages offered by this procedure. Firstly, the requirement of binning the data is removed so no loss of information occurs. Not having to bin and using a non-parametric test of significance avoids the problems encountered when using the TPCF and a χ^2 test. The significance levels for differences between

the observed and hypothesised CDFs for the Lyman clouds are unambiguous in the sense that they do not depend on choice of bin size nor velocity scale, as with the correlation function. Also, for small samples, the KS test is more powerful than a chi-squared test and at least as powerful for larger samples.

There are two ways of obtaining the CDF expected for randomly distributed clouds.

6.1.2.1 Analytic CDF

In any dataset the smallest velocity splitting detected, v_*, is determined by 4 effects:-
(1) the spectral signal to noise,
(ii) the column density and velocity dispersion distribution functions,
(iii) the instrumental resolution,
(iv) the line identification technique.

For the data used here, the instrumental resolution is much less than the intrinsic line widths and so (iii) is negligible. Item (iv) refers to the method used to locate significant absorption features and deblend them into individual components.

The line blending problem complicates procedures for generating test CDFs, and a simplifying assumption is necessary. If we assume that all splittings greater than or equal to v_* are detected, then for a random distribution of N redshifts in a total velocity interval V_t, the number of lines that will be missed due to blending is given by

$$n_m = N\left[1 - e^{-Nv_*/V_t}\right] \tag{6.1.4}$$

where $N = n_o + n_m$, and n_o is the number of lines observed. The number of separations less than or equal to v and greater than or equal to v_* is then

$$n_s(\leq v) = (n_o - 1)\left[1 - e^{-N(v-v_*)/V_t}\right] \tag{6.1.5}$$

Equations (6.1.4) and (6.1.5) can be used to compute the CDF for randomly distributed clouds for comparison with the CDF observed for any contiguous spectral region. To combine distributions for different objects or spectral regions, the CDFs are simply added using suitably small data bins (1 km/s) so that information loss is negligible.

Consequences of the speed function approximation for V*: Equations (6.1.4) and (6.1.5) are based on a single value of v_* (for a given dataset) and the assumption that all separations greater than or equal to this value are detected. Since there is a distribution of the absorption line profile properties and a finite signal to noise ratio, in reality this assumption must be incorrect. However, one or two simple considerations demonstrate that the step-function assumption is a reasonable approximation and at worst should only lead to a slight underestimate of the significance of any small scale clustering provided that v_* is properly chosen.

Consider two curves obtained from equations (6.1.4) and (6.1.5), using two slightly different values of v_*, v_* and v'_*. As v_* increases in (6.1.4), n_m increases and therefore so does N. The two curves cross at some point given by $v_x = (v'_* N' - V_* N)/(n'_m - n_m)$. At values of $v \leq v_x$, $n'_s(\leq v) \leq n_s(\leq v)$. Therefore, providing v_x is larger than any small scale clustering scales observed, the step-function approximation for v_* leads to an underestimate of the significance. Numerical trials demonstrate that both n_s and v_x vary slowly with v_* over the relevant velocity range and also that the value of v_x is above clustering

scales of interest.

The conclusion is therefore that a step-function approximation for v_* is adequate and can only lead to a slight underestimate of the significance of any clustering.

6.1.2.2 Monte Carlo CDF

An alternative approach is to numerically simulate the CDF for each object. For each spectrum, N lines are cast down at random into the observed redshift interval, where N is such that only n_o will be seen once all lines closer together than v_* have been formed into blends. In order to obtain a smooth 'noise-free' distribution, several iterations are carried out averaging the CDF at the end. In general, 50-100 iterations gave satisfactory CDFs. This numerical method was used as a check on the analytic one and the agreement was found to be excellent.

6.1.2.3 Statistical tests

If $F_n(v)$ is the sample distribution of n data points, and $F(v)$ is the hypothesised distribution, the Kolmogorov—Smirnov statistic uses the maximum numerical difference $D_n = [F_n(v) - F(v)]$. (For a thorough treatment of the theoretical background to this statistic see, for example, Lindgren, 1968). For $n \leq 40$, the significance level, s, of the observed D_n may be well approximated by

$$D_n \geq [0.5m \ln(k/(1.0 - s)]^{1/2} \tag{6.1.6}$$

where $k = l$ for one-sided differences, and $k = 2$ for two-sided differences, and where

$$m = n + \sqrt{n/10} \tag{6.1.7}$$

gives slightly more accurate results than $m = n$ (Conover, 1971).

6.1.3 Two point correlation function

As before, the separation in velocity space for any pair of absorption lines is, to high accuracy over the scales of interest, $v = c\Delta z/(1+\bar{z})$. v is calculated for every pair of lines in the spectrum and all of the $n_o(n_o-1)/2$ values are binned in bins of size δv. since the data window has finite length, the resulting distribution has a small gradient and may be flattened by multiplying by the normalising function

$$\phi(v) = \frac{v_t}{(V_t - v)}.$$

For a uniform distribution of n_o redshifts, the mean count per bin would then be

$$\frac{n_o(n_o-1)\delta v}{2V_t}$$

However, at small v, the blending problem results in reduced counts, with zero below v_*. In practice, the mean count level can be estimated empirically for $500 \leq v \leq V_t$ km/s, avoiding the test region.

6.1.3.1 Correlation function statistics

Let the count in any bin in the correlation function be $c(v)$. The normalised count then becomes

$$c'(v) = c(v)\phi(v) \tag{6.1.8}$$

If Poisson counting statistics apply, the error on this is

$$\sigma(c'(v)) = c(v)^{1/2}\phi(v) \tag{6.1.9}$$

We may rescale this, to express the amplitude of the correlation function in terms of probabilities, to give

$$1 + \xi(v) = \frac{c'(v)}{\langle c'(v)\rangle} \tag{6.1.10}$$

where

$$\langle c'(v)\rangle = \frac{\sum c'(v)}{p} \tag{6.1.11}$$

and the summation is made over p bins, avoiding the test region. The error is now

$$\sigma(1+\xi(v)) = \frac{c(v)^{1/2}\phi(v)}{\langle c'(v)\rangle} \tag{6.1.12}$$

If we wish to obtain an estimate of the average value of $(1+\xi(v))$ over some scale length Δv corresponding to a mean velocity u, and M bins in the correlation function, then $s(u) = \sum c(v)$ and $s'(u) = \sum c'(v)$.

Rescaling,

$$(1+\xi(u)) = \frac{s'(u)}{\langle s'(u)\rangle M} \tag{6.1.13}$$

and

$$\sigma(1+\xi(u)) = \frac{s(u)^{1/2}\phi(u)}{\langle s'(u)\rangle M} \tag{6.1.14}$$

The previous expressions relate to a single spectral region and correlation function. To produce a composite correlation function from q individual functions we simply add the correlation functions, obtaining $a(v) = \sum c(v)$ and $a'(v) = \sum c'(v)$. Rescaling, we get

$$(1+\xi(v)) = \frac{a'(v)}{\langle a('v)\rangle} \tag{6.1.15}$$

and

$$\sigma(1+\xi(v)) = \frac{a(v)^{1/2}\psi(v)}{\langle a'(v)\rangle} \tag{6.1.16}$$

where $\psi(v)$ is the composite response function and may be estimated most easily from $\psi(v) = a'(v)/a(v)$. If we now wish to obtain an estimate for an average value for $(1+\xi(v))$ taken over some range Δv, mean velocity u, corresponding to M bins in the composite two—point correlation function, we

get $b(u) = \sum a(v)$ and $b'(u) = \sum a'(v)$. Rescaling,

$$(l + \xi(u)) = \frac{b'(u)}{\langle b'(u) \rangle M} \tag{6.1.17}$$

with error

$$\sigma(1 + \xi(u)) = \frac{b(u)^{1/2}\theta(u)}{\langle b'(u) \rangle M} \tag{6.1.18}$$

where $\theta(u)$ is the composite response function over this velocity range, and may be estimated from

$$\theta(u) = \frac{b'(u)}{b(u)} \tag{6.1.19}$$

We may estimate significance levels in one of two ways; the expressions for $(1 + \xi)$ and $\sigma(l + \xi)$ provide significance levels in units of σ. Alternatively, a χ^2 test can be applied, where $\chi^2 = \sum(\xi/\sigma(1 + \xi))^2$. However a χ^2 test is inapplicable when the number of counts per bin is low, as it is for individual spectral regions and consequently we have not used χ^2.

6.1.4 Data analysis

6.1.4.1 Individual spectral regions

In the left hand column of figure 6.1.1 the observed and random cumulative distribution functions are plotted for each spectrum. To the right of each one is shown the difference between the two distributions. This is a convenient way of representing the distributions since significance levels may be illustrated as horizontal lines. Three sets of significance levels are plotted, corresponding to 1-, 2- and 3-sigma deviations. The solid line is for 2-sided differences and the dashed line is for l-sided positive deviations of the observed distribution from the random one. The significance levels were obtained using (6.1.6) and (6.1.7) which are good approximations for $n \geq 40$. However, in one case n is as low as 7, (Q2206-199). Comparing values of D_n obtained using (6.1.6) and (6.1.7) with tabulated values indicate that the plotted levels are slightly too high, by

about 6 percent where n is this low.

In defining the sample of Lyman alpha lines for each object, the restriction was imposed that only lines which were 3000 km/s or more away from the emission line were used. This was done to reduce any effects due to both the change in the line number density per unit redshift (Weymann, carswell and Smith, 1981; Murdoch et al., 1986) and also the change in detection levels due to variation in the spectral signal to noise ratio approaching the emission line.

Echelle data on two objects observed with the Cerro Tololo 4m telescope are also included, in addition to the AAT data, in order to extend the redshift baseline of the analysis. These are Q0420-388, (Atwood, Baldwin and Carswell, 1985), and PKS2000-330, (Carswell et al., 1986). The spectral resolution of this data is approximately one half that of the AAT data, but the majority of absorption lines was resolved. Also, the absorption line profiles were fitted using Lyman alpha and higher order lines. This probably compensates to some extent for the poorer resolution, although it is not clear that the AAT and CTIO samples are directly comparable.

6.1.4.2 Results

As can be seen from inspecting figures 6.1.1 and table 6.1.1, which summarises the results, in no individual case is there a significant difference between the observed and random cumulative distribution functions. (In some cases, where the difference between the cumulative distributions is small, the approximation used to obtain significance levels breaks down and s in table 6.1.1 becomes negative. These values have been left blank).

Figures 6.1.2 show the individual two-point correlation functions. The dashed line illustrates an approximate 1σ error contour. The bin size is 75 km/s with

the left hand edge of the first bin starting at 50 km/s. The value of 50 km/s was chosen arbitrarily but is above many of the values of v_* for individual correlation functions (see table. 6.1). Any residual blending effects beyond 50 km/s should only lead to lower counts. The results are summarised in table 6.1.2. In order to test for small scale clustering, the average value of $(1 + \xi)$ over the range $50-275$ km/s has been estimated. The upper limit of this range corresponds approximately to the lower limit in previous clustering analyses. The error on the average $(1+\xi)$ was estimated assuming Poisson statistics apply as discussed in the preceding section. In fact, as will be shown, the scatter in the correlation function is smaller than expected for uncorrelated bins. This should lead to slightly reduced estimates for significance levels of any observed departures from $\xi = 0$. For normalisation to $(1 + \xi)$ the mean count level ($\langle a'(v) \rangle$ in equation 6.1.15) was estimated over bins 8 to 30, corresponding to the velocity range 575 to 2300 km/s. The error estimates for $(1 + \xi)$ do not include the error on the mean count level since the latter is small; $\sigma(1 + \xi)$ would increase by slightly less than 7 percent.

The spectrum of Q2204-573 consists of three overlapping regions. These have been kept separate for the clustering analysis since the signal to noise ratio varies from region to region and hence the absorption line detection thresholds differ. The spectral regions used to calculate the clustering statistics however do not overlap.

As can be seen from table 6.1.2 there is generally no strong evidence in individual cases for $\xi > 0$ although there are three cases where the significance levels exceed 2σ. However, there does seem to be a trend for $\xi > 0$ on average. To test for this we sum the correlation functions.

6.1.4.3 Summed statistics

Several selection criteria have been used to define different samples of absorption lines.

Sample A:- all the AAT data (i.e. everything except Q0420-388 and PKS2000-330). The spectral resolution is roughly constant. The signal to noise ratio varies from object to object but providing there is no significant change along a given spectrum over the range used this should not matter.

Sample B:- all the CTIO data (i.e. only Q0420-388 and PKS2000-330). The spectral resolution is again roughly constant at about half that of the AAT sample.

Sample C:- samples A and B combined.

Samples D and E:- the AAT data divided into two redshift intervals. There are thirteen individual spectral regions. Sample D comprises the seven lowest redshift regions and sample B comprises the remaining six. The motive here is to investigate any possible redshift dependence of ξ.

Sample F:- all the AAT data but only lines with N(HI) $\geq 3 \times 10^{13}$ atoms/cm^2 have been used. If weak Lyman alpha lines, which would not be detected as isolated features in the spectrum, are found preferentially when they lie close to stronger features, there might be an apparent excess of small scale splittings. The cutoff of 3×10^{13} is significantly above the detection limits, reducing the full sample (A) by approximately one third.

Sample G:- all the AAT data but only Lyman alpha lines with N(HI) $< 5 \times 10^{15}$

atoms/cm^2 have been used. This cutoff was chosen in an attempt to remove systems which may be weak unidentified metal line systems, which probably do cluster. In fact the effect of the cutoff was negligible, removing only six absorption lines, and the cutoff should have been lower.

Samples H and I:- the AAT data divided into two column density bins. Sample H has N(HI) $\leq 10^{13}$ and sample I has N(HI) $> 6 \times 10^{13}$ atoms/cm^2. The partition of 6×10^{13} was chosen so that each sample contained a reasonably large number of absorption lines and the intention was to check whether ξ has any column density dependence.

Random sample:- this is a large (601 absorption lines) sample of data generated by Carswell and Lewis with the aim of investigating systematic differences between the true and observed parameter distribution functions. Seventeen spectra of Lyman alpha absorption lines were synthesised with column density and velocity dispersion distribution functions chosen to match those derived from the real data. The redshift distribution of lines was random subject to the constraint that the number density of absorption lines $dn/dz = k(1+z)^\gamma$ within an individual spectrum. The value of γ used was 2 and k was estimated from the real data at the corresponding redshift. The redshift interval for each simulation was small ($\Delta z \approx 0.2$). Consequently, the results of any clustering analyses should not be sensitive to the choice of γ. The spectral resolution used in the simulations was the same as that of the AAT sample. Three signal to noise ratios were used in the simulations. The majority of the spectra were generated with S/N=5; some spectra with S/N=3 and S/N=10 were also produced. The simulated spectra were subjected to the same procedures as the real data, extracting the profile parameters N(HI), b and z.

6.1.4.4 Results

Figures 6.3 and 6.1.4 show the summed cumulative distributions and two-point correlation functions for the 10 different samples. A slightly smaller bin size of 60 km/s has been used for the correlation functions for these summed statistics. The results are summarised in tables 6.3 and 6.1.4. Samples H and I were not included in the CDF analysis; problems were encountered in solving equation (6.1.4) for n_m where n_o was small and v_* large. The way round this difficulty may be to adopt v_* as that value found from the unedited absorption line sample for that particular spectrum, rather than the value found after applying the selection criteria.

The first striking result is that in sample A (all the AAT data) there is significant evidence for clustering at a significance level of around 4σ. Over the scale investigated (50-290 km/s) $\langle 1 + \xi \rangle = 1.32 \pm 0.08$.

Incrementing the mean redshift by approximately 1 to $\bar{z} = 3.39$ seems to destroy this effect (sample B) assuming the two samples are comparable in their ability to detect line splittings over the velocity range of interest. The two-point correlation functions for samples A and B differ by 2.6σ.

In sample C (A and B combined) the residual effect from A is strong enough to show a 3.2σ excess in the correlation function and a probability that the observed and random cumulative distributions differ of 0.98.

Sample D ($\bar{z} = 2.191$) shows significant evidence for clustering whilst sample E ($\bar{z} = 2.581$) does not, although sample E is smaller. The correlation functions for the two samples differ at a level of only 1.6σ.

Sample F (N(HI) $\geq 3 \times 10^{13}$ atoms/cm^2) also appears significantly clustered, as does sample G (although this is not surprising since it is almost the same as A). In fact $\langle \xi \rangle$ has increased compared to sample A; this would only be expected if lines with N(HI) $\leq 3 \times 10^{13}$ atoms/cm^2 had a tendency to be more regularly placed than randomly.

Neither samples H nor I show any evidence for clustering. The values of $(1+\xi)$ for each one are lower than for the parent sample (A), as may be expected from the way in which H and I are defined. There are no differences in the clustering properties of weak and strong lines.

Finally we turn to the results from the simulated spectra. The first bin in the correlation function is significantly below 1, in contrast with the real data. Beyond the first bin there is no evidence for systematic departures from $\xi = 0$. In the two-point correlation function, $\langle 1 + \xi \rangle$ over the range 50 to 290 km/s is 2.5σ below 1 due entirely to the effect of the first bin. This is confirmed by the result of the subtracted cumulative distribution functions which shows that the 'observed' and random distributions agree extremely well. The CDF statistic is insensitive to the depletion of small scale (50-110 km/s) splittings because of the way in which v_* is defined.

There are several possible explanations for this deficit. Firstly, although the synthetic and real spectra have the same resolution, the signal to noise ratio in the synthetic spectra is on average lower, so deblending on small scales may be more difficult. However there is no obvious trend in v_* with signal to noise.

Also, the number density of absorption lines used to generate the synthetic spectra was chosen to be approximately the same as the observed number density at the corresponding redshift. By comparing the generating and inferred

absorption line lists for the simulations we find that many of the lines thrown down are lost in blends, even at this high spectral resolution. Consequently, the observed (real) and observed (synthetic) line densities are different, although how or why this by itself could explain the depletion of small scale velocity splittings is not obvious.

A third unlikely possibility is that systematic differences between the profile fitting procedures for the real and synthetic datasets may have crept in, i.e. less care may have been exercised in deblending complex absorption features in the synthetic spectra. In the real data, the excess extends beyond the first bin. It seems unlikely that either over- or under-fitting could occur on such large scales. An unambiguous way of resolving this is to devise a completely automated profile fitting Procedure and re-analyse all of the data.

Another possibility and perhaps the most likely is that the real data may be somewhat more strongly clustered than is inferred from the clustering statistics. Numerical simulations could check this.

6.1.5 Scatter in the correlation function; comparison with Poisson noise

In sample A, the value of χ^2 over the normalisation region (bins 8 to 40) is 19.48 for 33 bins. For $\nu \geq 30$, $(2\chi^2)^{1/2} - (2\nu - 1)^{1/2}$ is normally distributed with zero mean and unit variance (Eadie et. a1, 1975). Using this relation, we find the scatter in the two—point correlation function to be 1.7σ below that expected for randomly distributed counts in each bin. For sample B, the highest redshift sample, $\chi^2 = 13.09$ over the same range. This suggests that the effect increases with the line number density. Note that the significance levels of the small scale clustering in the TPCF have been estimated assuming

$\sqrt{n}$ statistics, and are therefore probably underestimates. The same effect is not seen in the random sample, perhaps because of the slightly lower line density. Here, $\chi^2 = 32.45$ for 33 bins and the agreement with random counts is excellent. If a more detailed analysis and more data should prove this effect to be real, and not due to line blending or some other systematic effect, one possible explanation may be that the redshifts of the Lyman clouds are correlated in that they may be more regularly placed than random on scales larger than the clustering length.

6.1.5.1 Redshift evolution of ξ

Motivated by the apparent lack of clustering at high redShifts and yet significant clustering at $z \approx 2$ we explore the possibility that the correlation function may be evolving with redshift. To do this we simply plot $\langle 1 + \xi \rangle$ as given in Table 6.1.4 against $\bar{z}$ for each spectral region as shown in figure 6.1.5. There appears to be a tendency for $\langle 1 + \xi \rangle$ to increase with decreasing redshift although the sample is rather small. To test the significance of this weak trend, a least-squares line was fitted and the best fit is shown as a dashed line in figure 6.1.5. The linear regression coefficient (i.e. slope) of the fit is -0.29 with standard error 0.15 so the trend is significant at the 2σ level. However, a straight line does not appear to be a very good fit to the data, so the significance level may be unreliable. A more sophisticated analysis would be required once more data becomes available.

6.1.5.1.1 Metal line contamination In defining the sample of absorption lines used for this clustering analysis, all known metal lines and Lyman alpha lines associated with metal systems were removed; the remainder are assumed to comprise the Lyman forest. This is difficult to verify without having spectral coverage of the Lyman beta region, and then only Lyman alpha lines strong enough to have Lyman beta above the detection limit can be checked.

As an example, the only AAT data we have covering both the alpha and beta regions is for Q0207-398. The detection limit in the beta region corresponds approximately to a rest equivalent width of ≈ 0.033. At b$\approx$ 30 km/s, this translates to N(HI) $\approx 10^{14}$ atoms/cm^2. Out of the 19 lines with N(HI) $\geq 10^{14}$, all of these have detected Lyman beta lines, albeit badly blended in some cases.

It would be gratifying to find a simple discriminator against unidentified metal lines but this seems impossible. An initial idea was to use the b parameter to reject metals; one might expect b for metals to be, on average, lower than for the Lyman clouds. Unfortunately there is no evidence for this in our sample; a quick check on b(CIV) revealed a very large scatter.

Consequently, we are forced to adopt a less attractive approach of making a rough estimate of the contamination to see if it could account for the apparent clustering. Since the redshift distribution of metal lines (at our high spectral resolution) is poorly known, we have to make a series of worst-case assumptions. Consider firstly just the CIV systems. Bergeron and Boisse (1984) find an equivalent width distribution for the CIV 1548 lines of

$$\frac{dn}{dzdw} = ke^{-W_r/0.51} \tag{6.1.20}$$

where W_r is rest equivalent width and $k \approx 2$. Integrating (6.1.20) over the range $W_d < W_r < \infty$ where W_d is the rest equivalent width detection limit in our data, we find

$$\frac{dn}{dz} \approx e^{-W_d/0.51} \tag{6.1.21}$$

$W_d = 0.03$Å, so the number of CIV1548 lines per unit redshift with $W_r \geq W_d$ is 0.9. We have assumed here that the form of the equivalent width distribution, derived from intermediate resolution data, holds at higher resolution. We have also taken the most pessimistic view possible that all CIV lines with W(CIV)

above the detection limit could go unnoticed. A correction must be applied to the number derived above. In Bergeron's unbiassed sample, all multiple component systems with $\Delta v \leq 300$ km/s were counted as single. At the resolution of our AAT sample, any complex velocity structure present would be seen. A reasonable estimate for the smallest scale down to which such structure could be resolved is $\sim$40 km/s which limits the number of components detected in a 300 km/s interval to 8. The maximum number of CIV1548 per unit z above the detection limit is now 0.9x8=7.2. The total redshift range used in the AAT sample (sample A) is 1.2 making the maximum number of contaminants $\approx$9. CIV1550 lines are not counted in addition to the 1548 lines since if both were present the systems would have been detected and removed from the sample. No peaks in the correlation function are seen at the CIV pair splitting ($\approx$500 km/s) nor on scales for other ion pairs. Rather, we assume that either 1548 or 1550, but not both, are in the spectral window.

Now suppose that these 9 lines contribute maximally to the observed excess of small scale splittings, i.e. that they are all together in one clump and all separations are less than or equal to the value at which the observed and random cumulative distributions for sample A differ greatest. This occurs at $\Delta v = 136$ km/s, where the number of splittings is 32 more than expected for randomly distributed clouds. The modified excess becomes 23 which is still significant at the 2σ level. The conclusion is therefore that CIV contaminants alone cannot account for the observed clustering, even given a string of worst—case assumptions.

A more realistic estimate of the number of CIV contaminators can be made as follows. Rather than integrating (6.1.20) between W_d and ∞, we choose the limits to be W_d and $2W_d$. This corresponds to the ratio of the CIV 1548/1550 oscillator strengths. For unsaturated systems, once W(CIV1548)

$\geq 2W_d$, the CIV 1550 line also becomes detectable providing it falls in the data window (which is likely more often than not since AΔv(CIV) $\approx$ 500 km/s - much less than the average spectral length). The previous assumption of allowing all of the unidentified lines to cluster together is also invalid since this would be apparent in figure 6.1.5 - the plot of $\langle\xi\rangle$ for each spectral region against z; the observed clustering is not strongly dominated by one object. These modifications lead to a maximum number of CIV 1548 lines with $W_d < W_r < 2W_d$ of 0.52. So far only CIV lines have been considered. Some other possible contaminators are CII, SiII(989,1190,1193,1260,1304,1526), SiIII, SiIV(1393,1402), MgII(2796,2803), OI, CaII(H and K), NaI(D). Even allowing some or all of the above to be present, it is difficult to see how they could account for the apparent excess. A further detail relevant to this discussion is the apparent $\langle\xi\rangle$ - z correlation. If correct, can it be explained by metal line contamination? In order for this to be so, either a) the degree of contamination must increase as z decreases, or b) the degree of contamination could remain constant (or even decrease) provided that $\langle\xi\rangle$ for the contaminants increases as z decreases. Bergeron and Boisse (1984) estimate that $dn/dz \propto (l+z)^2$ which is the same rate of evolution as for the Lyman clouds (although her sample is also consistent with no evolution) which suggests that a) may be wrong.

In conclusion, it seems improbable that our sample of absorption lines contains enough contamination to account for the observed clustering. A virtually unambiguous test would be to obtain Lyβ coverage for all the Lyα lines, and only to use those systems which have both lines detected. However, this limits the sample to strong systems only and also to $z \geq 2.4$ where the clustering appears to become weaker. space—borne observations evidently can overcome the latter constraint.

6.1.6 Summary of conclusions

The results of two independent statistical analyses of the clustering properties of the Lyman clouds indicate that clustering exists on scales of around 300 km/s down to 50 km/s, the resolution limit. Estimates of the likely contamination due to unidentified metal lines suggest that this is not likely to be a serious form of error.

6.2

6.2.1 The N(HI) and b parameter distributions

The distribution functions for N(HI) and b are shown in Figures 6.2.1 and 6.2.2. All of the AAT sample in Tables 5.1 to 5.11 was used. The data on Q2206—199 included in the clustering analysis (Carswell et al., in preparation) was not used since it has a lower s/N; whilst this is unimportant for clustering it would reduce the useful range in N(HI) for parameterising the distribution function. For the N(HI) distribution, a maximum. likelihood estimate of the best fit

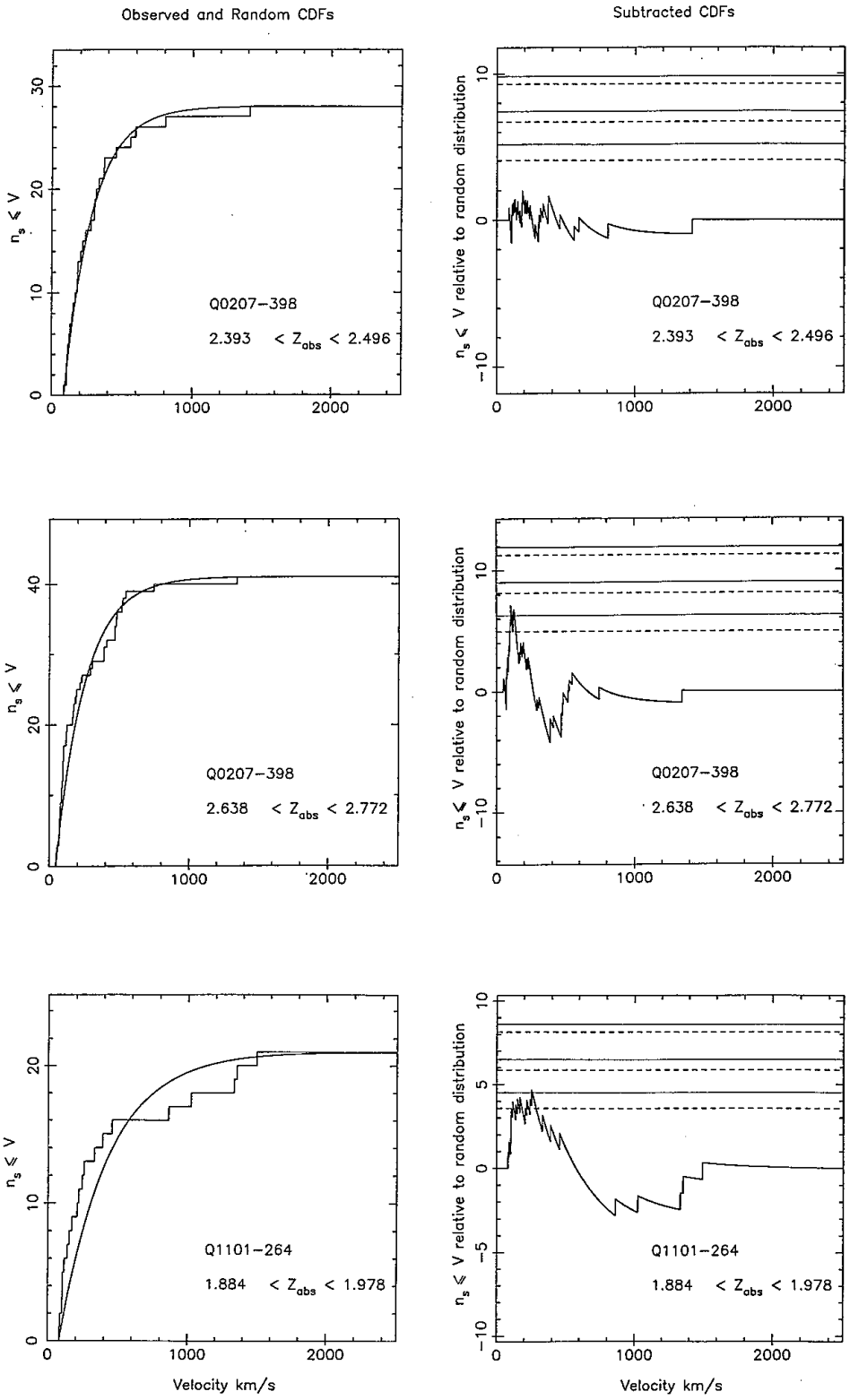

Figures 6.1.1 Cumulative distributions of velocity splittings for individual objects/wavelength regions

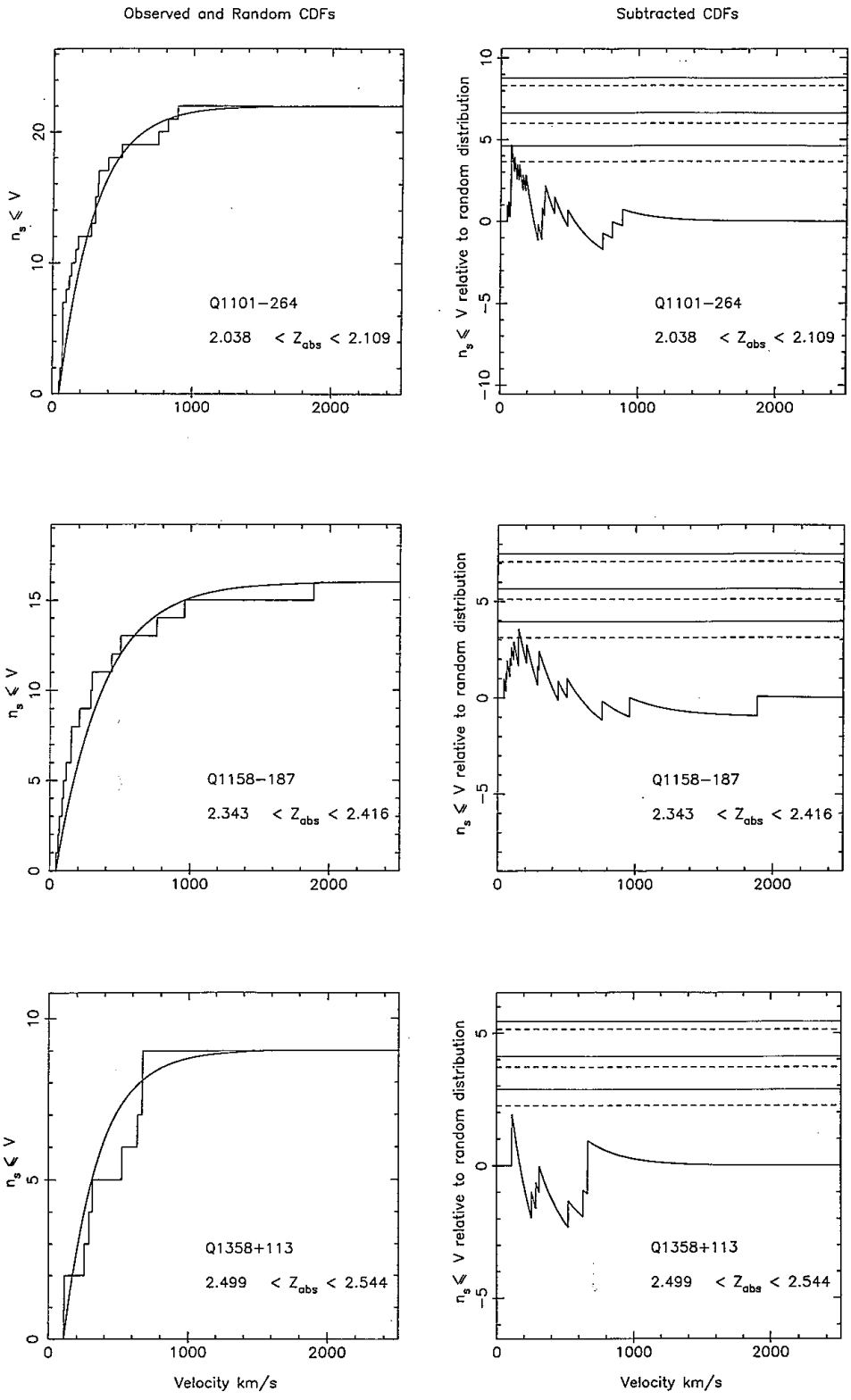
Observed and Random CDFs
Subtracted CDFs
$n_s \leqslant V$
$n_s \leqslant V$ relative to random distribution
Q1101−264
2.038 < Z_{abs} < 2.109
Q1158−187
2.343 < Z_{abs} < 2.416
Q1358+113
2.499 < Z_{abs} < 2.544
Velocity km/s

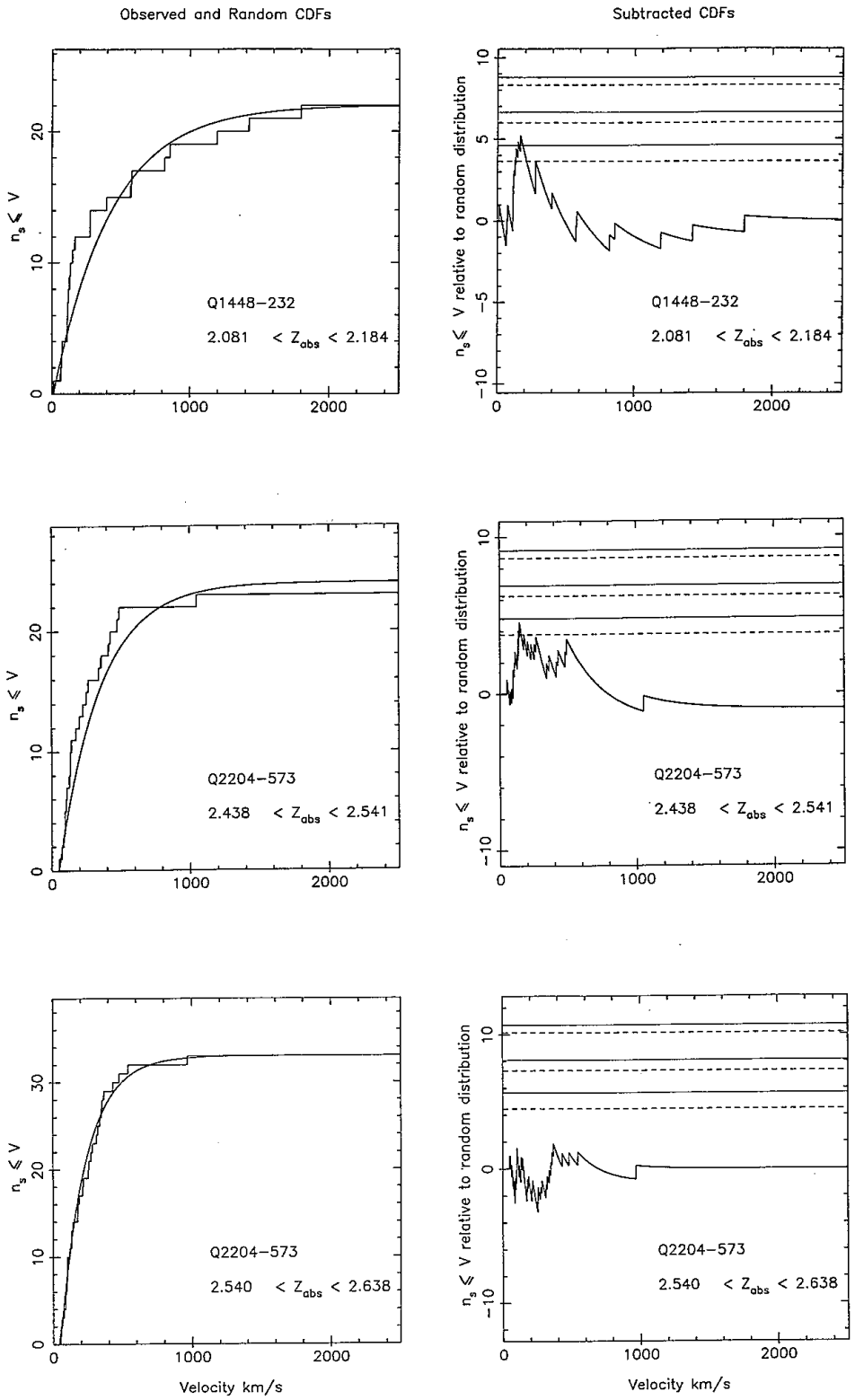
Observed and Random CDFs
Subtracted CDFs
n_s ⩽ V
n_s ⩽ V relative to random distribution
Q1448−232
2.081 < Z_abs < 2.184
Q2204−573
2.438 < Z_abs < 2.541
Q2204−573
2.540 < Z_abs < 2.638
Velocity km/s
0
1000
2000

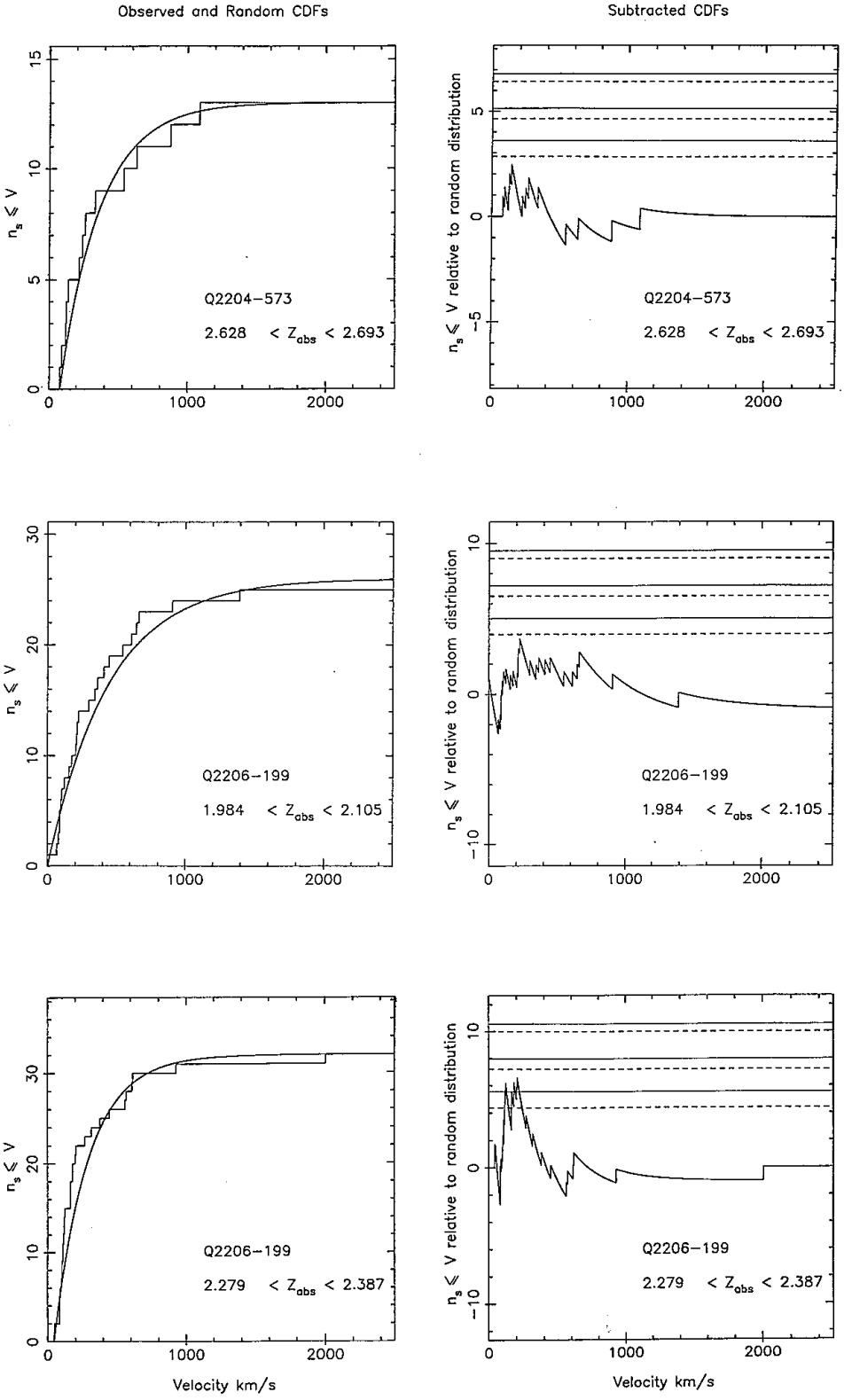
Observed and Random CDFs
Subtracted CDFs
$n_s \leqslant V$
$n_s \leqslant V$ relative to random distribution
Q2204−573
2.628 < Z_{abs} < 2.693
Q2206−199
1.984 < Z_{abs} < 2.105
Q2206−199
2.279 < Z_{abs} < 2.387
Velocity km/s

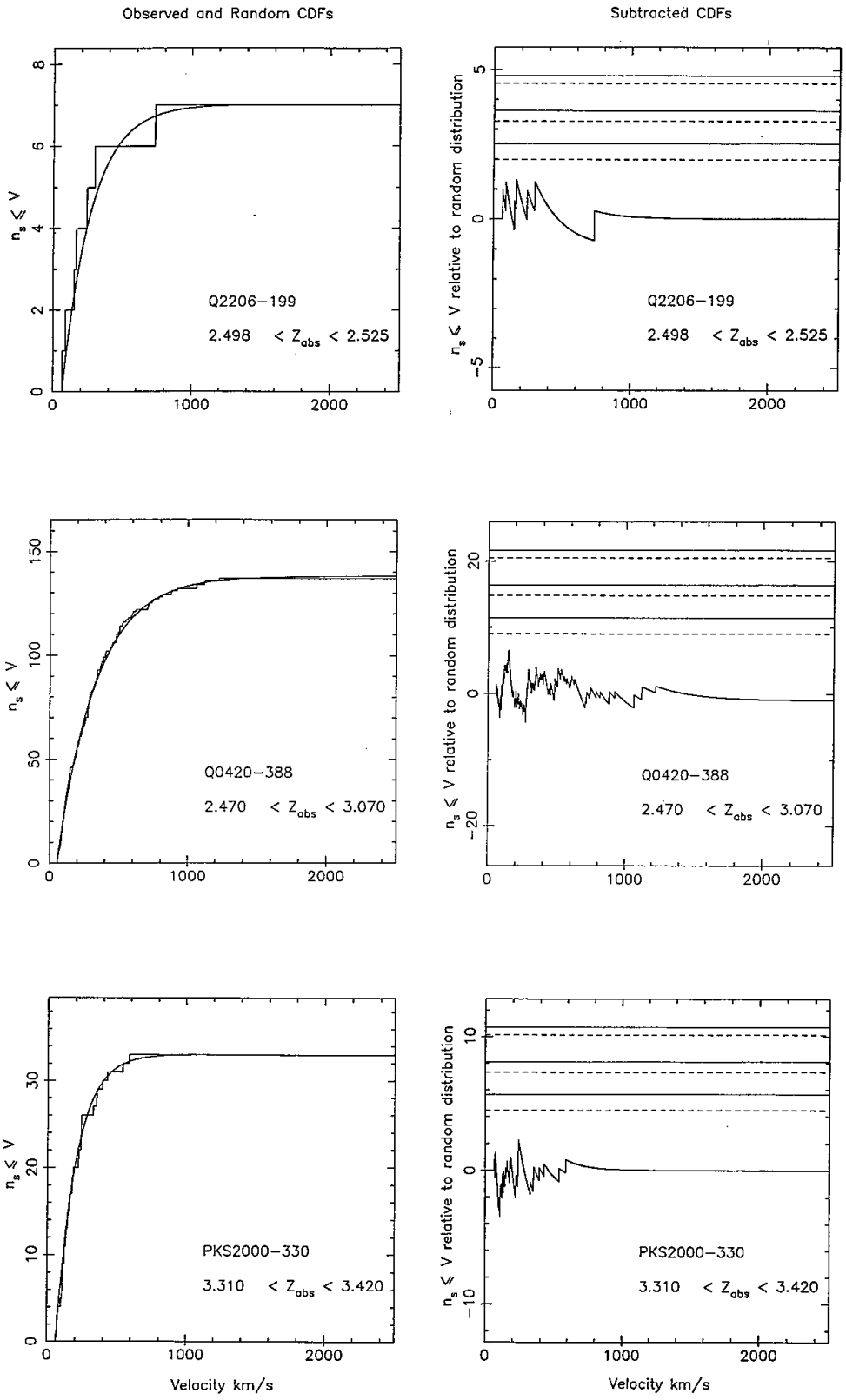
Observed and Random CDFs
Subtracted CDFs
$n_s \leqslant V$
$n_s \leqslant V$ relative to random distribution
Q2206−199
2.498 < Z_{abs} < 2.525
Q0420−388
2.470 < Z_{abs} < 3.070
PKS2000−330
3.310 < Z_{abs} < 3.420
Velocity km/s

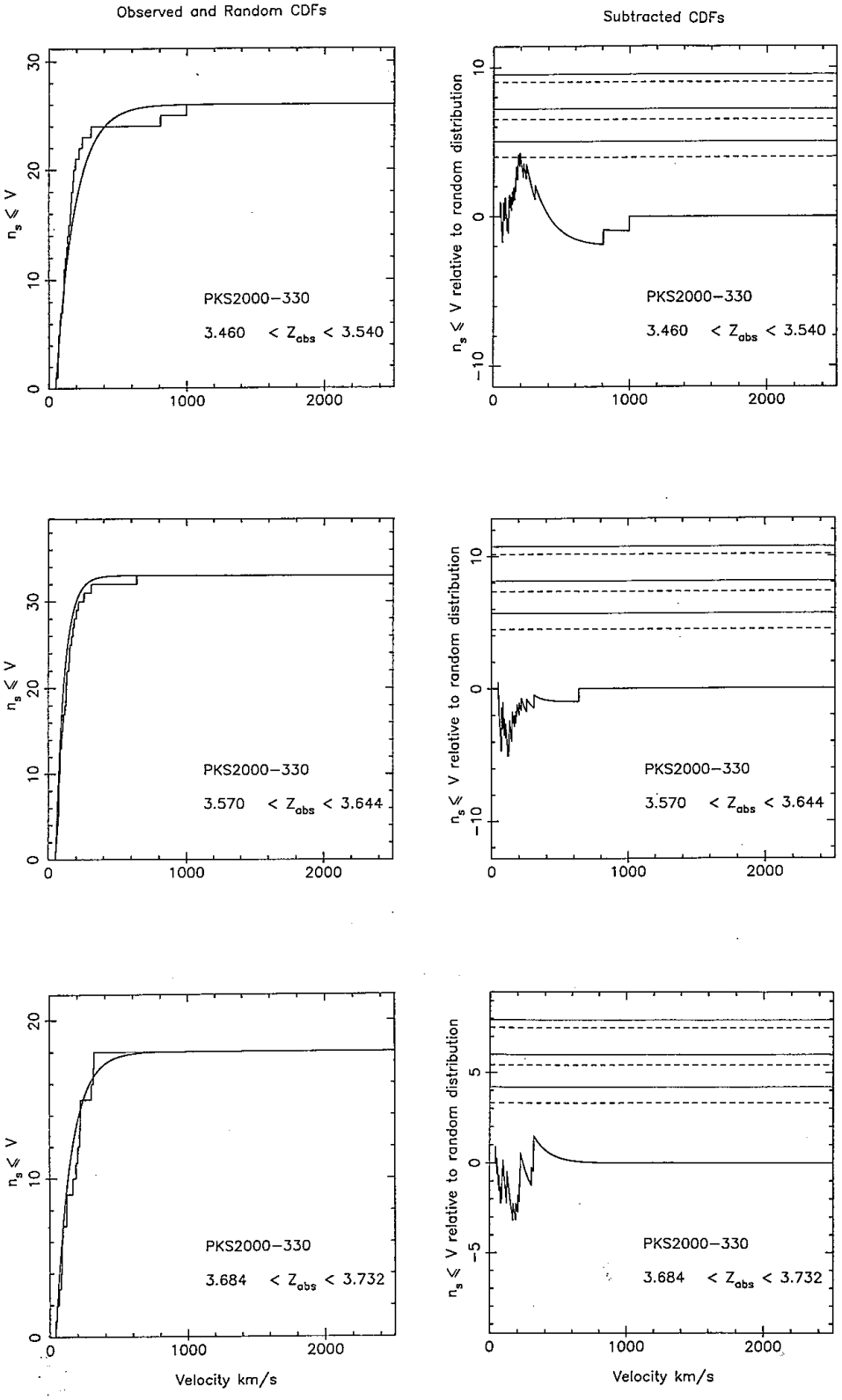
Observed and Random CDFs
Subtracted CDFs
$n_s \leqslant V$
$n_s \leqslant V$ relative to random distribution
PKS2000−330
3.460 < Z_{abs} < 3.540
PKS2000−330
3.570 < Z_{abs} < 3.644
PKS2000−330
3.684 < Z_{abs} < 3.732
Velocity km/s
Velocity km/s

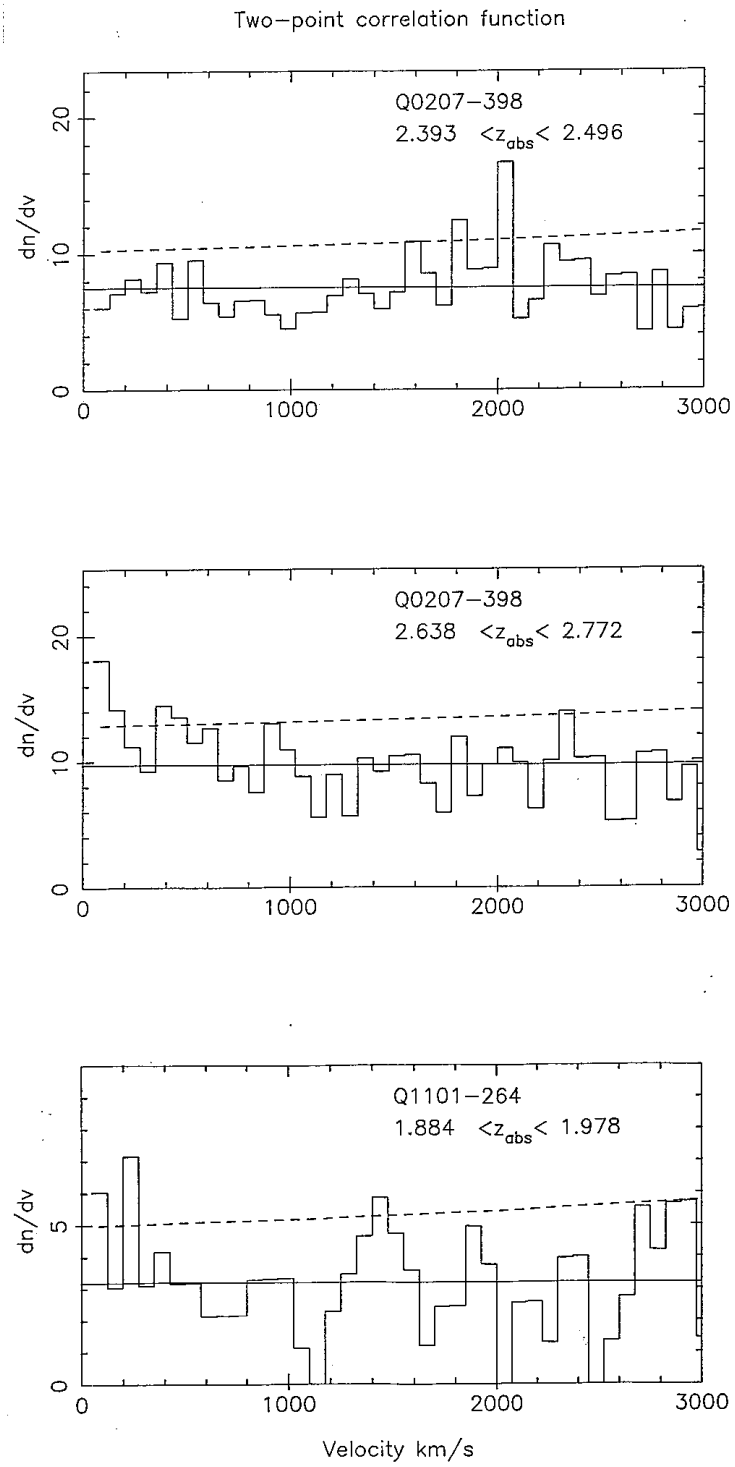

Figures 6.1.2 Two-point correlation functions for individual objects/wavelength regions

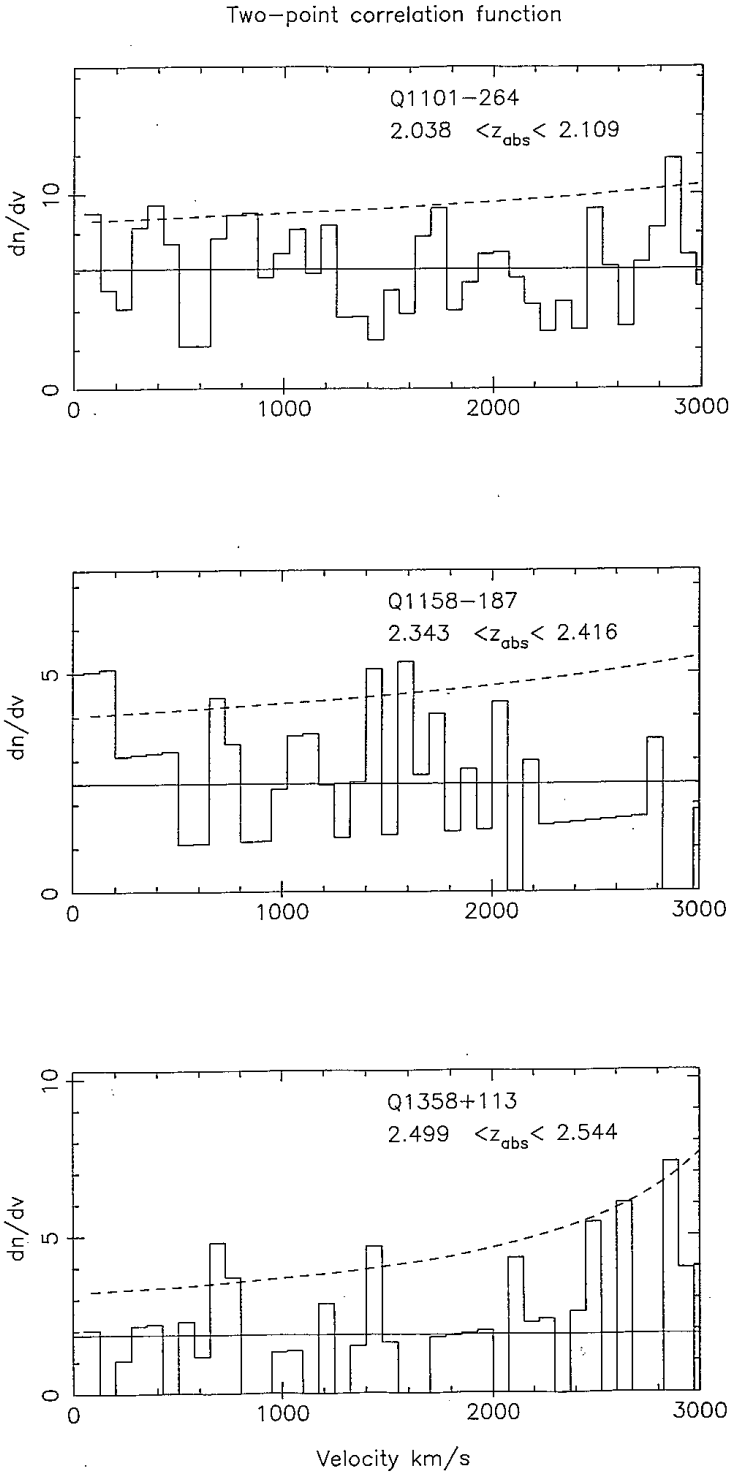
Two−point correlation function
Q1101−264
2.038 <z_abs< 2.109
Q1158−187
2.343 <z_abs< 2.416
Q1358+113
2.499 <z_abs< 2.544
dn/dv
0
5
10
1000
2000
3000
Velocity km/s

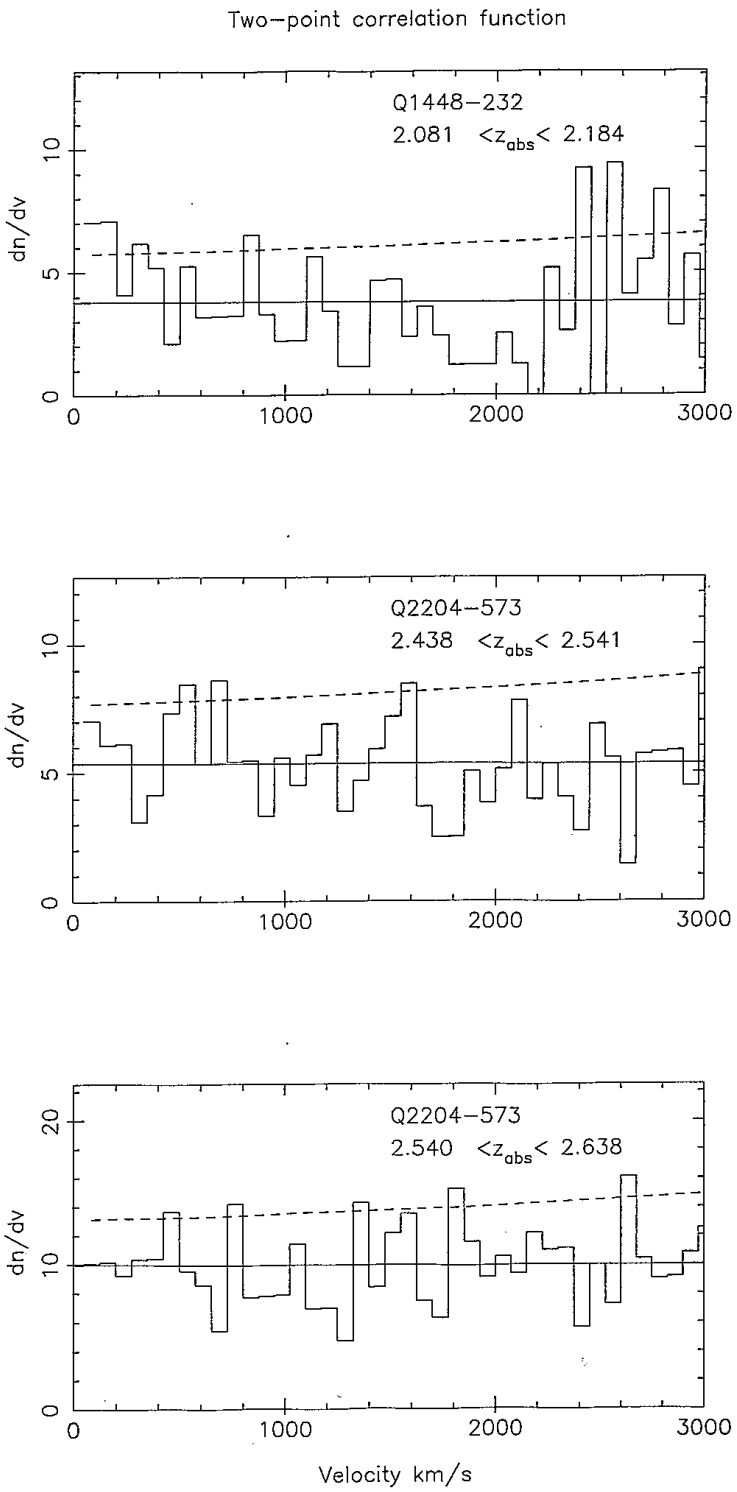
Two−point correlation function
Q1448−232
2.081 <z_abs< 2.184
Q2204−573
2.438 <z_abs< 2.541
Q2204−573
2.540 <z_abs< 2.638
dn/dv
0
5
10
20
1000
2000
3000
Velocity km/s

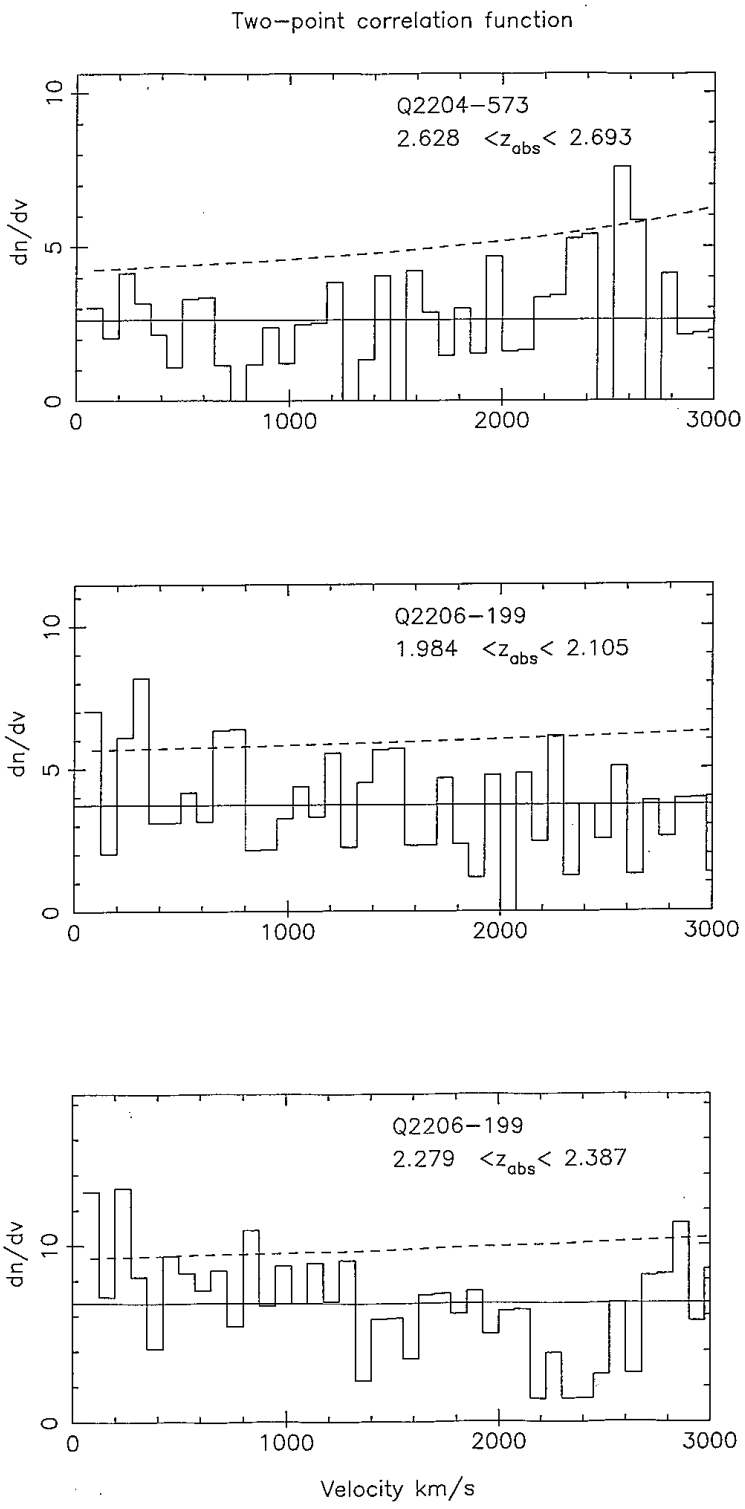
Two−point correlation function
Q2204−573
2.628 <z_abs< 2.693
Q2206−199
1.984 <z_abs< 2.105
Q2206−199
2.279 <z_abs< 2.387
dn/dv
0
5
10
0
1000
2000
3000
Velocity km/s

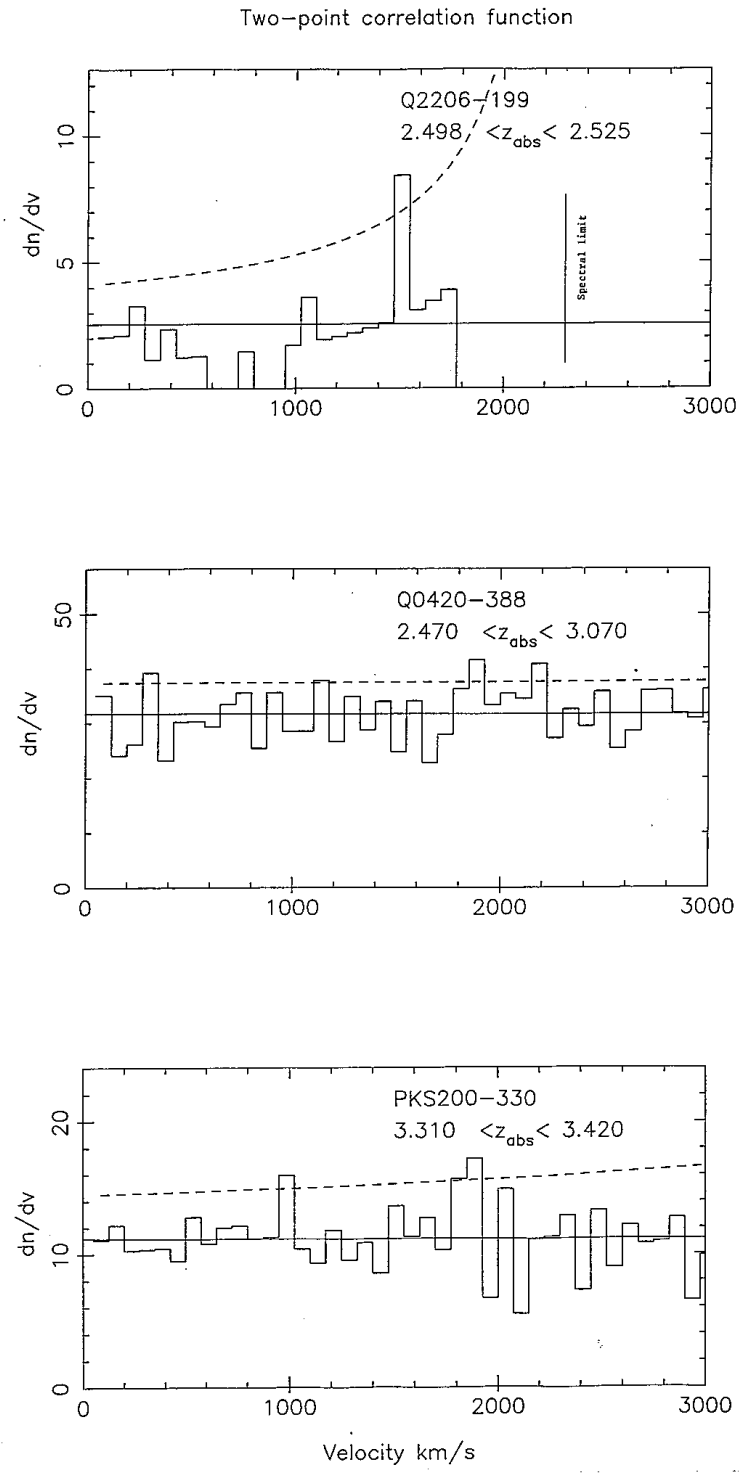
Two−point correlation function
Q2206−199
2.498 <z_abs< 2.525
Spectral limit
dn/dv
0
5
10
0
1000
2000
3000
Q0420−388
2.470 <z_abs< 3.070
dn/dv
0
50
0
1000
2000
3000
PKS200−330
3.310 <z_abs< 3.420
dn/dv
0
10
20
0
1000
2000
3000
Velocity km/s

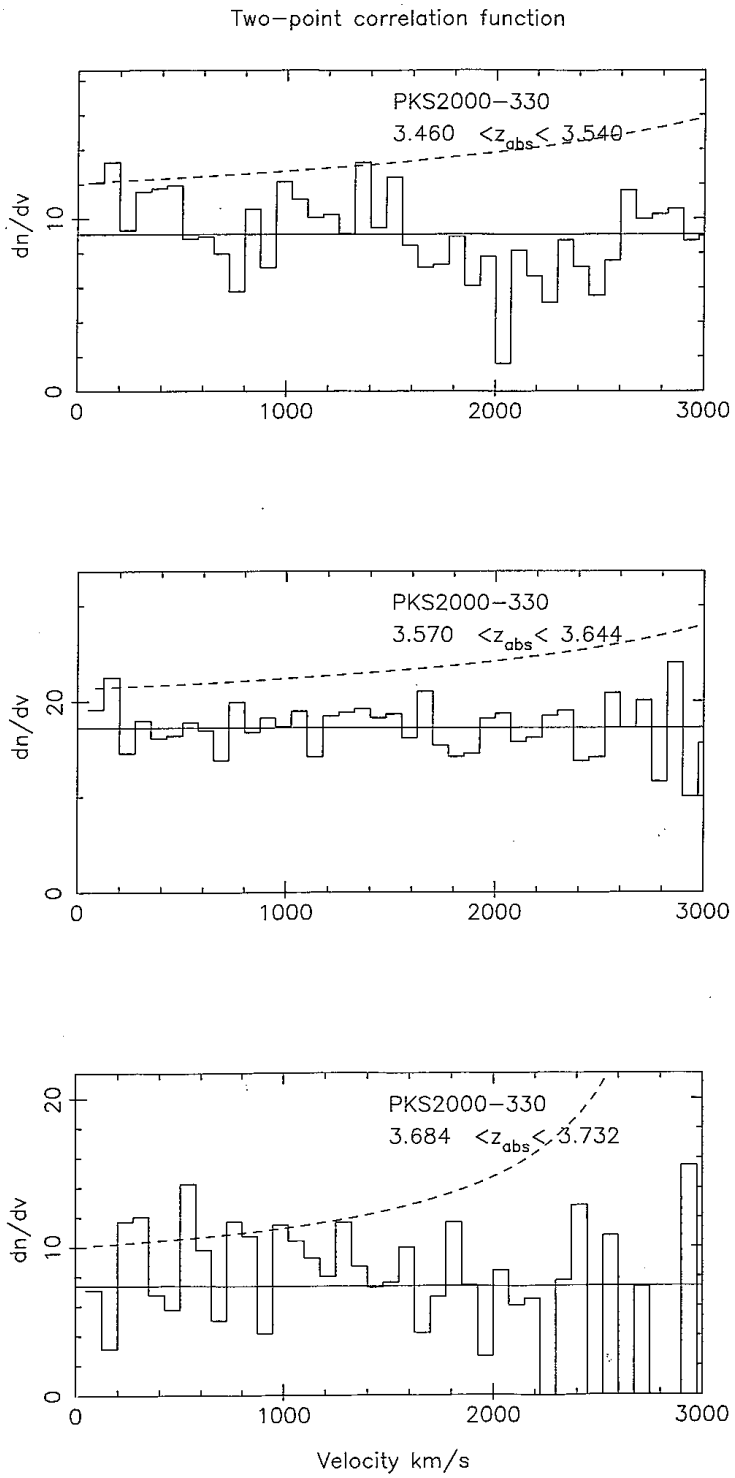
Two−point correlation function
PKS2000−330
3.460 <z_abs< 3.540
dn/dv
0
10
0
1000
2000
3000
PKS2000−330
3.570 <z_abs< 3.644
dn/dv
0
20
0
1000
2000
3000
PKS2000−330
3.684 <z_abs< 3.732
dn/dv
0
10
20
0
1000
2000
3000
Velocity km/s

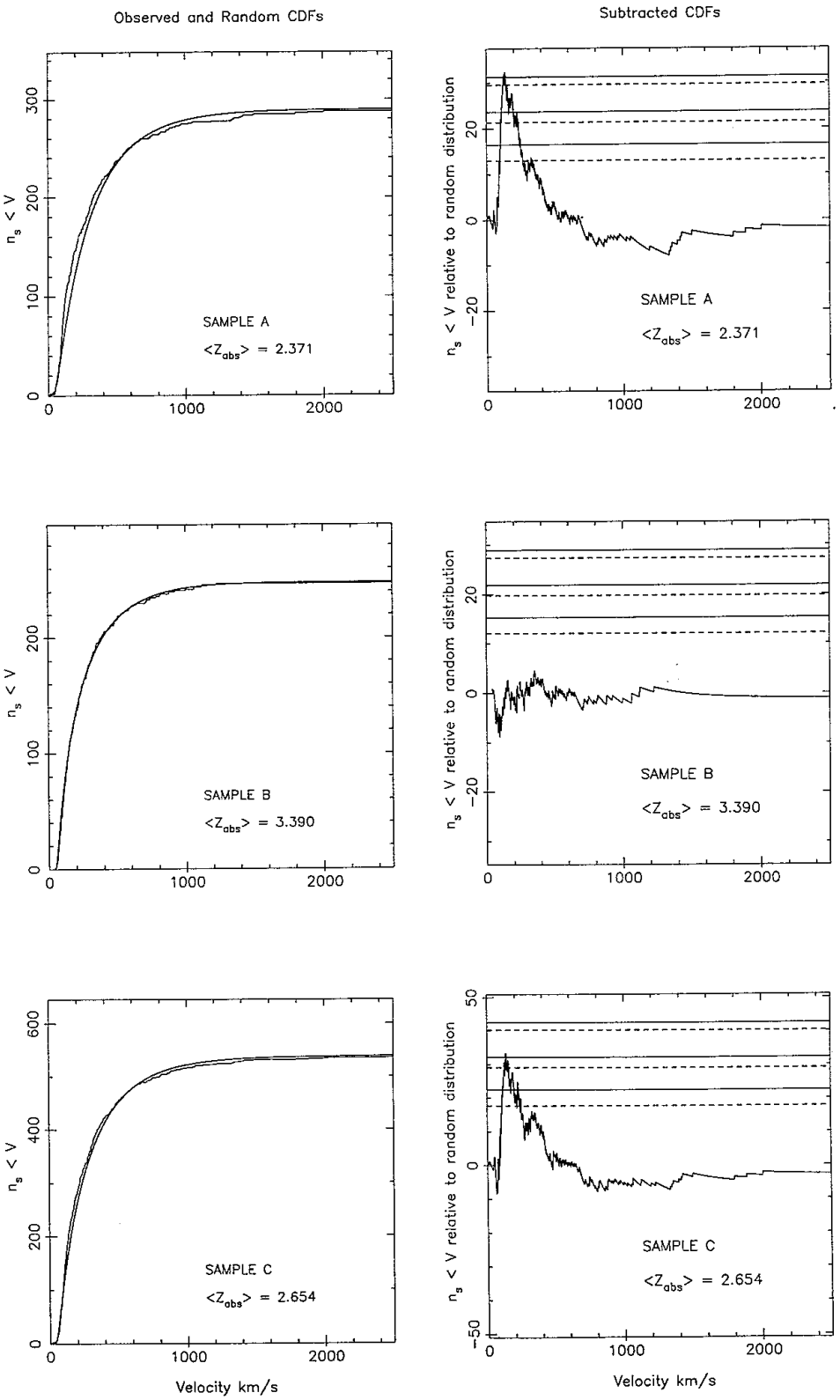

Figures 6.1.3 Cumulative distributions of velocity splittings for summed samples

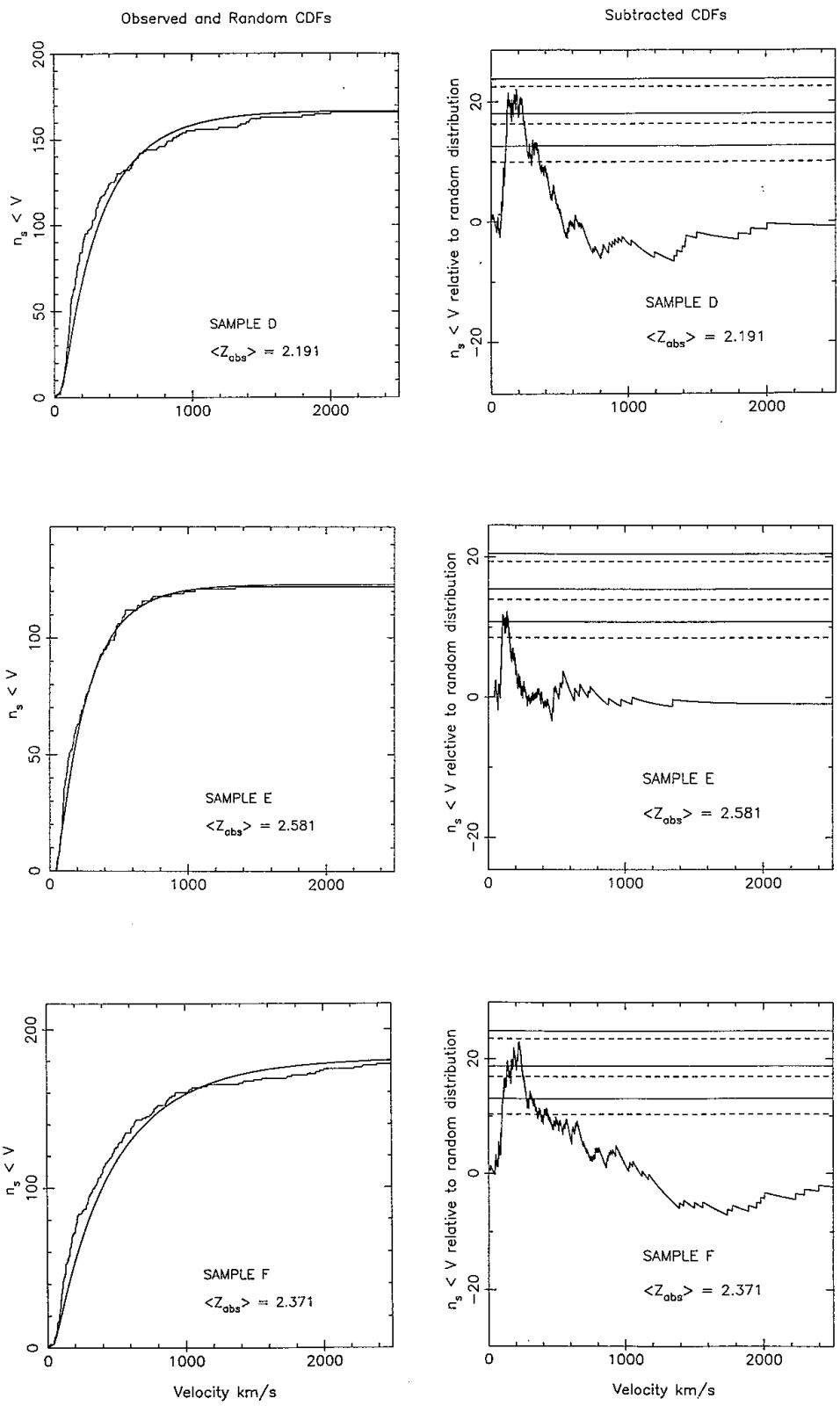
Observed and Random CDFs
Subtracted CDFs
$n_s < V$
$n_s < V$ relative to random distribution
SAMPLE D
$<Z_{abs}>$ = 2.191
SAMPLE E
$<Z_{abs}>$ = 2.581
SAMPLE F
$<Z_{abs}>$ = 2.371
Velocity km/s

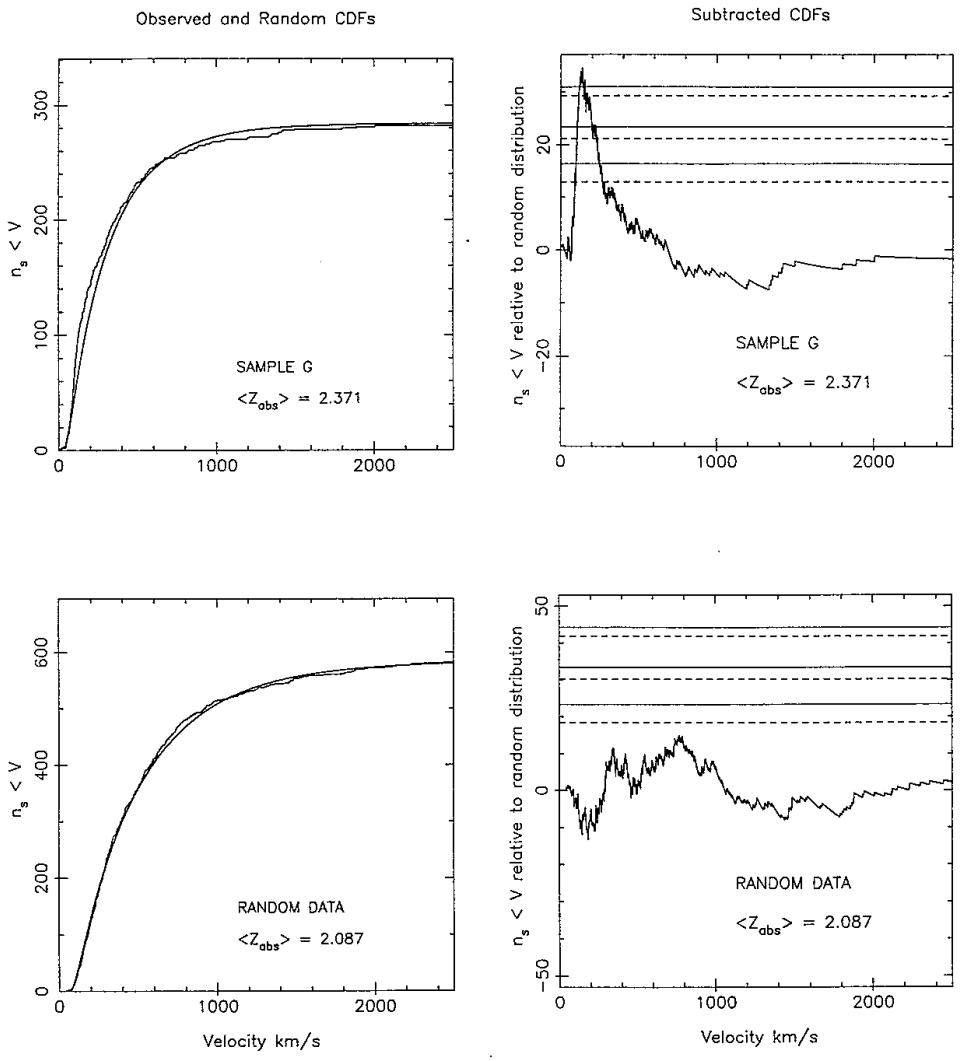
Observed and Random CDFs
Subtracted CDFs
$n_s < V$
$n_s < V$ relative to random distribution
SAMPLE G
$<Z_{abs}>$ = 2.371
SAMPLE G
$<Z_{abs}>$ = 2.371
RANDOM DATA
$<Z_{abs}>$ = 2.087
RANDOM DATA
$<Z_{abs}>$ = 2.087
Velocity km/s
Velocity km/s

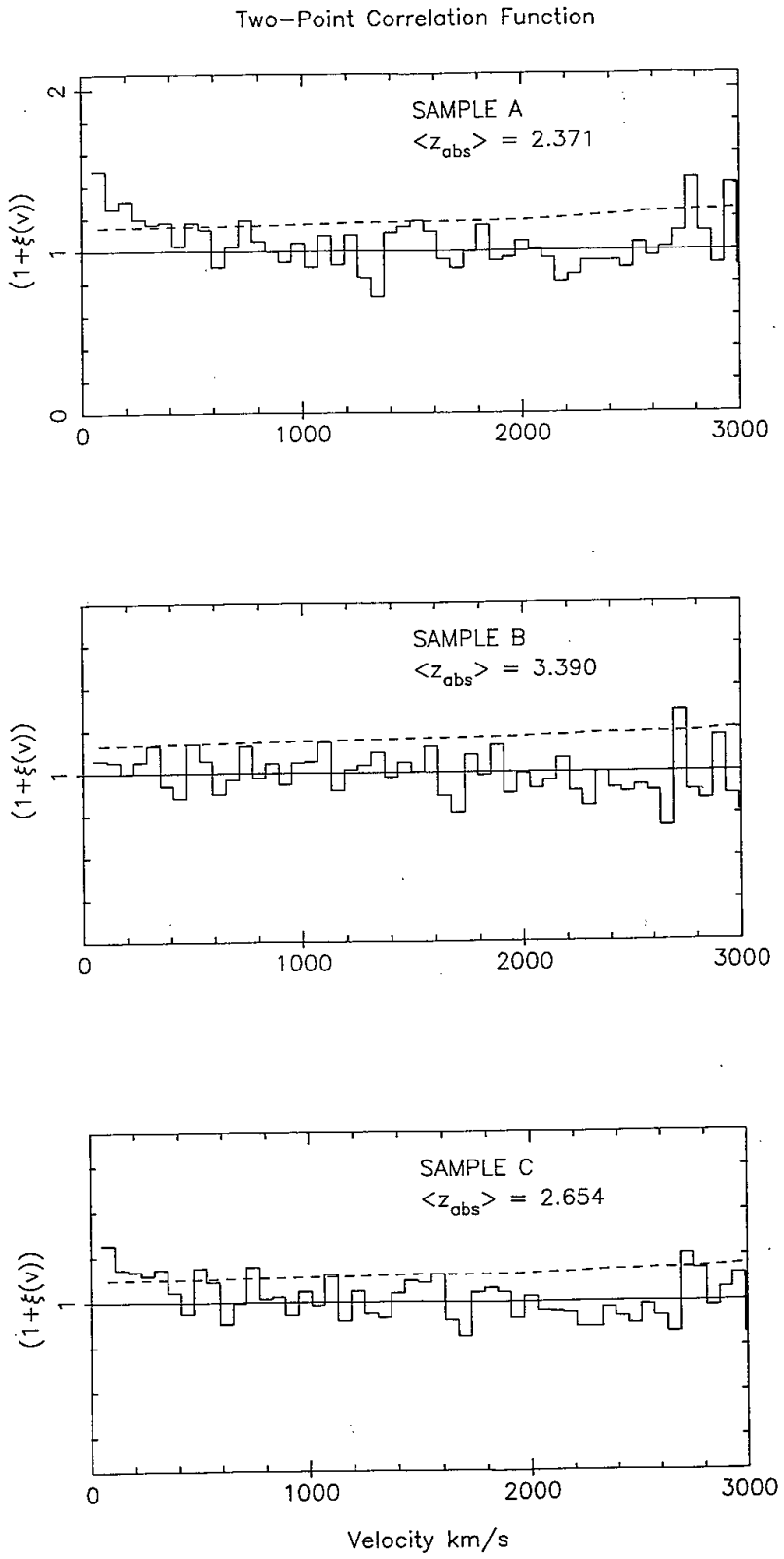

Figures 6.1.4 Two-point correlation functions for summed samples

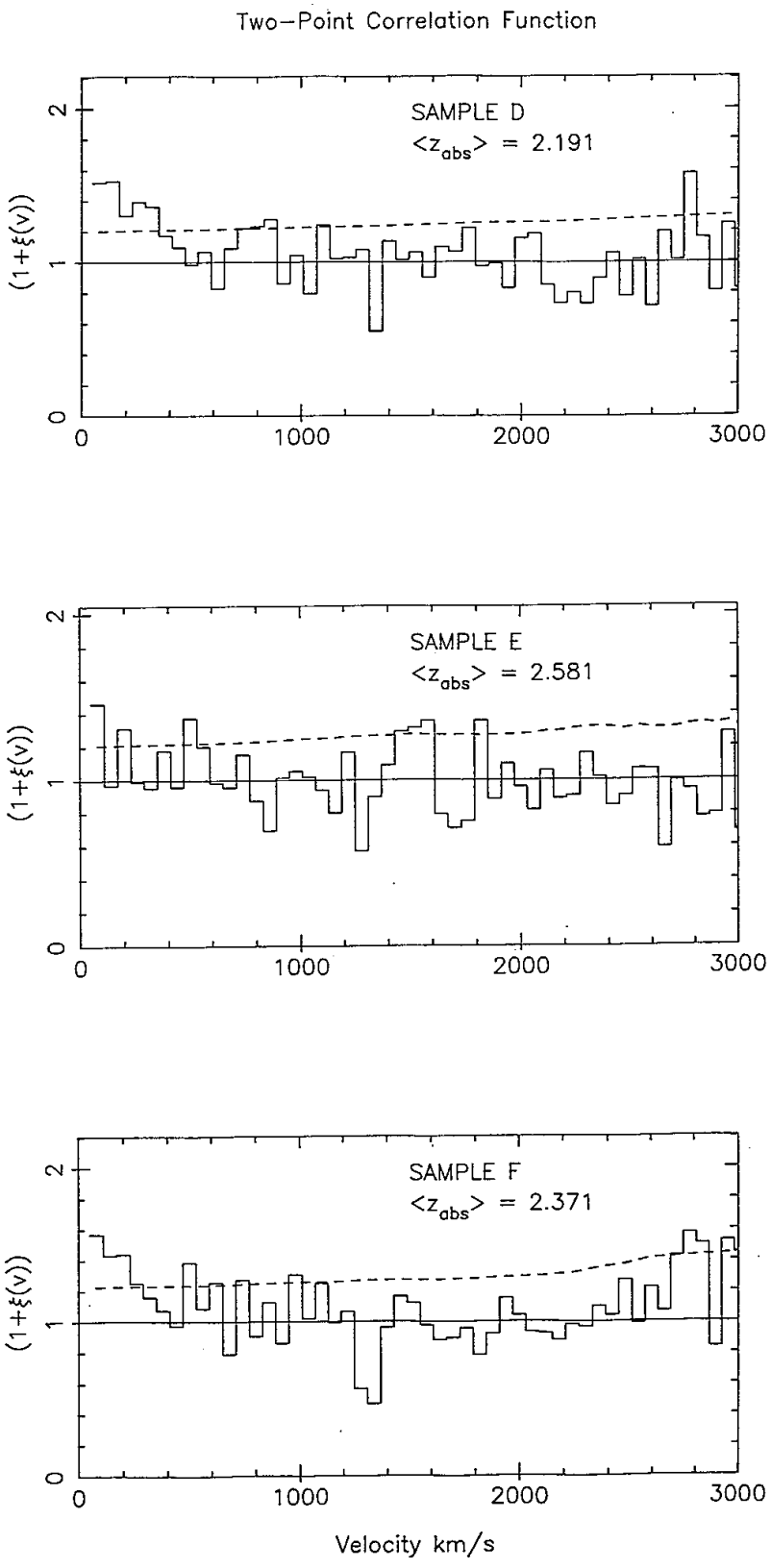
Two−Point Correlation Function
SAMPLE D
<z_abs> = 2.191
SAMPLE E
<z_abs> = 2.581
SAMPLE F
<z_abs> = 2.371
(1+ξ(v))
0
1
2
0
1000
2000
3000
Velocity km/s

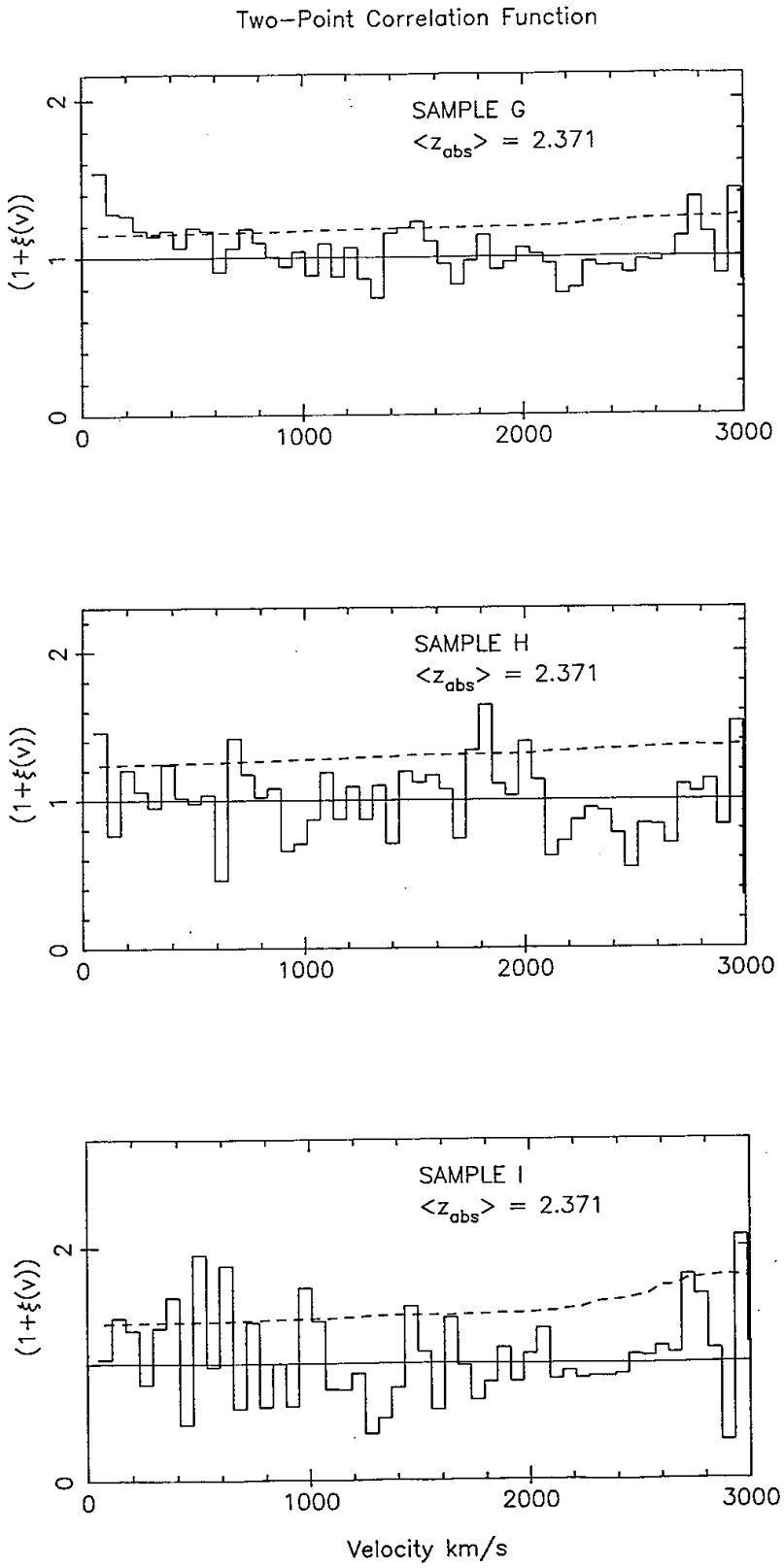
Two-Point Correlation Function
SAMPLE G
<z_abs> = 2.371
SAMPLE H
<z_abs> = 2.371
SAMPLE I
<z_abs> = 2.371
(1+ξ(v))
0
1
2
0
1000
2000
3000
Velocity km/s

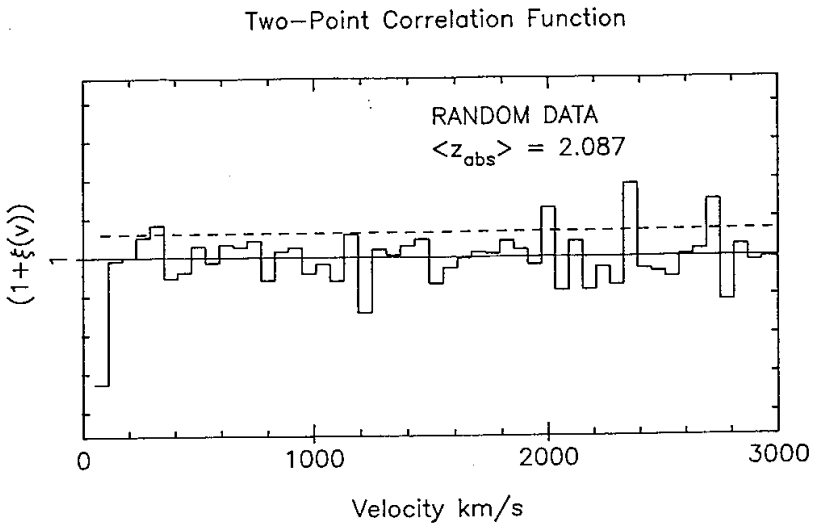

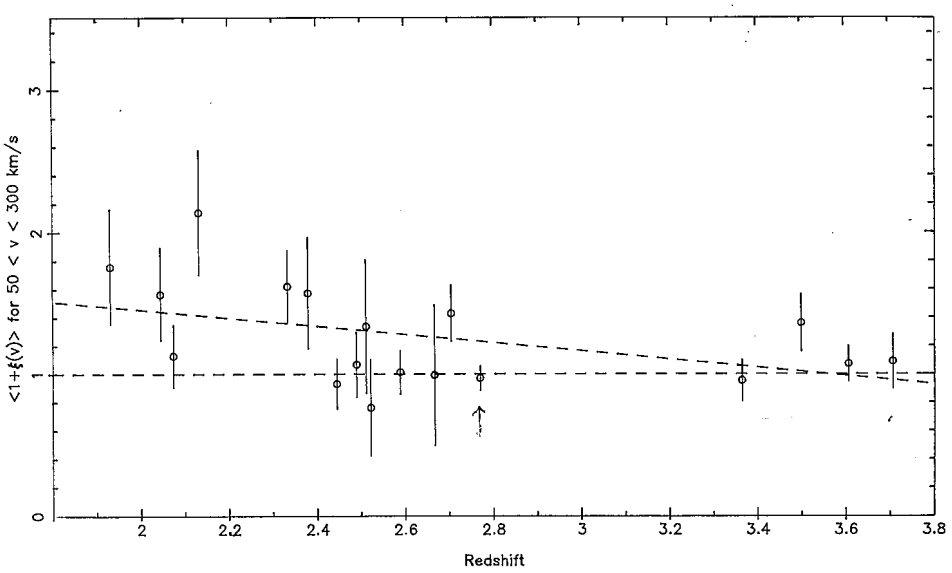

Figure 6.1.5 Redshift evolution in the clustering of the Lyα clouds

Object	Δz	n_o	v_*	V_t	n_m	D_n/n_s	p	D_n^+/n_s	p^+
0207-398	2.393-2.496	29	88.0	8971	16.2	0.07	-	0.07	0.24
0207-398	2.638-2.772	42	47.6	10857	11.0	0.17	0.81	0.17	0.91
1101-264	1.884-1.978	22	81.3	9621	5.8	0.22	0.73	0.22	0.87
1101-264	2.038-2.137	23	48.8	6907	5.0	0.21	0.71	0.21	0.85
1158-187	2.343-2.416	17	44.8	6451	2.5	0.22	0.56	0.22	0.78
1358+113	2.499-2.583	10	110.0	3866	5.7	-0.26	0.39	0.21	0.56
1448-232	2.081-2.184	23	13.5	9864	5.2	0.24	0.81	0.24	0.90
2204-573	2.438-2.541	25	51.1	8855	4.7	0.19	0.63	0.19	0.81
2204-573	2.540-2.638	34	47.9	8192	10.0	-0.10	-	0.06	0.19
2204-573	2.641-2.693	10	93.0	4245	3.4	0.13	-	0.13	0.27
2206-199	1.984-2.105	27	1.0	11923	0.1	0.14	0.26	0.14	0.63
2206-199	2.279-2.387	33	45.0	9721	6.7	0.21	0.86	0.21	0.93
2206-199	2.498-2.525	8	66.5	2271	3.1	0.19	-	0.19	0.39
0420-388	2.470-3.070	139	55.9	47745	30.1	0.05	-	0.05	0.45
2000-330	3.310-3.420	34	64.2	7560	19.6	-0.10	0.01	0.07	0.27
2000-330	3.460-3.540	27	49.7	5333	11.8	0.16	0.47	0.16	0.74
2000-330	3.570-3.644	34	51.0	4819	42.1	-0.15	0.56	0.01	0.01
2000-330	3.684-3.732	19	41.6	3086	8.5	-0.18	0.31	0.08	0.21

Explanation of columns:-

column 3 - number of lines in the sample
4 - smallest splitting detected
5 - total velocity range
6 - estimate of the number of line missed due to blending, obtained from equation 6.1.4
7 - the 2-sided maximum deviation, normalised by the number of splittings in the sample, $n_s = n_o - 1$
8 - the approximate significance level, obtained from equations 6.1.6 and 6.1.7
9 - as column 7 but for 1-sided differences
10 - " " 8 " " " "

TABLE 6.1.1

Object	Δz	n_o	1+ξ	σ	s
0207-398	2.393-2.496	29	0.93	0.20	-0.36
0207-398	2.638-2.772	42	1.57	0.24	2.38
1101-264	1.884-1.978	22	1.97	0.49	1.97
1101-264	2.038-2.137	23	1.03	0.24	0.14
1158-187	2.343-2.416	17	1.70	0.47	1.48
1358+113	2.499-2.583	10	0.60	0.35	-1.16
1448-232	2.081-2.184	23	2.13	0.50	2.25
2204-573	2.438-2.541	25	1.22	0.28	0.80
2204-573	2.540-2.638	34	1.01	0.19	0.06
2204-573	2.641-2.693	10	1.13	0.46	0.28
2206-199	1.984-2.105	27	1.35	0.35	1.01
2206-199	2.279-2.387	33	1.73	0.30	2.43
2206-199	2.498-2.525	8	1.55	0.58	0.93
0420-388	2.470-3.070	139	0.89	0.10	-1.19
2000-330	3.310-3.420	34	0.97	0.17	-0.17
2000-330	3.460-3.540	27	1.36	0.23	1.55
2000-330	3.570-3.644	34	1.08	0.15	0.56
2000-330	3.684-3.732	19	0.94	0.20	-0.31

Explanation of columns :-

column 3 - the number of lines in the table
4 - the mean value of (1+ξ) over the range 50 - 275 km/s, corresponding to 3 bins in the correlation function; the bin size was 75 km/s with the first bin starting at 50 km/s.
5 - 1σ error on above
6 - s = {[(1+ξ)-1]/σ(1+ξ)}

TABLE 6.1.2

Sample	<z>	n_s	D_n/n_s	p	D_n^+/n_s	p^+	Comments
A	2.371	287	0.11	0.9983	0.11	0.9992	AAT data
B	3.390	248	-0.04	-	0.02	0.1538	CTIO data
C	2.654	535	0.06	0.9657	0.06	0.9829	AAT + CTIO data
D	2.191	167	0.13	0.9930	0.13	0.9965	AAT $z \leq 2.42$
E	2.581	120	0.10	0.8142	0.10	0.9071	AAT $z > 2.42$
F	2.371	182	0.13	0.9930	0.13	0.9965	AAT $N(HI) \geq 3.10^{13}$
G	2.371	281	0.12	0.9995	0.12	0.9997	AAT $N(HI) \leq 5.10^{15}$
Random	2.087	584	0.03	0.0568	0.03	0.5284	No selection

Table 6.1.3 Summed CDF statistics; see table 6.1.1 for explanation of columns.

Sample	<z>	n_o	1+ξ	σ	s	Comments
A	2.371	300	1.32	0.08	3.85	AAT data
B	3.390	253	1.04	0.07	0.63	CTIO data
C	2.654	553	1.16	0.05	3.17	AAT + CTIO data
D	2.191	174	1.44	0.12	3.66	AAT z≤2.42
E	2.581	126	1.18	0.11	1.64	AAT z>2.42
F	2.371	195	1.42	0.13	3.19	AAT N(HI)≥3.10^{13}
G	2.371	294	1.32	0.08	3.79	AAT N(HI)≤5.10^{15}
H	2.371	174	1.12	0.12	0.99	AAT N(HI)≤6.10^{13}
I	2.371	126	1.14	0.18	0.75	AAT N(HI)≥6.10^{13}
Random	2.087	601	0.86	0.06	−2.55	No selection

Table 6.1.4 Summed TPCF statistics; see table 6.1.2 for explanation of columns.

power law (Carswell et al., 1987, hereafter CWBA; Atwood, Baldwin and Carswell, 1985, hereafter ABC) of the form $dp \propto N^{-\beta}dN$ gives$\beta = 1.57 \pm 0.04$. To avoid incompleteness effects, a cutoff of logN(HI)=13.3 was adopted for the fit. The redshift range is 1.9 to 2.8. A Kolmogorov—Smirnov test indicates that a single power law is a statistically acceptable fit. CWBA find $\beta = 1.71 \pm 0.10$ for a sample of Lyα lines from spectra of the two high redhift QSOs Q0420—388 and PKS2OOO—330. A higher column density cutoff of logN(HI)=13.75 was used for this sample which covers a redshift range of 2.7 to 3.7. Although the two exponents are consistent, CWBA find that a single power law does not give an adequate fit. Instead their data indicates a flattening towards lower values of N(HI).

The velocity dispersion parameters for the two samples are comparable; for the AAT data $\langle b \rangle = 38.8 \pm 1.4$ and for the CWBA sample $\langle b \rangle = 35.8 \pm 1.3$ so there is no significant change in the b parameter with redshift.

However, it is difficult to make simple comparisons between the N(HI) and b distributions for each sample because of differences in both the data and also the way in which the samples are selected. Systematic effects can be introduced

by differences in the spectral resolution and S/N, the analysis technique used to extract profile information (compare ABC's method with that in chapter 3), and the number of lines in the Lyman series used in the fitting. The number density of lines per unit redshift affects the amount of blending and the reliability of the adopted continuum level; both of these affect the parameter and error estimates. Also, the way in which the Lye sample is selected (see ABC, CWBA, and section 6.2.3) clearly biases the results.

6.2.2 The log N(HI)-b parameter diagram

It is of interest to ask whether there is any correlation between N(HI) and b for the Lyman alpha clouds. If for example gravity plays an important part in the confinement of the clouds, we might expect a correlation to exist. In the simple pressure confined picture, if all clouds have the same particle density, than clouds at the same epoch should have the same temperature and hence b parameter, unless there is a significant non—thermal component to the observed velocity dispersion which varies from cloud to cloud. Although the presence or absence of such a correlation would not unambiguously determine the confinement process, it would certainly supply another piece of the (perhaps continually expanding) jigsaw, and provide constraints for candidate cloud models.

The nature of the log N(HI) w b scatter diagram is made complex because the two variables are not randomly distributed. This has been illustrated by Carswell et al., (1984) by plotting constant probability parameter error contours for a profile fit to an absorption line in the spectrum of Q1101—264. Furthermore, not only are the error contours asymmetric, but the degree of asymmetry and the magnitude of the error depend on the parameter values themselves, or more accurately, on the location of the absorbing cloud on the

curve of growth relating to the absorption transition observed. In other words, the degree of asymmetry and the magnitude of the error depend not only on the parameter value, but also on whether just Lyα has been used for profile fitting, or Lyα with Lyβ etc. In practice, the situation is complicated still further by line blending which can contort the χ^2-parameter space even more severely. Given any particular absorption complex it is, in principle, possible to map the parameter-error space but this is a tedious operation, requiring large amounts of computing time, and is not really feasible for many more than three parameters (i.e. a single absorbing cloud). The consequence of all this is that care must be taken in the interpretation of any observed correlation between any of the three parameters N(HI), b and z.

Figure 6.2.3 shows the logN(HI)-b scatter diagram for the AAT sample. The CTIO data on Q0420—388 (Atwood, Baldwin and Carswell, 1985) and PKS2000—330 (Carswell et al., 1986) have not been included because it seems likely that the higher 1ine number densities and the slightly lower resolution could lead to spurious results. Only the AAT sample has been used, excluding that on Q2206—199. In Figure 6.2.4, the same variables are plotted but this time the data used are the synthetic sample, provided by Carswell and Lewis (unpublished), which has been profile fitted in the same way as the real data. The N(HI) distribution from which absorption lines were selected corresponded to the one inferred from the real data. The input b distribution function was peaked at 35 km/s with some small dispersion. The simulated data comprise several separate spectra. Some were generated with a dispersion around $b = 35$ km/s, some were not; this point is dealt with later. The spectral resolution is the same for the real data, but the average signal—to—noise may be marginally lower. It appears that three contours delineate the points in the logN(HI)-b plot for the simulated data, labelled A, B and C.in Figure 6.2.5. The shape of these illustrative curves can be understood in terms of the curve of growth

for hydrogen, which is shown in Figure 6.2.6. Curves B and C indicate that the measurement error is large at low N(HI) values, reducing rapidly towards higher N(HI). This is to be expected from the shape of the curve of growth; at low N(HI), on the linear part of the curve of growth, the dependence of the velocity dispersion parameter on equivalent width is weak, so the expected vertical scatter in the plot is large. Moving on to the flat part of the curve of growth, the velocity dispersion becomes rapidly more sensitive to equivalent width and increasingly less sensitive to N. This reduces the vertical scatter in the log N(HI)-b plot and increases the horizontal scatter. The line marked A corresponds to where lines are too weak to be detected above the noise in the spectra. The slight positive slope in A is slightly surprising since it suggests that low N(HI), high b lines are more difficult to detect than low N(HI), low b lines. One possible reason for this slope is that at low N, low b, lines which individually would be rejected by the initial equivalent width selection criterion are being detected in complex blends through profile information. If this were the case, a potential result would be the apparent small scale clustering which has been found. However. it is not observed in the simulated data sample. Nor is the observed clustering stronger for weaker lines than for the whole sample. These two facts suggest that the effect is not significant. Alternatively, perhaps the slope in A is due simply to the fact that as the velocity dispersion increases, the probability of blending with another line increases, and so the fraction of high b lines deblended is less than for lower b. Probably the most likely explanation is that since high b lines are spread over more data channels than low b lines, the noise in lines of fixed equivalent width increases as b increases. Consequently, high b lines could escape detection in the initial absorption feature selection procedure.

A visual inspection of Figures 6.2.3 and 6.2.4 suggests that the two distributions are rather different; above about logN(HI)=13.5 there appears to be

much more scatter in the b direction in the real data than in the simulations. There also seem to be relatively more lines compared to the whole sample at logN(HI) > 13.5 in the simulated data than in the real data; this might indicate that the input column density distribution function was not quite correct. This probably does not have any major consequences.

6.2.3 logN(HI)-b parameter correlation

Armed with a qualitative understanding of the logN(HI) - b diagram we now test for a possible correlation between the two variables. For simplicity, we compare the mean value of b in two column density bins: $2 \times 10^{13} <$ N(HI) $< 10^{l4}$ and $10^{14} <$ N(HI)$< 10^{17}$. The lower limit is chosen to be slightly above the detection limit and the upper limit so as to reject any possible metal containing systems. In addition, the criterion $5 < b < 50$ km/s is imposed since lines below 5 km/s could arise as a consequence of over-fitting to the data, and lines with b above 50 km/s may be unresolved blends. The results for both the real data and the simulated data are given in Table 6.2.1.

	Real data <b>	lines	Simulations <b>	lines
2.10^{13}<N(HI)<10^{14}	28.5±9.7	144	34.7±7.0	202
10^{14}<N(HI)<10^{17}	32.9±9.0	77	35.0±6.7	235

Table 6.2.1. All lines with 5≤b≤50 km/s were used.

In Table 6.2.2, the same quantities are tabulated, except this time the extra line selection criteria of σ(b)/b and σ(N)/N ≤ 0.4 were imposed to reject all lines which have large error estimates.

	Real data <b>	lines	Simulations <b>	lines
2.10^{13}<N(HI)<10^{14}	30.3±8.6	113	35.1±6.4	202
10^{14}<N(HI)<10^{17}	35.2±7.9	44	37.4±5.4	128

Table 6.2.2. All lines with 5≤b≤50 km/s were used. In addition, the criteria σ(b)/b, σ(N)/N ≤ 0.4 were imposed to select only the most reliable lines.

The results are quite enlightening. In the first case (Table 6.2.1) there is a difference of 4.4 km/s between the mean velocity dispersion parameters for the two column density bins. The 'error on this difference is 1.3 km/s, so there is apparently a significant tendency for b to increase as N(HI) increases. There is no such trend in the simulated dataset. The results in table 6.2.2 indicate that selecting on the basis of the parameter error may be unwise. Although the b difference for the AAT sample has increased to 4.9 km/s with error 1.4 km/s, a significant effect has now appeared in the simulated data. A difference of 2.3 km/s is found, with error 0.7 km/s. A possible cause for this is that using $\sigma(b)/b$ to select lines introduces a bias against low b lines in general, but particularly at higher N(HI) where the equivalent width changes more slowly with b so that $\sigma(b)/b$ is larger.

6.2.4 Discussion and future work

From the results of the analysis described, two alternative conclusions may be drawn concerning the existence of a logN(HI)-b correlation. In the case where the absorption lines were selected only on the basis of their b parameters (in the two N(HI) bins), there appears to be a significant trend for $\langle b \rangle$ to increase as N(HI) increases. However, if there is more intrinsic scatter in the b values for the real data compared to the simulated data, truncating the sample at lower and upper b values must result in a biased result for $\langle b \rangle$ unless the b distribution is symmetric and the two cutoffs are placed symmetrically about the true mean value. In other words, the mean is probably not a good estimator of the distribution in this case. Nevertheless, since the same correlation does not appear in the simulations, then we must conclude that either (i) N(HI) does correlate with b in the real data, or (ii) that there is a larger intrinsic dispersion in the b values for the real data than was present in the simulations. If either or both of these alternatives is correct, then the simple constant particle density-pressure confined model for the Lyman alpha clouds must be incorrect.

The conclusions outlined here should be considered as tentative since they are based on the assumption that the properties of the simulated and real samples are sufficiently similar for the two logN(HI)-b scatter plots to be directly comparable. At this stage, no tests have been carried out to verify this.

In future analyses, perhaps a more suitable method for exploring the b distribution as a function of N(HI) may be found. One possibility that should be explored is to fit an asymmetric distribution (such as the Weibull distribution for example) to the observed b histogram. The estimator could then be taken as the peak value. Some procedure like this would probably be statistically more efficient and reliable.

We have discovered that systematic errors can arise when using $\sigma(b)/b$ and/or $\sigma(N)/N$ as line selection criteria. Ideally, however, one would like selection criteria for rejecting badly blended lines, and bad blending must be reflected in the parameter error estimates. Perhaps we can get round the problems encountered by using 'normalised' error estimates to select lines; if $\sigma(\theta)_o$ is the observed error for the parameter θ, and $\sigma(\theta)_e$ is the expected error for the same feature unblended (determined from simulations), then using $\sigma(\theta)_o/\sigma(\theta)_e$ as a selection procedure might be better. A suitably chosen value for n should throw out blends and not preferentially select lines of any particular θ.

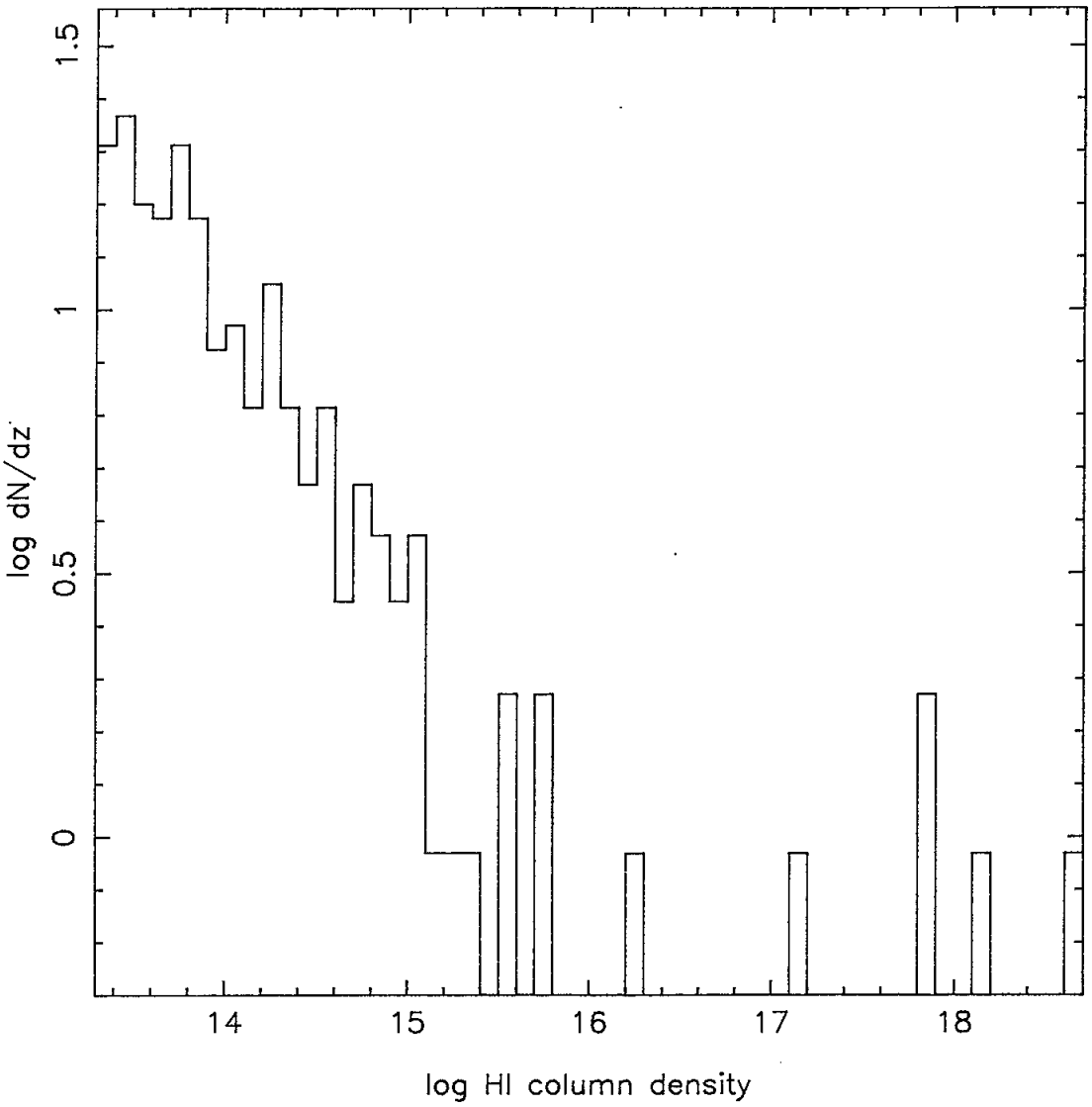

Figure 6.2.1 N(HI) distribution for the AAT sample

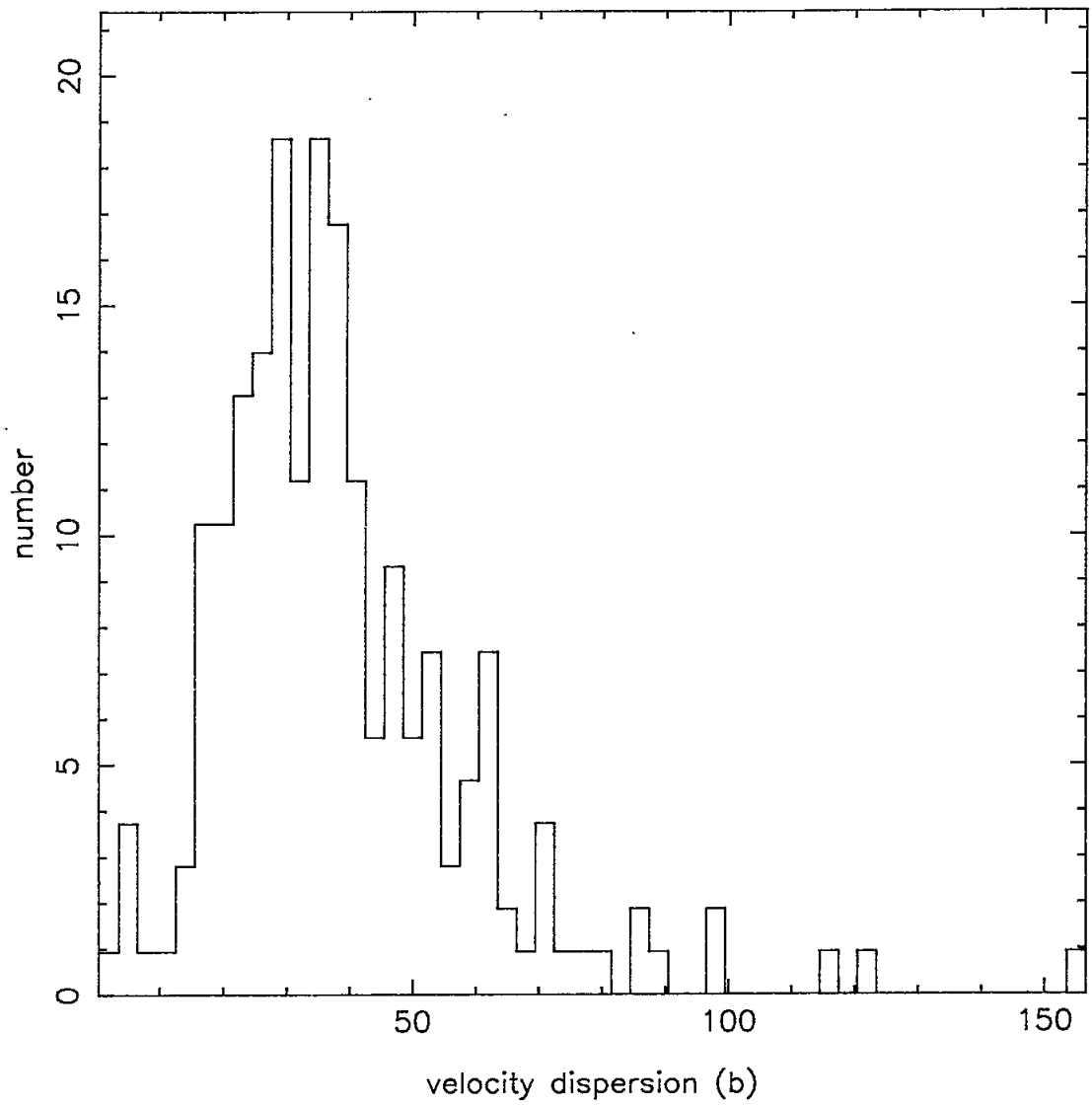

Figure 6.2.2 b parameter distribution for the AAT sample

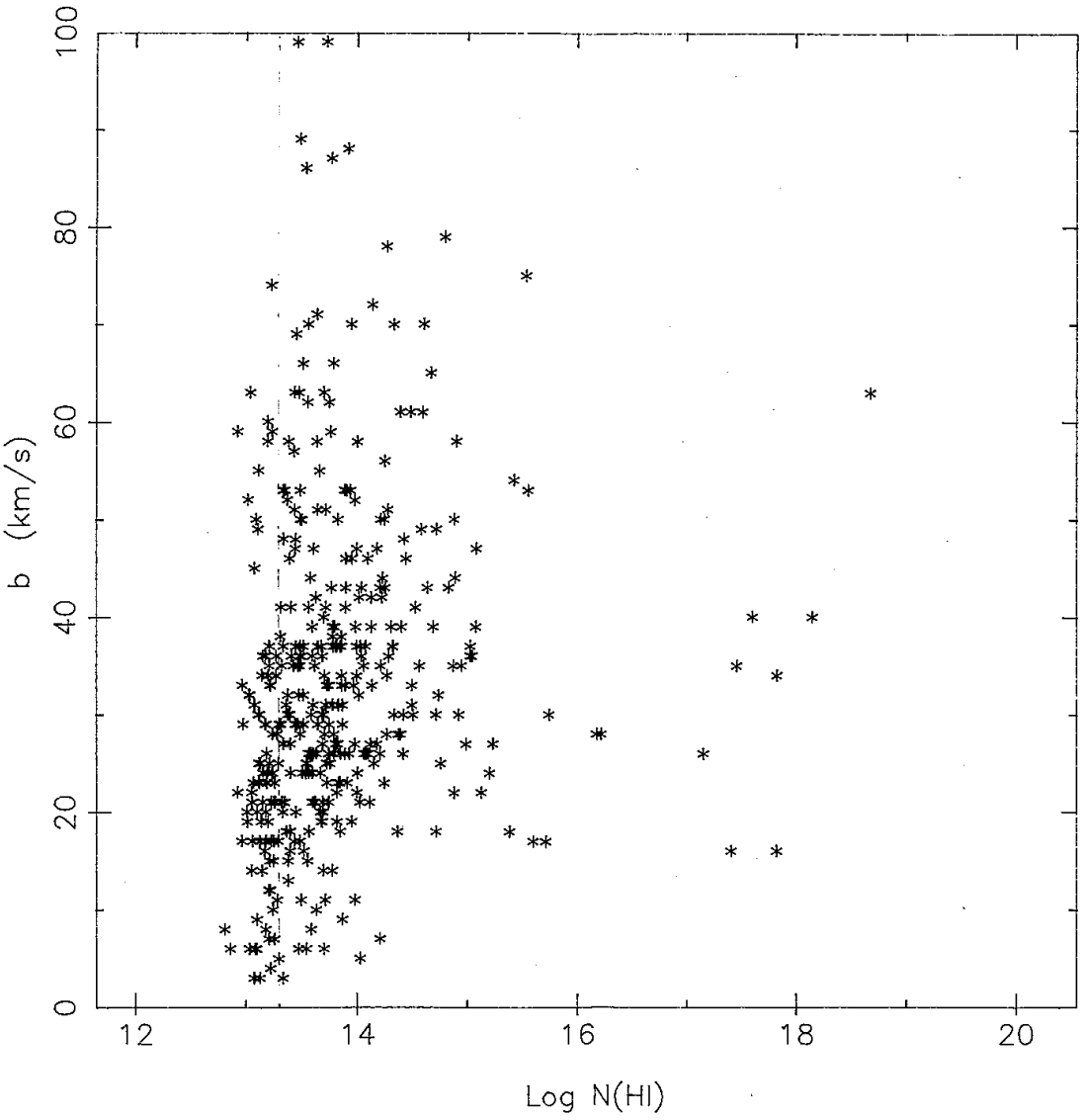

Figure 6.2.3 AAT sample

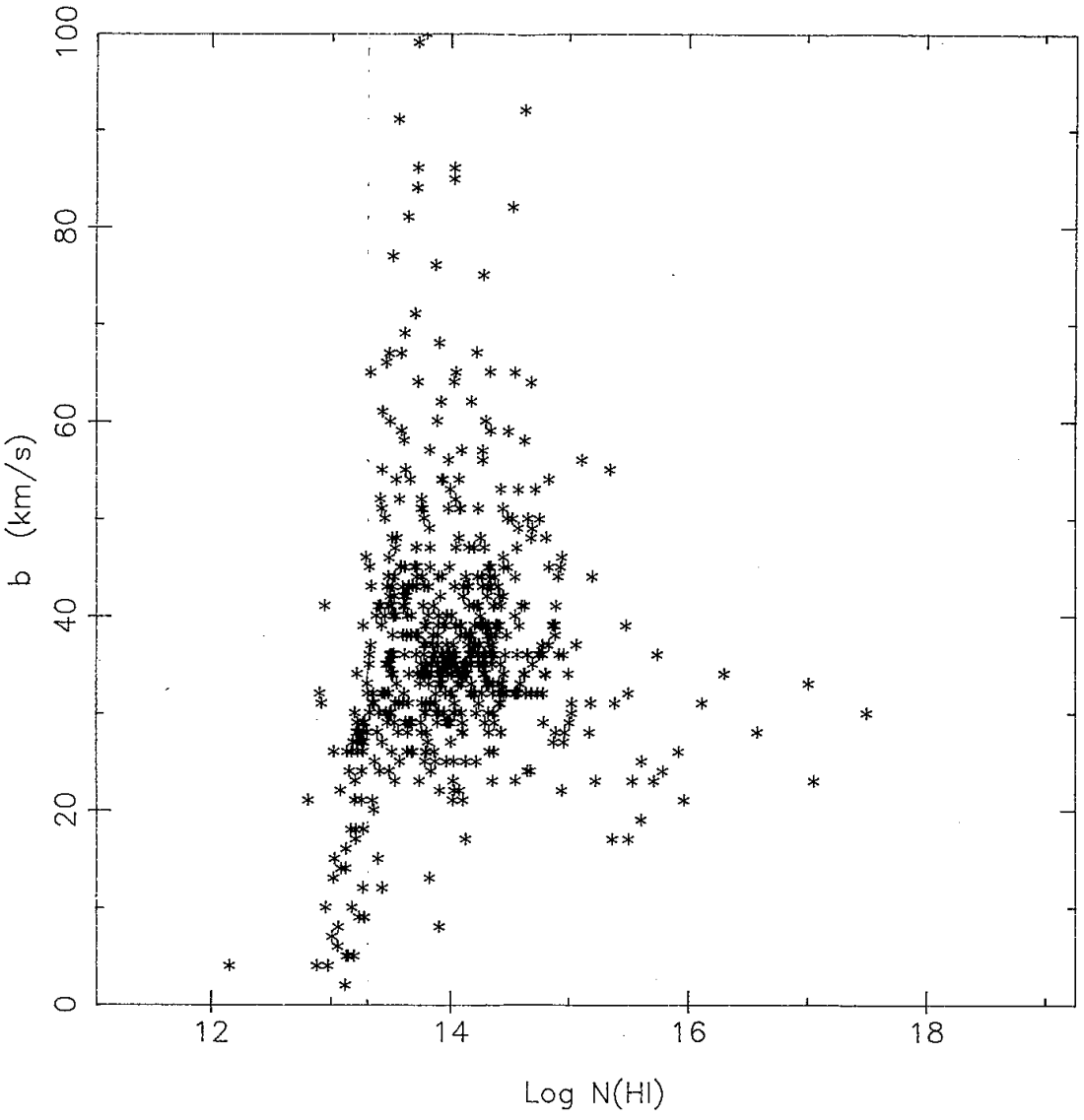

Figure 6.2.4 Synthetic sample

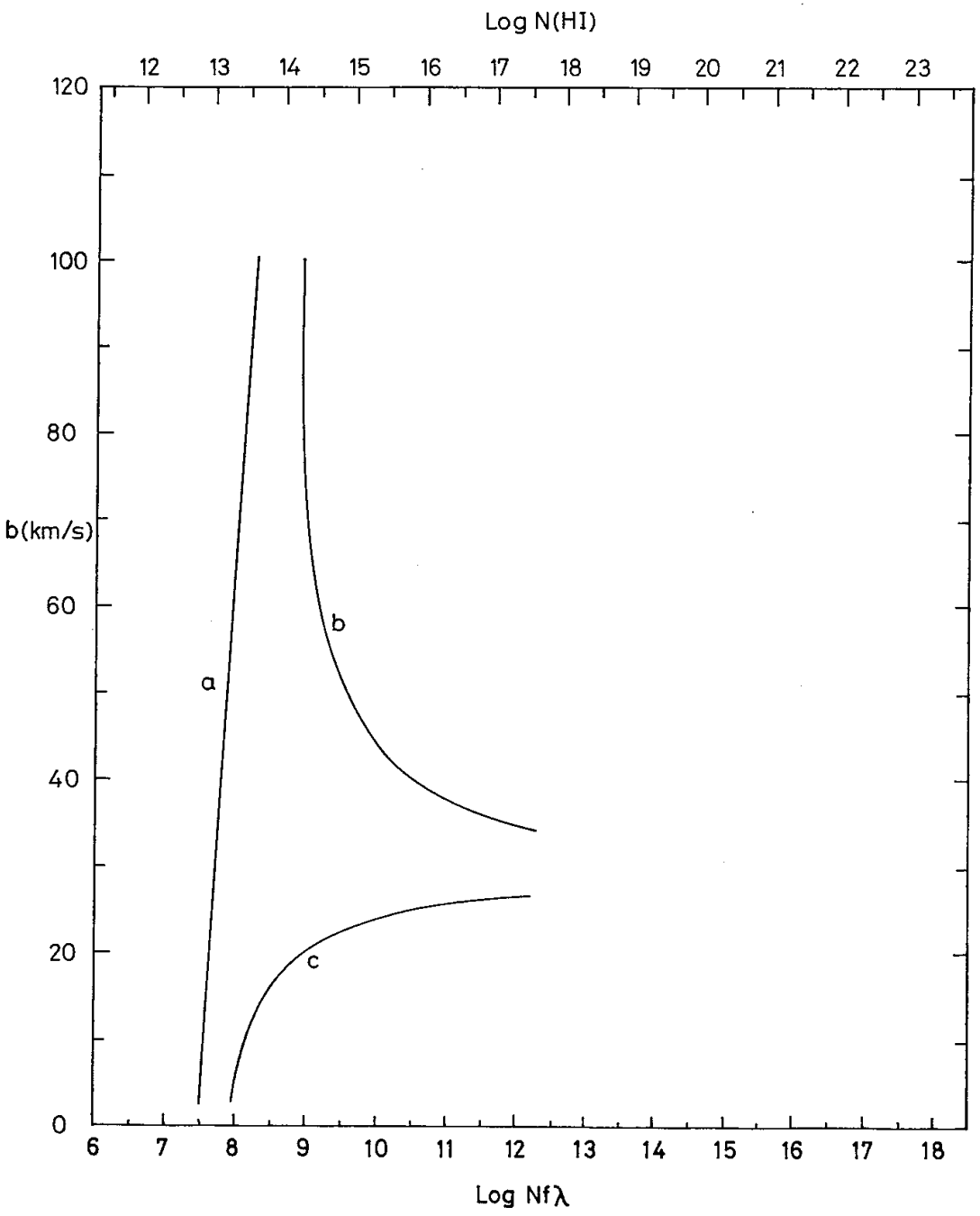

Figure 6.2.5 Schematic representation of the N(HI)-b relation

7 Conclusions and discussion

7.1 Summary of main points

There are essentially three important results arising from the work described in previous chapters and these points are now briefly summarised.

1) Profile fitting

There are numerous practical difficulties associated with profile fitting to high resolution absorption line spectra. These problems are due to uncertainties in the placement of the continuum level and line blending and become more severe at higher redshifts because of the increased number density of absorption lines. The procedure developed in Chapter 3 is a considerable advance over previous techniques and is an efficient and objective method for reliably estimating the parameters and their errors associated with each absorbing cloud.

2) D/H ratio

The importance of estimating or obtaining limits on the primordial D/H ratio has been discussed. Extensive numerical simulations have been carried out with the aim of establishing regions in parameter space which are most likely to provide useful constraints, so that candidate absorption systems can be explored in detail. The numerical simulations also served as a test of the

profile fitting method. The main point is that by using several transitions in the Lyman series a much larger region in N(HI)-b space becomes available than if only Lyα is used. In a multi-author collaboration, several spectra of the $z = 3.08$ metal containing absorption system in Q0420-388 were combined and analysed to obtain limits on the D/H ratio. This analysis demonstrated some of the practical difficulties encountered. It also showed that where metal transitions are available, the turbulent component of the velocity dispersion can be obtained and used to constrain the strength of the deuterium lines.

3) Lyman cloud clustering properties

A clustering analysis of the Lyα clouds has been carried out using two statistics; the two-point correlation function, and a new method, the cumulative distribution of line splittings which is sensitive only to small scale clustering. Both reveal that the Lyα clouds are weakly clustered on scales below about 300 km/s down to the resolution limit of around 50 km/s. This appears to be true only for clouds with $z \leq 2.4$; there is no evidence that higher redshift systems are clustered. Potential selection effects have been discussed in detail. None seem to be severe enough to account for the observed clustering. Possible interpretations of this result are outlined in the following section.

7.2 Inferences of the cloud clustering

I have demonstrated that the Lyα clouds are clustered with small amplitude on small velocity scales. There is a weak trend for the clustering strength to grow with time (i.e. as the redshift decreases). This new information on the Lyα clouds does not unambiguously favour any particular origin for these objects since it is consistent with several theoretical ideas.

For example, Fransson and Epstein (1982) suggested that Lyα absorption lines

could arise in winds from dwarf galaxies, caused by periods of enhanced star formation activity. They predicted that a detailed line profile analysis should reveal double minima corresponding to the intersection of the sight line with an expanding shell of neutral hydrogen. It is possible that the small scale clustering found represents a distribution of expansion velocities. However, if the apparent growth in with time is correct, one explanation in the context of Fransson and Epstein's model is that the star formation rate must have increased with time between $z = 3$ and $z = 2$. Alternatively, since the universe has aged by about 6×10^8 years between $z = 3$ and $z = 2$ (for $q_0 = 1/2$), it seems reasonable to expect a significant change in the absorption cross section between these two epochs. For example, for an expansion velocity of 150 km/s, the shell diameter should have increased by about 200 kpc between $z = 3$ and $z = 2$.

Chernomordik and Ozernoy (1983) have proposed that shock waves caused by explosive events in young galaxies or quasars might result in shock waves propagating through the IGM. These could lead to Lyα absorption doublets. If this is the case, we might expect the clustering amplitude (and indeed the number of Lyα lines per unit z) to follow the QSO number density.

Oort (1981) has suggested that the Lyα lines could be due to gas in superclusters of galaxies. Sargent et al. (1982) rejected this hypothesis on the basis of observations of a QSO pair whose transverse separation is less than that of a characteristic supercluster size; the positions of the absorption lines in the two adjacent lines of sight are uncorrelated. The gravitationally lensed QSO 2345+007 (Foltz et al., 1984) provide the best constraints to date on the cloud sizes. Some, but not all, of the absorption features are common to both spectra. Foltz et al. suggest that a characteristic cloud size could lie in the range 5 to 25 kpc. However the small scale clustering which has been found

implies that care should be taken in interpreting Foltz et al.'s observations; the individual cloud sizes could conceivably be somewhat smaller than 25 kpc with common absorption being the result of correlated clouds. The fact that some of the absorption lines are not common to both spectra means that at least some clouds may be smaller than the line of sight separation. Whatever the size distribution, it is clear that an individual Lyα cloud does not have the dimensions of a supercluster. Nevertheless, as Oort (1984) has pointed out, filamentary structures within superclusters could give rise to Lyα absorption; the QSO pair/lens observations do not eliminate this possibility. If, however, Lyα clouds do reside in superclusters, then some mechanism must be invoked to ensure that the Lyα clouds do not closely follow the galaxy distribution in velocity space; Sargent et al. (1980) showed that the distribution of CIV absorption doublets in QSO spectra is markedly different from that of the Lyα clouds. Selection effects could be in operation here: it is probably easier to disentangle badly blended CIV absorption complexes than Lyα ones. CIV absorption comprises a doublet with rest wavelengths 1548 and 1550. For unsaturated lines, the ratio of line strengths is the ratio of the oscillator strengths (2:1) and this extra profile information helps in locating individual lines in the presence of confusing velocity structure. In the case of HI, observations of the Lyβ line as well as the Lyα line are useful for deblending, but the difficulties are more severe since the Lyβ feature may itself be blended with lower redshift Lyα lines. Nevertheless it is hard to imagine that selection effects alone could account for the distinct difference between the CIV and Lyα correlation functions.

If the Lyα cloud distribution is completely independent of the galaxies, then the possibility exists that instead they follow the distribution of dark matter in the universe (e.g. Rees 1986). In that case we may use the observed clustering properties of the Lyα clouds to place constraints on a cold dark matter model

for the gravitational evolution of the universe. Consider an $\Omega = 1$ universe, so that the correlation function (for gravitational clustering) evolves self-similarly (Press and Schecter, 1974; Kaiser, 1986) and suppose that the observed small scale clustering found for the Lyα clouds is predominantly due to gravity. We may then write the following expression for the evolution of the correlation function

$$\xi(v_1, z_1) = \xi(v_2, z_2) \tag{7.2.1}$$

where $v_2 = v_1(1 + z_2/1 + z_1)^\gamma$, $\gamma = (n-1)/(2n+6)$ and n is the spectral index in the spectrum of initial mass perturbations in the universe (see for example Peebles, 1980, section 26). The longest baseline available to test the clustering evolution of the Lyα clouds is given by samples D and B in Chapter 6. (As discussed earlier, the two samples have slightly different spectral resolutions and signal to noise ratios but I will ignore this for the purposes of this illustrative argument.) For sample D, $\bar{z} = 2.191$, $\xi(\bar{v}) = 0.44 \pm 0.12$ and for sample B $\bar{z} = 3.390$, and $\xi(\bar{v}) = 0.04 \pm 0.07$. The first four bins (binsize 60 km/s) were used to calculate ξ and splittings less than 50 km/s were ignored because of incompleteness effects (i.e. the first bin in the correlation function starts at 50 km/s) so $\bar{v} = 170$ km/s with $50 < v < 290$ km/s. At around the 3σ level then, it seems that the clustering properties of the Lyα clouds at $z = 2.2$ differ from those at $z = 3.4$, there being no discernible clustering at the higher redshift.

According to the similarity relation (7.2.1), the clustering amplitude at $z_2 = 3.4$ on a scale v_2 may be compared with that at $z_1 = 2.2$ on a scale v_l, i.e.

$$\xi(z_2 = 3.4, \bar{v_2} = 170) = \xi(z_1 = 2.2, \bar{v_1})$$

where $\bar{v}_1/\bar{v}_2) = /(1 + \bar{z}_1/l + \bar{z}_2)^\gamma$. For the two redshifts of interest, values of the velocity scaling factor are shown below for a range of values of the index n.

n	-4	-3.5	-2.5	-2	-1	0	1	2	3
$(1+\bar{z}_2/1+\bar{z}_1)^\gamma$	2.2	4.2	0.3	0.6	0.9	1.0	1.0	1.0	1.1

In Figure 7.1, two curves are plotted: the straight line is the difference between the two correlation functions, using a fixed velocity interval for each. The mean velocity (i.e. scale) is constant for the high redshift sample (at 170 km/s), so the variable is $\bar{v}_1$. Strictly, the velocity interval should be scaled with the mean value but for this simple analysis has been kept constant; the effect is small or negligible. That the data points are so highly correlated is not surprising since adjacent bins overlap. The lower horizontal dashed line indicates the lσ error on the difference. The point of intersection of these two lines gives the minimum velocity scale shift required for compatibility between the two correlation functions. The smooth curve shows the theoretical velocity scaling factor as a function of the spectral index n. The diagram is intended to demonstrate that values of n more positive than about -2.3 are excluded at the lσ level. Note that adopting a 2σ limit lowers this limit only to around -2.0. This is consistent with the value expected in the CDM scenario for objects having a mass comparable to that of a galaxy or smaller (Blumental et al., 1984).

Finally, it is worth noting that the observed clustering scale is comparable to the velocity dispersion in a single galaxy. As pointed out by Sargent and Boksenberg (1983), if Lyα lines arise in diffuse hydrogen halos around galaxies, the cloud number density demands a halo radius of around 200 kpc or more. This seems unlikely in view of the QSO pair/lens observations. However, if the gas in these extended halos was in clumps rather than smoothly distributed, then perhaps some fraction of the Lyα absorption lines may be caused by galactic halos.

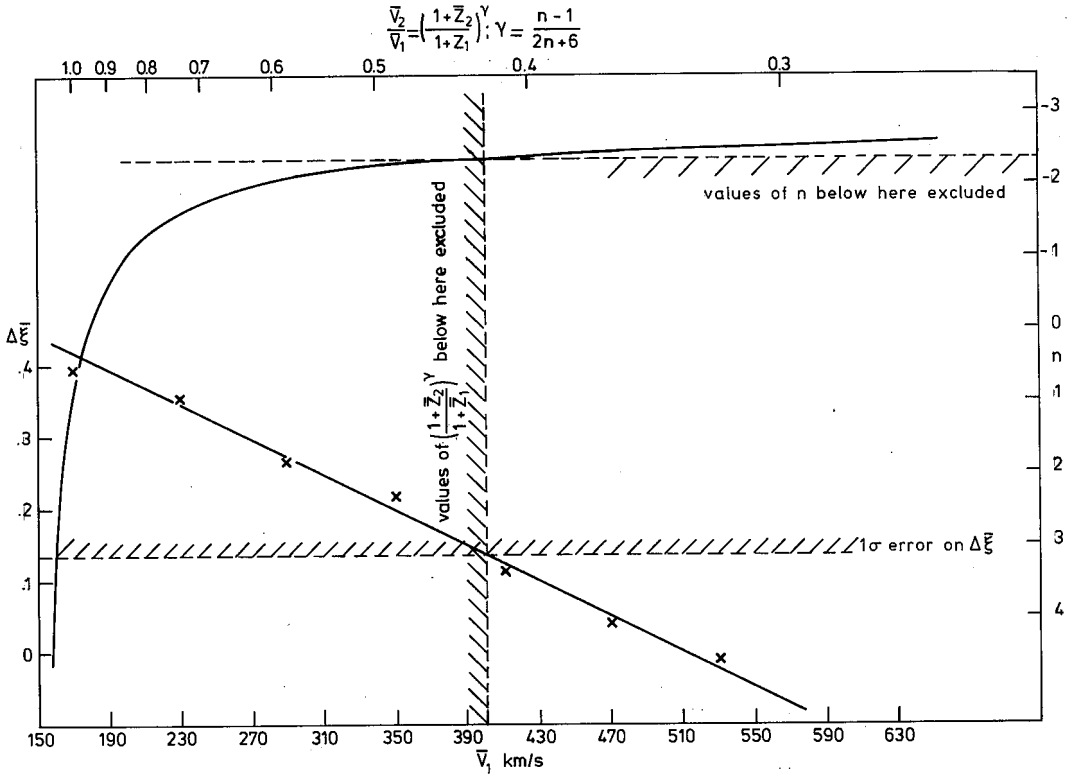

Figure 7.1 Constraints on the initial fluctuation spectrum

References

T. F. Adams. The detectability of deuterium Lyman alpha in QSOs. *A&A* , 50:461, August 1976.

B. Atwood, J. A. Baldwin, and R. F. Carswell. Echelle spectrometry of the Seyfert galaxies NGC 3783 and Markarian 509. *ApJ* , 257:559–569, June 1982. doi: 10.1086/160011.

B. Atwood, J. A. Baldwin, and R. F. Carswell. Redshift evolution of the Lyman-line-absorbing clouds in quasar spectra. *ApJ* , 292:58–71, May 1985. doi: 10.1086/163132.

J. Audouze and B. M. Tinsley. Galactic Evolution and the Formation of the Light Elements. *ApJ* , 192:487–500, September 1974. doi: 10.1086/153081.

J. N. Bahcall and E. E. Salpeter. On the Interaction of Radiation from Distant Sources with the Intervening Medium. *ApJ* , 142:1677–1680, November 1965. doi: 10.1086/148460.

J. Bergeron and P. Boisse. The evolution and origin of the sharp metal-rich absorption lines in QSO spectra. *A&A* , 133:374–386, April 1984.

P. R. Bevington. *Data reduction and error analysis for the physical sciences*. New York: McGraw-Hill, 1969, 1969.

G. R. Blumenthal, S. M. Faber, J. R. Primack, and M. J. Rees. Formation of galaxies and large-scale structure with cold dark matter. *Nature* , 311: 517–525, October 1984. doi: 10.1038/311517a0.

A. M. Boesgaard and G. Steigman. Big bang nucleosynthesis - Theories and observations. *ARA&A* , 23:319–378, 1985. doi: 10.1146/annurev.aa.23.090185.001535.

J. G. Bolton and A. Savage. New optical identifications from the twelfth part of the Parkes 2700 MHz survey: declinations -45 to -65 , right ascensions 22^h to 06^h. *Australian Journal of Physics Astrophysical Supplement*, 41:25–43, 1977.

R. F. Carswell, J. A. J. Whelan, M. G. Smith, A. Boksenberg, and D. Tytler. Observations of the spectra of Q0122-380 and Q1101-264. *MNRAS* , 198: 91–110, January 1982.

R. F. Carswell, D. C. Morton, M. G. Smith, A. N. Stockton, D. A. Turnshek, and R. J. Weymann. The absorption line profiles in Q1101-264. *ApJ* , 278: 486–498, March 1984. doi: 10.1086/161815.

R. F. Carswell, J. K. Webb, J. A. Baldwin, and B. Atwood. High-redshift QSO absorbing clouds and the background ionizing source. *ApJ* , 319:709–722, August 1987. doi: 10.1086/165491.

F. H. Chaffee, Jr., C. B. Foltz, R. J. Weymann, H.-J. Roeser, and D. W. Latham. High-resolution spectroscopy of selected absorption lines toward quasi-stellar objects. II - The metal-to-hydrogen ratio in a 'metal-free' cloud toward S5 0014 + 81. *ApJ* , 292:362–370, May 1985. doi: 10.1086/163167.

J.-S. Chen, D. C. Morton, B. A. Peterson, A. E. Wright, and D. L. Jauncey. Absorption lines in the spectra of the QSO PKS 1448 - 232. *Proceedings of the Astronomical Society of Australia*, 5:355–359, 1984.

V. V. Chernomordik and L. M. Ozernoi. Intergalactic shock waves. *Nature* , 303:153–155, May 1983. doi: 10.1038/303153a0.

D. D. Clayton. Astration of cosmological deuterium. *ApJ* , 290:428–432, March 1985. doi: 10.1086/163000.

W.J. Conover. *Practical Nonparametric Statistics*. John Wiley & Sons, 1971. ISBN 9780471168515. URL `http://books.google.com.au/books?id=NV4YAAAAIAAJ`.

G. Dahlquist and A. Bjorck. *Numerical methods*. Prentice-Hall Series in Automatic Computation, Englewood Cliffs: Prentice-Hall, 1974, 1974.

P. Delbourgo-Salvador, C. Gry, G. Malinie, and J. Audouze. Effects of nuclear uncertainties and chemical evolution on the standard big bang nucleosynthesis. *A&A* , 150:53–61, September 1985.

W. T. Eadie, D. Drijard, and F. E. James. *Statistical methods in experimental physics*. Amsterdam: North-Holland, 1971, 1971.

R. I. Epstein, J. M. Lattimer, and D. N. Schramm. The origin of deuterium. *Nature* , 263:198–202, September 1976. doi: 10.1038/263198a0.

G. D. Finn and D. Mugglestone. Tables of the line broadening function H(a,v). *MNRAS* , 129:221, 1965.

R.A. Fisher. *Statistical Methods for Research Workers*. Biological monographs and manuals. Hafner, 1958. URL `http://books.google.com.au/books?id=qqNpAAAAMAAJ`.

C. B. Foltz, R. J. Weymann, H.-J. Roser, and F. H. Chaffee, Jr. Improved lower limits on Lyman-alpha forest cloud dimensions and additional evidence supporting the gravitational lens nature of 2345 + 007A,B. *ApJ* , 281:L1–L4, June 1984. doi: 10.1086/184271.

C. Fransson and R. Epstein. Winds from dwarf galaxies and Lyman-alpha absorption features in quasar spectra. *MNRAS* , 198:1127–1141, March 1982.

P. E. Gill, W. Murray, and M. H. Wright. *Practical optimization*. London: Academic Press, 1981, 1981.

J. E. Gunn and B. A. Peterson. On the Density of Neutral Hydrogen in Intergalactic Space. *ApJ* , 142:1633–1641, November 1965. doi: 10.1086/148444.

D. L. Harris, III. On the Line-Absorption Coefficient due to Doppler Effect and Damping. *ApJ* , 108:112, July 1948. doi: 10.1086/145047.

C. Hazard, D. C. Morton, R. G. McMahon, W. L. W. Sargent, and R. Terlevich. High-redshift QSOs selected from IIIa-J objective prism plates of the UK Schmidt Telescope. *MNRAS* , 223:87–111, November 1986.

D. G. Hummer. The Voigt function: An eight-significant-figure table and generating procedure. *MmRAS* , 70:1, 1965.

M. J. Irwin. Automatic analysis of crowded fields. *MNRAS* , 214:575–604, June 1985.

N. Kaiser. Evolution and clustering of rich clusters. *MNRAS* , 222:323–345, September 1986.

D. Kunth, W. L. W. Sargent, and C. Kowal. A spectroscopic survey of emission-line objects in two fields. *A&AS* , 44:229–239, May 1981.

W. B. Landsman, R. C. Henry, H. W. Moos, and J. L. Linsky. Observations of interstellar hydrogen and deuterium toward Alpha Centauri A. *ApJ* , 285:801–807, October 1984. doi: 10.1086/162558.

D. Mihalas. *Stellar atmospheres*. Series of Books in Astronomy and Astrophysics, San Francisco: Freeman, —c1970, 1970.

H. S. Murdoch, R. W. Hunstead, M. Pettini, and J. C. Blades. Absorption spectrum of the Z = 3.78 QSO 2000-330. II - The redshift and equivalent width distributions of primordial hydrogen clouds. *ApJ* , 309:19–32, October 1986. doi: 10.1086/164573.

J. H. Oort. Superclusters and Lyman-Alpha Absorption Lines in Quasars. *A&A* , 94:359, February 1981.

J. H. Oort. Superclusters at large redshifts - Can protosuperclusters and the birth of 'pancakes' be observed? *A&A* , 139:211–214, October 1984.

P. S. Osmer and M. G. Smith. The emission-line spectra of nine newly discovered, optically selected quasars with redshift 2.5 to 3.1. *ApJ* , 210:267–276, November 1976. doi: 10.1086/154827.

B. E. J. Pagel. Abundances of elements of cosmological interest. *Royal Society of London Philosophical Transactions Series A*, 307:19–35, October 1982. doi: 10.1098/rsta.1982.0097.

B. E. J. Pagel. Nucleosynthesis. *Royal Society of London Philosophical Transactions Series A*, 320:557–564, December 1986. doi: 10.1098/rsta.1986.0136.

P. J. E. Peebles. Primordial Helium Abundance and the Primordial Fireball. II. *ApJ* , 146:542, November 1966. doi: 10.1086/148918.

P. J. E. Peebles. Primeval helium abundance and the primeval fireball. *Phys. Rev. Lett.*, 16:410–413, Mar 1966. doi: 10.1103/PhysRevLett.16.410. URL `http://link.aps.org/doi/10.1103/PhysRevLett.16.410`.

P. J. E. Peebles. *The large-scale structure of the universe*. Research supported by the National Science Foundation. Princeton, N.J., Princeton University Press, 1980. 435 p., 1980.

B. A. Peterson. QSO absorption lines and intergalactic hydrogen clouds. In M. S. Longair and J. Einasto, editors, *Large Scale Structures in the Universe*, volume 79 of *IAU Symposium*, pages 389–392, 1978.

D. W. Posener. The Shape of Spectral Lines : Tables of the Voigt Profile $(a/\pi)\int^{inf}_{-inf} e^{-y2} dy/\{a^2+(\nu\text{-}y)^2\}$. *Australian Journal of Physics*, 12:184, June 1959. doi: 10.1071/PH590184.

W. H. Press and P. Schechter. Formation of Galaxies and Clusters of Galaxies by Self-Similar Gravitational Condensation. *ApJ* , 187:425–438, February 1974. doi: 10.1086/152650.

M. J. Rees. Lyman absorption lines in quasar spectra - Evidence for gravitationally-confined gas in dark minihaloes. *MNRAS* , 218:25P–30P, January 1986.

W. L. W. Sargent and A. Boksenberg. The Lyman-Alpha absorption lines in QSO spectra. In J.-P. Swings, editor, *Liege International Astrophysical Colloquia*, volume 24 of *Liege International Astrophysical Colloquia*, pages 518–537, June 1983.

W. L. W. Sargent, P. J. Young, A. Boksenberg, and D. Tytler. The distribution of Lyman-alpha absorption lines in the spectra of six QSOs - Evidence for an intergalactic origin. *ApJS* , 42:41–81, January 1980. doi: 10.1086/190644.

W. L. W. Sargent, P. Young, and D. P. Schneider. Intergalactic Lyman-alpha absorption lines in a close pair of high-redshift QSOs. *ApJ* , 256:374–385, May 1982. doi: 10.1086/159914.

A. Savage, I. W. A. Browne, and J. G. Bolton. Redshifts of southern quasars. *MNRAS* , 177:77P–81P, December 1976.

A. Savage, J. G. Bolton, and A. E. Wright. Identification of southern radio sources. III. *MNRAS* , 179:135–141, April 1977.

P. A. G. Scheuer. A Sensitive Test for the Presence of Atomic Hydrogen in Intergalactic Space. *Nature* , 207:963, August 1965. doi: 10.1038/207963a0.

M. Schmidt. 3C 273 : A Star-Like Object with Large Red-Shift. *Nature* , 197: 1040, March 1963. doi: 10.1038/1971040a0.

P. A. Shaver, D. Kunth, and K. Kjar, editors. *ESO Workshop on Primordial Helium, Garching, West Germany, February 2, 3, 1983, Proceedings*, 1983.

M. G. Smith. A survey for emission-line galaxies and quasars. III - A list of nine new optically selected QSOs with Z between 2.5 and 3.1. *ApJ* , 206: L125–L127, June 1976. doi: 10.1086/182148.

O. Struve and C. T. Elvey. The Intensities of Stellar Absorption Lines. *ApJ* , 79:409, May 1934. doi: 10.1086/143551.

A. S. Trew and P. W. J. L. Brand. Detection of lines by a calibrated algorithm in a close pair of quasars. *MNRAS* , 211:485–495, November 1984.

D. Tytler. The distribution of QSO absorption system column densities - Evidence for a single population. *ApJ* , 321:49–68, October 1987. doi: 10.1086/165615.

A. Vidal-Madjar and C. Gry. Deuterium, helium, and the Big-Bang nucleosynthesis. *A&A* , 138:285–289, September 1984.

R. V. Wagoner, W. A. Fowler, and F. Hoyle. On the Synthesis of Elements at Very High Temperatures. *ApJ* , 148:3, April 1967. doi: 10.1086/149126.

R. J. Weymann, R. F. Carswell, and M. G. Smith. Absorption lines in the spectra of quasistellar objects. *ARA&A* , 19:41–76, 1981. doi: 10.1146/annurev.aa.19.090181.000353.

E.E. Whiting. An empirical approximation to the voigt profile. *Journal of Quantitative Spectroscopy and Radiative Transfer*, 8(6):1379 – 1384,

1968. ISSN 0022-4073. doi: http://dx.doi.org/10.1016/0022-4073(68)90081-2. URL http://www.sciencedirect.com/science/article/pii/0022407368900812.

J. Yang, M. S. Turner, D. N. Schramm, G. Steigman, and K. A. Olive. Primordial nucleosynthesis - A critical comparison of theory and observation. *ApJ* , 281:493–511, June 1984. doi: 10.1086/162123.

P. J. Young, W. L. W. Sargent, A. Boksenberg, R. F. Carswell, and J. A. J. Whelan. A high-resolution study of the absorption spectrum of PKS 2126-158. *ApJ* , 229:891–908, May 1979. doi: 10.1086/157024.

Z. L. Zou, J. S. Chen, Y. L. Bian, X. Y. Tang, and Z. X. Cui. The Statistical Analysis of L-Alpha Absorption Lines from a Uniform Sample of Nine High Redshift QSOS. *Acta Astrophysica Sinica*, 2:253, 1982.